Development and Characterization of Polypropylene, Cellulose Acetate, Magnesium Hydroxide Materials

by

Omar Mustafa Hussein Al-Kubaisi

A thesis
presented to the University of Waterloo
in fulfillment of the
thesis requirement for the degree of
Doctor of Philosophy
in
Chemical Engineering

Waterloo, Ontario, Canada, 2019

Examining Committee Membership

The following served on the Examining Committee for this thesis. The decision of the Examining Committee is by majority vote.

External Examiner:	Denis Rodrigue Professor, Dept. of Chemical Engineering, Université Laval
Supervisor(s):	Christine Moresoli Professor, Dept. of Chemical Engineering, University of Waterloo
Internal-External Member:	Beth Weckman Professor, Dept. of Mechanical & Mechatronics Engineering, University of Waterloo
Internal Member:	David Simakov Professor, Dept. of Chemical Engineering, University of Waterloo
Internal Member:	Tizazu Mekonnen Professor, Dept. of Chemical Engineering, University of Waterloo

Declaration

This thesis consists of material all of which I authored or co-authored: see Statement of Contributions included in the thesis. This is a true copy of the thesis, including any required final revisions, as accepted by my examiners.

I understand that my thesis may be made electronically available to the public.

Statement of Contribution

Chapter 4 of the thesis consists of a paper that was co-authored by myself, my supervisor, and a PhD student, Mr. Rasool Naseeri. I developed and documented the methodology. Mr. Rasool implemented the numerical integration methods (NIM) within software and conducted the numerical evaluation

Abstract

The urgency to develop and commercialize multi-component materials containing bio-based material is growing. Such materials can reduce the widespread dependence on petroleum and at the same time can reduce pollution while contributing to the economy. The demand for polymeric materials in applications such as automotive components, building materials, and the aerospace industry is increasing; however, one of the main drawbacks to use polymeric materials is their limited fire resistance.

The objective of this work was to develop polypropylene plasticized cellulose acetate materials and to explore the use of magnesium hydroxide to enhance the flame retardant properties of these materials. Specifically, the thermal stability, flammability, crystallization, and mechanical properties were investigated.

Material fabrication was accomplished using a two-step extrusion process. In the first step, cellulose acetate was plasticized with 30% triethyl citrate. The effects and viability of triethyl citrate as a plasticizer for the cellulose acetate were investigated by using differential scanning calorimetry, X-ray diffraction, and thermogravimetric analysis. Based on differential scanning calorimetry, the glass transition and the melting temperature were lowered by 39 °C and 77 °C, respectively. The effects of triethyl citrate on the degree of crystallinity of cellulose acetate was examined by X-ray diffraction. The degree of crystallinity of plasticized cellulose acetate was lower than that of cellulose acetate. According to thermogravimetric analysis, triethyl citrate lowered the thermal stability of the cellulose acetate by shifting the onset temperature of degradation and the temperature of maximum weight loss to lower temperature. According to the aforementioned analysis, cellulose acetate and cellulose acetate plasticized with triethyl citrate is applicable to be blended with polypropylene.

Formulation of the polypropylene materials was investigated according to the thermal analysis by the thermogravimetric analysis. Choosing the level of each component in the fabrication was developed sequentially, polypropylene-grafted-maleic anhydride, plasticized cellulose acetate, and magnesium hydroxide. Different levels of polypropylene-grafted-maleic anhydride (1, 2, 3 wt.%), plasticized cellulose acetate (20, 30, and 40 wt.%), and magnesium hydroxide (10, 20, 30 wt.%) were used in order to choose the optimum level of each component. Based on the thermal analysis and activation energy estimation, the highest level of each component was chosen to fabricate the multicomponent material. The results of scanning electron microscopy imaging showed that plasticized cellulose acetate

had better compatibility with polypropylene matrix. The addition of plasticized cellulose acetate was affected negatively by the addition of magnesium hydroxide. Elemental mapping was carried out by energy dispersive X-ray spectroscopy attached to the scanning electron microscope. The results show good dispersion of plasticized cellulose acetate and magnesium hydroxide.

After choosing the level of each component, which was 3 wt.% , 40 wt.% and 30 wt.% for polypropylene-grafted-maleic-anhydride, plasticized cellulose acetate, and magnesium hydroxide, respectively, the extruded materials were produced and cut into pellets. Injection molding and hot press compression molding were used to prepare the samples for characterization. Various characterization techniques were used to evaluate the inclusion of plasticized cellulose acetate and magnesium hydroxide in the polypropylene matrix.

Thermal stability and kinetic studies were investigated by using thermogravimetric analysis (TGA) under non-isothermal conditions. The thermal stability of the polypropylene materials was evaluated through their TGA and DTGA curves at four heating rates (5, 10, 20, and 30 $^{o}C{\cdot}min^{-1}$). The results revealed that polypropylene materials with presence of plasticized cellulose acetate and magnesium hydroxide had good thermal stability where the thermal decomposition took place over a wide range of temperature and the maximum weight loss temperature was shifted to higher temperature. The Kissinger, Kissinger-Akhira-Sunose (KAS), and numerical integration methods were employed to estimate the activation energy. The activation energy of polypropylene materials with presence of plasticized cellulose acetate and magnesium hydroxide was higher than those of other polypropylene materials.

Flammability and combustion behavior were examined through vertical burning, oxygen index, cone calorimeter and adiabatic bomb calorimeter tests. The results show that polypropylene with plasticized cellulose acetate and magnesium hydroxide ranked as V-0 according to the vertical burning test. The limiting oxygen index of polypropylene containing plasticized cellulose acetate and magnesium hydroxide was higher than that of polypropylene by 29%. According to the cone calorimeter test, the peak heat release rate and total heat release when the plasticized cellulose acetate and magnesium hydroxide were present in the polypropylene matrix were lower than that of polypropylene by 80% and 30%, respectively. The carbon monoxide and carbon dioxide yields revealed that polypropylene materials with plasticized cellulose acetate and magnesium hydroxide were significantly lower than that of polypropylene. The effective heat of combustion, estimated from the cone calorimeter and the heat of combustion from adiabatic bomb calorimeter, confirmed that the polypropylene material with plasticized cellulose acetate and magnesium hydroxide was less exothermic due to the reduction in the estimated heat of combustion. According to the stoichiometry of the carbon in the fuel and combustion products, the

polypropylene material with higher yield of residue in the form of soot and char showed better flame retardancy than material with lower yield of residue. The results showed that polypropylene containing plasticized cellulose acetate and magnesium hydroxide had a higher yield of residue.

Non-isothermal crystallization and nucleation morphology of the polypropylene materials was investigated by differential scanning calorimetry (DSC) and polarized optical microscopy. DSC thermograms showed that the crystallization temperature of polypropylene materials shifted to lower temperature with presence of polypropylene-grafted-maleic anhydride, plasticized cellulose acetate, and magnesium hydroxide. Development of the relative crystallinity was determined at four cooling rates. Avrami model was employed to analyze the data obtained from the DSC. Polarized optical microscopy was used to show the nucleation and crystal growth of the pure polypropylene and polypropylene plasticized cellulose acetate materials. Nucleation activity was estimated for the polypropylene materials. The results demonstrated that polypropylene-grafted-maleic anhydride, plasticized cellulose acetate, and magnesium hydroxide modified the nucleation and the crystal growth of the polypropylene materials.

The mechanical properties of the polypropylene materials showed a marginal reduction in tensile strength and the elongation at break due to the inclusion of the plasticized cellulose acetate and magnesium hydroxide. The reduction was 13% and 30% due to the addition of plasticized cellulose acetate and magnesium hydroxide, respectively. However, the addition of plasticized cellulose acetate and magnesium hydroxide increased the Young's modulus of the polypropylene materials. According to the impact test, there was a reduction in the impact strength of the polypropylene materials due to the addition of plasticized cellulose acetate and magnesium hydroxide. The impact strength reduced by 35% and 80% due to the addition of plasticized cellulose acetate and magnesium hydroxide, respectively. Differential scanning calorimetry and X-ray diffraction were used to study the effect of plasticized cellulose acetate and magnesium hydroxide on the degree of crystallinity and the crystal forms of the polypropylene materials. The addition of plasticized cellulose acetate reduced the degree of crystallinity of the polypropylene. On the other hand, plasticized cellulose acetate induced the β crystal form, positively influencing the thermal and mechanical properties. The addition of cellulose acetate and magnesium hydroxide increased the degree of crystallinity.

The most significant finding to emerge from this study is the feasibility of obtaining materials from polypropylene, plasticized cellulose acetate and magnesium hydroxide. The results of this study indicate that the materials have improved thermal stability and flame retardancy with the combination of plasticized cellulose acetate and magnesium hydroxide. Furthermore, the level of magnesium hydroxide could be reduced and reasonable flame

retardancy maintained compared to the level reported in the literature. The inclusion of the plasticized cellulose acetate and magnesium hydroxide affected some mechanical properties of the material. Polypropylene material containing plasticized cellulose acetate and magnesium hydroxide would be suitable for interior automotive components and other non-structural building materials such as electrical power insulation.

Acknowledgements

My most heartfelt gratitude, sincere respect, and immense appreciation go to my honorable supervisor Prof. Christine Moresoli. I am truly grateful for all the guidance, encouragement and support. I highly admire her knowledge and I sincerely praise her splendid kindness and exceptional generosity.

I am very grateful to my thesis committee members Professors Denis Rodrigue, Beth Weckman, David Simakov, and Tizazu Mekonnen for giving their time to review my thesis.

Special thanks go to our lab manager Ralph Dickhout and Tom Dean whose support and assistance have been invaluable.

I would like to thank Jennifer Moll and Jen Coggan for their permission to access laboratory equipment.

I would like to thank Judy Caron, Liz Bevan, and Rose Guderian from the administrative office of the Chemical Engineering Department for their utmost friendly and supportive attitude.

Many thanks to my fellow lab members Rasool Nasseri Pourtakalo, Joseph Khouri, Mohammed Elsholkami, Huayu Niu, Nikole Lyn, and Chu Yin Huang for their advice, valuable discussions, and friendship.

My special thanks go to all the faculty and staff of the Department of Chemical Engineering at the University of Waterloo for their assistance and support during this research.

My deep thanks and gratitude to my wife and my daughters, Mina and Jasmine, for their encouragement and support. I would like to say this success is a result of their dedicated effort.

I want to thank the Iraqi Ministry of Higher Education and Scientific Research and the University of Anabr, Iraq for the financial support; my sincere gratitude to them.

Table of contents

List of Figures

List of Tables

List of Abbreviations

AH	Aluminum hydroxide
APP	Ammonium polyphosphate
ASTM	American Society for Testing Materials
CA	Cellulose acetate
CA*	Plasticized cellulose acetate
CCT	Cone calorimeter test
CO_2P	Carbon dioxide production ($g \cdot s^{-1}$)
CO_2Y	Carbon dioxide yield ($kg \cdot kg^{-1}$)
COP	Carbon monoxide production ($g \cdot s^{-1}$)
COY	Carbon monoxide yield ($kg \cdot kg^{-1}$)
DS	Degree of substitution
DSC	Differential Scanning Calorimetry
E	Generic constant (13.1 $MJ \cdot kg^{-1}$ oxygen consumed)
EDAP	Ethylenediamine modified ammonium polyphosphate
EDX	Energy dispersive X-ray spectroscopy
EHC	Effective heat of combustion estimated by cone calorimeter
FE-SEM	Field emission scanning electron microscope
FIGRA	Fire growth rate index
FPI	Fire performance index
HRR	Heat release rate ($kW \cdot m^{-2}$)
ICTAC	Kinetics Committee of the International Confederation for Thermal Analysis and Calorimetry
ISO	International Organization for Standardization
KAS	Kissinger-Akhira-Sunose method for calculating kinetics parameters
LOI	Limited oxygen index method
MAH	Maleic anhydride
MH	Magnesium hydroxide
PFRs	Phosphorus flame retardants

PHRR	Peak heat release rate ($kW \cdot m^{-2}$)
POM	Polarizing optical microscope
PP	Polypropylene
PPMA	Polypropylene-grafted-maleic anhydride
SEA	Average specific extinction for smoke development ($m^2 \cdot kg^{-1}$)
TEC	Triethyl citrate
TGA	Thermogravimetric analysis
THR	Total heat release rate ($MJ \cdot m^{-2}$)
WF	Wood fiber
XRD	X-Ray Diffraction

List of Symbols

α	Confidence interval
β^*	Cooling/heating rate (^{o}C·min^{-1})
β^*_{Act}	Actual heating rate (^{o}C·min^{-1})
β^*_{Cal}	Calculated heating rate (^{o}C·min^{-1})
ΔH	Enthalpy of the decomposition reaction (kJ·g^{-1})
ΔH^o_m	Heat of fusion for 100 % crystalline polymer (J·g^{-1})
Δh_c	Heat of combustion (kJ·g^{-1})
$\Delta h^o_{f.p}$	Heat of formation of products in the standard state at 298 K (kJ·g^{-1})
$\Delta h^o_{f.r}$	Heat of formation of reactants in the standard state at 298 K (kJ·g^{-1})
ΔT	Temperature change (^{o}C)
ΔT_p	Supercooling (^{o}C)
Δt	Time corresponds to the measurement of heat release (s)
Δt_c	Apparent crystallization time (min)
Δt_{inc}	Apparent incubation time (min)
θ	Angle of X-ray incidence
λ	Wave length of the incident X-rays
φ	Nucleation efficiency
A	Frequency factor or pre-exponential factor
A_a	Area of the peaks assigned to the amorphous domain
A_c	Area of the peak assigned to the crystalline domain
A_o	Initial cross-section area of the specimen (m^2)
A_s	Surface area of specimen exposed to heat (m^2)
B	Parameters related to pure polypropylene
B, C	Parameter constant
B^*	Parameters related to multi-component polypropylene material
C^*	Calibration factor of the bomb calorimeter
C_1, C_2	Constants

C_F	Volume percent of final oxygen (%)
C_p	Molar heat capacity at constant pressure ($J{\cdot}mol^{-1}{\cdot}K^{-1}$)
c_p	Specific heat capacity ($J{\cdot}kg^{-1}{\cdot}K^{-1}$)
d	Interplanar spacing of the crystal
d_o	Interval between oxygen concentrations level
dt	Change in time (s)
dH_c/dT	Rate of heat flow ($W{\cdot}g^{-1}{\cdot}^oC^{-1}$)
E	Modulus of elasticity (GPa)
E_a	Apparent activation energy ($kJ{\cdot}mol^{-1}$)
e	Engineering strain
e_1	Correction factor to account for the combustion of the Nichrome wire
e_2	Correction factor to account for the combustion of the gelatin capsule
e_3	Correction factor to account for the formation of MgO
F	Force applied (N)
$f(x)$	Mathematical relationship of conversion with time
H_c	Heat of combustion of materials estimated by bomb calorimetry ($kJ{\cdot}g^{-1}$)
I	Intensity of the beam of the smoke detector
I_o	Intensity of reference beam of the smoke detector
K^*	Extinction coefficient
k	Constant reaction rate (s^{-1})
k_o	Factor obtained from ASTM standard for limiting oxygen index estimation
L_o	Initial length of the specimen (m)
L	Light path length
l_f	Guage length before failure (m)
l_o	Initial guage length (m)
m	Mass of the benzoic acid sample (g)
m_f	Mass of sample at the end of reaction (g)
m_o	Mass of sample at time (t = 0) (g)
m_t	Mass of sample at time (t) (g)
$\dot{m}^o_{O_2}$	Mass flow rate of oxygen in the intake air ($kg{\cdot}s^{-1}$)
$\dot{m}_a$	Mass flow rate of intake gas ($kg{\cdot}s^{-1}$)
$\dot{m}_e$	Mass flow rate of exhaust gas ($kg{\cdot}s^{-1}$)
$\dot{m}_{O_2}$	Mass flow rate of oxygen in the exhaust gas ($kg{\cdot}s^{-1}$)
n	Order of reflection of X-ray
n	Avrami exponent
OI	Oxygen index (%)
Q	Heat ($J{\cdot}g^{-1}$)
q	Total heat release ($MJ{\cdot}m^{-2}$)

$q^{'}$	Heat release rate (kW)
$q^{''}$	Heat release per unit area (kW·m^{-2})
R	Universal gas constant (R=8.314 J·K^{-1}·mol^{-1})
S	Engineering stress (MPa)
T_{∞}	Temperature at the end of crystallization (°C)
T_d	Decomposition temperature (°C)
$T_{x,i}$	Temperature corresponding to a certain heating/cooling rate and relative crystallinity or conversion (K)
T_f	Final temperature (°C)
T_g	Glass transition temperature (°C)
T_m	Melting temperature (°C)
T_o	Initial temperature (°C)
T_p	Crystallization temperature (°C)
T_{bp}	Boiling point temperature (°C)
T_{max}	Temperature at maximum rate of weight loss (°C)
t	Time (s)
$t_{1/2}$	Time required to reach 50% relative crystallinity (min)
t_{ign}	Time to ignition (s)
t_{tot}	Apparent total crystallization time (min)
V_i	Volumetric flowrate of the exhaust of cone calorimeter test (liter·s^{-1})
V_m	Molar volume (cm^3·mol^{-1})
w	Mass fraction
X_c	Degree of crystallinity
X_T	Relative crystallinity according to temperature
X_t	Relative crystallinity according to time
x	Conversion
Z_t	Rate constant containing both nucleation and growth rate information

Chapter 1

Motivation, Scope, and Thesis Structure

1.1 Motivation

Lightweight, low-cost cellulosic materials offer the potential to replace a large segment of common fillers (e.g., glass and mineral fillers) in numerous automotive interior and exterior parts. European car manufacturers have started using natural-fiber composites with thermoplastic and thermoset matrices for certain car components, including door panels, seat backs, headliners, package trays, dashboards, and interior parts [1]. European Union and Asian countries have released rigorous rules for utilizing bio-composite materials in the automotive industry. European Union legislation introduced in 2006, increased the insertion of bio-composite materials in automotive components to around 80% [2]. In Asian countries, such as Japan, 88% of a vehicles composition is needed to be recoverable by 2005 and it was expected to rise to 95% in 2015. As a result, automakers have been paying more attention to a vehicles entire life cycle; the impact on the environment from raw materials, to manufacturing, to disposal.

The interest in polypropylene (PP) materials coincides not only with legislation enacted in large markets, but with the priority being given by many major automakers to global sustainability. For instance, Daimler Chrysler's sustainability efforts have focused on the development and utilization of bio-based materials. They have gone one step further by identifying bio-based materials as key part of their plan to create a global sustainability network.

For automotive applications, PP is the most commonly used thermoplastic material, particularly for non-structural components. PP is preferred to other materials due to its low density, excellent processability, adequate mechanical properties, excellent electrical properties, good dimensional stability, and high impact strength [2].

1.2 Research aims

Developing multi component PP material containing bio-based materials is the aim of this research. Plasticized cellulose acetate was chosen to be the bio-based material component. Cellulose acetate is attractive due to its renewability, non toxic, and low cost compared to other bio-based materials. Polymers are susceptible to fire limiting their practical use for a wide variety of industrial and domestic applications [3]. In particular, the flammability of PP materials is of serious concern. The most commonly used method to control the flammability of PP is the addition of flame retardant fillers to the polymer matrix. Metallic hydroxides such as magnesium hydroxide (MH) are becoming more popular due to their high endothermic decomposition temperature (above 340 °C) and low cost. The decomposition products of magnesium hydroxide are water and magnesium oxide, which are non-toxic and produce limited smoke during burning [4].

One of the drawbacks of MH is the high loading (at least 50 wt.%) required to obtain significant flame retardancy [5]. This level makes processing difficult [6]. Furthermore, the inclusion of mineral fillers in thermoplastic materials improves some mechanical properties, for example stiffness, while other properties such as impact strength are compromised [3]. Finally, dispersion of a filler requiring high loading is very difficult to achieve [7].

1.3 Research hypothesis

Increasing the environmental and sustainability of polypropylene material can be achieved by substituting a portion of the polypropylene with cellulose acetate, a bio-based materials. One draw back to this approach is an increase of vulnerability to fire. On one hand, the application of conventional flame retardant, magnesium hydroxide, is beneficial for fire properties. On the other hand, magnesium hydroxide may compromise the mechanical properties. It is desirable to obtain reasonable flame retardancy while maintaining mechanical properties.

1.4 Thesis objectives and structure

The primary objective of this PhD research was to create a PP material with reasonable flame retardancy for use in interior automotive components and building materials. The research consisted of a series of steps:

- Define the formulation of plasticized cellulose acetate magnesium hydroxide polypropylene materials.
- Characterize the thermal behavior of plasticized cellulose acetate magnesium hydroxide polypropylene materials.
- Investigate the combustion behavior of plasticized cellulose acetate magnesium hydroxide polypropylene materials.
- Evaluate the crystallization characteristics and the mechanical properties of plasticized cellulose acetate magnesium hydroxide polypropylene materials.

The thesis is structured as follows:

Chapter 1, motivation and thesis structure

Chapter 2, literature review

Chapter 3, the formulation and fabrication of the PP materials. First, the plasticization of cellulose acetate with TEC was investigated by DSC, XRD, and TGA. Second, the formulation of PP materials was investigated according to thermal stability and activation energy estimation for different contents of polypropylene-grafted- maleic anhydride (PPMA), plasticized cellulose acetate (CA*) and MH.

Chapter 4, the thermal stability of the plasticized cellulose acetate magnesium hydroxide polypropylene materials was evaluated using TGA, and by estimating the changes in the activation energy of the thermal degradation process.

Chapter 5, the fire properties of the PP materials was evaluated by vertical burning, oxygen index (OI%), cone calorimeter, and adiabatic bomb calorimeter tests

Chapter 6, the non-isothermal crystallization of the plasticized cellulose acetate magnesium hydroxide polypropylene materials were investigated.

Chapter 7, the mechanical properties and morphology of the PP materials were scrutinized to study the effects of the inclusion of CA* and MH.

Chapter 8, the overall conclusion drawn from this work is presented with the recommendation for future work.

Chapter 4 to 7 are presented in the manuscript format. As a results of this format, some information will be repetitive, particularly in the introduction and experimental methods. The thesis structure are presented in Table 1.1.

Table 1.1: Thesis structure with steps and associated details

Chapter	Materials	Fabrication	Characterization
3	CA,CA* PP PP* 60PP*/40CA* 70PP*/30MH 70(60PP*/40CA*)/30MH	Extruder	DSC XRD TGA SEM EDS
4	PP PP* 60PP*/40CA* 70PP*/30MH 70(60PP*/40CA*)/30MH	Extruder	TGA
5	PP 60PP*/40CA* 70PP*/30MH 70(60PP*/40CA*)/30MH	Extruder Compression Molding	OI Vertical burning Cone Calorimeter Adiabatic bomb Calorimeter
6	PP PP* 60PP*/40CA* 70PP*/30MH 70(60PP*/40CA*)/30MH	Extruder	DSC
7	PP 60PP*/40CA* 70PP*/30MH 70(60PP*/40CA*)/30MH	Extruder Compression Molding Injection Molder	Tensile Test Impact Test DSC XRD

Chapter 2

Literature Review and Background

2.1 Polypropylene

Polypropylene (PP) is a versatile thermoplastic material, compatible with many processing techniques and used in various commercial applications. It is one of the fastest growing classes of commodity thermoplastics [4]. The PP market growth has been around 6-7% per year [8], and the volume of PP production has exceeded that of polyethylene and polyvinyl chloride in 2013. The strong growth of PP comes from its moderate cost and favorable properties [3].

PP has excellent and desirable physical, mechanical, and thermal properties when used for room temperature applications [9]. It is relatively stiff and has a high melting temperature. It has the highest melting temperature (160-170 °C) of the thermoplastic materials. PP is considered one of the lightest thermoplastic materials (0.9 $g \cdot cm^{-3}$); thus, finished parts for a given application weigh less. The elastic modulus for PP is between 1.05-2.1 GPa (homopolymer), and it has good temperature resistance up to 135 °C [10]. It has excellent electrical insulation capacity. These properties can be easily varied by altering the chain regularity, tacticity, content and distribution, and average chain length.

The monomer propylene contains an asymmetric carbon at the C_2 position (CH_2-CH-CH_3) which leads to three potential molecular configurations: isotactic, syndiotactic, and atactic, as shown in Figure 2.1 and Figure 2.2. The propylene monomers can link together such that the methyl groups can be situated in one spatial arrangement or another in the polymer. If the methyl groups are all on one side of the chain, the arrangement is known as isotactic PP; if the methyl groups are on alternate sides of the chain, the arrangement

is known as syndiotactic PP. A random arrangement of the methyl groups along the chain is known as atactic PP.

Isotactic PP has the highest crystallinity because of its structure, resulting in excellent mechanical properties such as stiffness and tensile strength. Its glass transition temperature (T_g) ranges from -30 to 25 °C, depending on the method of measurement and heat annealing treatments [8]. Syndiotactic PP is less stiff than the isotactic variety but has better impact strength and better clarity. Atactic PP has low crystallinity due to its irregular structure, resulting in sticky, amorphous materials.

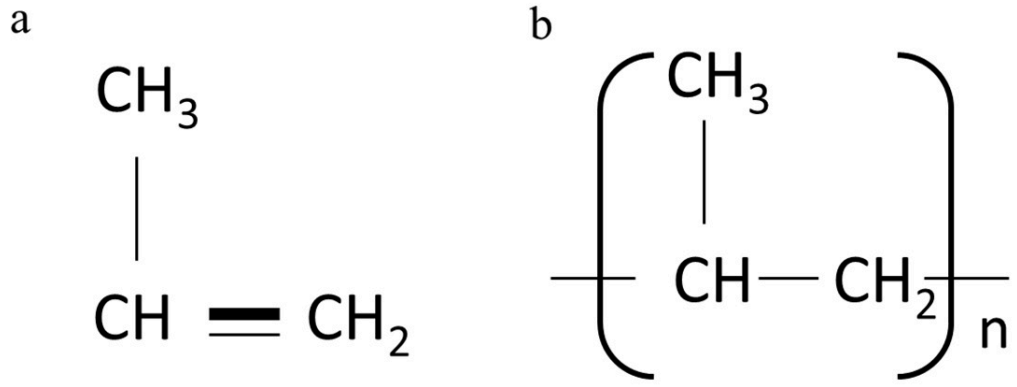

Figure 2.1: Chemical representation: a. propylene b. polypropylene

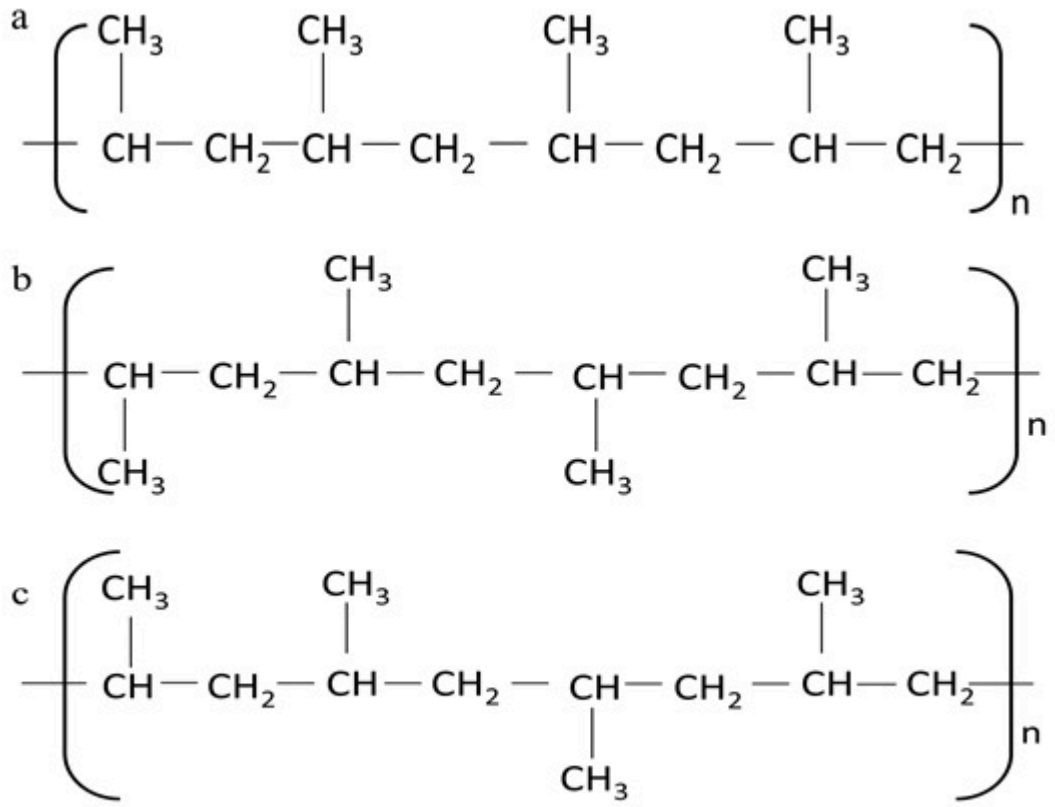

Figure 2.2: Stereochemical configuration of polypropylene a. isotactic, b. syndiotactic, and c. atactic

The chain in PP forms a helical arrangement as it crystallizes due to the presence of a pendant methyl group. Polymers with closely spaced bulky groups form an helix to pack atoms closely together without distortion of the bonds along the chains [10]. Homopolymer PP (isotactic) is one of the common products that contain only a propylene monomer in the semi-crystalline solid form. The homopolymer PP is a two-phase system because it contains both crystalline and non-crystalline regions. From the crystallization of the chains, the thickness of the crystallites can be determined, as well as how much heat energy is required to melt them. The crystallization rate is dependent on the nucleation and crystal growth rates; as the melt becomes cooler, the nucleation rate increases, and the rate of crystal growth decreases. Spherulites are spherical semi-crystalline regions and

are associated with crystallization of polymers from the melt [11]. The spherulite of PP has a size ranging from 1-50 μm [10]. Spherulite can be observed by optical microscopy under crossed polarizers as Maltese cross patterns (Figure 2.3), consisting of a central dark cross with wings coincident with planes of the polarizer and analyzer.

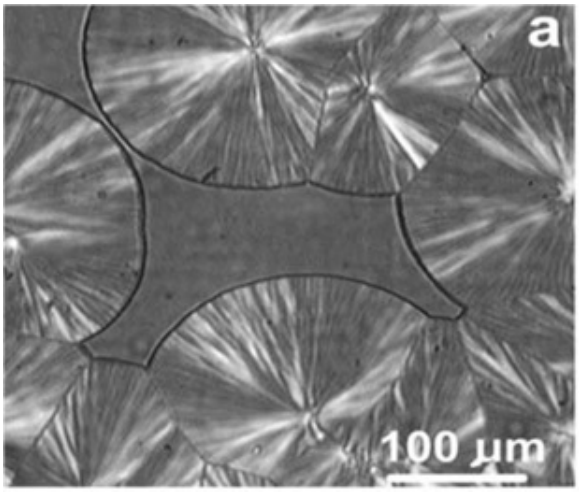

Figure 2.3: A Maltese cross pattern of PP during crystallization using optical microscopy under crossed polarizers [12]

2.2 Polypropylene materials

PP materials have been developed to alter their properties, e.g. lower density, increased strength, and biodegradability. For example, PP materials may contain inorganic fillers and reinforcements such as calcium carbonate, talc, mica, barite, glass spheres, and glass fibers to increase the strength.

Natural fillers have been considered to reduce the density while increasing the biodegradability of PP materials. However, these natural fillers are often polar while PP is non-polar. Therefore, poor adhesion between the filler surface and the polymer matrix prevents necessary wet-out by the molten polymer and helps to break up the aggregate of the filler particles, causing poor dispersion, insufficient reinforcement, and poor mechanical properties.

Different treatments and chemical modifications can be used to overcome these problems. One conventional method is to treat the filler surface to make the surface less

polar and more hydrophobic. Substances such as stearic acid, silanes, zirconates, and titanate have been used. Another approach is to modify the chemistry of PP by attaching polar groups, such as acrylic acid (AA) or maleic anhydride (MAH) as discussed in 2.6.1. It is estimated that around 90% of short fiberglass reinforced PP materials contain polypropylene-grafted-maleic anhydride (PPMA).

Reinforced and filled PP are used in the automotive, appliance, and electrical industries. For automotive applications, glass-fiber reinforced PP is utilized (e.g., fan mounting, shrouds, belt covers, air filters, spoilers, cooling system tanks). It is reported that mineral filler (20%) reinforced PP used in the interior trim in the VW Golf provides sound defeating properties and does not cause unpleasant rattling or squeaking noises. Talc-reinforced PP is used in the appliance industry for washing machine dispensers and pump housing components. Other applications include lawn and garden furniture, usually with the addition of an ultraviolet stabilizer to protect against degradation due to sunlight [10].

Table 2.1 presents the typical weight of natural fibers used in automotive components in 2006. The weight reduction of the components is one of the significant advantages of using these materials. The EcoCar is an example of a vehicle fully constructed from biofiber composite panels [13].

Table 2.1: Typical weight of natural fiber used in automotive components [1]

Automotive component	Typical weight of fiber (kg)
Front door liners	1.2-1.8
Rear door liners	0.8-1.5
Boot liners	1.5-2.5
Parcel shelves	2
Seat backs	1.6-2.0
Sun roof sliders	0.4
Headliners average	2.5

2.3 Processing of polymer materials

The fabrication of polymer materials is largely determined by their rheological properties. For example, when compounding is required, consideration must be given to a material's tendency to flow at an elevated temperature for a relatively long time, the material's softening temperature, and its stability.

2.3.1 Extrusion

The extrusion process involves the molding of a viscous thermoplastic under pressure through an open-ended die. The pelletized material is successively compacted, melted, and formed into a continuous charge of the viscous fluid by a rotating screw through a chamber. The molten phase of the material is pushed through a die orifice of the extruder to create the extrusion.

The extruder is divided into several sections and each section has a specific purpose. The feed section picks up raw material from a hopper and propels it into the main part of the extruder. In the compression section, the feed is compacted, melted and formed into a continuous stream of molten plastic. External heat can be supplied, and part of the heat is also generated from friction. The metering sections contribute to the uniform flow rate required to ensure uniform dimensions in the finished products and provide sufficient pressure in the polymer melt through the rest of the extruder. Different types of extruder are used currently including the multiple-screw extruder (provides more working of the melt), and the vented extruder (allows extraction of the volatiles from the polymer melt).

2.3.2 Injection molding

Most thermoplastic materials are molded by the process of injection molding. The material is softened and conveyed with a screw as in extrusion, then pushed through a runner system into a cavity or multiple cavities of a mold. The melt temperature may be higher than the compression molding temperature (> 150 °C), and a pressure of 100-1000 psi is common. The mold is cooled and eventually, the mold separates; solid parts are ejected and stacked.

2.3.3 Compression molding

Compression molding is another technique used for the fabrication of multicomponent materials. In compression molding, the appropriate amount of thoroughly mixed polymer and necessary additives are placed between the male and female mold members, which are both heated. One of the mold members is moveable, and the other is fixed. The mold is closed and subjected to heat and pressure, causing the plastic to become viscous and flow to conform to the mold shape. This molding technique can be used with thermoplastic and thermosetting polymer. However, its use with thermoplastic is more time consuming. The necessary pressure and temperature range vary considerably depending on the thermal and rheological properties of the polymer. The temperature and pressure in compression

molding could be near 150 °C and 1000-3000 psi, respectively. An excess of material is required to ensure the mold is adequately filled. The residual material, known as flash, is squeezed out and can easily be removed.

2.4 Fillers, reinforcement, and additives

Fillers, reinforcements, and additives such as flame retardants can be added to reduce the cost or to enhance the mechanical and fire properties of the materials. Reinforcing fillers can provide substantial improvements to the mechanical properties (e.g., tensile strength, heat distortion temperature, modulus of elasticity) of a material. The properties of the finished material depend on the relative volume of the filler added [14]. The inclusion of filler can chemically or physically modify the polymer phase. The changes can be in the crystallization, such as the nucleation, crystal growth, or in the crystal phase of the polymer [15–17]. The chemical degradation of the polymer may be catalyzed by the filler or its impurities [18].

2.5 Cellulosic fillers

Cellulosic fillers, such as wood and natural fibers derived from renewable resources, can be used as reinforcement for thermoplastic and thermoset composites and provide favorable environmental benefits in terms of ultimate disposability and raw material utilization. Wood and natural fibers such as flax, hemp, and ramie are cheap, possess low density, high toughness, acceptable specific strength properties, and biodegradability [19]. Their main drawbacks are their hydrophilic nature, low thermal stability, and high moisture sensitivity.

It has been reported that wood fiber (WF) reinforced PP has properties like traditional glass-fiber reinforced PP composites [20]. WF polypropylene materials have gained interest for the manufacture of products in several fields, such as automotive components, decking, and fencing due to their sustainability, relatively high strength and stiffness, low maintenance and cost, and excellent durability [21–23]. In general, the addition of cellulose can increase Young's modulus, while the tensile strength does not improve or sometimes decreases due to the poor interfacial interaction [24]. According to Luz et al. [25], the addition of cellulose fibers to PP shows intermediate thermal stability compared to the fibers and PP matrix.

Cellulose is a semi-crystalline polysaccharide made up of D-glucopyranose units linked together by β-(1-4)- glucosidic bonds [26], as shown in Figure 2.4. The hydroxyl groups

present in cellulose give hydrophilicity, which has minimal interaction with hydrophobic matrices, resulting in materials with an inferior interface and lower mechanical properties [27]. The cellulose molecule is rigid and contains strong hydrogen bonding, so it is insoluble and decomposes before softening on heating.

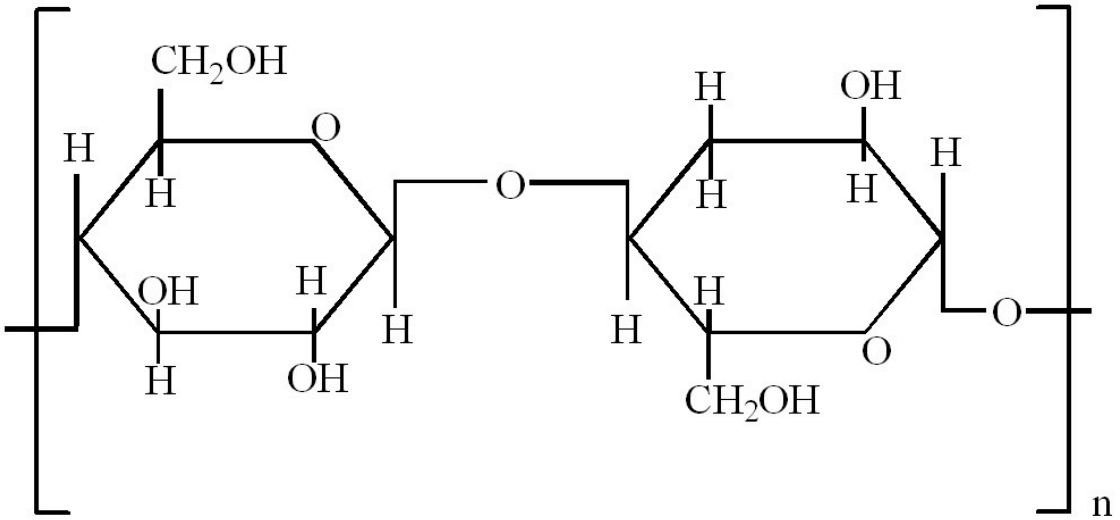

Figure 2.4: Cellulose structure

Cellulosic materials can be treated or modified to enhance their compatibility with polymer matrix. Several works have studied the effects of different treatment approaches and chemical modifications on the dispersion of these materials and the interaction between the cellulosic materials and the PP matrix. Chemical modifications include mercerization, isocyanate treatment, latex coating, acetylation, silane treatment, and alkali treatment. The use of coupling agents and the modification of cellulose are the two major approaches to enhance the interfacial interaction between cellulose and polymeric matrices.

2.6 Surface modification of cellulosic materials

2.6.1 Coupling agents

Coupling agents are molecules possessing two functions. For cellulose composite materials, the first function is to react with the OH groups of cellulose, and the second is to react with

the functional groups of the matrix. The selection of a coupling agent that can combine a considerable degree of both strength and toughness is essential for composite materials to facilitate the optimum stress transfer at the interface between fiber and matrix. An example of a coupling agent developed for PP is PP grafted with maleic anhydride (MAH) creating polypropylene-grafted-maleic anhydride (PPMA) for increased polarity, leading to better adhesion with polar additives [28]. The addition of MAH to PP results in a significant increase in tensile strength for levels as low as 1%, and maximal tensile strength is achieved at 5%. PPMA coupling agents generally differ according to their MAH content [29].

The treatment of cellulose fibers with PPMA provides covalent bonds across the interface. The reaction mechanism of PPMA with fiber can be divided into two steps: the activation of PPMA by heating (170 °C) as shown in Figure 2.5a before the fiber treatment, and the esterification of the cellulose (Figure 2.5b). After treatment, the surface energy of the cellulose is increased and approximates that of PP; showing better wettability and higher interfacial adhesion between the fibers and the matrix.

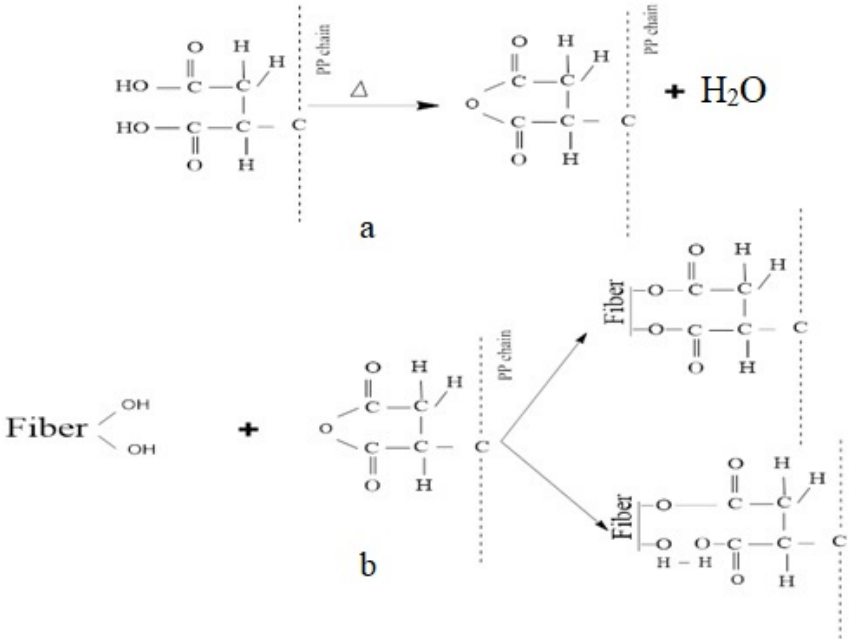

Figure 2.5: Reaction mechanism of PPMA coupling agent with cellulose fibers [30]. a. before fiber treatment. b. after fiber treatment

2.6.2 Acetylation

Acetylation of cellulose consists of the replacement of hydroxyl groups by acetyl groups. This reduces the interchain hydrogen bonding, increases interchain separation, and reduces the hydrophilic nature of cellulose. Cotton, WF, and recycled paper are examples of raw materials used to make cellulose esters in powder form [31].

Acetylation can be done with and without an acid catalyst to graft acetyl groups onto the cellulose structure. The cellulose is initially soaked in acetic acid and subsequently treated with acetic anhydride ($CH_3 - C(=O)\text{-}O\text{-}C(=O)\text{-}CH_3$) for 1-3 hours; higher temperatures accelerate the reaction [32]. The reaction of acetic anhydride with cellulose is shown as:

$$\text{Cellulose-OH} + CH_3 - C(=O)\text{-}O\text{-}C(=O)\text{-}CH_3 \longrightarrow \text{Cellulose-OCOCH}_3 + CH_3COOH \quad (2.1)$$

The product cellulose acetate (CA), will have different properties according to chain length and degree of substitution (DS), the replacement of the hydroxyl group with acetyl group. The structure of CA is illustrated in Figure 2.6 and its properties and uses presented in Table 2.2. CA is one of the most important organic esters and is used for many industrial applications in the form of film and fiber. Its global production was over 800,000 metric tons in 2008 [33, 34]. The main properties of CA are hardness, good resistance to impact, high shine, transparency, pleasing texture, lack of static electricity, and resistance to hydrocarbons. It has been reported to be biodegradable, depending on the degree of substitution (DS). The acetylation renders the cellulosic structure; CA will still decompose below its softening point and still required to be plasticized after the acetylation. CA has been widely used in the fabrication of membranes [35]. In addition, CA has been reported in the fabrication of flexible, conductive, and high transparent composite films in the plasticized state [36, 37]. CA (US$ 2.5/kg) is less expensive than PLA (US$ 5.0/kg) but more expensive than PP (US$ 1.78/kg) and polyethylene (US$ 1.52/kg) [38]. CA is also studied as a blend with polylactic acid (PLA) with potential use in packaging, and the results show that CA did not improve the mechanical properties of the blends in comparison to pure PLA due to the poor adhesion. On the other hand, the thermal stability and elongation at break increased [39].

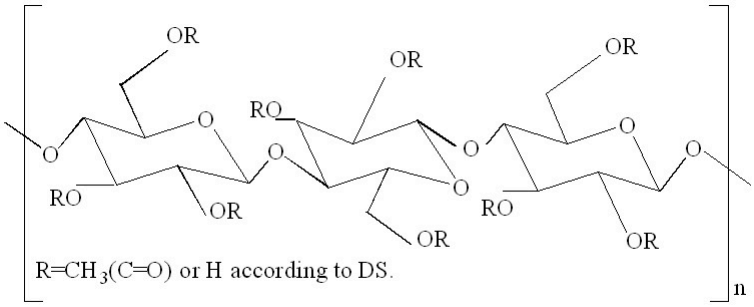

Figure 2.6: General structure of cellulose acetate

Table 2.2: Influence of degree of substitution on the properties and uses of cellulose acetate [40]

Degree of substitution	Acetyl content (-$COCH_3$)(%)	Solubility	Uses
2.2-2.3	36.5-38	Soluble in acetone	Injection moulding
2.3-2.4	38.0-39.5		film
2.5-2.6	39.5-41.5		lacquers
2.8-3.0	42.5-44	Insoluble in acetone, soluble in chloroform	Triacetate film and fiber

2.7 Plasticization of cellulose acetate

The main drawback of CA is that its melting temperature is very close to its decomposition temperature. Due to this, CA needs to be plasticized [34, 41]. The primary functions performed by plasticizers include [42]:

1. Lowering of the material hardness as well as other mechanical properties.
2. Acting as a fiber-to-fiber bonding agent [42].
3. Lowering of the melt viscosity, viscoelasticity, and melt flow [43].

There are two main groups of plasticizers known as internal and external plasticizers. External plasticizers consist of low volatility molecules added to interact with polymers and produce swelling without chemical reaction. Internal plasticizers, on the other hand, form part of polymer molecules. They are copolymerized into the polymer structure by grafting or by reaction with the original polymer; thereby making it less ordered and more difficult for the chain to fit closely together. Their effects appear by reducing the glass transition temperature (T_g) and elastic modulus [44].

Table 2.3: Typical properties of triethyl citrate (TEC)

Properties	Value
Molecular weight ($g \cdot mol^{-1}$)	276.3
Density ($g \cdot cm^{-3}$)	1.13
V_m ($cm^3 \cdot mol^{-1}$)	244.5
T_{bp} at 760 mmHg (^oC)	126

Common plasticizers reported in the literature for CA include diethyl phthalate, dimethyl phthalate, triphenyl phosphate, and glycerol triacetate. Phthalate plasticizers are the primary plasticizers used in commercial cellulose ester plastics and are now under examination due to their potential effects on human health [45]. The desire to replace this type of plasticizer has led to studies evaluating the effectiveness of alternative plasticizers for CA such as citrate esters.

TEC (triethyl citrate) is an eco-friendly plasticizer which can be used to plasticize CA [41]. The general structure of TEC is shown in Figure 2.7. TEC can be classified as a hydrophobic plasticizer with limited miscibility with water, and was reported in the literature to be miscible with CA [46]. Typical properties of TEC are presented in Table 2.3.

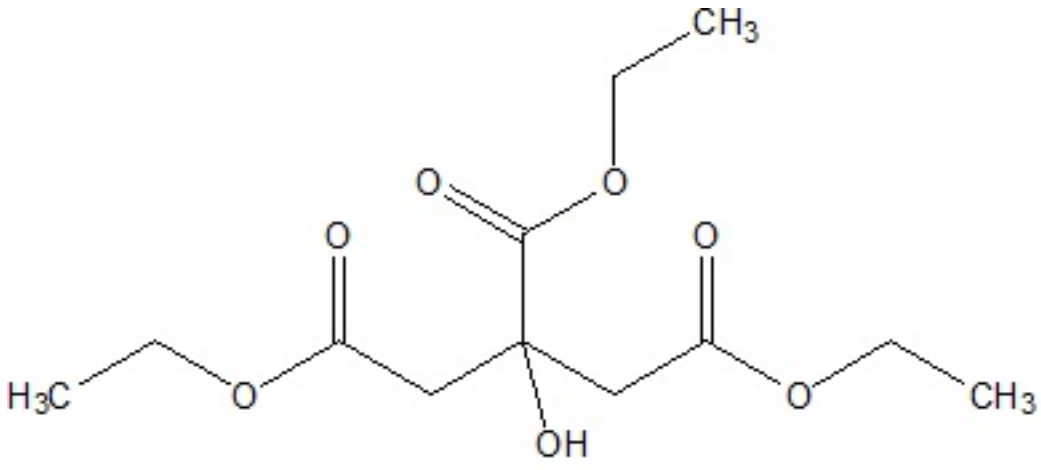

Figure 2.7: General structure of triethyl citrate

TEC plasticized CA (CA*) melts at 170-180 °C, approximately 50 °C below the melting point of neat CA [34]. The effects of TEC as on the performance and thermal properties of CA have been reported [45, 47]. In order to obtain CA* with an optimum balance of stiffness and strength, 30 wt.% TEC was identified, according to Mohanty et al. [34]. The addition of TEC shifts the maximum decomposition temperature to lower values. Furthermore, it has been reported that the glass transition temperature (T_g) decreases as TEC content increases [48]. The T_g of pure CA is reported to be 170 °C, while T_g for CA* is around 30 to 50 °C below when using 20 wt.% [49] and 30 wt.% [46] TEC content, respectively. Furthermore, mechanical properties are affected as plasticizer concentration increases. It was reported that an increase of impact strength and elongation at break was accompanied by a drop in tensile strength of the cellulose acetate when it was plasticized [34].

2.8 Combustion of polymer

Combustion is a complex combination of physical and chemical phenomena that interact in balance for combustion to occur. Figure 2.8 shows the three components necessary to support combustion fuel, heat, and oxygen, which form the classic fire triangle [50]. Combustion refers to the oxidation reaction between a fuel, an oxidant (oxygen) and an external source of intense energy, such as a spark or flame. The combustion process consists of five elements: preheating, decomposition, ignition, combustion, and propagation [5]. The distinction between each element is generally not well defined. The preheating stage involves irradiation of the material by an external heat source, raising its temperature. The rate at which temperature increases depends on the thermal intensity of the heat source as well as the thermal properties of the material: its thermal conductivity, specific heat and latent heat of fusion. An increase in thermal energy induces bond scission in the material leading to the release of volatile substances. Ignition occurs when these gases mix sufficiently with atmospheric oxygen, and their temperature reaches either the auto-ignition temperature or the flash point of the fuel (material). Combustion becomes self-propagating if sufficient heat is generated and radiated back to the materials to sustain the decomposition process [51].

The decomposition of a polymer, i.e., covalent bond dissociation, is an endothermic phenomenon. For most C-C polymers, the amount of energy that must be supplied to initiate bond dissociation is in the order of 200-400 $kJ \cdot mol^{-1}$ [50]. The decomposition mechanism depends on the scission of the weakest bonds of the polymer [52]. Thermal decomposition requires heat and oxygen to occur. There are two possible mechanisms of

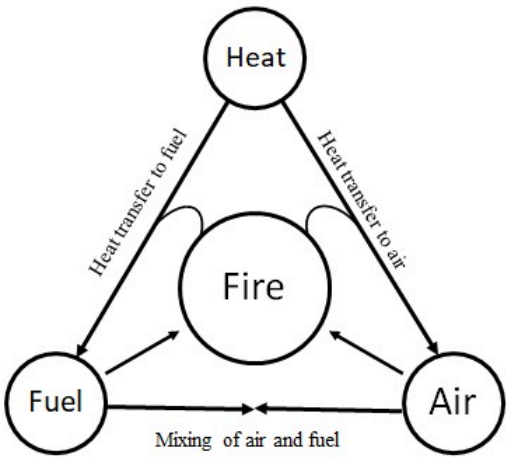

Figure 2.8: Fire triangle showing the three components necessary to support combustion [8]

thermal decomposition, depending on the temperature and amount of oxygen available [53]:

I. Formation of free radicals. The mechanism is self-propagating because these radicals start a chain/cascade reaction which occurs under oxidizing and non-oxidizing conditions. The formation of radicals can be illustrated by the following reaction:

$$R_1 - CH_2 - CH_2 - R_2 \rightarrow R_1 - CH_2 + CH_2 - R_2 \tag{2.2}$$

II. Migration of hydrogen atoms. This mechanism results in the formation of two stable molecules, one of which has a reactive carbon-carbon bond and is illustrated as follows:

$$R_1 - CH_2 - CH_2 - CH_2 - R_2 \rightarrow R_1 - CH = CH_2 + CH_3 - R_2 \tag{2.3}$$

2.8.1 Oxidizing thermal decomposition

During oxidizing thermal decomposition, atmospheric oxygen is present, generating the following substances:

1. Flammable, low molecular weight volatiles such as carboxylic acids, alcohols, ketones, and aldehydes.

2. Radicals such as $H^{\cdot}$ and $OH^{\cdot}$.

3. Solid particles such as soot and carbonaceous residue.

Above 300 °C, the non-oxidizing thermal decomposition is faster than the oxidizing thermal decomposition in the solid phase. Oxidation takes place in the gas phase due to the presence of low molecular weight species generated from the thermal decomposition. These gases mix with oxygen by convection, diffuse into the layer close to the solid surface, then ignite. Different strata develop in the solid as a result of combustion. At the surface of the solid, where most combustion occurs, a microporous char layer and subjacent rough porous cellular layer is formed. The gaseous decomposition products collect in the cavities of this porous layer and then migrate to the burning surface layer through the char layer as shown in Figure 2.9.

Flame retardancy is achieved by disruption of the combustion process. The incorporation of substances that can interfere with combustion is the most expeditious method to acquire flame retardancy. Different flame retardation mechanisms exist which can act physically (cooling, the formation of the protective layer or fuel dilution) or chemically (reaction in the condensed or gas phase).

2.8.2 Physical action

Flame retardant additives decompose endothermically, which result in the lowering of the temperature. The reaction medium thus cools below the temperature required for combustion. Further, when flame retardants decompose, inert gases (H_2O, CO_2, NH_3, etc.) are released causing dilution of the combustible gas mixture and hence reducing the possibility of ignition. Some flame retardant additives lead to the formation of a protective layer. This layer reduces the transfer of combustible volatile gases and oxygen. In addition, the fuel gases can be physically separated from the oxygen, preventing the combustion process from being sustained [55].

2.8.3 Chemical action

Flame retardants acting by chemical modification of the combustion process can take place in the gaseous or condensed gas phase. Flame retardants in this category act by releasing

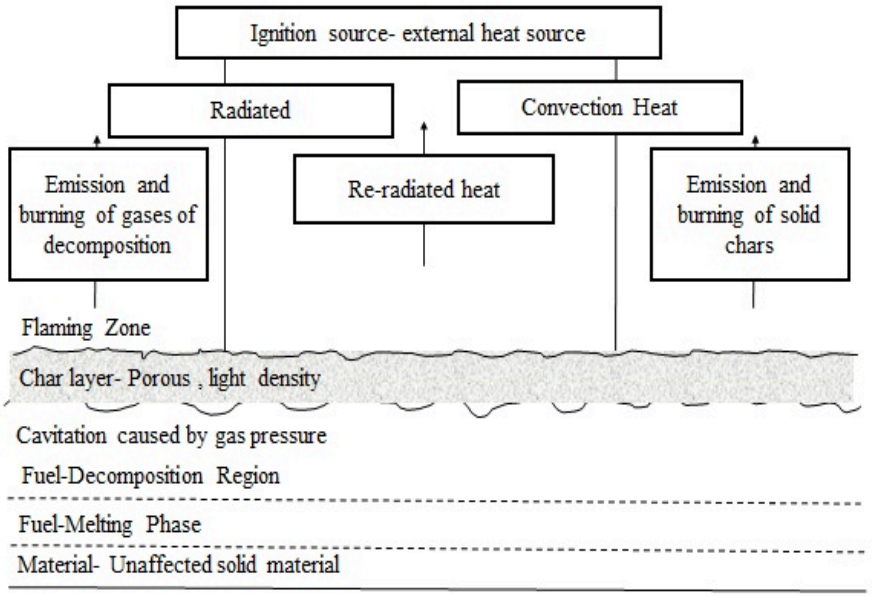

Figure 2.9: Polymer behavior during combustion [54]

in the gas phase radicals such as $Cl^{\cdot}$, $Br^{\cdot}$. These radicals can react with reactive species such as $H^{\cdot}$ or $OH^{\cdot}$ to form less reactive or even inert molecules. Accordingly, there is a marked decrease in the heat released during the reaction, leading to a reduction in the amount of fuel produced. In the condensed phase, flame retardants of this category can act in two ways. First, flame retardants can accelerate the rupture of the polymer chains; the polymer thus melts and moves away from the flame action zone. Alternatively, flame retardants can lead to the formation of a carbonized layer at the surface of the polymer, which will act as a physical insulating layer between the gas phase and the condensed phase [55].

Due to the poor char forming ability of PP, additives can be considered a source of char (typically >20% w/w) for PP in order to get reasonable flame retardancy [10]. In addition, the additive can act as diluent and reduce the concentration of decomposition gases. Hydrated additives can release non-flammable gases or decompose endothermically to cool the pyrolysis zone at the combustion surface. Furthermore, the decomposition products could act as a protective layer to insulate the materials beneath the flaming zone.

2.8.4 Free radical scavenger halogenated flame retardants

Free radical scavengers halogenated flame retardants are the organic compounds which contain halogens (bromine or chlorine). These compounds act in the gas phase by scavenging free radicals formed during combustion. The flame retardants dissociate to form free radicals at thermal decomposition temperature as shown in the chemical reaction equation:

$$R^{'}X \rightarrow R^{'\cdot} + X^{\cdot} \tag{2.4}$$

where X is either chlorine (Cl) or bromine (Br) , and $R^{'}$ is the organic part of the molecule, with the unpaired electron on a carbon atom.

Br is more widely used and more effective than chlorine due to the weaker $(R' - Br)$ bond [56]. The hydrogen from the gaseous hydrocarbons (RH) will be abstracted by the halogen-free radical, forming a free radical $(R^{\cdot})$ and the active flame retardant species, hydrogen halide (HX) [57]:

$$X^{\cdot} + RH \rightarrow R^{\cdot} + HX \tag{2.5}$$

After, hydrogen halide (HX) reacts with $H^{\cdot}$, and $OH^{\cdot}$ radicals to produce inert and lower energy radicals as shown in Equation 2.6 and Equation 2.7:

$$HX + H^{\cdot} \rightarrow H_2 + X^{\cdot} \tag{2.6}$$

$$HX + HO^{\cdot} \rightarrow H_2O + X^{\cdot} \tag{2.7}$$

There are some problems with halogenated flame retardants including interaction with hindered amine light stabilizer, corrosion due to the production of gaseous, acidic hydrogen halides, and potentially toxic decomposition products. Nowadays, restrictions on brominated flame retardants are increasing due to possible environmental and health risks of brominated diphenyl ethers. Brominated dioxins and furans, which are toxic materials, can form under some conditions from brominated diphenyl ethers [58, 59].

2.8.5 Phosphorus

There is a wide range of phosphorus containing flame retardant (PFRs) since phosphorous exists in several oxidation states. Phosphines, phosphine oxides, phosphates, and elemental red phosphorus are examples of PFRs used in polymers, but only a few of these compounds

are applicable in polyolefins and especially PP. PFRs efficiency is lower in polyolefins due to the poor char formation of the polyolefins.

Ammonium polyphosphate (APP) is a common flame retardant in PP. There are various physical modes of action reported in the literature for APP [60]. Alkylamine acid phosphate, such as ethylenediamine modified ammonium polyphosphate (EDAP) is an effective phosphate salt used in PP as a flame retardant, a reasonable flame retardant with a V-0 rating achieved with loadings of 30-40 wt.%. The higher loading is required due to the polymer flow during burning which results in flaming drips [61, 62].

PFRs exhibit moderate, to low toxicity [63]. PFRs have come under intense environmental scrutiny. It was reported that PFRs show acute toxicity to aquatic algae, invertebrates, and fish. The Environmental Protection Agency has summarized these acute toxicities of the PFRs as well as the apparent need for additional testing [64, 65].

2.8.6 Metallic hydroxides

Metallic hydroxide flame retardants are attractive for use in PP due to their low toxicity, corrosion properties, and lower emission of smoke during processing and burning [66]. Metallic hydroxides provide effective flame retardant effects by releasing a significant amount of water when exposed to high temperatures, absorbing heat from the combustion zone and hence reducing the prospect of sustained combustion. Furthermore, the decomposition of metallic hydroxides generates a metal oxide coating that can act as an insulating layer during combustion. However, very high metallic hydroxide levels are usually required to achieve reasonable flame retardancy, and these tend to result in poor mechanical strength. A suitable flame retardant of this group must have the following properties [67]:

1. Relatively high endothermic decomposition temperature, preferably in the 100-300 °C temperature range with at least 25% of its weight converted to water vapor or carbon dioxide.

2. Low cost and availability.

3. Small particle size and no color.

Metallic hydroxides meeting these requirements are predominantly hydroxides, hydroxyl carbonates, and hydrates of aluminum, calcium and magnesium [68]. Of these, the two most common are aluminum hydroxide and magnesium hydroxide. These materials exhibit low toxicity before or after decomposition. For example, the decomposition

products of magnesium hydroxide are water vapor in the gas phase and magnesium oxide as a residue. Furthermore, these materials have high corrosion resistance and low smoke emission during processing and combustion [4].

2.8.7 Magnesium hydroxide

Magnesium hydroxide (MH) is the most widely used metal hydroxide flame retardant. The decomposition of MH is given as follows:

$$\mathrm{Mg(OH)_2} \rightarrow \mathrm{MgO} + \mathrm{H_2O} \qquad \Delta H = 1.37 \ \mathrm{kJ \cdot g^{-1}} \tag{2.8}$$

The hydroxyl groups bonded to the metal have to undergo endothermic decomposition to produce free water. The enthalpy of the decomposition reaction is ΔH=1.37 kJ·g^{-1}. The water vapor dilutes the combustion gases, and the endothermic reaction absorbs heat. Magnesium oxide formed during decomposition provides an insulating char layer on the solid surface. The decomposition temperature of the magnesium hydroxide is about 300-320 °C. It can, therefore, be incorporated with a polymer such as polypropylene [5]. High levels are needed to produce appreciable flame retardancy [6, 69].

Hornsby and Watson [70] found that MH starts to decompose at 350 °C and showed a water loss (26-28%) occurring between 350 and 500 °C. This compares with a stoichiometry calculation of water loss to be 31%. As the temperature rises further, the remaining water diffuses slowly from within the oxide body. As the temperature increases (650 °C), an active form of magnesium oxide is formed. MH action can be considered to act in the condensate phase. The magnesium oxide as a decomposition product of MH appears to have participated in condensed phase reactions with adsorbed hydrocarbon fragments [70]. This could be the reason for the improved char formed during the combustion of the materials.

Studies have been reported on the effects of the particle size and geometry of MH. The particle size not only has effects on the mechanical and fluid properties of the materials but also might influence the flame retardancy [71–73]. Zhang [72] reported that mechanical properties improved with decreasing particle size, while fire properties showed no relation between the particle size and the fire properties. For example, the peak value of the heat release rate of untreated MH (1250 μm) was lower than that 800 μm and 2500 μm of mesh size. These results were also confirmed by another study indicating that the effect of particle size is not linear for MH with micro-scale [74]. It is known that the dispersion

of the MH tends to provide better flame retardancy, so appropriate methods for good dispersion are required.

Magnesium hydroxide is hydrophilic, while PP is nonpolar and hydrophobic. The interfacial adhesion between MH and PP is poor. PP modification with polar molecules such as polypropylene-grafted-maleic anhydride (PPMA) is an efficient way to enhance interfacial adhesion [75, 76].

The effects of PPMA on thermal stability and mechanical properties of magnesium hydroxide PP materials have been reported [77, 78]. Hao et al. [79] reported the effects of PPMA in PP/MH materials. The improvement was in the tensile strength. The dispersion of MH particles in the untreated PP (Figure 2.10a) was not uniform and poor compatibility resulted in a distinct interface between the PP matrix and MH particles. The addition of PPMA (Figure 2.10b) showed that MH particles were embedded in the PP matrix. The compatibility was also improved as detected from the images after modification. This could be attributed to MAH which might interact with the hydroxyl groups on the surface of MH particles.

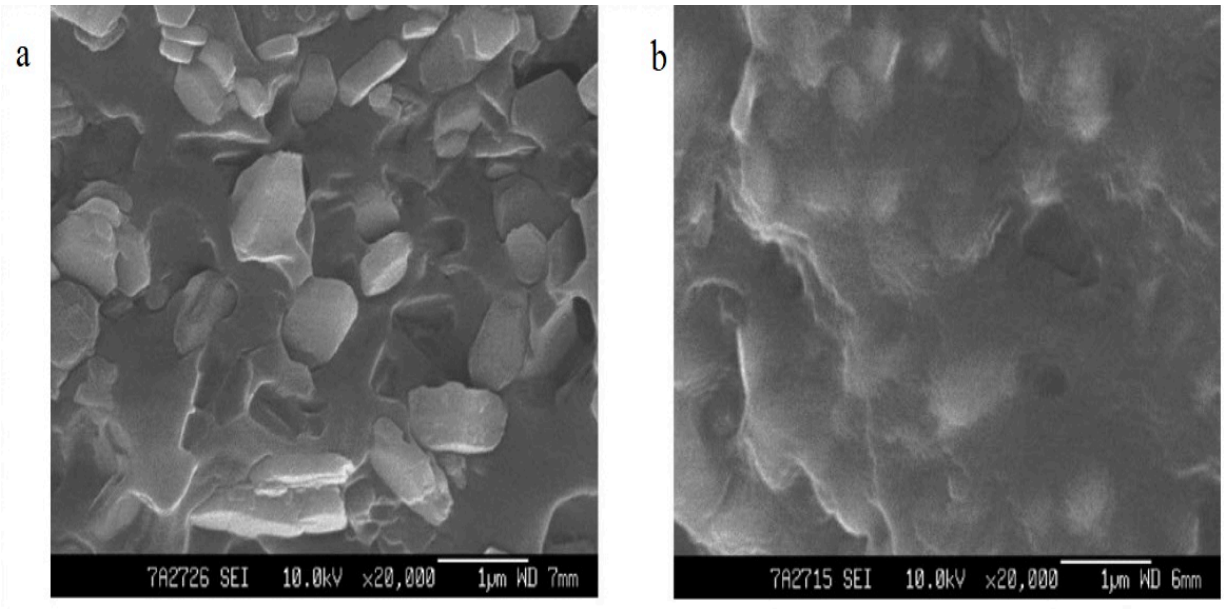

Figure 2.10: SEM cryo-fractographs of PP/MH composites modified with PPMA (20,000×). a. PP/MH before PPMA addition. b. after PPMA addition [79]

2.9 Combustion of polypropylene

One of the drawbacks of PP is poor flammability resistance, which limits its broad application. PP begins to decompose at temperatures between 320 °C to 400 °C forming gaseous decomposition products which initiate combustion with no char left at the end of the combustion. Soot, in small amounts, is formed during the combustion process of PP. Polypropylene is one of the most challenging polymers to improve its flame retardant [10]. In order to meet the standards of applications such as in the electronics industry, a high level of flame retardant (25%) is required in PP materials [80].

The high level of flame retardant affects some mechanical properties, reducing the processability, and interfering with the action of other additives [10]. The heat of combustion data suggests that polypropylene is more susceptible to thermal degradation than most synthetic and natural polymers. Its heat of combustion is 40 $kJ \cdot g^{-1}$ while that of nylon, cellulose acetate, and polyester is 15 $kJ \cdot g^{-1}$, 15 $kJ \cdot g^{-1}$, and 6.3 $kJ \cdot g^{-1}$, respectively [81]. PP has a self-ignition temperature (570 °C) and a rapid decomposition rate compared to wood and other cellulosic materials [29].

The pre-combustive oxidative behavior of PP has been evaluated by thermogravimetric analysis (TGA) and differential thermal analysis. It was found that thermal oxidation was initiated by the rapid carbonyl formation at the labile tertiary hydrogen atoms in the chain [82]. Volatile products were identified during the oxidation of PP: water, formaldehyde, acetaldehyde, acetone, methanol, hydrogen, hydrogen peroxide, carbon monoxide, and carbon dioxide.

Subsequently, the chain decomposition occurs by breaking the weaker bonds at the polymer surface with the presence of the chemisorbed oxygen. The oxidation is initiated by the formation of free radicals. Then inner oxygen-free zone, C-C bond scission begins resulting in the formation of shorter radicals and biradicals. These volatile compounds include: dienes, alkanes, and alkenes. Other compounds released during pyrolysis include C_9 compounds such as 2-methyl-4-octene, 2-methyl-2-acetone, 2,6-dimethyl-2,4-heptadine, 2,4- dimethyl-1-heptene, 2-methyl-1-octene [83]. The remaining heated surface of the polymer and less volatile molecules behave as secondary fuel sources [51]. Above 350 °C, dehydration of the polymer radicals occurs, producing alkene species [84].

The oxidative degradation of PP is related to its microstructure such as stereoregularity, molecular weight, crystallinity, spherulite size, and molecular orientation [85]. When the degree of crystallinity increases, the oxygen diffusion or penetration is restricted and results in the slow down of the oxidation process. Furthermore, the influence of degradation on the small crystals is much more significant than for larger ones [86, 87].

2.10 Material characterization

2.10.1 Differential scanning calorimetry (DSC)

Differential scanning calorimetry (DSC) is a technique used to estimate the glass transition temperature (T_g), melting temperature (T_m) and degree of crystallinity (X_c) of materials. DSC is based on changes of heat flow of a material exposed to different temperature conditions. During DSC, the difference in heat flow between the sample and the inert reference is recorded as function of time and temperature. The difference in temperature of the sample pan and the reference pan is also recorded. The sample and reference temperature increase at constant rate. DSC works at constant pressure and is equivalent to the heat flow.

$$Heat\ flow = heat/time = Q/t \tag{2.9}$$

where Q is the heat ($J \cdot g^{-1}$) and t is the time (s).

The heating rate is the rate of change of temperature according to time:

$$Heating\ rate = \Delta T/dt \tag{2.10}$$

where ΔT is the change of temperature (°C) and dt is the change in time (s).

The heat flow difference between the sample and the reference can be either positive or negative. Polymer chains have higher mobility above the glass transition temperature. At specific temperature, the chains have enough energy to form ordered arrangements and hence crystallization proceeds. Crystallization is an exothermic process, so the heat difference between the reference and the sample will be negative. An exothermic peak will appear in the DSC thermograms, the crystallization temperature (T_p) can be detected, and the latent heat of crystallization can be obtained by calculating the area under the peak. At T_m, the polymer chains move around easily. The heat difference between the reference and the sample is positive, so an endothermic peak will appear in the DSC thermograms [88].

The melting point of isotactic polypropylene (90-95% isotactic material content) with a crystallinity around 45% is 165 °C. The T_g of isotactic polypropylene ranges from -30 to 25 °C, depending on the measurement method and the heat annealing treatments [89].

2.10.2 Thermogravimetric analysis (TGA)

Thermogravimetric analysis (TGA) provides information on the thermal stability of a material obtained from the mass change of a material subjected to increasing temperature. This information can be used to investigate the kinetics of the thermal decomposition of polymeric materials from which the thermal stability can be evaluated [90]. The first requirement for the kinetic study is the high quality of data. Temperature errors have two types of effects on the kinetic parameter and the resulting kinetic predictions [91]. For example, a 3 °C error in temperature leads to a 5% error in the activation energy estimation (E_a) [92–94]. TGA instrumentation controls the furnace temperature, while the sample temperature can deviate from the furnace temperature due to the thermal conductivity of the sample or due to the thermal effect of the process that may cause self-heating or cooling. This problem could be serious with larger sample masses and high heating rates. Due to this, it is recommended to demonstrate that there is no mass dependence. Some approaches are used to reduce the deviation of the temperature by decreasing the mass of the sample as well as the heating rate.

The kinetics of thermal decomposition are generally expressed in terms of conversion (x) defined by Equation 2.11 and Equation 2.12. The conversion, x, is determined experimentally and can be evaluated as the fraction of the total mass loss of the sample in a TGA experiment.

$$x = \frac{m_o - m_t}{m_o - m_f} \tag{2.11}$$

where m_o is the initial mass of sample in (g), m_t is the mass of the sample at any time (g), and m_f is the final mass of solid (i.e. residue and unreacted substrate) remaining after the reaction in (g).

$$\frac{dx}{dt} = k(T) \cdot f(x) \tag{2.12}$$

where x is the conversion, dx/dt is the rate of change of conversion, $k(T)$ is the temperature-dependence rate constant (s^{-1}) , and $f(x)$ is the reaction function expressing the dependence of the reaction rate on the conversion.

According to the Arrhenius equation, the temperature dependence of the rate constant $k(T)$ is given by:

$$k(T) = A \cdot e^{-E_a/RT} \tag{2.13}$$

where $k(T)$ is the temperature dependent rate constant, A is the frequency factor, or pre-exponential factor, E_a is the apparent activation energy of the reaction (kJ·mol^{-1}), R is the universal gas constant (8.314×10^{-3} kJ·K^{-1}·mol^{-1}), and T is the absolute temperature in K.

Combining Equation 2.12 and Equation 2.13 gives:

$$dx/dt = A \cdot e^{-E_a/RT} \cdot f(x) \tag{2.14}$$

The temperature is controlled in thermogravimetric analysis with a program defined by the user. The temperature (T) will change linearly with time so that:

$$\beta^* = dT/dt \tag{2.15}$$

where β^* is the heating rate.

The combination of Equation 2.14 and Equation 2.15 is used to relate the kinetics of the reaction to TGA results [95, 96]:

$$\beta^* \cdot (dx/dT) = A \cdot e^{-E_a/RT} \cdot f(x) \tag{2.16}$$

Rearrangement of Equation 2.16 and its subsequent integration:

$$\int_0^x dx/f(x) = A/\beta^* \int_0^T exp(-E_a/RT)\ dT \tag{2.17}$$

The model free method also called the isoconversional method, is the most common method for the study of the kinetics of thermal decomposition. The advantages of the model free method are its simplicity and the avoidance of errors induced by the selection of a kinetic model. This method can be further classified as differential or integral. The differential isoconversional method is sensitive to experimental noise and affects the estimates. The integral method is less sensitive to experimental noise and is therefore preferred. The Kinetics Committee of the International Confederation for Thermal Analysis and Calorimetry (ICTAC) recommends using at least three different heating rates for the isoconversional method [92]. The isoconversional method can be used for the estimation of the activation energy, E_a, at specific extent of conversion. The disadvantage of this method is the need for measurements at different heating rates for the same sample mass and volumetric flow rate of gas. Their fluctuation may cause errors [95, 97].

2.10.2.1 Integral isoconversional methods

Isoconversional methods are based on isoconversional principles that state the reaction at constant extent of conversion is only a function of temperature. The right hand side of Equation 2.17 does not have an analytical solution for an arbitrary temperature program. Due to this, there are several isoconversional methods which differ in their approximation of the temperature integral (right hand side in Equation 2.17).

Many of these approximations result in a linear equation:

$$ln(\beta_i^*/T_{x,i}^B) = const. - C \cdot (E_{a,x}/RT_{x,i}) \tag{2.18}$$

where $T_{x,i}$ is the temperature at specific conversion, B and C are parameters determined by the type of temperature integral approximation.

The approximation proposed by Murray and White gives rise to B=2, C=1 and leads to the Kissinger-Akhira-Sunose (KAS) method [98]:

$$ln(\beta_i^*/T_{x,i}^2) = const. - (E_{a,x}/RT_{x,i}) \tag{2.19}$$

According to Starink [99], increased accuracy can be obtained by setting B=1.92 and C=1.0008 and Equation 2.18 becomes:

$$ln(\beta_i^*/T_{x,i}^{1.92}) = const. - 1.0008 \cdot (E_{a,x}/RT_{x,i}) \tag{2.20}$$

Alternatively, Equation 2.16 may be used to estimate the activation energy at the maximum reaction rate of thermal degradation, $d^2x/dt^2 = 0$ [94]:

$$d^2x_{max}/dt^2 = [E_a\beta_i^*/RT_{max}^2 + Af`(x_{max})\, exp\,(-E_a/RT_{max})](dx/dt)_{max} = 0 \tag{2.21}$$

where $f`(x_{max}) = df(x_{max})/dx$ and the subscript max denotes the values related to the maximum rate of thermal degradation. Equation 2.21 can be written as:

$$E_a\,\beta^*/RT_{max}^2 = -Af`(x_{max})\, exp\,(-E_a/RT_{max}) \tag{2.22}$$

After additional rearrangements, Equation 2.22 is transformed into the Kissinger equation:

$$ln\,(\beta^*/T_{max}^2) = ln\,(-AR/E_af`(x_{max})) - E_a/RT_{max} \tag{2.23}$$

A plot of the left hand side of Equation 2.23 against $1/T_{max}$ for each heating rate gives straight line with the slope, yielding the activation energy. The Kissinger method gives a single value of the activation energy at the maximum rate of thermal degradation. This could be considered one of the limitations of the Kissinger method.

2.10.3 Cone calorimeter

The most versatile bench scale instrument for measuring fire properties of materials is the cone calorimeter. The name cone comes from the truncated cone heater used to heat the specimen during fire testing. The cone calorimeter can be used to [54]:

- Compare and rank fire performance of materials
- Pass or fail a material according to specific fire criteria
- Assess the likely response of a material when exposed to a large fire
- Generate data to aid in development of a fire model

A schematic of the cone calorimeter is presented in Figure 2.11.

ASTM first issued a full standard for the cone calorimeter in 1990 under the designation: Standard test method for heat and visible smoke release rates for materials and products using cone calorimeter (ASTM E1354-90) [100]. Heat is not measured directly in the cone calorimeter because of the difficulty in recording the thermal energy with precision. Instead, the heat release rate is estimated indirectly.

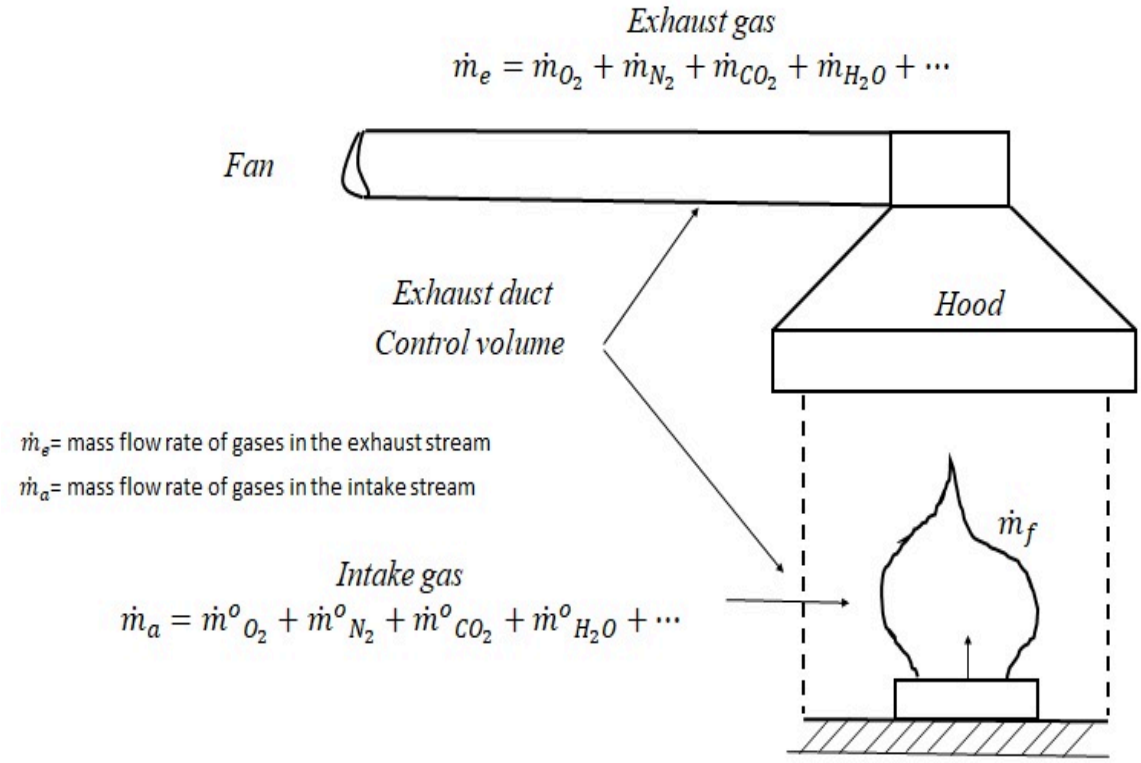

Figure 2.11: Schematic of the cone calorimeter where $\dot{m}_e$ represents the mass flow rate of the exhaust gas [101]

For complete combustion, $q^{'}$, the heat release rate in (kW) is given in terms of the mass flow rate of oxygen in the intake air ($m^o_{O_2}$) in (kg·s^{-1}), the mass flow rate of oxygen in the exhaust gas ($m^{'}_{O_2}$) in (kg·s^{-1}) and the generic constant, E (13.1 MJ·kg^{-1} oxygen consumed) [101, 102]. The heat release rate can be calculated using Equation 2.24:

$$q^{'} = E(m^o_{O_2} - m^{'}_{O_2}) \tag{2.24}$$

Equation 2.25 is used to calculate the heat release rate due to the low concentration of other gases compared to the oxygen content [103, 104].

$$q^{'} = E \cdot \frac{M_{O_2}}{M_{air}} \cdot m_e \cdot (\frac{X^o_{O_2} - X_{O_2}}{[1-(b-1)X^0_{O_2}] - bX_{O_2}}) \tag{2.25}$$

where M_{O_2} is the molecular weight of oxygen ($g \cdot mol^{-1}$), M_{air} is the molecular weight of air ($g \cdot mol^{-1}$), m_e is the mass flow rate of the exhaust stream ($kg \cdot s^{-1}$), b is a stoichiometric factor, $X^o_{O_2}$ and X_{O_2} are the mole fraction of oxygen before combustion and in the exhaust stream.

The heat release rate can be expressed as heat per unit area ($q^{''}$) is give by Equation 2.26 [6]:

$$q^{''}(t) = q^{'}(t)/A_s \tag{2.26}$$

where A_s is the surface area of the specimen exposed to heat.

The total heat released q can be determined by Equation 2.27:

$$q = \sum q^{''}(t) \cdot \Delta t \tag{2.27}$$

where Δt is the time corresponding to the measurement of the heat release.

The concentration of combustion gases such as CO_2 and CO are measured with a real-time CO/CO_2 analyzer connected to the same sampling line serving the oxygen analyzer. Other combustion products such as HCl, HCN, NO_x cannot be measured continuously. In some cone calorimeters, a Fourier-transform Infrared (FTIR) spectrometer is present to obtain real-time analysis of the combustion gases. The cone calorimeter can also be used to analyze smoke production during combustion [105]. The helium-neon laser photometer with a split beam and silicon photodiode detector is used to measure the smoke content. The sensing beam passes through smoke in the exhaust duct, while the reference beam travels directly to the detector. The intensity (I) of the sensing beam is then compared with the reference beam intensity (I_o) [105]. The smoke obscuration is defined by the extinction coefficient (K^*) (m^{-1}).

$$K^* = \frac{1}{L} \cdot ln(\frac{I_o}{I}) \tag{2.28}$$

where L is the light path length,

The average specific extinction area, σ_f ($m^2 \cdot kg^{-1}$):

$$\sigma_{f(avg.)} = \frac{\sum_i V_i K^*_i \cdot \Delta t_i}{m_o - m_f} \tag{2.29}$$

where V_i is the volumetric flow rate of the exhaust, m_o is the initial mass of the specimen, and m_f is the mass of the specimen at the end of the test. The mass loss of the specimen is also recorded continuously by a load cell located beneath the sample holder [106].

2.10.4 Vertical burning test

The vertical burning test is a small-scale laboratory procedure for determining the burning characteristics of material. It is used to measure and describe the response of the materials to heat and flame under controlled conditions. The test procedure for plastic materials is conducted according to ASTM D3801-10 [107]. This test is used to measure the ignitability and the flame-spread of vertical bulk materials exposed to a small flame. Materials are classified into three categories, V-0, V-1, or V-2 [107].

The test consists of subjecting a set of preconditioned specimens of identical composition and geometry to a standard test flame for two 10 s flame applications. The after flame time is recorded after the first flame application, and the after flame and after glow times are recorded after the second flame application. Information is also recorded on whether or not flaming material drips from the specimen (and whether these drips ignite a cotton indicator) and total flame time for a particular specimen set. See Appendix B for the materials classification according to this test.

2.10.5 Oxygen index

Combustible materials have been evaluated according to ignitability and flammability for many years by using bench scale equipment. The oxygen index test (OI) was developed in the 1960. This test is known as Limiting Oxygen Index (LOI) and known as the Critical Oxygen Index test. The LOI method is explained in various standards, including ASTM 2863, ISO 4589-2, and NES 714. Figure 2.12 shows the LOI apparatus, which consists of a vertical chimney standing 450 or 500 mm high with an internal diameter of 75 or 100 mm. The chimney is made from heat resistant glass that allows the burning of the sample to be observed. The controlled concentration of two mixed gases, oxygen and nitrogen, is pumped at the base of the chimney where they flow through a layer of glass beads that ensure even mixing before entering the main chamber. The gas mixture flows upwards to a vertical test specimen. To ignite the upper end of the sample, the burner is used, and the subsequent burning behavior is monitored.

Figure 2.12: General view of the limiting oxygen index apparatus

2.10.6 Bomb calorimetry

For many years, combustion with oxygen only in bomb calorimetry, has been accepted as a standard test method for converting solid and liquid combustible samples into soluble forms for chemical analysis and for heat of combustion estimation.

The calorific value (heat of combustion) of a sample can be defined as the heat liberated by unit mass of the sample when burned in oxygen in an enclosure of constant volume. The heat from the combustion or oxidation of the sample is obtained by calculating the total change in enthalpy expressed as the change in internal energy U plus any pressure volume work ΔPV according to:

$$\Delta H = \Delta U + (\Delta PV) \tag{2.30}$$

Equation 2.30 can be written as:

$$\Delta H = \Delta U + \Delta P \cdot V + P \cdot \Delta V \tag{2.31}$$

The use of a bomb calorimeter ensures no volume change ($\Delta V = 0$). The change of pressure could be calculated from the change in number of moles of gas by assuming an ideal gas:

$$PV = nRT \tag{2.32}$$

$$\Delta PV = RT\Delta n \tag{2.33}$$

where Δn=moles of gaseous product -moles of gaseous reactant, R=8.314 J·K^{-1}·mol^{-1}.

2.11 Fire properties

2.11.1 Time to ignition (t_{ign})

Ignition is one of the most important phenomena associated with the thermal degradation of combustible materials. It signals the onset of flaming combustion. One measure of the ease of ignition is generally the time to ignition, the minimum time required to achieve ignition and continuous flaming of a combustible material when exposed to an external heat flux. The time to ignition is estimated experimentally by techniques such as the ISO ignitability test and cone calorimetry [108].

2.11.2 Heat release rate (HRR)

Heat released by burning materials can be a source of energy required for the growth and spread of fire [54]. Heat release rate (HRR) is the thermal energy produced, per unit surface area, when flammable products ignite and burn close to the surface of a material or are subjected to an external heat flux. The peak of HRR (PHRR) occurs after ignition and the time required to reach that peak is usually a good indication of the maximum flammability of the material. The peak heat release rate, shown in Figure 2.13 [109], is a measure of fire intensity. The average heat release rate is the total heat released averaged for the combustion period. Total heat release (THR) is the integral of HRR with respect to time. THR depends strongly on the total mass loss, the effective heat of combustion of the volatiles, and the combustion efficiency in the flame zone [110]. Different apparatus can be

used to measure HRR and include the cone calorimeter and the Ohio State University heat release calorimeter. HRR fluctuates considerably over time due to chemical and physical changes occurring during combustion.

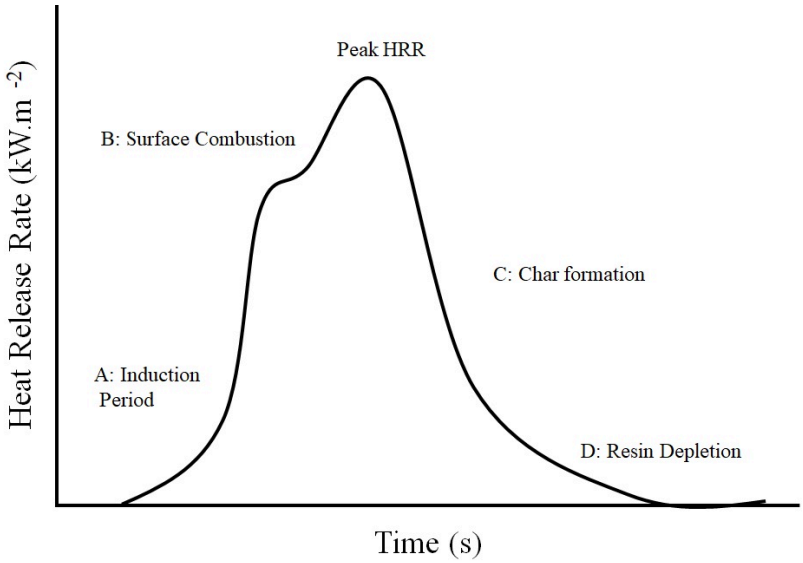

Figure 2.13: Heat release rate profile for polymer materials exposed to a heat flux [111]

Different profiles of HRR curves versus time can be obtained during the cone calorimeter experiment reflecting the burning behavior of the materials. This gives rise to the characterization of the curves for HRR vs time as shown in Figure 2.14. A sample which shows a strong initial increase in the HRR followed by an average HRR and a peak heat release rate can be categorized as a thick non-charring material (Figure 2.14 a). Intermediate thick non-charring material (Figure 2.14 b) possess HRR only marked by shoulders, for the materials behaving in between the thermally thick non-charring and thin sample. Materials which form residue show an initial increase in HRR until a char layer is formed followed by a decrease in the HRR due to the char layer thickening. The PHRR reached at the beginning equals both average or steady HRR. This type of material can be categorized as thick charring (Figure 2.14 c). Some thermally thick charring materials tend to show PHRR at the beginning before formation of the residue, and a second PHRR at the end of the measurements (Figure 2.14 d). The reason behind the formation of the second PHRR can be attributed to the failure of the char or increase in the effective pyrolysis. Thermally thin samples are categorized by a sharp peak in the HRR, and the whole sample is pyrolyzed as shown in Figure 2.14 e. In the case of unsteady development of combustion

as shown in Figure 2.14 f, which occurs due to flashing before a sustained flame, or deformation during burning, can be manipulated by changing the surface area and/or distance to the cone [6, 110].

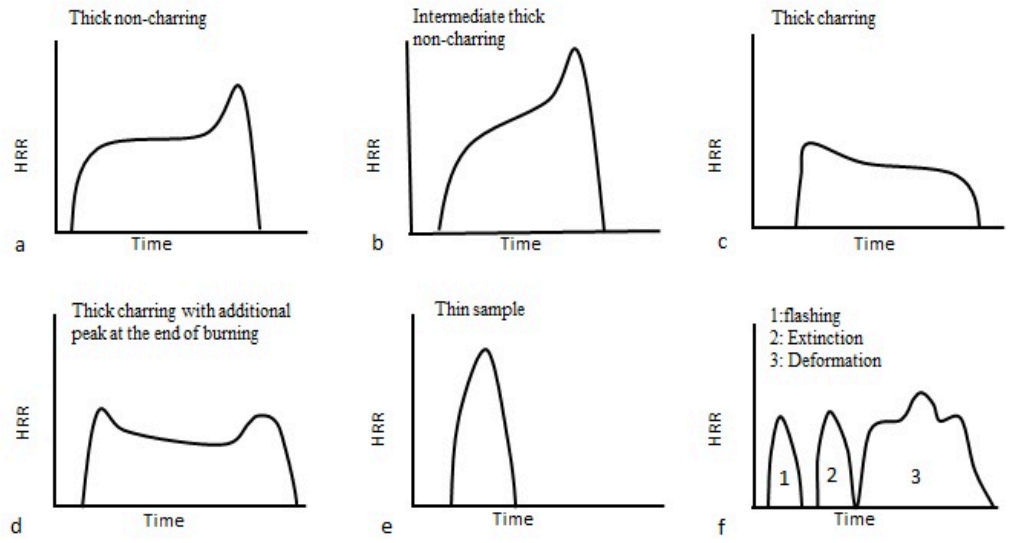

Figure 2.14: Typical HRR curves for different characteristic burning behaviors [110]

Indices have been used to assess the hazard of developing fires in order to simplify the interpretation of the cone calorimeter data, such as fire growth rate (FIGRA) which can be estimated according to the following equation:

$$\text{FIGRA} = \frac{\text{PHRR}}{t} \tag{2.34}$$

where PHRR is the peak heat release rate and t (s) is the time required to reach PHRR

Fire performance index (FPI) can used be for the same purpose as FIGRA, and estimated according to the following equation:

$$\text{FPI} = \frac{t_{ign}}{PHRR} \tag{2.35}$$

2.11.3 Limiting oxygen index (LOI)

The limiting oxygen index (LOI) can be used to rank the flammability of materials [111]. The LOI is defined as the minimum percentage of oxygen needed to sustain flaming combustion, and thus may be considered as the measure of the ease of self-extinguishment of materials [112]. The limiting oxygen index is experimentally determined with the oxygen index test. LOI cannot be used to accurately rate the fire behavior of materials because the sample is not tested under realistic fire environment conditions [26]. In the ASTM standard D-2863 [113], the minimum percentage of oxygen in atmosphere needed to support ignition and combustion is measured. A limitation of the test is the sensitivity to temperature conditions which can affect the relative flammability ranking of materials. The LOI depends on factors such as sample geometry, orientation of the sample with respect to the flame, the air or gas temperature around the sample, and the formation of char or similar barriers. LOI estimates must be complemented with other methods for the evaluation of flame retardant systems [114].

2.11.4 CO and smoke production

The toxicity of gases produced during the burning of materials is the main cause of death in fires [115]. Of these gases, carbon monoxide (CO) in particular represents the most severe health hazard. CO produced by a burning material depends on the composition of the organic constituents, the temperature, and oxygen availability. CO and smoke production result from incomplete combustion. The quantity of gas produced tends to vary over the course of a fire, with the CO yield usually increasing in the later stages of the combustion process when the material is extensively carbonized [111, 116]. A linear correlation exists between the CO level and the heat release rate which suggests that health hazards associated with CO can be minimized by designing materials with low heat release properties [111].

2.11.5 Heat of combustion

Combustion of organic compounds including polymers leads to the generation of heat which can be quantified by the molar heat of combustion (ΔH_c). Heat of combustion can be used to evaluate the flammability of materials. It is noted that the flame resistance of materials increases as less heat is evolved during combustion.

The heat of combustion can be obtained from the principles of molar additivity of the heat of formation of the combustion products and reactants [117]. The molar heat capacity

(C_p) can be obtained by multiplying the molar mass of the structural unit, by the specific heat capacity (c_p). The group contribution to the molar heat capacity which can be used to estimate the heat of combustion is shown in Table 2.4 [118].

The molar heat capacity (C_p) ($\mathrm{J{\cdot}mol^{-1}{\cdot}K^{-1}}$) at constant pressure can be formulated:

$$C_p = Mc_p = (\frac{\delta H}{\delta T})_p \tag{2.36}$$

where M is the molar mass ($\mathrm{mol{\cdot}kg^{-1}}$), c_p is the specific heat capacity ($\mathrm{J{\cdot}kg^{-1}{\cdot}K^{-1}}$), H is the heat content per mole.

The molar heat capacity of polymers can be estimated with the method of Satoh and Shaw [118]. The sum of enthalpies of the components represents the heat of reaction, which can be formulated according to the following equation:

$$\Delta h_c = \sum_i n_p \Delta h^o_{f.p} - \sum_i n_r \Delta h^o_{f.r} \tag{2.37}$$

where Δh_c is the heat of formation , p and r denote products and reactants in the standard state at 298 K.

Table 2.4: Specific heat capacity of some molar groups, given as crystalline ($C^s_p \times 298$) and amorphous region ($C^1_p \times 298$) ($\mathrm{J{\cdot}mol^{-1}}$) for some molar group contribution [119]

Molar group	$C^s_p \times 298$	$C^1_p \times 298$
$-CH_3$	9.20	10.99
$-CH_3-$	7.55	9.05
$>CH-$	4.64	6.24
$>C<$	1.84	2.20
$=CH_2$	6.73	6.49
$=CH-$	5.55	6.37
$=CH<$	3.12	15.90
$-O-$	5.00	10.60
$-CO-$	6.86	15.52
$-COO-$	13.70	19.37
$-COOH-$	14.90	29.47
$-OH-$	5.06	13.35
$C=O$	120.08	
$-C-$	61.72	

2.12 Mechanical properties

2.12.1 Tensile properties

A tensile test provides the response of a material to uniaxial tensile loading. It is generally conducted according to a standard established by the American Society of Testing Materials (ASTM) known as D-638 [120]. The test involves a sample of specified geometry and thickness clamped vertically and then pulled at a constant rate. The force required to produce a certain elongation is monitored, resulting in a load versus elongation curve [121]. Information on the mechanical characteristics of the material are obtained by normalizing the data for sample geometry (area and length) using Equation 2.38 and Equation 2.39 [121–123]:

$$\text{Stress } (S) = \frac{F}{A_o} \tag{2.38}$$

$$\text{Strain } (e) = \frac{\Delta L}{L_o} \tag{2.39}$$

where S and e are the engineering stress and strain, respectively; F is the force applied on the specimen in Newtons (N), A_o is the initial cross-section area of the specimen before testing (m^2), L is the change in the length of the specimen (m), and L_o is the initial length of the specimen before testing (m).

A typical plot of engineering stress versus engineering strain is illustrated in Figure 2.15. The curve can be divided into two distinct regions: a region of elastic deformation and a region of plastic deformation. These regions represent the behavior of the sample once the load is removed. In the region of elastic deformation, the sample regains its original dimensions after the force is withdrawn. During plastic deformation, the original dimensions are not recovered, though a small elastic component is recovered.

The yield strength of a material is defined as the intersection of the deformation curve with a straight-line parallel to the elastic portion and offset 0.2 % on the strain axis [121]. It denotes the onset of plastic deformation. Ultimate tensile strength, or simply, tensile strength, is the maximum engineering stress that a material can withstand [121, 122]. The slope of the stress strain curve in the elastic region is called the modulus of elasticity, or Young's modulus (E). Equation 2.40, called Hooke's Law, expresses the linearity of the stress strain curve in the elastic region [122].

$$\text{Modulus of elasticity (E)} = \frac{S}{e} \tag{2.40}$$

The ability of a material to deform permanently is called its ductility [121]. A quantitative measure of ductility is the relative elongation at failure, given by Equation 2.41:

$$\text{Relative elongation at failure} = (\frac{l_f - l_0}{l_0}) \times 100 \tag{2.41}$$

where l_f is the gauge length just before failure (m), and l_0 is the initial gage length (m).

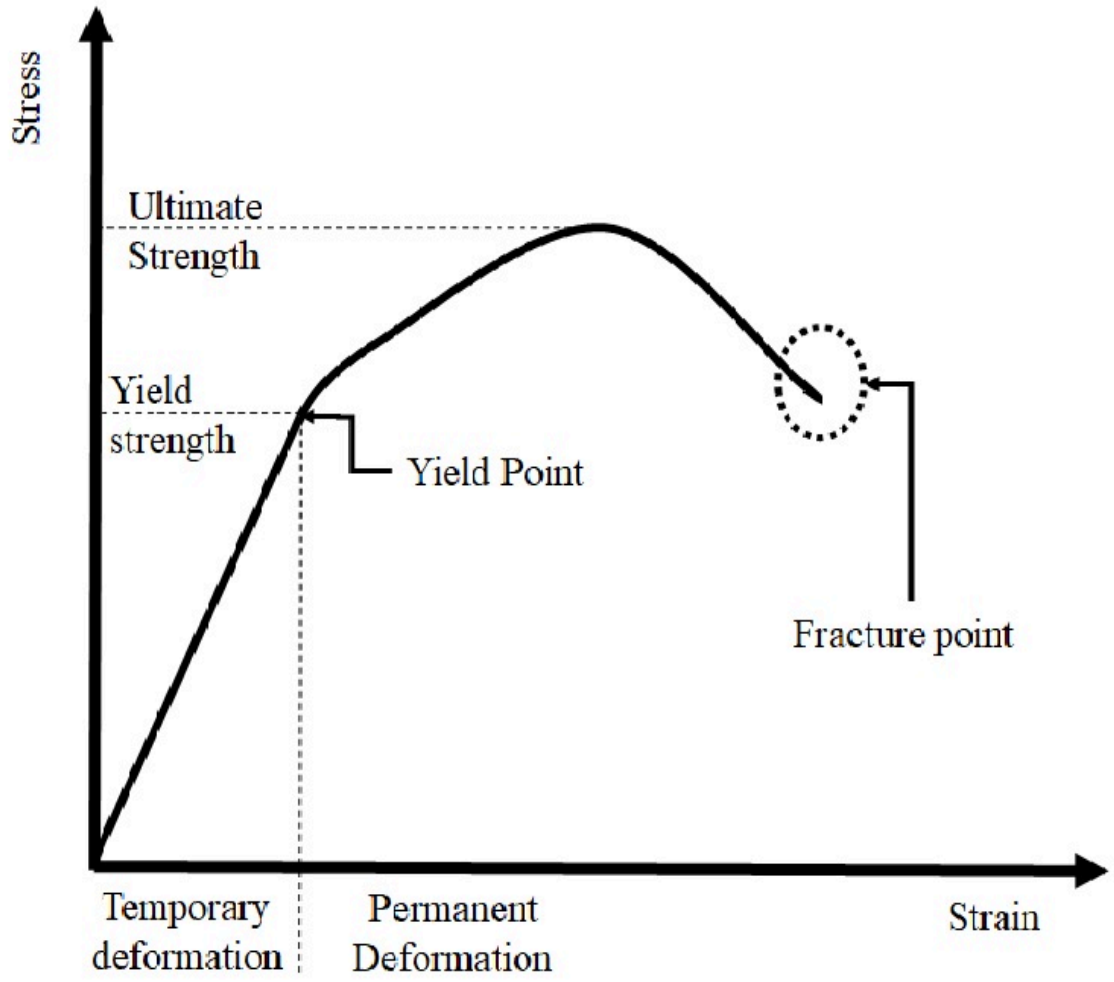

Figure 2.15: Typical stress-strain curve [124]

2.12.2 Impact properties

A notched impact test measures the energy during impact, i.e. the energy necessary to fracture a standard test piece [121]. It is generally conducted according to a standard established by the American Society of Testing Materials (ASTM) known as D-256 [125]. The impact energy is analogous to toughness in the stress vs. strain curve. The sample is clamped vertically, and a pendulum impacts the sample on the same side as the notch. The impact energy is calculated from the difference in the initial and final height of the pendulum [121].

2.13 Structure and morphology

2.13.1 X-ray diffraction (XRD)

XRD is one of the techniques which is used for phase identification of crystalline materials and can provide information on crystalline structure. X-ray are generated by a cathode ray tube, filtered to produce monochromatic radiation, collimated to concentrate, and directed toward the sample. Bragg's law(Equation 2.42) can be applied to convert the diffraction peaks to d-spacing, allowing identification of the material because each material has a unique d-spacing [126].

$$\mathrm{n}\,\lambda = 2\,d\,sin\,\theta \tag{2.42}$$

where n (an integer) is the order of reflection, λ is the wave length of the incident X-ray, d is the interplanar spacing of the crystal, and θ is the angle of incidence.

The degree of crystallinity can be estimated with the method of Nara and Komiya [127]. The method consists of assigning the crystalline and amorphous domains. By creating a smooth curve connecting the baseline of the peaks, the area above the smooth curve is considered the crystalline domain and the area between the smooth curve and the linear baseline is considered as the amorphous domain. The expression for calculating the degree of crystallinity (X_c) based on the information which is acquired from the diffracted rays is as follows:

$$X_c\,(\%) = \frac{A_c}{A_a + A_c} \times 100 \tag{2.43}$$

where A_c is the area of the peak assigned to the crystalline domain, and A_a is the area of the peaks assigned to the amorphous domain.

2.13.2 Field emission scanning electron microscopy (FESEM)

Scanning electron microscopy (SEM) can provide information related to topographical features, morphology, phase distribution, compositional differences, crystal structure, among others. In addition, SEM is capable of determining elemental composition of micro-volumes with the addition of an x-ray or electron beam (EDX). Field emission SEM (FESEM) merits special mention because of its ability to produce small probing diameters at low voltage [128]. Low voltage scanning electron microscopy has the advantage of revealing more details of the surface since there is less penetration of the beam into the specimen and it is thus less damaging to the material [129].

Chapter 3

Investigation of the Formulation of Plasticized Cellulose Acetate Magnesium Hydroxide Polypropylene Materials

The first part of the chapter (3.1) aimed to evaluate the viability of TEC as a plasticizer for CA in order to proceed to the second step of the fabrication of the cellulose acetate polypropylene material. The evaluation of its viability was accomplished by using DSC and XRD equipment. Furthermore, the effects of TEC on the thermal stability of CA were studied using TGA. The second part of this chapter (3.2 and 3.3) was to define the formulation of plasticized cellulose acetate magnesium hydroxide polypropylene materials which was based on the thermal stability of the material obtained by TGA.

3.1 Plasticization of cellulose acetate

Cellulose acetate (CA) is one of the most important cellulose derivatives, and it is widely used as fibrous content and in plastics applications [130]. CA is a thermoplastic material produced from the esterification of cellulose. Different raw materials are used in making cellulose acetate in its powdered form such as cotton, recycled paper, and wood cellulose [34]. CA has several attractive characteristics, including being derived from a renewable source, and being non-toxic, low cost, and biodegradable. However, CA has several limitations such as high viscosity and glass transition temperature (T_g), as well as the fact

that melt processing of CA requires modification of the material due to the close proximity of melting temperature (T_m) and its decomposition temperature (T_d). This means CA should be plasticized in order to be used with other materials.

The primary role of plasticizers is to improve the flexibility and processability of a material by lowering the glass transition temperature. Plasticizers are low molecular weight compounds which form a secondary bond to the material chains and spread them apart. Plasticizers can be either internal or external. In external plasticizers, molecules are not attached to the chains by primary bonds and therefore can be lost by evaporation, while internal plasticizers remain part of the materials [131].

The main plasticizers used in CA materials are phthalate plasticizers, now under scrutiny due to health and environmental issues. Other compounds such as triethyl citrate (TEC) and glycerol have also been used successfully. Citrate-based plasticizer can be derived from naturally occurring citric acid [47]. Citric acid esters are non-toxic and have been proven as effective plasticizers for many applications [46].

Many studies are available concerning the influence of plasticizer on the properties of CA [45, 46, 132]. Ghiya et al. [46] reported that TEC with 30 wt.% reduces the glass transition temperature by 50-60 °C and depresses the melting temperature. Mohanty et al. [34] stated that the presence of plasticizer limits the crystallinity in the matrix and increases the free volume present in the system. In addition, the crystalline melting peak disappears upon plasticization. These results confirm that plasticized CA (CA*) is an amorphous material and its properties shift from rigid to ductile.

The usefulness of CA is influenced by its degradation and stabilization. Different factors can lead to the degradation of CA, such as temperature and atmospheric oxygen level. There exists comprehensive data for plasticizer effects on the thermal stability of CA [133, 134]. It was reported that the degradation of CA consists of a series of reactions: dehydration below 100 °C, evaporation of TEC starting at 126 °C (TEC boiling point), deacetylation beginning at 250 °C, and carbonization and formation of ash occurring above 500 °C [135]. It has also been reported that the addition of plasticizers makes CA degrade at a lower temperature [136].

3.1.1 Experimental methods

3.1.1.1 Materials

Cellulose acetate (CA) (approx. 50000 g·mol^{-1} Missouri, United States. 39% acetyl), and triethyl citrate (TEC), were purchased from Sigma Aldrich (USA). All materials were used

as received.

3.1.1.2 Materials preparation

An amount of 2.1 g (2.37 ml) of TEC was added drop-wise to 4.9 g of pre-dried CA powder and then mixed with a vortex mixer for five minutes. The TEC plasticized CA (CA*) pellets were made in a twin-screw extruder (SJSZ-7A, Wuhan Ruiming Plastic Machinery Company, China). The four temperature zones of the extruder were between 170 °C-190 °C, and the residence time was five minutes. TEC comprised 30 wt.% of the final CA* mixture. The extruded materials were then cut as pellets by using a cutter (SZS-20, Wuhan Ruiming Plastic Machinery, China).

3.1.1.3 Differential scanning calorimetry (DSC)

DSC analysis was used to estimate the glass transition temperature and characterize the effect of TEC plasticization on CA. DSC (model Q2000, TA Instrument Company, USA) was performed under nitrogen with a flowrate of 30 mL·min^{-1} at 10 °C·min^{-1} heating rate. CA and CA* pellets were heated from room temperature up to 180 °C, cooled to 25 °C, then equilibrated for five minutes followed by heating up to 300 °C. The sample initial mass was 8 mg. Glass transition temperature and melting temperature were calculated using the TA Universal Analysis version 5.5.20 software.

3.1.1.4 Wide angle X-ray diffraction analysis (WAXRD)

The crystalline structure of cellulose acetate and plasticized cellulose acetate was analyzed by wide angle X-ray diffraction. The sample was laid on the sample holder and analyzed with CuK radiation (λ =1.54 Å) generated at a voltage of 45 kV and tube current of 35 A. The X-ray diffraction patterns were recorded in a 2θ angle. The range was from 5° to 80° and scan step size was 0.004° under continuous scan mode. The degree of crystallinity was estimated as the ratio of the crystalline area to the total area under the diffraction peaks. Data analysis was performed using Origin -Pro software.

3.1.1.5 Thermogravimetric analysis (TGA)

Thermogravimetric analysis (TGA) was performed in a Q500 TA instrument. TGA was conducted under air with flowrate of 40 mL·min^{-1}. Each sample (about 10 mg) was heated

from room temperature to 650 °C at 10 °C · min^{-1}. The mass change over time was analyzed with TA Universal Analysis version 5.5.20 software to estimate the temperature for the onset of degradation ($T_{5\%}$) and the temperature at the maximum rate of degradation (T_{max}) of CA and CA*.

3.1.2 Results and discussion

Cellulose acetate (CA) requires plasticization to be processed by extrusion. TEC was selected as the plasticizer. Based on the DSC thermogram shown in Figure 3.1, CA* melted at 160-175 °C, approximately 75 °C below the melting point of CA. Moreover, the sharp crystalline peak of CA disappeared upon TEC addition, suggesting a shift of properties from rigid to ductile.

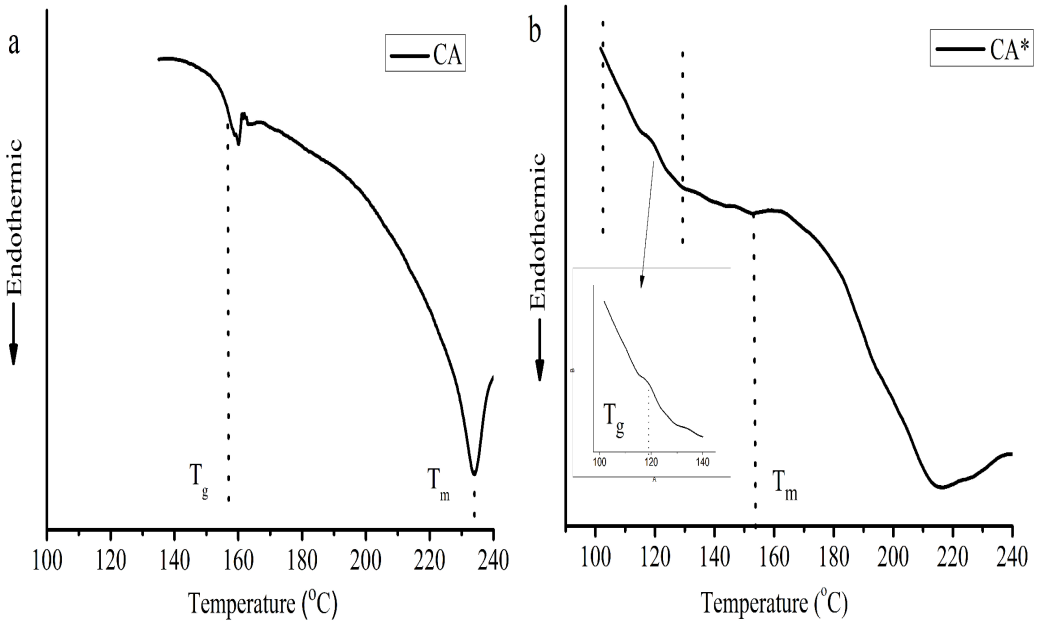

Figure 3.1: DSC thermograms for cellulose acetate before and after adding TEC. a. CA, b. CA*. The dotted lines represent the temperature range where T_g was expected to be located as illustrated in the close up (b)

Table 3.1 summarizes the effect of TEC on CA measured by DSC. The lower glass transition temperature (T_g) of CA* confirmed that it was miscible with TEC. The addition of TEC may have reduced the intermolecular forces between the CA chains by shielding functional groups along these chains. Shielding leads to an increase in free volume and chain mobility [137].

Table 3.1: Effect of TEC on CA

Material	T_g (°C)	T_m (°C)	X_c (%)
CA	157	234	21
CA*	118	157	10

Some insight into the plasticization process was obtained by comparing the XRD patterns and the degree of crystallinity (X_c) for the CA before and after plasticization. XRD provides a measure of the average intersegmental chain spacing in the macromolecules. The degree of crystallinity (X_c) depends on the degree of substitution of hydroxyl groups with acetyl groups that have greater volume [130]. For CA, it is difficult to precisely determine X_c due to the high overlap between the melting endotherm and the glass transition temperature [138].

Figure 3.2 shows the XRD patterns of CA and CA*. The results feature a wide halo around 2θ=20^o, known as van der Waals or amorphous, and this is normally found in all organic polymers [139]. For CA, the peak intensity can be determined at 8.5°, 10.5°, 13.5°, 17°, and 21.5°. The maxima at 2θ=10.5° is known as a low van der Waals halo, and according to the literature, it is attributable to the existence of regions of parallel chain segments. The peak at 2θ =8.5° is an indication of the disorder when cellulose is acetylated [140]. For CA*, there are only two main broad peaks located at 8.5° and 21.5°. In addition, the peak intensity of CA* is less than CA which can be attributed to the impacts of TEC, which increases the disorder of the CA structure.

The degree of crystallinity of CA was estimated by Nara and Komiya [127] as shown in Appendix C. It is based on the ratio of the area above the amorphous profile, as a standard, to the total area.

$$X_c\,(\%) = \left(\frac{A_c}{A_c + A_a}\right) \times 100\% \tag{3.1}$$

where A_c is the area of the peak assigned to the crystalline domain, and A_a is the area of the peak assigned to the amorphous domain in the XRD diffractograms.

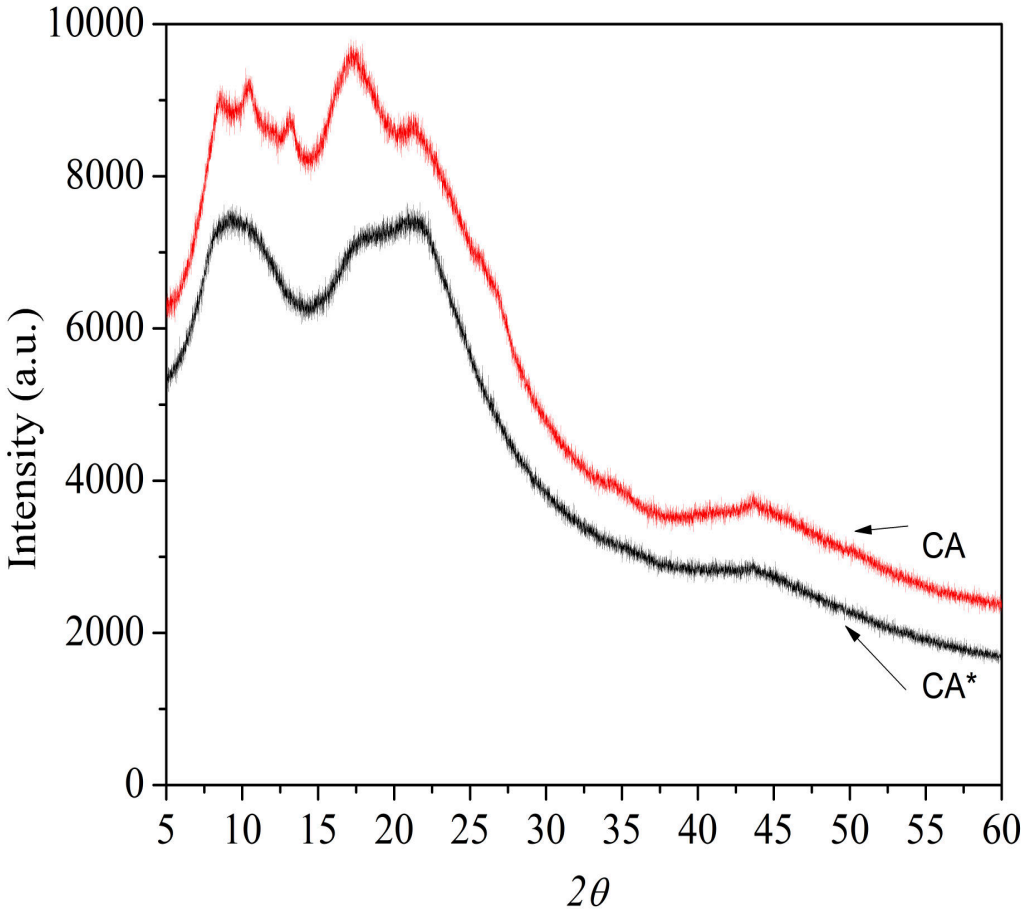

Figure 3.2: XRD patterns of CA and CA*

CA has a higher X_c (Table 3.1) than CA* which means that it is now more amorphous, confirming the results from DSC.

The TGA and DTGA of CA and CA* are presented in Figure 3.3. The TGA curves revealed a minor weight loss for CA* which is attributed to water desorption and evaporation of the TEC beginning at 126 °C (boiling point of TEC=126 °C). For CA, TGA shows a smooth degradation. The temperature for the onset of degradation ($T_{5\%}$) for CA was 266 °C. The maximum weight loss temperature (T_{max}) was 350 °C. For CA*, $T_{5\%}$ was 191

°C and T_{max} was 329 °C. After the addition of TEC, CA* began to degrade at a lower temperature; $T_{max}$was lower than for CA.

DTGA thermograms taken at 10 °C·min^{-1} (Figure 3.3b) were used to differentiate key features of degradation of the thermal decomposition of CA and CA*. For CA, its DTGA curve contained only one major step within temperature range 223-410 °C, at which 87% mass loss occurred. Another minor step could be detected within 410-580 °C at which 12% mass loss occurred. DTGA curve of CA* shows a different pattern than that of CA. Its DTGA contains two major steps and one minor step at the end of the thermal decomposition. The first step within 58-288 °C, with mass loss of 33%, reflects the evaporation of moisture and the TEC. The second step occurred with temperature range 288-388 °C and mass loss of 57%, which could be attributed to the degradation of CA*. A minor step (388-555 °C) with mass loss of 9% can be attributed to the carbonization of the remaining materials resulting in the formation of ash. Table 3.2 summarizes these steps with their temperature range and the mass remaining after each step.

Table 3.2: DTGA steps of CA and CA* in air at 10 °C·min^{-1} heating rate

Materials	Temperature range (°C) Residual (%)		
Steps	1	2	3
CA	223-410	410-580	
	13	0.7	
CA*	58-288	288-388	388-555
	67.6	10.5	0.1

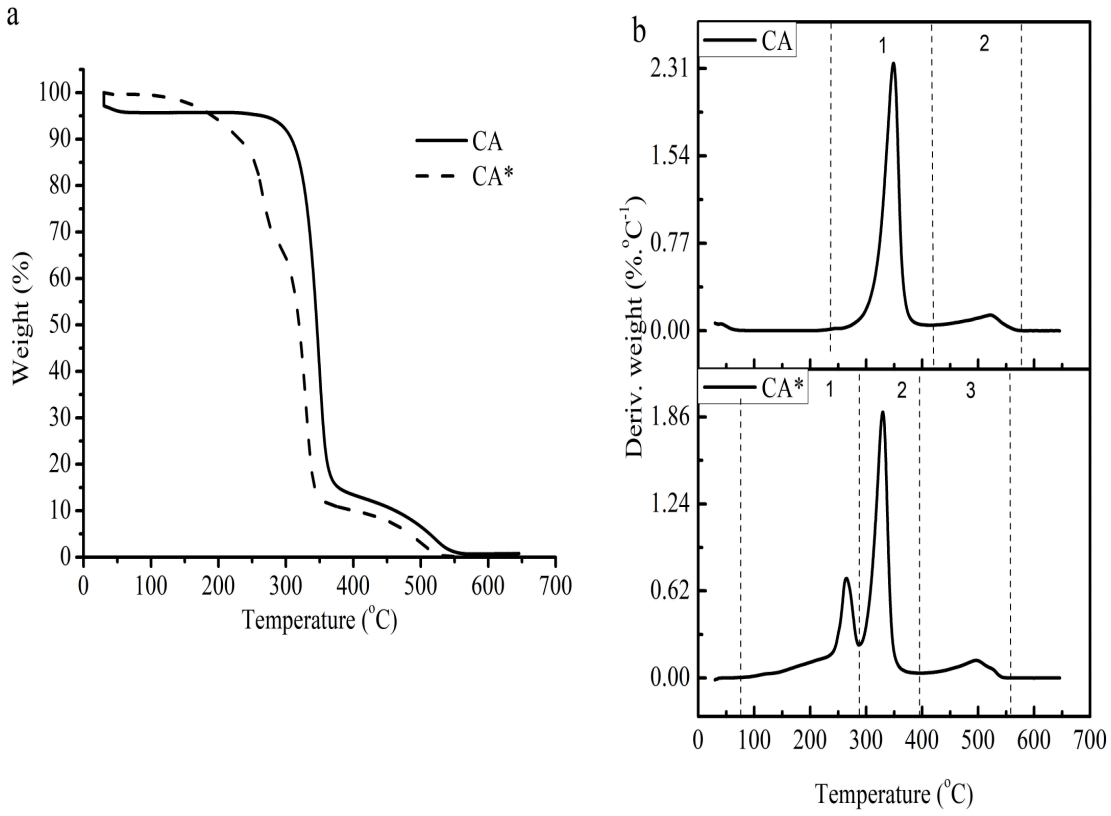

Figure 3.3: TGA and DTGA curves of CA and CA* in air at 10 °C·min^{-1} heating rate. a. TGA, b. DTGA. Conversion level along with onset and end of each step are presented in Table 3.2.

3.2 Investigation of plasticized cellulose acetate magnesium hydroxide polypropylene materials

The formulation of polypropylene materials was investigated from the thermal stability of the materials obtained by thermogravimetric analysis (TGA). The thermal stability was assessed from the TGA curves and activation energy estimates. The formulation was developed sequentially, polypropylene-grafted- maleic anhydride, plasticized cellulose acetate and magnesium hydroxide.

3.2.1 Experimental methods

3.2.1.1 Materials

Polypropylene (PP) fine powder (HM20/70P), was purchased from GOONVEAN Fibres Company, United Kingdom. The melt flow index is 23-59 g·10min^{-1}. Magnesium hydroxide (MH), cellulose acetate (CA) (approx. 50000 g·mol^{-1} Missouri, United States. 39% acetyl), triethyl citrate (TEC), and polypropylene-grafted maleic anhydride (PPMA) were purchased from Sigma Aldrich (USA). All materials were used as received.

3.2.1.2 Materials preparation

PP materials were produced by a two-step process. The first step consisted of the plasticization of CA. A mass of 2.1g (2.37 ml) of TEC was added drop-wise to the 4.9 g of pre-dried CA powder would be mixed via vortex mixer for 5 minutes. The CA and TEC mixture was extruded by twin-screw extruder (SJSZ-7A, Wuhan Ruiming Plastic Machinery Company, China). The four temperature zones of the extruder were set to be in the range of 170-190 °C. The extruded materials were pelletized with a speed of 10 rpm.

The second step was to mix the plasticized CA with other ingredients (PPMA and MH) to obtain polypropylene materials. This was done in the twin-screw extruder operated with four temperature zones ranging from 160 °C-180 °C with 5 minutes as residence time. Table 3.3, 3.4, 3.5, and 3.6 list the formulation of the polypropylene materials. PPMA was added with loading of 3 wt.% as a replacement portion of PP and produced PP*. The extruded materials were then cut as pellets by using a cutter (SZS-20, Wuhan Ruiming Plastic Machinery, China).

Table 3.3: Sample composition and coding of PP and PPMA materials

Material	PP wt. %	PPMA wt. %
PP	100	0
99PP/1PPMA	99	1
98PP/2PPMA	98	2
97PP/3PPMA	97	3

Table 3.4: Sample composition and coding of PP, PP*, and CA* materials

Material	PP wt.%	CA* wt.%	PPMA wt.%
PP	100	0	0
80PP*/20CA*	77.6	20	2.4
70PP*/30CA*	68.9	30	2.1
60PP*/40CA*	58.2	40	1.8

PP* refers to 97PP /3PPMA.

CA* refers to plasticized cellulose acetate with triethyl citrate.

Table 3.5: Sample composition and coding of PP, PP*, and MH materials

Material	PP wt.%	MH wt.%	PPMA wt.%
PP	100	0	0
80PP*/10MH	87.3	10	2.7
80PP*/20MH	77.6	20	2.4
70PP*/30MH	67.9	30	2.1

PP* refers to 97PP /3PPMA.

Table 3.6: Sample composition and coding of PP, PP*, CA*, and MH materials

Material	PP wt.%	CA* wt.%	MH wt.%	PPMA wt.%
PP	100	0	0	0
90(60PP*/40CA*)/10MH	52.38	36	10	1.6
80(60PP*/40CA*)/20MH	46.56	32	20	1.4
70(60PP*/40CA*)/30MH	40.74	28	30	1.3

PP* refers to 97PP /3PPMA.

CA* refers to plasticized cellulose acetate with triethyl citrate.

3.2.1.3 Thermogravimetric analysis (TGA)

PP materials were analyzed by TGA (Q500, TA instruments, USA). TGA was conducted under air with flowrate of 40 mL·min^{-1} at four different heating rates 5, 10, 20, and 30 ^{o}C·min^{-1}. The temperature range was 30-650 ^{o}C. The initial mass of each sample was approximately 10 mg. The TGA and DTGA curves were analyzed with TA Universal Analysis version v5.5.20 software to estimate the temperature for the onset of degradation ($T_{5\%}$) and the maximum weight loss temperature (T_{max}) of PP materials. The maximum weight loss rate (MWLR) was the lowest for 97PP/3PPMA.

TGA data were used to obtain activation energy at the maximum rate of degradation according to Kissinger method , and the activation energy as a function of conversion according to KAS method (methodology presented in section 2.10.2).

3.2.1.4 Scanning electron microscopy

The morphology of PP materials was observed using a scanning electron microscope (SEM) (Quanta FEG 250). Rectangular-shaped samples (6 cm×1.5 cm×0.5 cm) were frozen in liquid nitrogen and cryofractured. In order to avoid charging, all surfaces were coated with a thin layer of gold. Elemental mapping was performed using Energy Dispersive X-ray Spectroscopy (EDX) in the equipment.

3.2.2 Polypropylene-grafted-maleic anhydride polypropylene materials

3.2.2.1 Thermal stability

Table 3.7 summarizes the analysis results of the TGA and DTGA for PP materials According to the TGA curves (Figure 3.4 and Figure 3.5), the addition of polypropylene-grafted-maleic-anhydride (PPMA) increased $T_{5\%}$ compared to that of PP. No residue was left at the end at all heating rates. DTGA curves show that the addition of PPMA shifts the maximum weight loss temperature to higher temperature, as shown in Figure 3.5. The increase in T_{max} was directly proportional to the level of PPMA for all heating rates. The highest T_{max} was for 97PP/3PPMA compared to PP.

Table 3.7: Thermal analysis of PP and PP/PPMA in air for 5, 10, 20, and 30 $^{o}C{\cdot}min^{-1}$ and different levels of of PPMA

Heating rate ($^{o}C{\cdot}min^{-1}$)	Material	$T_{5\%}$ (^{o}C)	T_{max} (^{o}C)	Residue (wt.%)	MWLR (wt.% $\cdot^{o}C^{-1}$)
5	PP	252	312	0	1.38
	99PP/1PPMA	259	331	0	1.12
	98PP/2PPMA	261	341	0	0.96
	97PP/3PPMA	266	360	0	0.82
10	PP	270	347	0	1.26
	99PP/1PPMA	278	357	0	1.40
	98PP/2PPMA	283	362	0	1.40
	97PP/3PPMA	289	384	0	1.04
20	PP	290	397	0	1.07
	99PP/1PPMA	304	404	0	1.22
	98PP/2PPMA	304	403	0	1.10
	97PP/3PPMA	313	406	0	1.24
30	PP	317	427	0	1.25
	99PP/1PPMA	320	432	0	1.12
	98PP/2PPMA	321	419	0	1.33
	97PP/3PPMA	344	443	0	1.28

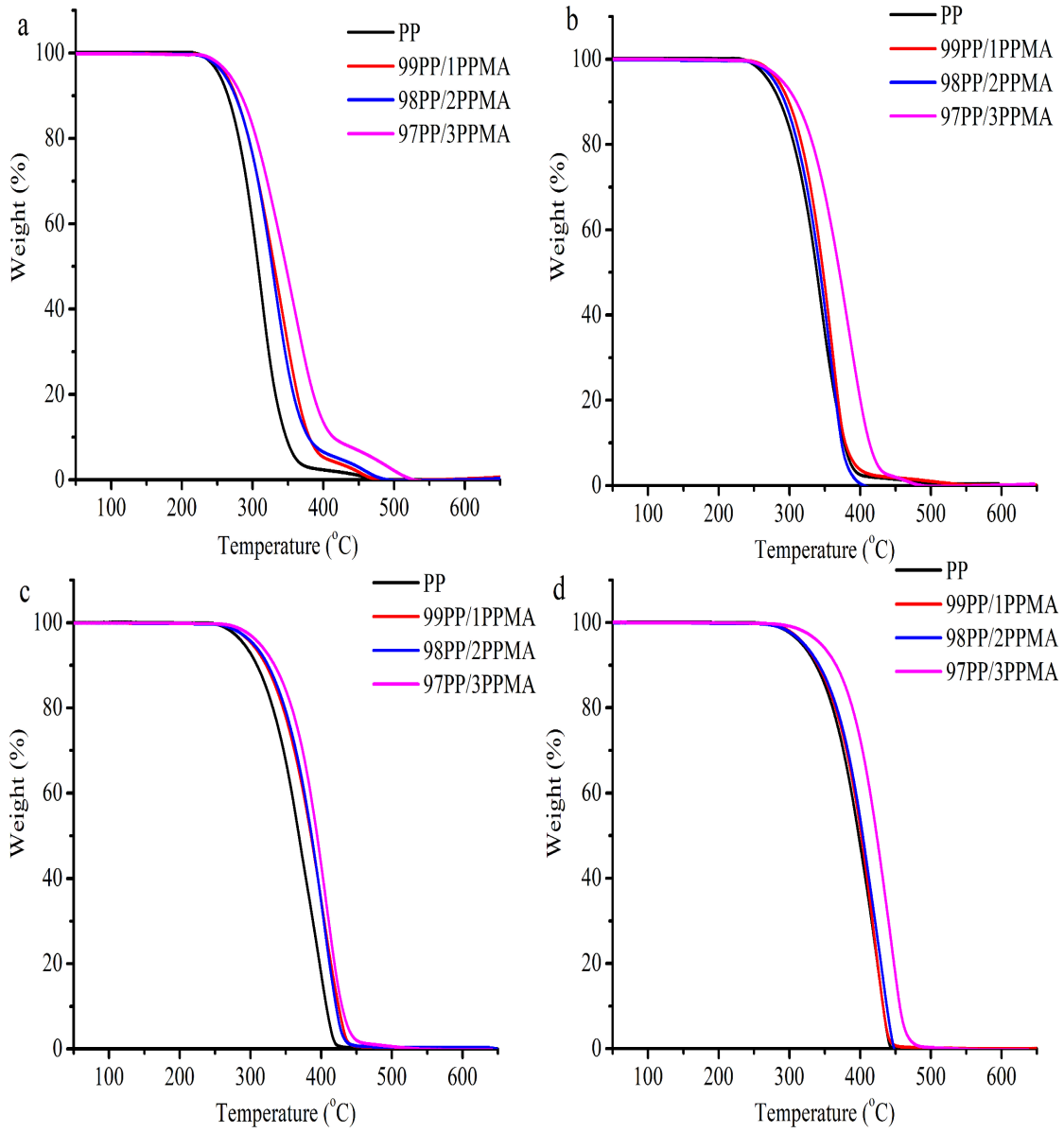

Figure 3.4: TGA curves of PP and PP/PPMA in air at four heating rates and different levels of PPMA. a. 5 °C·min^{-1}, b. 10 °C·min^{-1}, c. 20 °C·min^{-1}, and d. 30 °C·min^{-1}

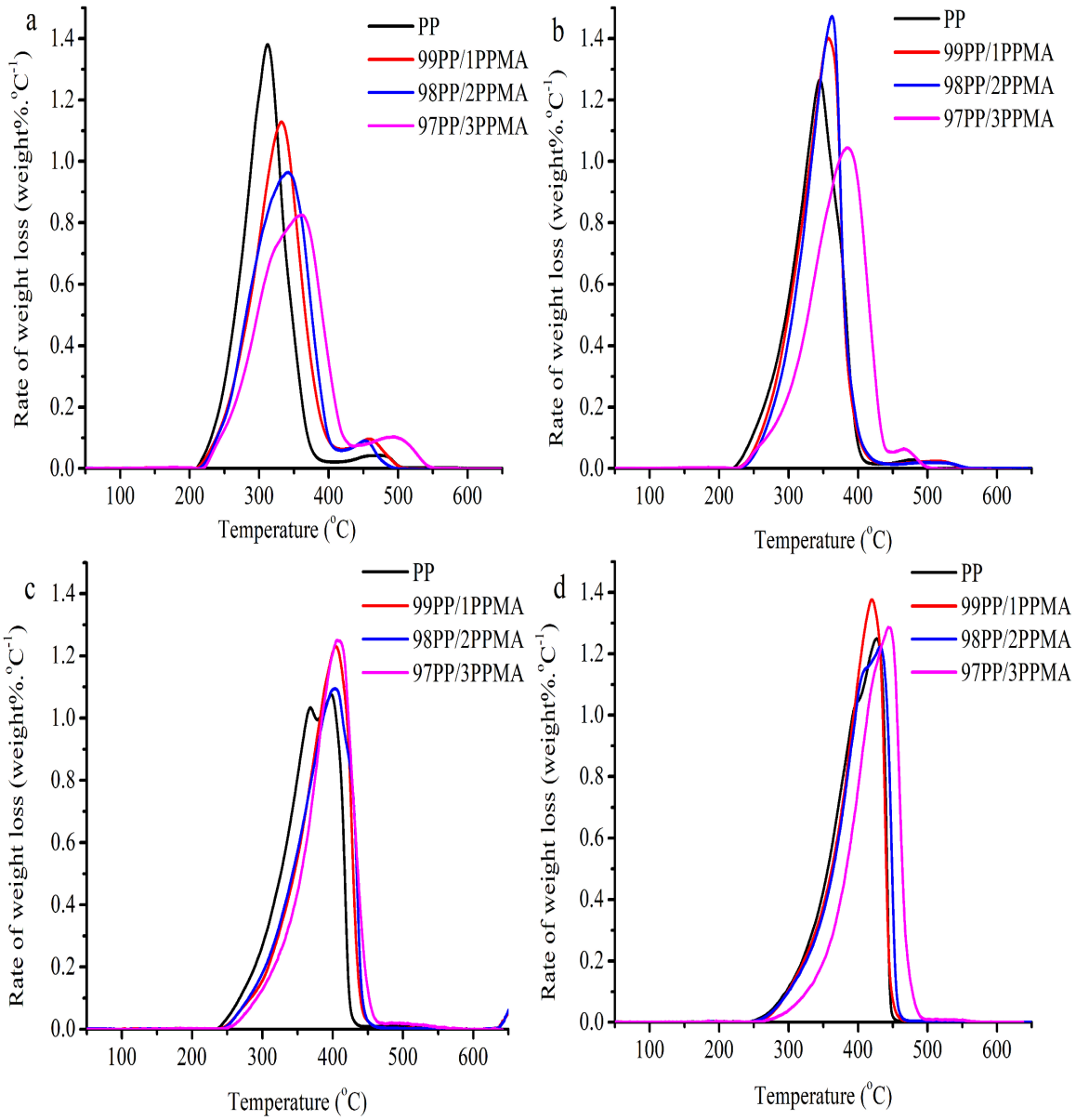

Figure 3.5: DTGA curves of PP and PP/PPMA in air at four heating rates and different levels of PPMA. a. 5 °C·min^{-1}, b. 10 °C·min^{-1}, c. 20 °C·min^{-1}, and d. 30 °C·min^{-1}

3.2.2.2 Kinetics of thermal degradation

The apparent activation energy at the maximum rate of conversion was estimated with the Kissinger method, and its linearized form expressed in terms of T_{max} (Table 3.7) and the linear plots of PP and different levels of PPMA are shown in Figure 3.6. The estimated E_a for PP, 99PP/1PPMA, 98PP/2PPMA, and 97PP/3PPMA were 41, 50, 66, 70 kJ·mol^{-1}, respectively. It can be seen with increasing the level of PPMA there is an increase in the estimated E_a.

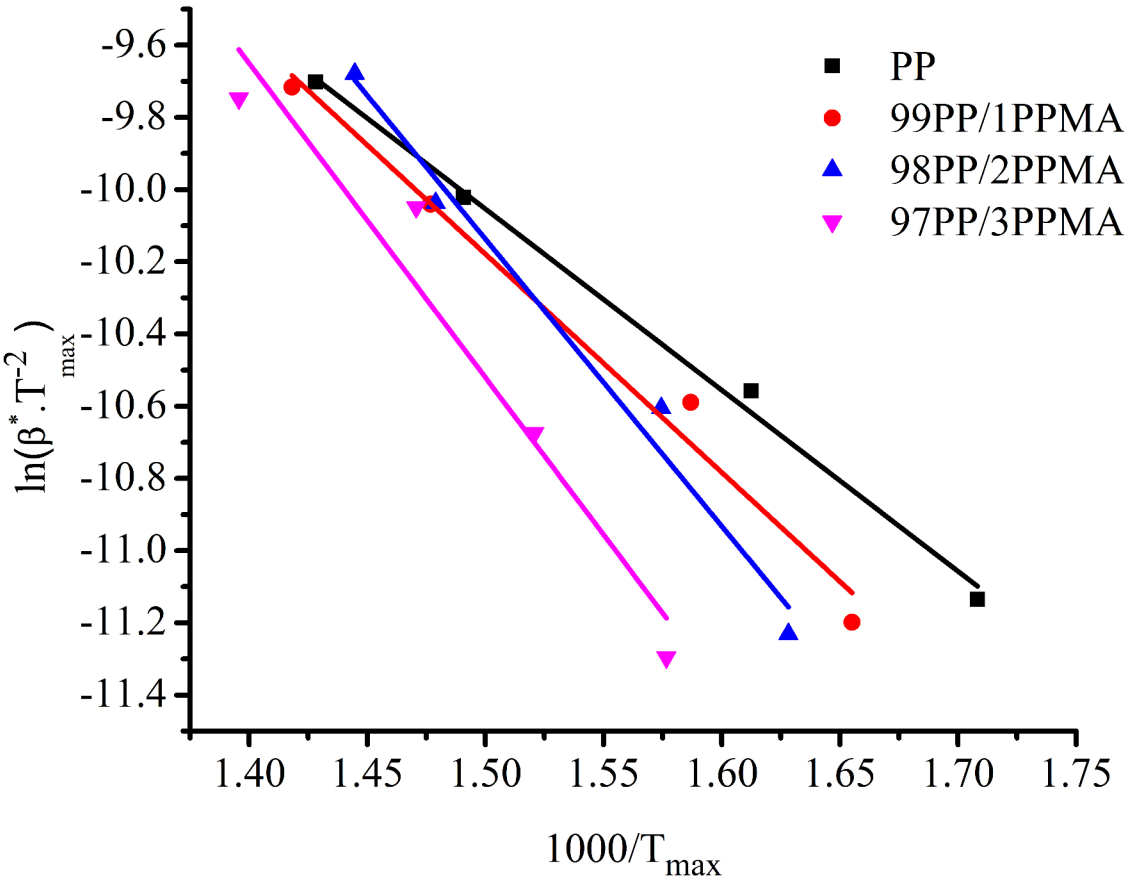

Figure 3.6: Linear plots for calculating E_a by using Kissinger method for PP/PPMA materials

The activation energy ($E_{a,x}$) according to the conversion was also estimated by using the KAS method (Figure 3.7). The activation energy for PP was relatively constant, approximately 60 kJ·mol^{-1} for the entire conversion range. The activation energy of 99PP/1PPMA and 98PP/2PPMA was also constant for the entire conversion range but higher than that of PP. For 97PP/3PPMA, $E_{a,x}$ increased with constant rate with increasing the levels of conversion.

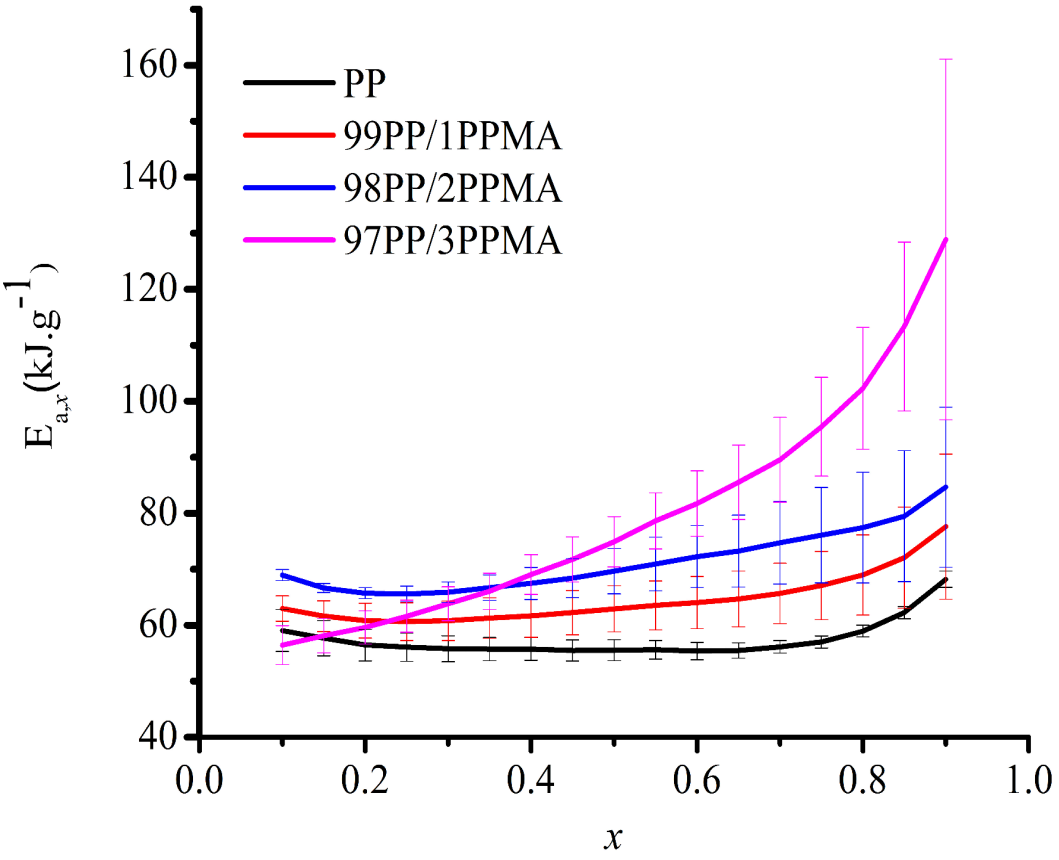

Figure 3.7: Activation energy ($E_{a,x}$) of PP materials according to PPMA content and conversion level obtained with the KAS method. Error bars represents 95% confidence interval

3.2.3 Plasticized cellulose acetate polypropylene materials

3.2.3.1 Thermal stability

Table 3.8 summarizes the analysis of TGA and DTGA curves for the PP*/CA* materials. Thermogravimetric analysis of the PP*/CA* blend was done for 20%, 30%, and 40% content of CA* at four heating rates, as shown in Figure 3.8. As it can be seen, $T_{5\%}$ decreased with increasing CA* level, and no residue was left at the end of the experiment for all materials at all heating rates. For 60PP*/40CA*, there was a shift in the temperature to the higher temperature after 350 °C for all heating rates which could be attributed to the decomposition of CA*. The maximum weight loss rate (MWLR) was the lowest for 60PP*/40CA* at all heating rates.

Based on DTGA curves at all heating rates (Figure 3.9), T_{max} for 80PP*/20CA* and 70PP*/30CA* was lower than PP, while T_{max} for 60PP*/40CA* was higher than that of PP and other materials.

Table 3.8: Thermal analysis of PP and PP*/CA* in air for 5, 10, 20, and 30 (°C·min^{-1}) and different levels of CA*

Heating rate (°C·min^{-1})	Material	$T_{5\%}$ (°C)	T_{max} (°C)	Residual (wt.%)	MWLR (wt.%·°C^{-1})
5	PP	252	312	0	1.38
	80PP*/20CA*	215	283	0	1.05
	70PP*/30CA*	190	324	0.7	0.88
	60PP*/40CA*	192	365	0.6	0.72
10	PP	270	347	0	1.26
	80PP*/20CA*	227	314	0.6	1.17
	70PP*/30CA*	232	335	0.7	1.27
	60PP*/40CA*	222	375	0.3	0.76
20	PP	290	397	0	1.07
	80PP*/20CA*	252	359	0.7	1.23
	70PP*/30CA*	242	358	0.6	1.47
	60PP*/40CA*	259	400	0.6	1.32
30	PP	317	427	0	1.25
	80PP*/20CA*	279	382	0	1.43
	70PP*/30CA*	264	375	0.6	1.39
	60PP*/40CA*	276	418	0.3	1.33

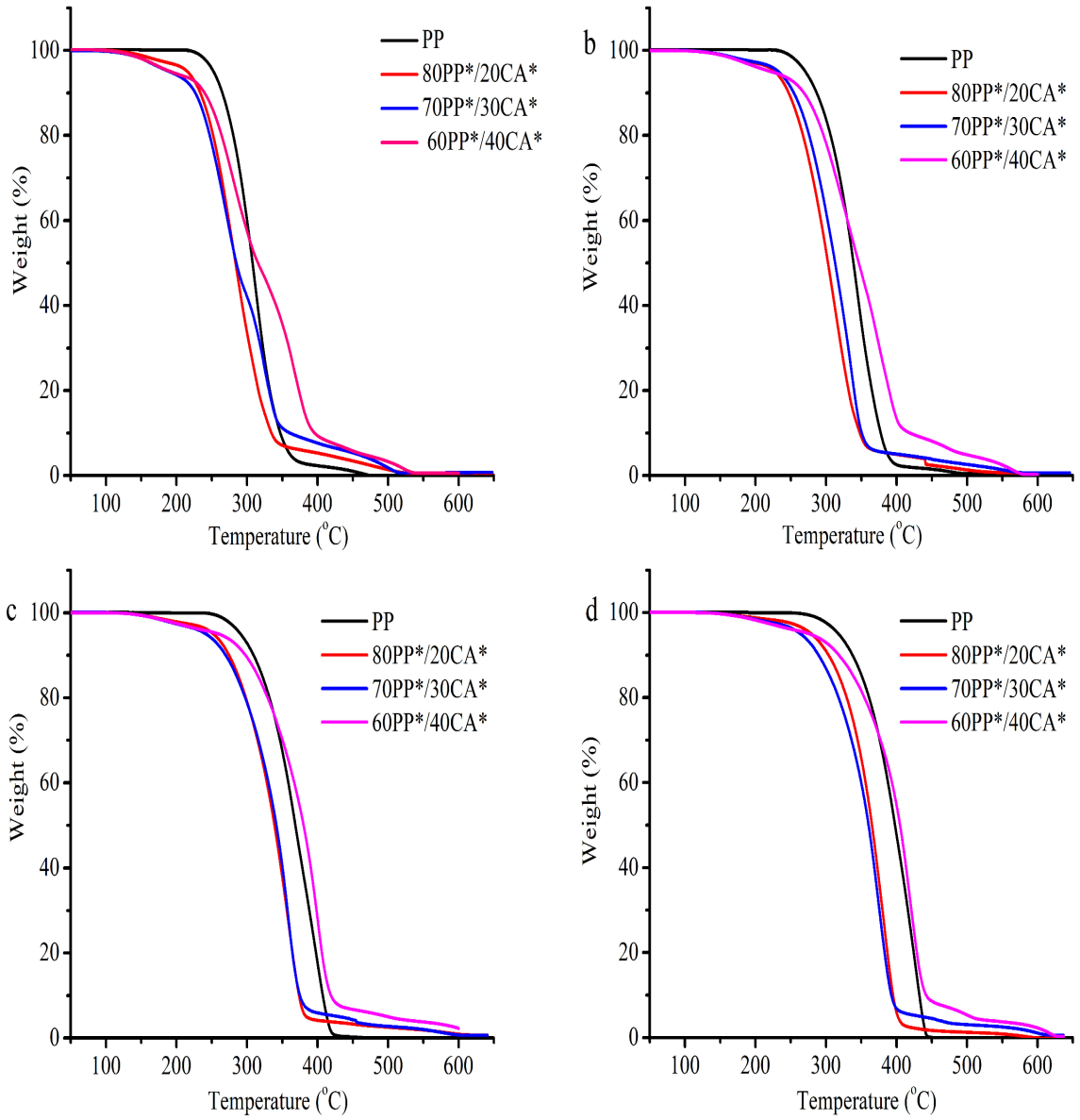

Figure 3.8: TGA curves of PP and PP*/CA* in air at four heating rates and different levels of CA*.a. 5 °C·min^{-1}, b. 10 °C·min^{-1}, c. 20 °C·min^{-1}, and d. 30 °C·min^{-1}

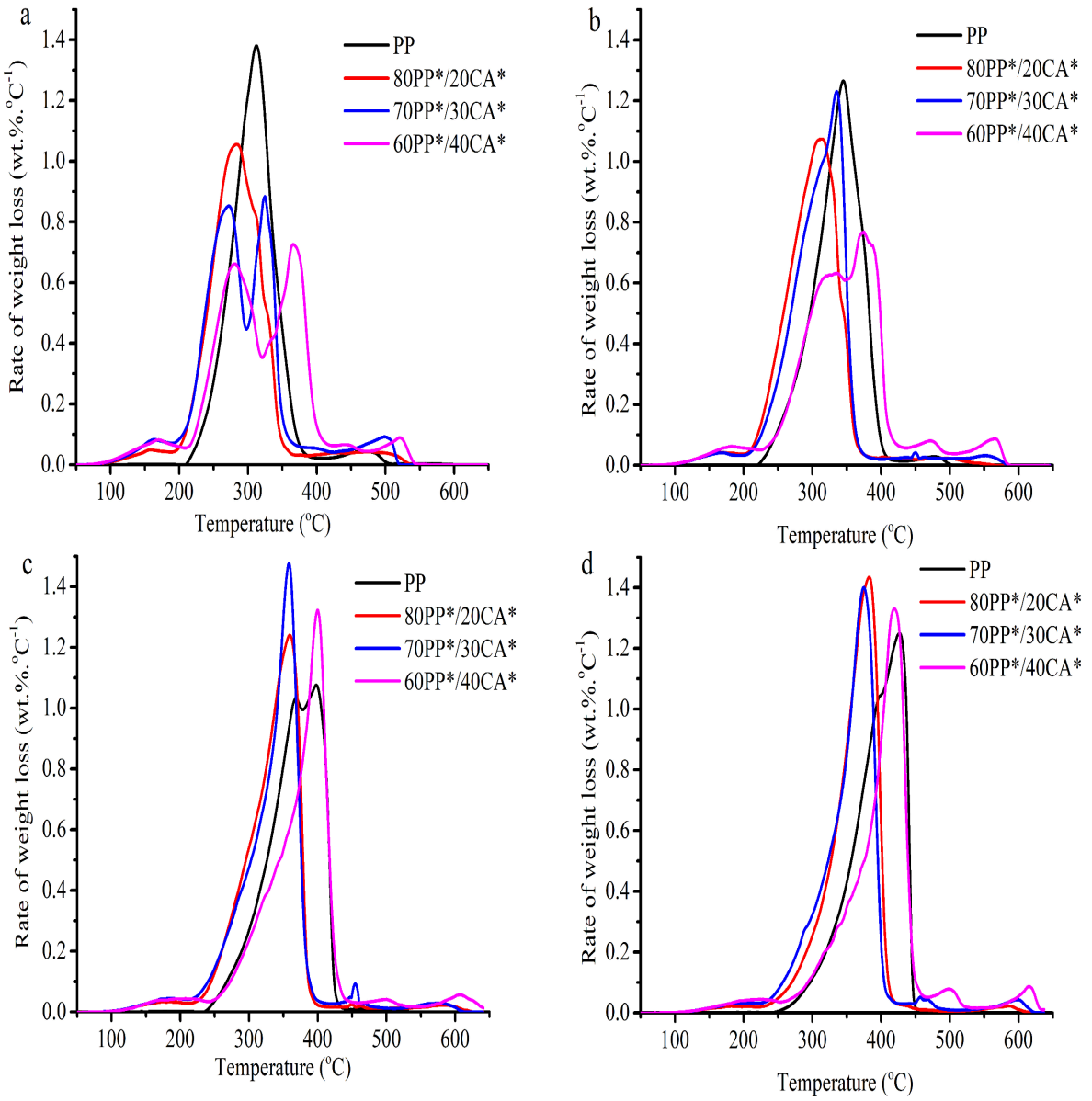

Figure 3.9: DTGA curves of PP and PP*/CA* in air at four heating rates and different levels of CA*. a. 5 °C·min^{-1}, b. 10 °C·min^{-1}, c. 20 °C·min^{-1}, and d. 30 °C·min^{-1}

3.2.3.2 Kinetics of thermal degradation

The linearized plots for calculating E_a are presented in Figure 3.10. The activation energy, according to Kissinger method, shows that with increasing CA* levels there was an increase in the estimated E_a. E_a was 41, 44, 99, and 106 (kJ·mol^{-1}) for PP, 80PP*/20CA*, 70PP*/40CA*, and 60PP*/40CA*, respectively.

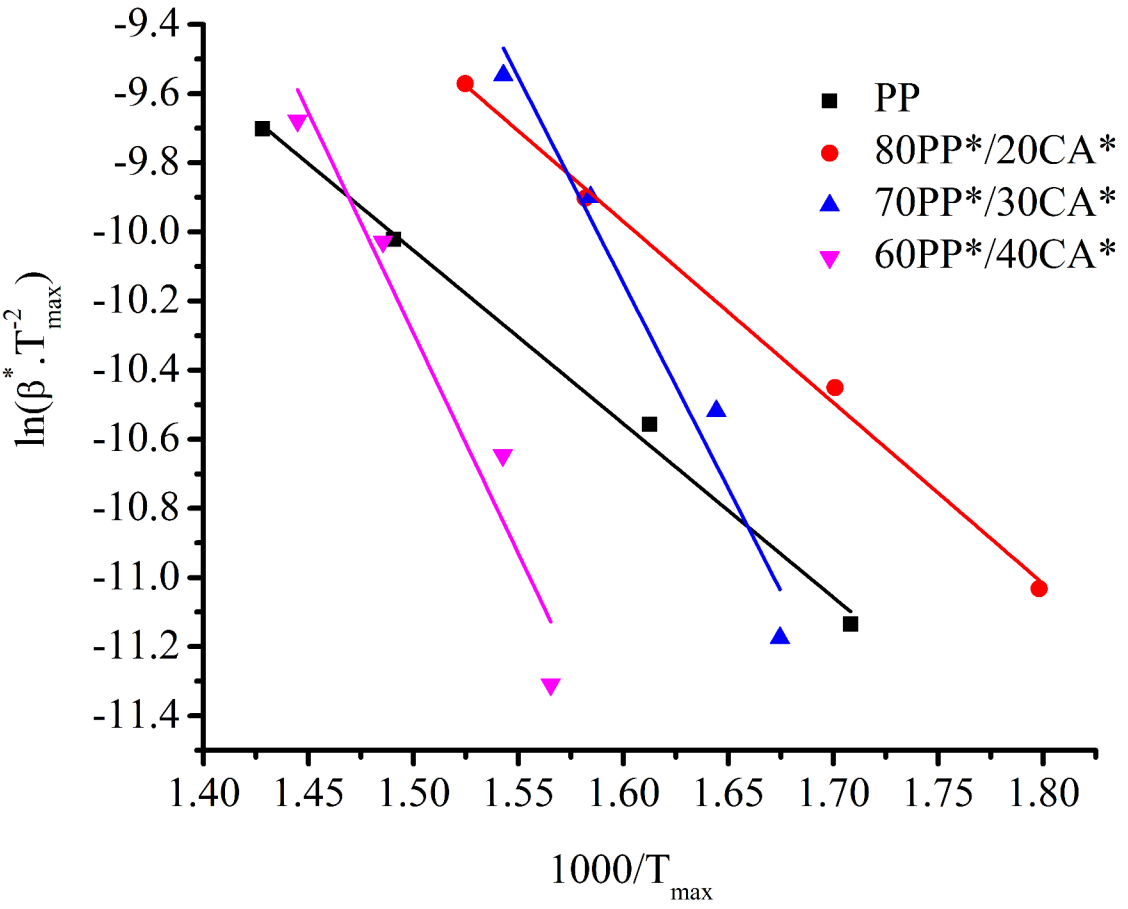

Figure 3.10: Linear plots for calculating E_a by using Kissinger method for PP and PP*/CA* materials

The activation energy, according to conversion, was also estimated by using the KAS method as shown in Figure 3.11. The results show that 80PP*/20CA* had a constant $E_{a,x}$ until 50% conversion and then increased. For 70PP*/30CA*, E_a had a similar trend to that of PP up to 50% conversion, and after that, there was a slight increase. 60PP*/40CA* had low activation energy at the beginning of decomposition and then there was an increase after 50% conversion level.

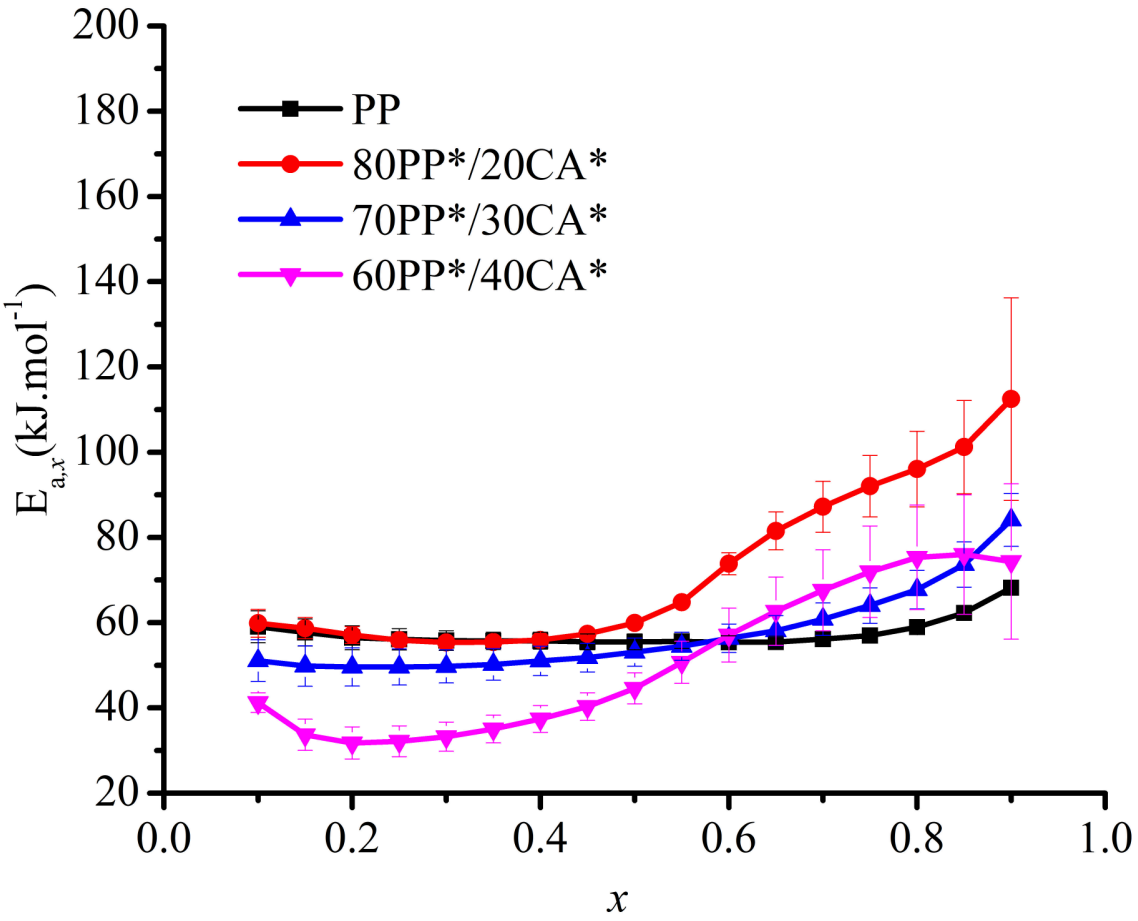

Figure 3.11: Activation energy ($E_{a,x}$) of PP materials according to CA* content and conversion level obtained with the KAS method. Error bars represents 95% confidence interval

3.2.4 Polypropylene magnesium hydroxide materials

3.2.4.1 Thermal stability

Thermogravimetric analysis for PP and PP*/MH materials for different levels of MH (10%, 20%, and 30%) and at four heating rates is summarized in Table 3.9. Based on the TGA curve (Figure 3.12), the results show that with increasing MH levels there was an increase in $T_{5\%}$ of PP materials and there was an increase in the residue left at the end reflecting the inorganic content. The residue left increased with increasing MH level, which is attributed to the formation of magnesium oxide as a result of the decomposition of MH. From DTGA curves (Figure 3.13), T_{max} was estimated. The results show that there was a shift in T_{max} to higher temperature which was directly proportional to the increase of MH levels. There was an increase in the MWLR with increasing MH levels.

Table 3.9: Thermal analysis of PP and PP*/MH for 5, 10, 20, and 30 ($^oC \cdot min^{-1}$) and different levels of MH

Heating rate ($^oC \cdot min^{-1}$)	Material	$T_{5\%}$ (^oC)	T_{max} (^oC)	Residual (wt.%)	MWLR (wt.% $\cdot ^oC^{-1}$)
5	PP	252	312	0	1.38
	90PP*/10MH	257	383	8.2	0.99
	80PP*/20MH	261	385	14.0	1.53
	70PP*/30MH	270	386	21.0	2.39
10	PP	270	347	0	1.26
	90PP*/10MH	277	395	8.0	1.15
	80PP*/20MH	282	400	14.3	1.48
	70PP*/30MH	292	423	20.6	2.28
20	PP	290	397	0	1.07
	90PP*/10MH	305	411	8.9	1.54
	80PP*/20MH	322	422	14.6	1.63
	70PP*/30MH	327	431	19.0	1.58
30	PP	317	427	0	1.25
	90PP*/10MH	340	431	8.6	1.55
	80PP*/20MH	340	431	13.6	1.54
	70PP*/30MH	334	431	18.8	1.55

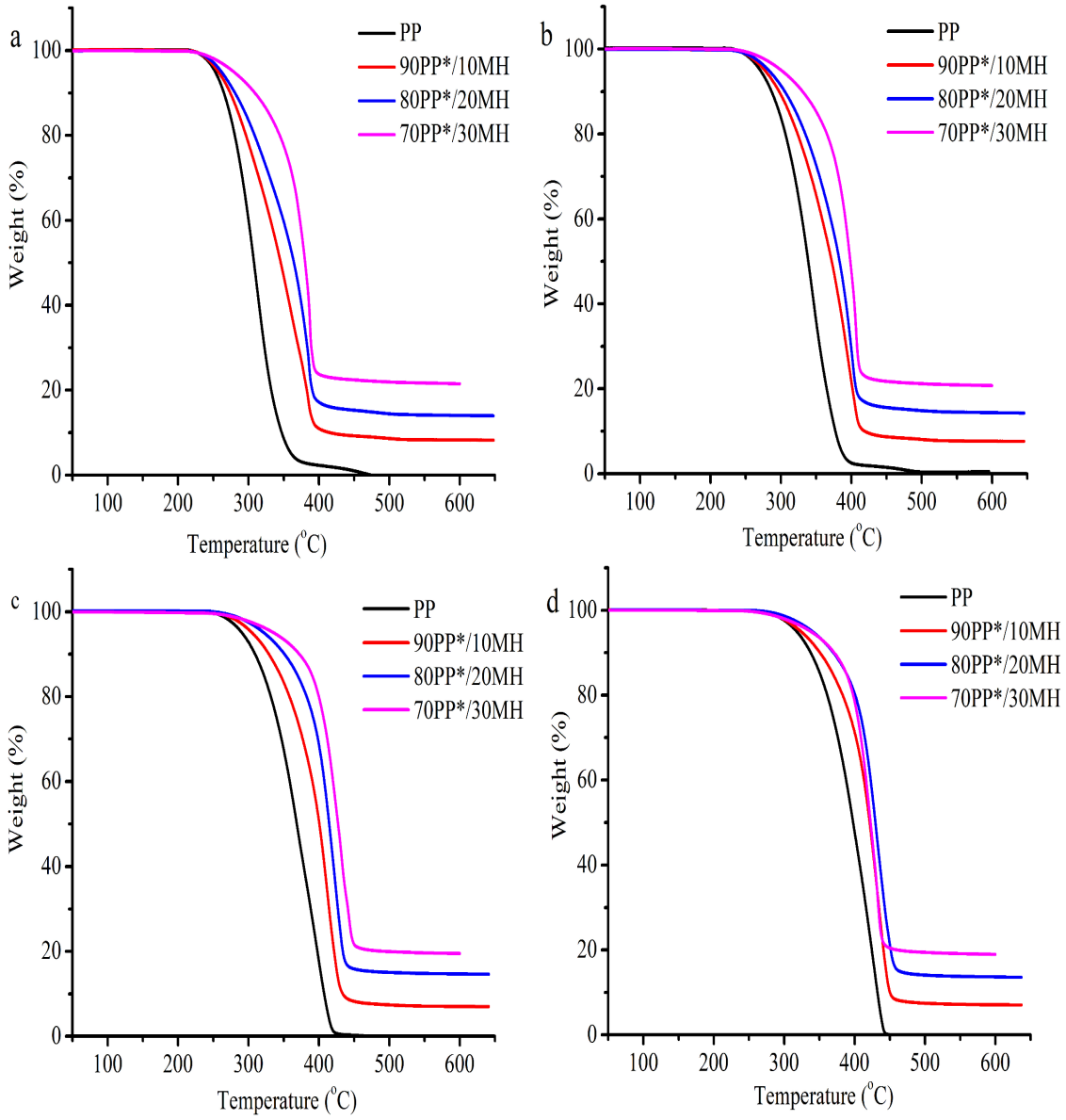

Figure 3.12: TGA curves of PP and PP*/MH in air at four heating rates and different levels of MH. a. 5 °C·min^{-1}, b. 10 °C·min^{-1}, c. 20 °C·min^{-1}, and d. 30 °C·min^{-1}

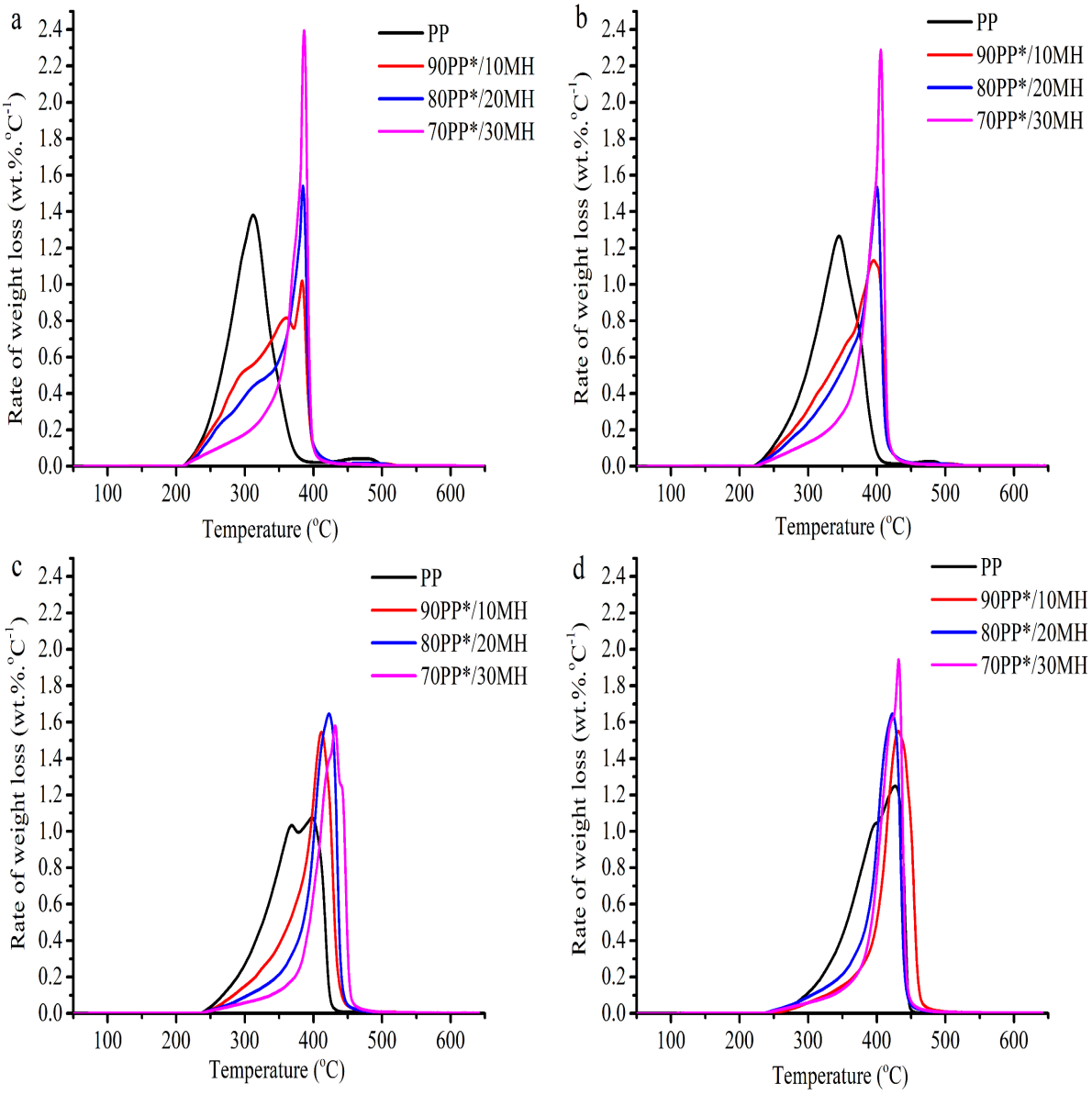

Figure 3.13: DTGA curves of PP and PP*/MH in air at four heating rates and different levels of MH. a. 5 °C·min^{-1}, b. 10 °C·min^{-1}, c. 20 °C·min^{-1}, and d. 30 °C·min^{-1}

3.2.4.2 Kinetics of thermal degradation

The activation energy (E_a) was estimated by using the Kissinger method for PP and PP*/MH materials. The results show that there was an increase in the estimated E_a with increasing MH levels. Linear plots for estimating E_a are shown in Figure 3.14. E_a was 41, 121, 123, and 125 kJ·mol^{-1} for PP, 90PP*/10MH, 80PP*/20MH, and 70PP*/30MH, respectively.

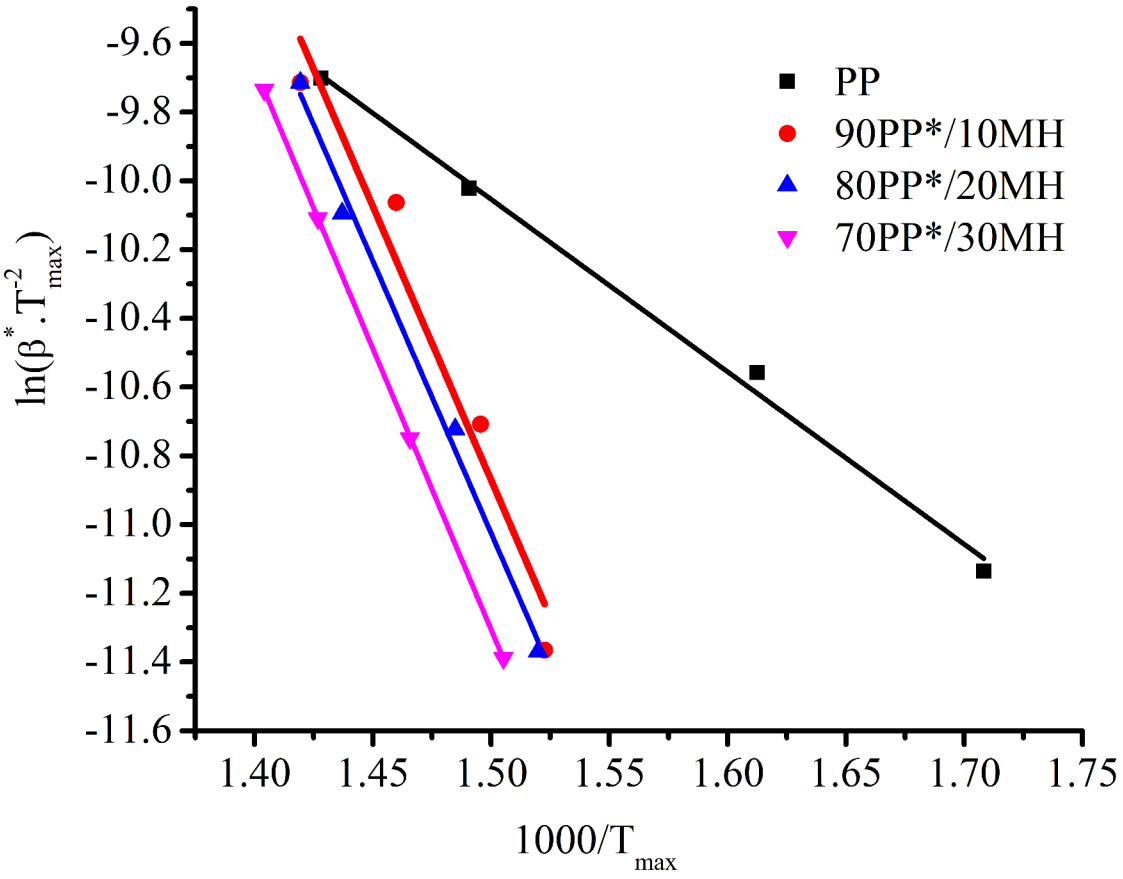

Figure 3.14: Linear plots for calculating E_a by using Kissinger method for PP and PP*/MH materials

The activation energy, according to the conversion, was estimated with the KAS method (Figure 3.15). For 90PP*/10MH, $E_{a,x}$ was lower than that of PP till 30% conversion reached and then increased after. For 80PP*/20MH, $E_{a,x}$ was similar to that of PP, and then gradual increase occurred after 30% conversion. For 70PP*/30MH, $E_{a,x}$ was higher than PP and other materials since the early stages of conversion. There was a rapid increase in the estimated $E_{a,x}$ up to 40% conversion, and there was a slight increase in $E_{a,x}$ afterwards.

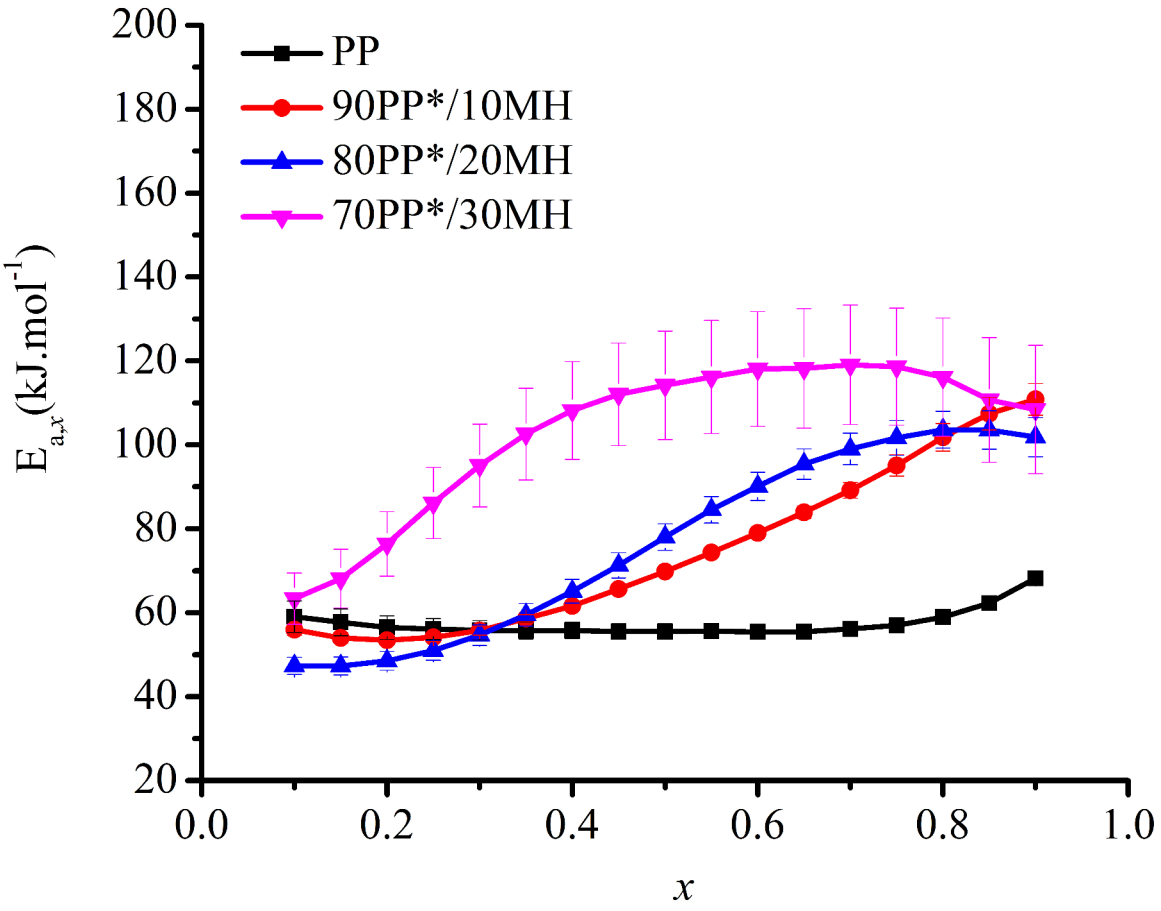

Figure 3.15: Activation energy ($E_{a,x}$) of PP materials according to MH content and conversion level obtained with the KAS method. Error bars represents 95% confidence interval

3.2.5 Plasticized cellulose acetate magnesium hydroxide polypropylene materials

3.2.5.1 Thermal stability

Table 3.10 summarizes the analysis results of the TGA and DTGA curves of PP materials. According to the TGA curves (Figure 3.16), there was a decrease in the $T_{5\%}$ and there was a significant increase in the residue left with increasing MH levels. Based on the DTGA curves (Figure 3.17), T_{max} shifted to a higher temperature with increasing MH in the PP*/CA* blend. The maximum weight loss rate was the lowest for 90(60PP*/40CA*)/10MH at all heating rates compared to the other PP materials.

Table 3.10: Thermal analysis of PP and its blend with CA* in air for 5, 10, 20, and 30 ($^oC \cdot min^{-1}$) heating rates with different levels of MH

Heating rate ($^oC \cdot min^{-1}$)	Material	$T_{5\%}$ (^oC)	T_{max} (^oC)	Residual (wt.%)	MWLR (wt.% $\cdot ^oC^{-1}$)
5	PP	252	312	0	1.38
	90(60PP*/40CA*)/10MH	243	393	8.3	0.90
	80(60PP*/40CA*)/20MH	186.93	398	14.4	1.32
	70(60PP*/40CA*)/30MH	189	391	19.4	1.30
10	PP	270	347	0	1.26
	90(60PP*/40CA*)/10MH	264	400	8.2	1.08
	80(60PP*/40CA*)/20MH	245	406	14.7	1.33
	70(60PP*/40CA*)/30MH	237	409	19.1	1.13
20	PP	290	397	0	1.07
	90(60PP*/40CA*)/10MH	264	418	8.7	1.12
	80(60PP*/40CA*)/20MH	258	430	14	1.32
	70(60PP*/40CA*)/30MH	262	427	18.6	1.23
30	PP	317	427	0	1.25
	90(60PP*/40CA*)/10MH	273	431	8.4	1.21
	80(60PP*/40CA*)/20MH	269	438	13.6	1.20
	70(60PP*/40CA*)/30MH	295	439	20.5	1.15

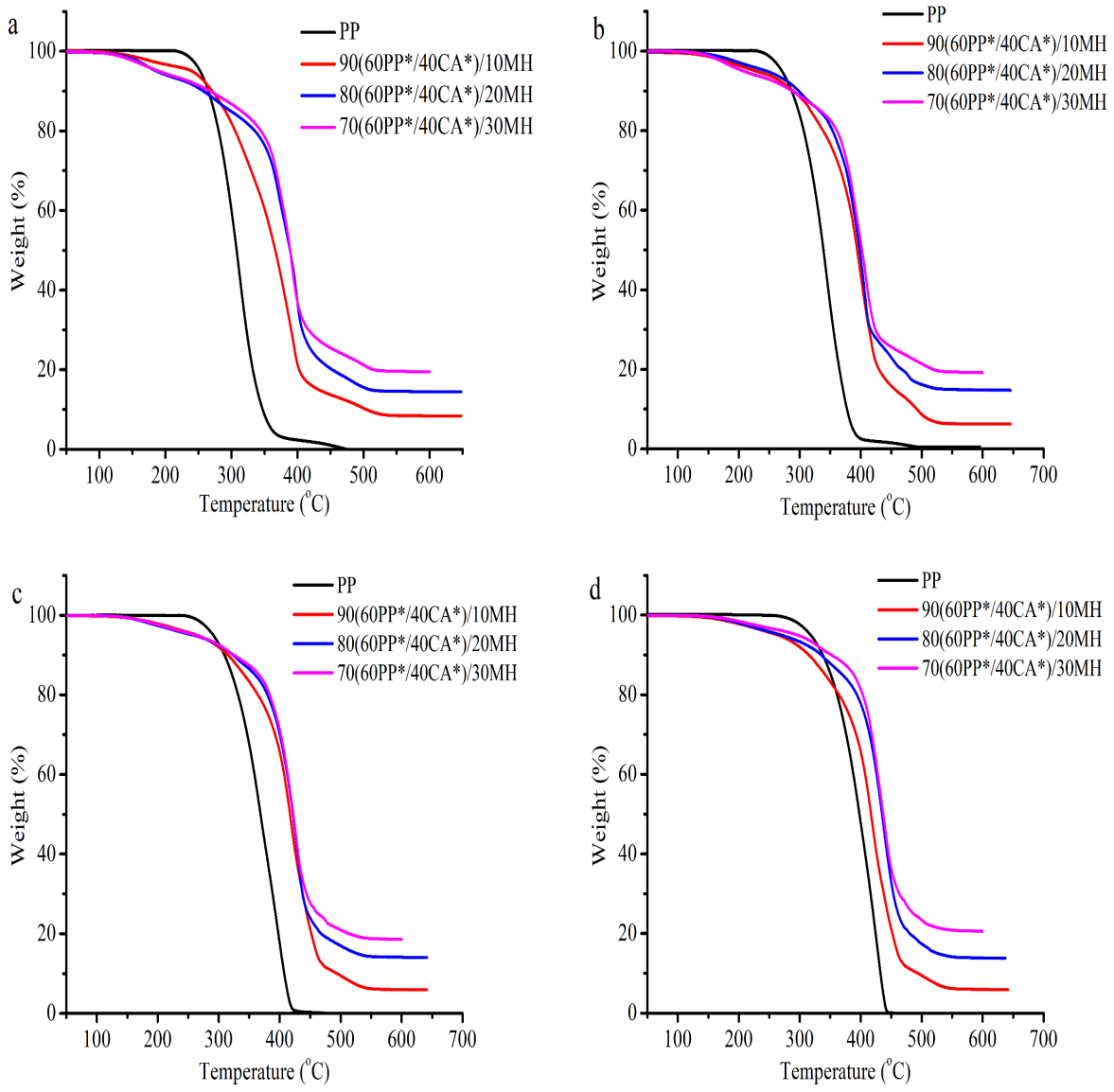

Figure 3.16: TGA curves of PP and its blend with CA* in air at four heating rates and different levels of MH. a. 5 °C·min^{-1}, b. 10 °C·min^{-1}, c. 20 °C·min^{-1}, and d. 30 °C·min^{-1}

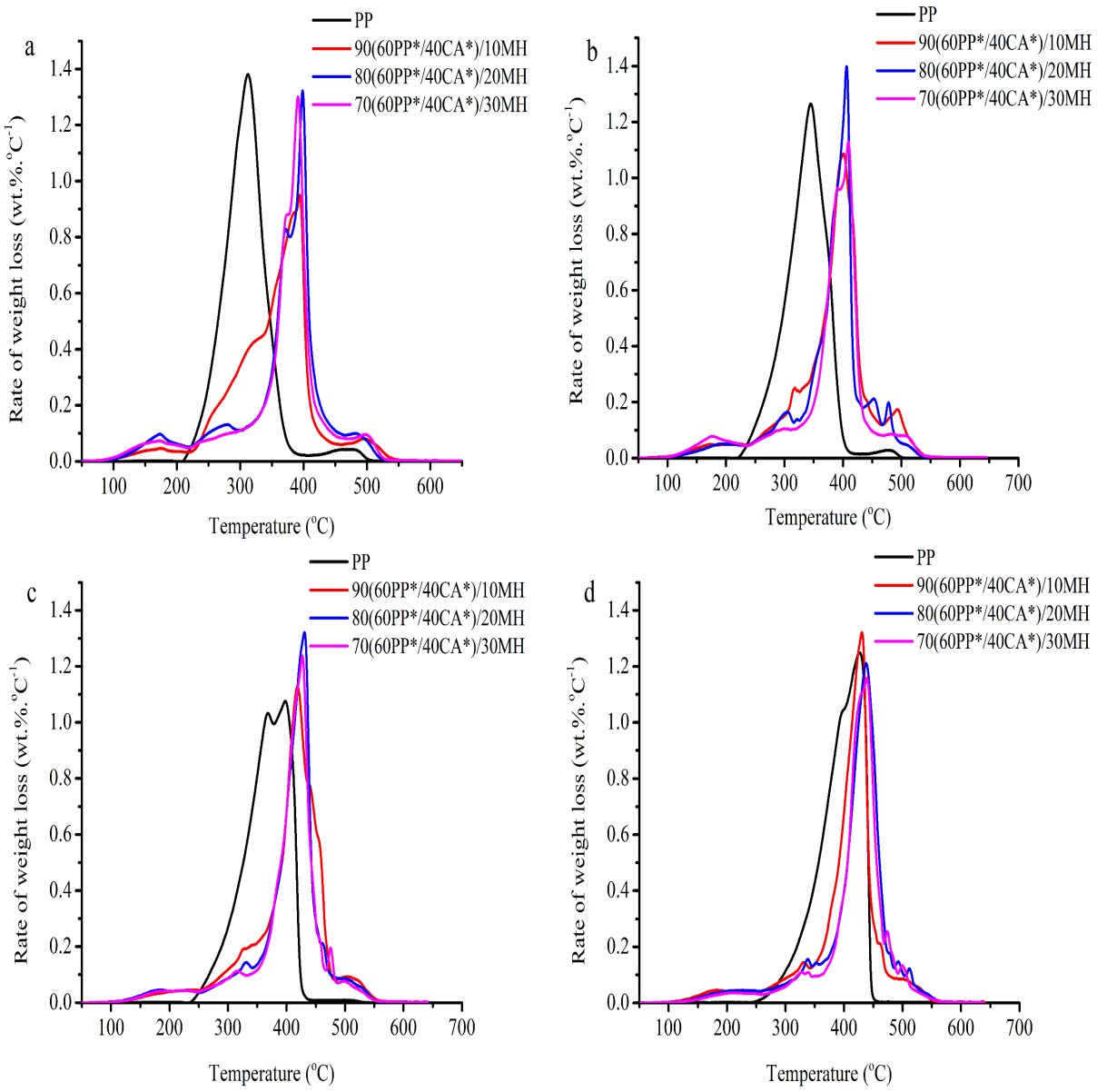

Figure 3.17: DTGA curves of PP and its blend with CA* in air at four heating rates and different levels of MH. a. 5 °C·min^{-1}, b. 10 °C·min^{-1}, c. 20 °C·min^{-1}, and d. 30 °C·min^{-1}

3.2.5.2 Kinetics of thermal degradation

The estimated values of E_a according to Kissinger method show that PP materials with high level of MH was lower. E_a was 41, 164, 148, and 136 kJ·mol^{-1} for PP, 90(60PP* /40CA*) /10MH, 80(60PP*/40CA*)/20MH, 70(60PP*/40CA*)/30MH, respectively. The linearized plots for calculating the E_a are presented in Figure 3.18.

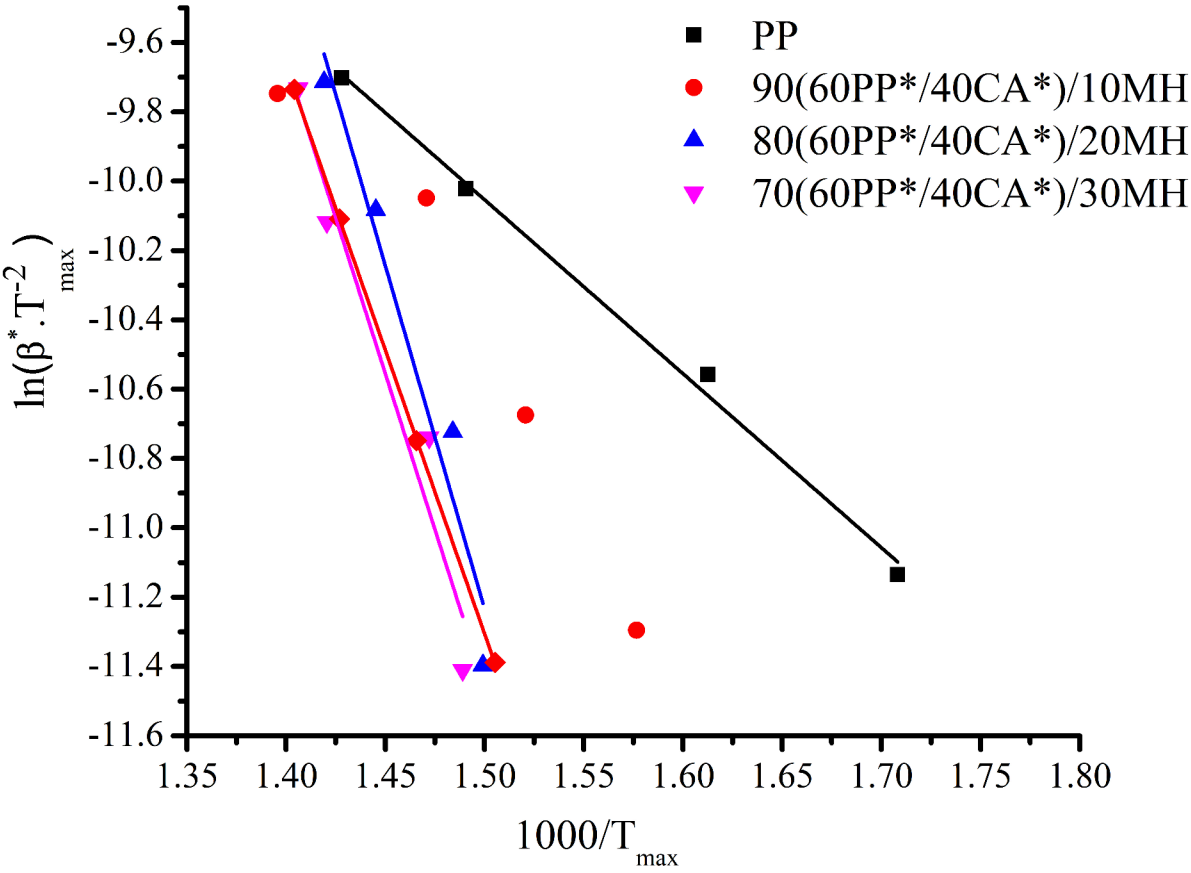

Figure 3.18: Linear plots for calculating E_a by using Kissinger method for PP and its blend with CA* for different levels of MH

The activation energy, according to the conversion estimated with the KAS method (Figure 3.19) show an increase in the estimated value of $E_{a,x}$ with increasing the conversion. There was a gradual increase in $E_{a,x}$ for 90(60PP*/ 40CA*) /10MH up to 70% conversion and then became stable. The $E_{a,x}$ values for 80(60PP*/40CA*)/20MH and 70(60PP*/40CA*)/30MH were lower than PP until 20% conversion was reached and then increased rapidly until 40% conversion. After 40% conversion, there was a gradual increase until 75% conversion reached. After 75% conversion, $E_{a,x}$ stabilized at 80% since the residue left is inorganic and cannot degrade.

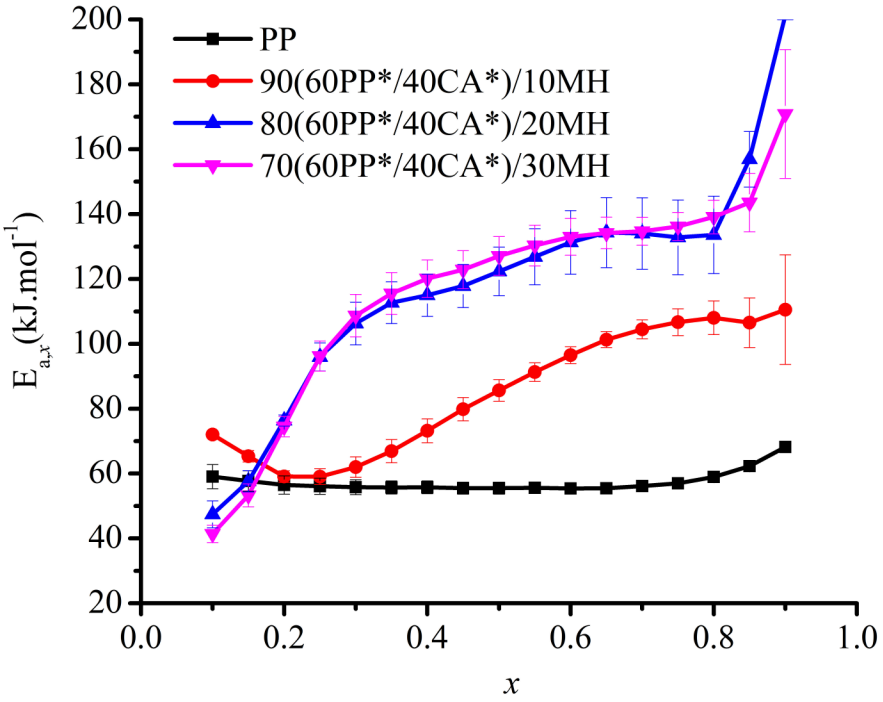

Figure 3.19: Activation energy ($E_{a,x}$) of PP and its blend with CA* according to MH content and conversion level obtained with the KAS method. Error bars represents 95% confidence interval

3.2.6 Material morphology

SEM images and EDX mapping analyses were used to evaluate the behavior and compatibility of CA* and MH. The materials, 60PP*/40CA*, 70PP*/30MH, and 70(60PP*/40CA*) /30MH were selected based on their high thermal stability (TGA analysis). As shown in Figure 3.20, the incorporation of CA* demonstrated greater compatibility than the inclusion of MH. Strongly interactions between CA* and PP* were observed. The firm bonding was adversely affected by increasing the levels of MH inside the matrix.

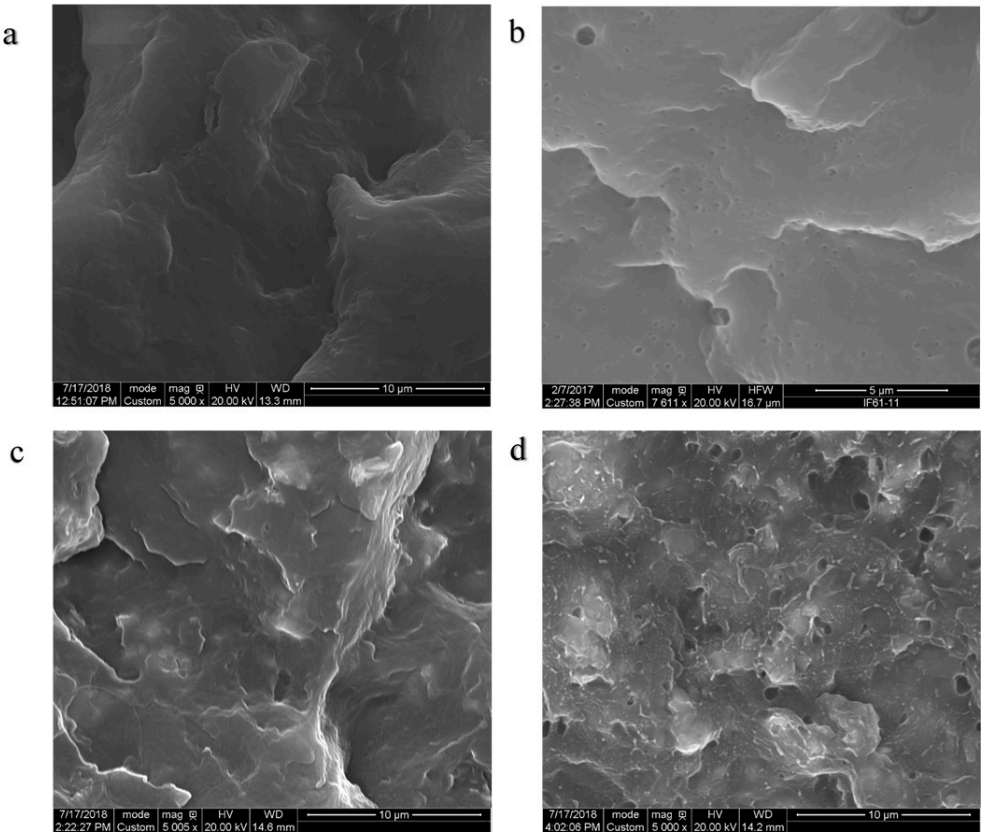

Figure 3.20: SEM images of PP materials a. PP, b. 60PP*/40CA*, c. 70PP*/30MH, and d. 70(60PP*/ 40CA*)/30MH

It is well-known that a materials dispersion in the polymer matrix is key to the enhancement of their mechanical properties. It is difficult to achieve a good dispersion of inorganic fillers in thermoplastics. SEM images show better dispersion for CA* than MH, and this could be attributed to the compatibility of CA* being higher than MH. SEM images of 70PP*/30MH shows minimal agglomeration of MH in the PP matrix.

Energy-dispersive-beam mapping images of the dispersion of CA* and MH through the PP* matrix are shown in Figure 3.21. CA* can be detected from the presence of oxygen in its molecules. The mapping of PP* materials show good dispersion of CA* and MH in PP*. For 70(60PP*/40CA*)/30MH, it was difficult to detect the CA* because MH can also be detected from the presence of oxygen.

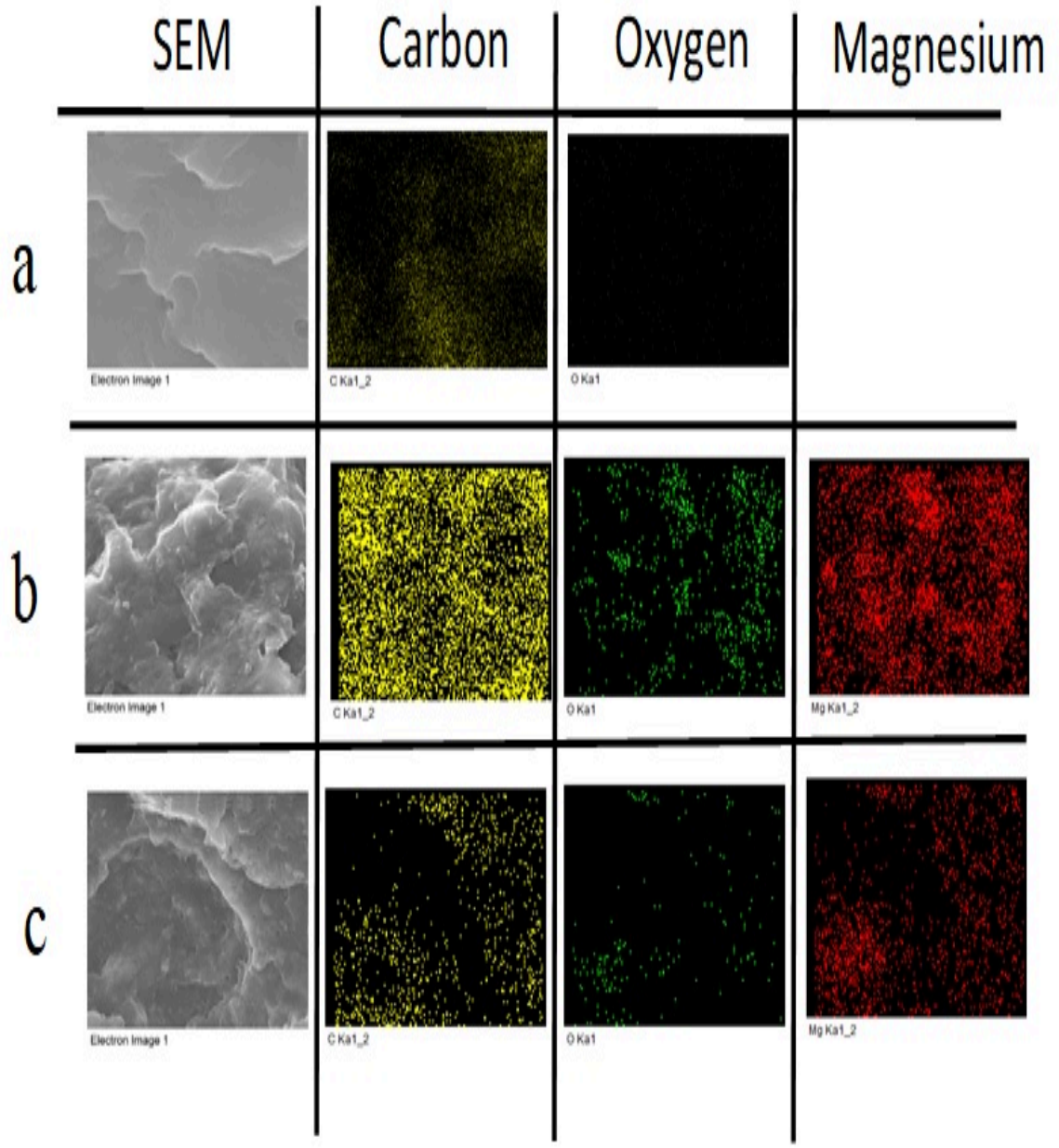

Figure 3.21: Mapping analysis of PP materials. a. 60PP*/40CA*, b. 70PP*/30MH, and c. 70(60PP*/40CA*)/30MH

3.3 Conclusion

The plasticization of cellulose acetate (CA) by triethyl citrate (TEC) investigated by DSC, XRD, and TGA, demonstrate that CA plasticization was achieved. The glass transition temperature and the melting temperature of plasticized CA (CA*) was lowered by 39 °C and 77 °C, respectively. The XRD patterns were quite different where CA* had two broad intensity peaks compared to five peaks for CA. The degree of crystallinity of CA* was considerably lower compared to CA. The addition of TEC to CA lowered the temperature of the onset of degradation and the temperature of the maximum weight loss compared to CA. These observations indicate that the addition of TEC to CA induced plasticization such that the extrusion of CA with PP should be feasible.

The formulation of the PP materials was based on the thermal analysis and was used to identify the levels of CA* and MH for PP materials fabrication. Based on the thermal analysis of PP/PPMA blends, the level of PPMA was chosen to be 3% due to the higher activation energy obtained, and the material was thermally more stable than PP, 99/1PPMA, and 98PP/2PPMA. According to thermal analysis of PP, and PP*/CA* materials, 60PP*/40CA* was more stable based on the higher estimated E_a with Kissinger method. Furthermore, TGA analysis showed a shift in temperature to the higher temperature above 350 °C for 60PP*/40CA* compared to 80PP*/20CA* and 70PP*/30CA*. From DTGA curves at four heating rates, T_{max} was the highest for 60PP*/40CA*. The addition of MH to PP* and PP*/CA* materials showed that with increasing the level of MH shifted $T_{5\%}$ and T_{max} to the higher temperature. Based on the calculation of E_a, materials with a higher level of MH have the highest E_a. Based on the aforementioned results, the levels of PPMA, CA*, and MH were chosen according to their impact on the thermal stability of the materials. The highest levels of CA* and MH, namely 40% and 30%, and PPMA with 3% as a replacement portion of the PP are selected for the PP materials fabrication. According to the morphology of the materials obtained by SEM, 40% and 30% of CA* and MH are well dispersed respectively inside the PP matrix. The compatibility of CA* was adversely impacted by the MH addition.

Chapter 4

Thermal Behavior and Kinetic Study of Plasticized Cellulose Acetate Magnesium Hydroxide Polypropylene Materials

In this chapter, the thermal stability of polypropylene (PP) materials containing the polypropylene- grafted-maleic -anhydride (PPMA), plasticized cellulose acetate (CA*) and magnesium hydroxide (MH), was investigated. The thermogravimetric analysis (TGA) conducted under air conditions revealed distinct degradation patterns when CA*, MH or MH/CA* were added to PP*. The addition of MH to PP*/CA* improved the thermal stability by shifting the maximum rate of mass loss to a higher temperature. But the MH addition could not counterbalance the lower temperature for the onset of degradation when CA* was blended with PP*. The improved thermal stability of PP*/CA* when MH was added is supported by the higher activation energy (E_a) of the MH/CA*/PP materials. This study also presents a numerical integration method that is recommended to improve the accuracy of E_a estimates from TGA data at multiple heating rates when is small. The results indicate that the combined use of MH and CA* leads to materials with the highest thermal stability.

4.1 Introduction

There is a growing need to develop and commercialize bio-based materials and reduce the dependency on petroleum resources to promote environmental sustainability [45]. Cellulose acetate (CA) is one of the oldest bio-based polymers. CA is produced from wood, cotton, and recycled papers by a two-step esterification process. CA is lightweight, cheap, and biodegradable, and its degradation does not produce any toxic byproducts [134]. The main disadvantage of CA is that its melt processing temperature is very close to its decomposition temperature, so CA must be plasticized [43]. The addition of low molecular weight plasticizer causes an increase in free volume, lubricity, and chain mobility of the polymer, which leads to a decrease in glass transition temperature and improvement of processability [43]. Many of the commercial plasticizers are suspected of displaying health and environmental hazard threats [141]. Triethyl citrate (TEC) is an eco-friendly plasticizer, which can be used to plasticize CA. Ghiya et al. [46] reported that TEC is utterly miscible with CA.

The demand for polymeric materials for automotive components and building materials is increasing due to their ecological and economic advantages [5]. These materials are typically exposed to successive cycles of temperature fluctuations, which could lead to thermal degradation [142]. Polypropylene (PP) is a major synthetic polymer in industrial applications. Several studies have focused on the thermal degradation behavior of this polymer as it constitutes a significant share of the plastic industry [143]. PP has good insulating and processing properties, a small dielectric characteristic, and proper crack and chemical resistance. On the other hand, PP has low thermal resistance, which limits its applications [3].

Polymer combustion refers to the oxidation reaction between a polymer, an oxidant (oxygen), and an external source of intense energy such as a spark or flame. The combustion process consists of five elements: preheating, decomposition, ignition, combustion, and propagation [5]. The distinction between each element is generally not well defined. The preheating stage involves irradiation of the material by an external heat source and temperature increase. The rate at which temperature increases depends on the thermal intensity of the heat source as well as the thermal properties of the material including, its thermal conductivity, specific heat capacity, and latent heat of fusion. An increase in thermal energy triggers bond scission in the material leading to the release of volatile substances. Ignition occurs when these gases mix sufficiently with atmospheric oxygen, and their temperature reaches either the auto-ignition temperature or the flash point of the material. Combustion becomes self-propagating if sufficient heat is generated and radiated back to the materials to sustain the decomposition process [51]. Polypropylene itself

burns very rapidly without leaving a char residue because of its aliphatic hydrocarbon structure [8]. The heat of combustion data suggests that PP is more exothermic during thermal degradation than most synthetic and natural polymers. Its heat of combustion is 40 kJ·g^{-1} while that of nylon, cellulose acetate and polyester are 15 kJ·g^{-1}, 15 kJ·g^{-1}, and 6.3 kJ·g^{-1}, respectively. Polypropylene undergoes pyrolysis to yield volatile compounds and shorter chain hydrocarbons. These volatile compounds include dienes, alkanes, and alkenes. The other compounds released during pyrolysis are C_9 compounds such as 2-methyl-4-octene, 2-methyl-2-acetone, 2, 6-dimethyl-2,4-heptadine, 2,4- dimethyl-1-heptene, 2-methyl-1-octene. The remaining heated surface of the polymer and less volatile molecules behave as secondary fuel sources [51].

CA releases its absorbed water when it is heated up to 100 °C. The main decomposition of CA occurs around 285 °C [130] when it releases gaseous species like ketene, esters, aldehydes, and oligomers [144].

The most common approach for improving the flame retardancy of materials is the incorporation of flame retardants that can hinder the combustion stages. The most widely used flame retardants can be categorized as inorganic compounds, halogenated compounds, and phosphorous compounds. These flame retardant materials can act chemically or physically in the solid, liquid, or gas phase. There are environmental and health safety concerns associated with the use of common halogenated flame retardants [145]. Therefore, there is a growing interest in alternative flame retardant materials such as inorganic compounds, like metallic hydroxides [146]. Magnesium hydroxide (MH) is the most widely used metallic hydroxides. The decomposition of MH occurs through the following reaction:

$$\mathrm{Mg(OH)_2} \rightarrow \mathrm{MgO} + \mathrm{H_2O} \qquad \Delta H = 1.37 \ \mathrm{kJ \cdot g^{-1}} \tag{4.1}$$

The decomposition temperature of MH is about 300-320 °C [5] allowing it to be processed in plastics such as PP. MH can provide flame retarding effects by releasing a significant amount of water at higher temperature and hence diluting the amount of fuel available to sustain the combustion during a fire. MH absorbs heat from the combustion zone and produces a char layer that can act as an insulating protective layer during combustion. However, in order to produce reasonable flame retardancy, high levels of MH are required [6, 69].

The investigation of the kinetics of thermal degradation is generally performed under the assumption that all samples used in the study are practically identical. The similarity of the materials can be difficult to achieve with multi component formulations. Solid fillers or additives have the tendency to form large aggregates, and the materials become heterogeneous so that samples differ significantly from each other. Due to this, the mass

loss curves measured on different samples can show significant differences in their shape and temperature region of degradation.

The sample type such as powder, film, or chunk can give different mass loss curves. The powder grain size and/or film thickness may affect the temperature of degradation [92, 94]. It was reported that cross-linked high density polyethylene samples of various thickness measured in TGA under nitrogen flow at a heating rate of 20 ^{o}C·min^{-1}, showed differences exceeding 30 ^{o}C in the early stages of mass loss [94]. The sample thickness should be similar in order to have similar diffusion rates of volatile decomposition products. The sample thickness should always be kept as small as possible in order to improve heat transfer and minimize the thermal gradients within the sample.

The surface area increases by decreasing the particle size, and powder with lower particle size has a high surface area. Due to this, the heat transfer will improve, and TGA curves will be shifted to lower temperatures and reduce its thermal stability. Saifali [147] reported that the biggest particles (> 200 μm) of high-density polyethylene with higher molecular weight have maintained the superior thermal stability. Pradip et al. [148] study the effect of particle size of PP on the kinetics of thermal degradation. In their investigation, thermal stability and activation energy (E_a) of PP particles (up to 15% conversion) initially decreases and then increases as particle size further decrease to the nanoscale.

In the present study, the thermal decomposition of PP materials containing PPMA, CA*, and MH was studied using TGA. Also, E_a of the PP materials was established through a dynamic TGA analysis by applying model-free methods. A numerical integration method was developed to estimate E_a. In this chapter, the thermal stability of 60PP*/40CA*, 70PP*/30MH, 70(60PP*/40CA*)/30MH will be discussed using TGA and the associated analysis methods presented previously in section 2.11.2.

4.2 Experimental methods

4.2.1 Materials

Polypropylene (PP) fine powder (HM20/70P), was purchased from GOONVEAN Fibres Company, United Kingdom. Magnesium hydroxide (MH), Cellulose acetate (CA) (approx. 50000 g·mol^{-1} 39% acetyl), triethyl citrate (TEC), and polypropylene-grafted maleic anhydride (PPMA) were purchased from Sigma Aldrich (USA). All materials were used as received.

4.2.2 Materials preparation

Cellulose acetate (CA) was plasticized according to the methodology presented in Chapter 3. Polypropylene (PP) materials were produced by extrusion in a twin screw-extruder (SJSZ-7A), Wuhan Ruiming Plastic Machinery Company, China. The four temperature zones ranged from 160 °C-180 °C, and the circulation time was five minutes. The extruded materials were then cut as pellets by using a cutter (SZS-20, Wuhan Ruiming Plastic Machinery, China), and then compression molded using compression moulding (PHI, Pasadena Hydraulic Inc., USA) at 200 °C with 10 bar pressure for 2 minutes. Two different molds were used for preparing the sample according to the dimensions of the sample required for the vertical burning test, oxygene index, and the cone calorimeter following the ASTM standard for each test. The fabricated materials are listed in Table 4.1.

Table 4.1: Sample composition and coding of PP materials

Material	PP wt.%	CA* wt.%	MH wt.%	PPMA wt.%
PP	100	0	0	0
PP*	97	0	0	3
60PP*/40CA*	58.2	40	0	1.8
70PP*/30MH	67.9	0	30	2.1
70(60PP*/40CA*)/30MH	40.74	28	30	1.26

PP* refers to 97PP /3PPMA.

CA* refers to plasticized cellulose acetate with triethyl citrate.

4.2.3 Activation energy estimation by Kissinger and Kissinger-Akhira-Sunose (KAS) methods

TGA data were used to obtain activation energy at the maximum rate of degradation according to Kissinger method , and the activation energy as a function of conversion according to KAS method (methodology presented in section 2.10.2).

4.2.4 Activation energy estimation by numerical integration

In order to increase the accuracy of the activation energy estimation when $y = \frac{E_a}{RT} < 15$, we have developed a method based on the numerical integration of the integral on the

right-hand side of Equation 2.17. The integral on the right-hand side of Equation 2.17 is constant at each conversion level, so at a given conversion level, re-arrangement of Equation 2.17 leads to:

$$\beta^*_{cal} = g \int_{T_0}^{T} exp(-E_a/RT)\, dT \tag{4.2}$$

where $g = A/\int_0^x dx/f(x)$. With the assumption that the activation energy is constant at each conversion level for different heating rates, as in the KAS method, and using number of heating rates, the numerical integration method (NIM) is illustrated in Figure 4.1, depicting the components of the matrix, or different heating rates versus components of the matrix which are calculated by estimating A and E_a. In the developed method, β^* is calculated according to Equation 4.2 for different level of conversion (x). In the first step, the temperature associated with a given conversion is determined for the four heating rates. In the second step, the g and E_a values are modified to estimate new calculated heating rates (β^*_{Cal}). In the third step, the sum of squared errors (SSE) is calculated with β^*_{Cal} and β^*_{Act}. Then "fminsearch" (MATLAB R2014a) function was used to find the minimum of SSE by changing g and E_a. If values of β^*_{Cal} and β^*_{Act} are close to each other, i.e., the difference value are close to zero, points should lay on the $y = x$ line.

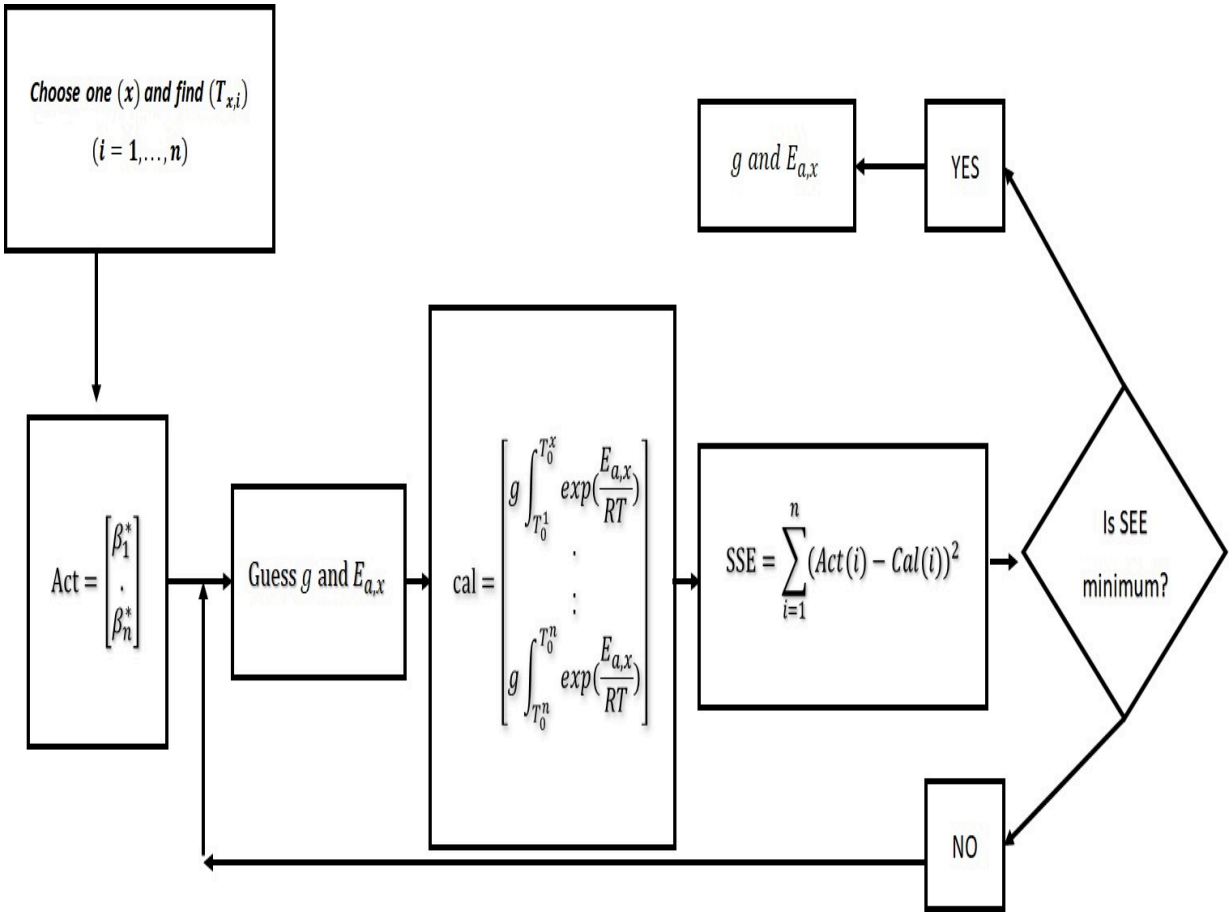

Figure 4.1: Flow chart of numerical integration method

4.3 Results and discussion

4.3.1 Decomposition characteristics of magnesium hydroxide

The decomposition of magnesium hydroxide (MH) to magnesium oxide involved thermal decomposition at 350 °C as shown in Figure 4.2. TGA curve of MH (Figure 4.2a) showed the residue left at the end of the experiment was 69 wt.%, which means that approximately 31 wt.% of water was lost, and it agrees with the MH decomposition (Equation 4.1) where 1 mole of MH produces 1 mole of water (See Appendix A).

The DTGA curve of MH (Figure 4.2b) shows that the main decomposition of MH

occurred between 290 °C and 430 °C with mass loss of 28 wt.%. It was reported that the remaining water slowly diffuses from within the magnesium oxide as the temperature raises further [70]. As the temperature increased (at 650 °C), magnesium oxide is formed.

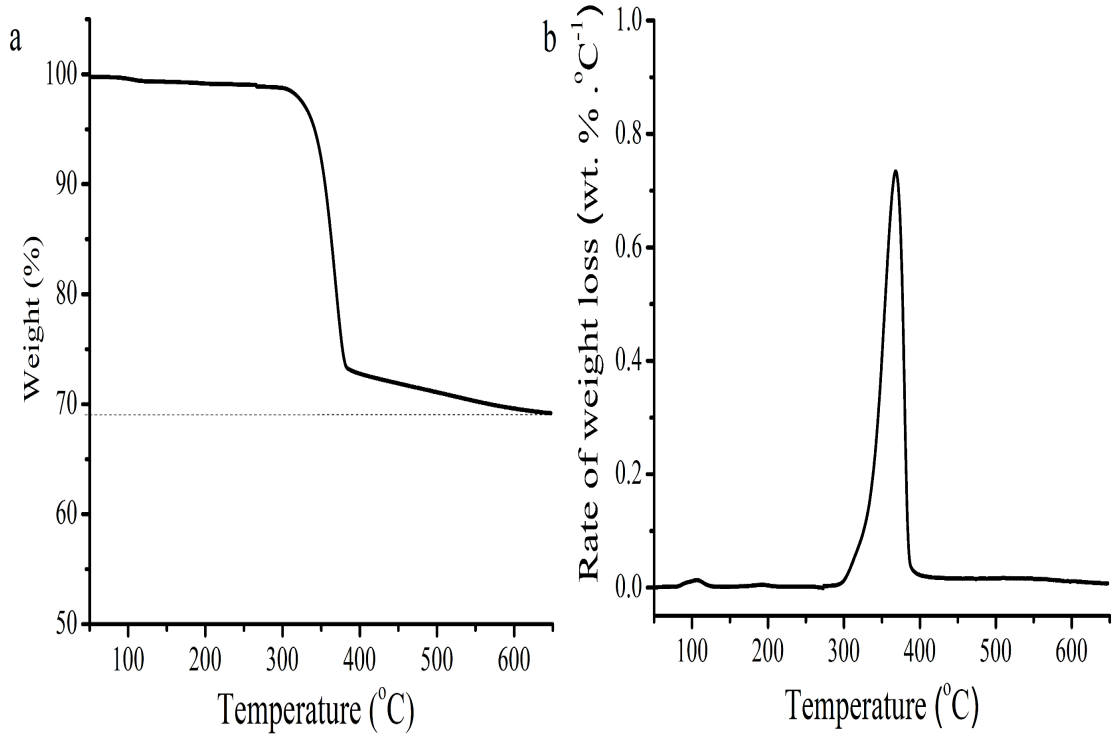

Figure 4.2: TGA and DTGA curves of MH in air at 5 °C·min^{-1} heating rate. a. TGA, b. DTGA

4.3.2 Thermal stability of PP materials

The effect of the sample mass on the parameters estimated from TGA curves was investigated following ICTAC recommendations [92]. Two different masses (5 and 10 mg) were used. The results show no significant effects for the change in mass, with ± 1 °C in the temperature associated with each conversion ($T_{x,i}$) as shown in Figure 4.3.

The thermal stability of PP and PP* materials obtained by TGA is shown in Figure

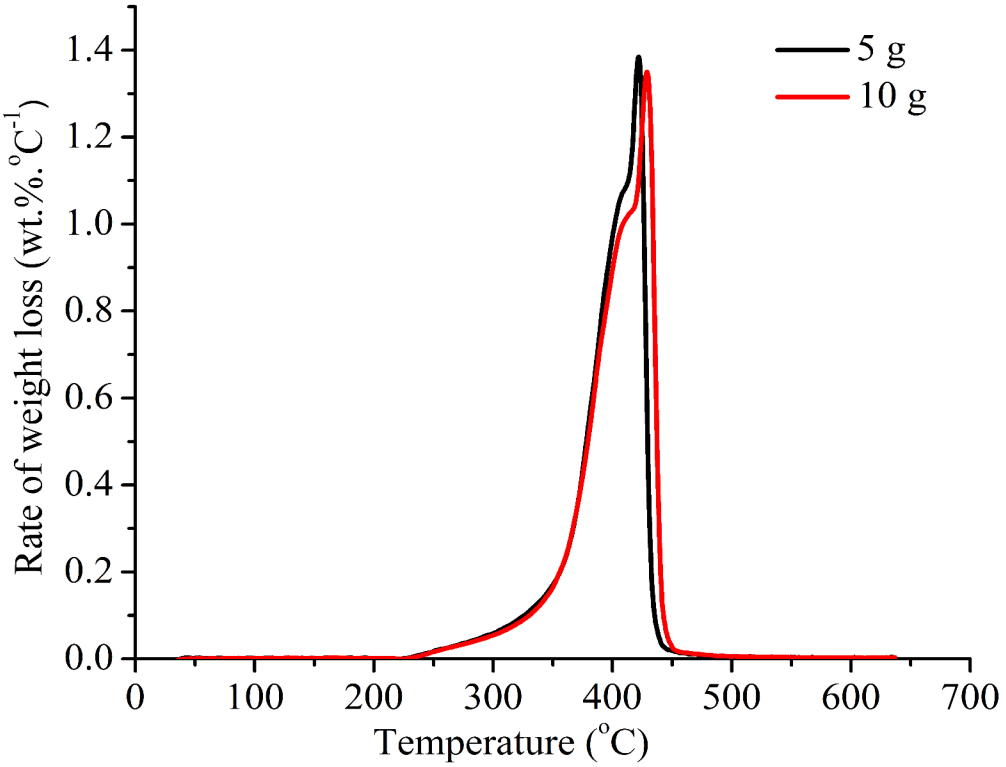

Figure 4.3: DTGA curves of 70PP*/30MH with two different sample mass

4.4. The TGA curve of PP and PP* (Figure 4.4a) show that $T_{5\%}$ of PP is less than that of PP*. The TGA curve showed no residue left for the PP and PP* materials because all organic materials were converted into volatile products. DTGA curve of PP and PP* showed a shift in T_{max} to higher temperature as shown in Figure 4.4b. The MWLR for PP* was less than that of PP at 5 and 10 °C·min^{-1} heating rates as shown in Table 4.2. Most likely, the morphology of PP* hindered the oxygen penetration inside the matrix. It was reported that PPMA improved the cohesion between the particles promoting the formation of intercalated structure [149]. This behavior could be due to the low viscosity and low molecular weight of PPMA compared to PP.

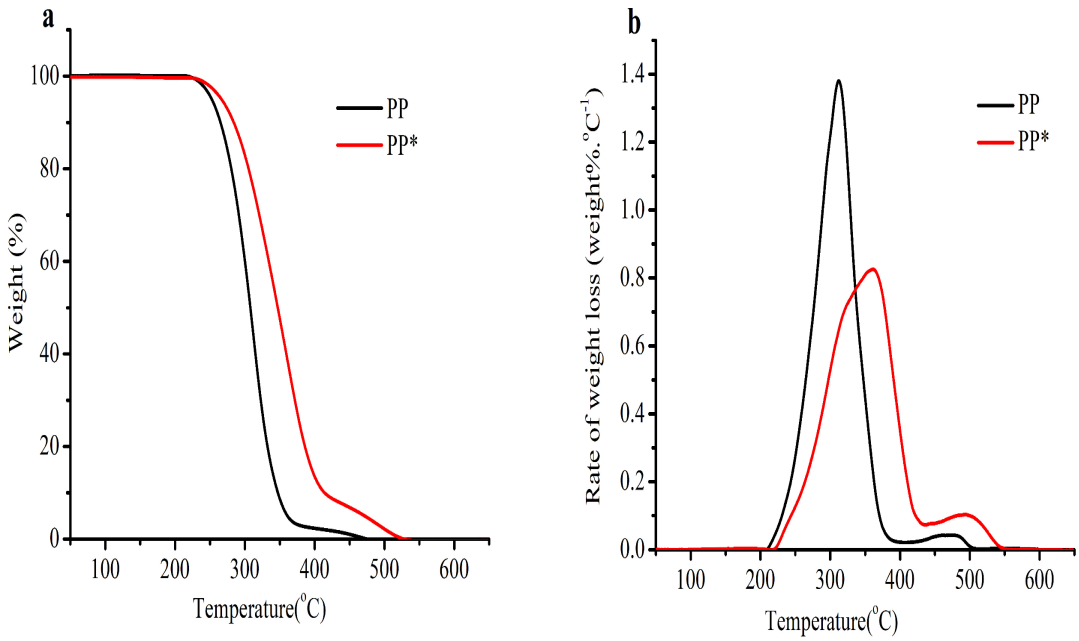

Figure 4.4: TGA and DTGA curves for PP and PP* in air at 5 °C·min^{-1} heating rate. a. TGA, b. DTGA

The thermal stability of PP materials was obtained from TGA and DTGA experiments conducted in the presence of air at different heating rates (Figure 4.5, Figure 4.6, and Appendix A). The temperature at which 5 % weight loss occurred ($T_{5\%}$), the maximum weight loss rate (MWLR), the temperature associated with the MWLR (T_{max}), and the residual mass for PP materials were used to evaluate the effect of CA* and MH on the thermal stability of PP materials (Table 4.2). For all heating rates, the addition of MH increased $T_{5\%}$ compared to PP; the addition of CA* had the opposite effect, lowering $T_{5\%}$ compared to PP. The presence of CA* and MH lowered $T_{5\%}$ compared to PP. The residue remaining at 650 °C was negligible (0%) for PP and 60PP*/40CA* and approximately 20 wt.% for 70PP*/30MH and 70(60PP*/40CA*)/30MH reflecting the inorganic content of MH.

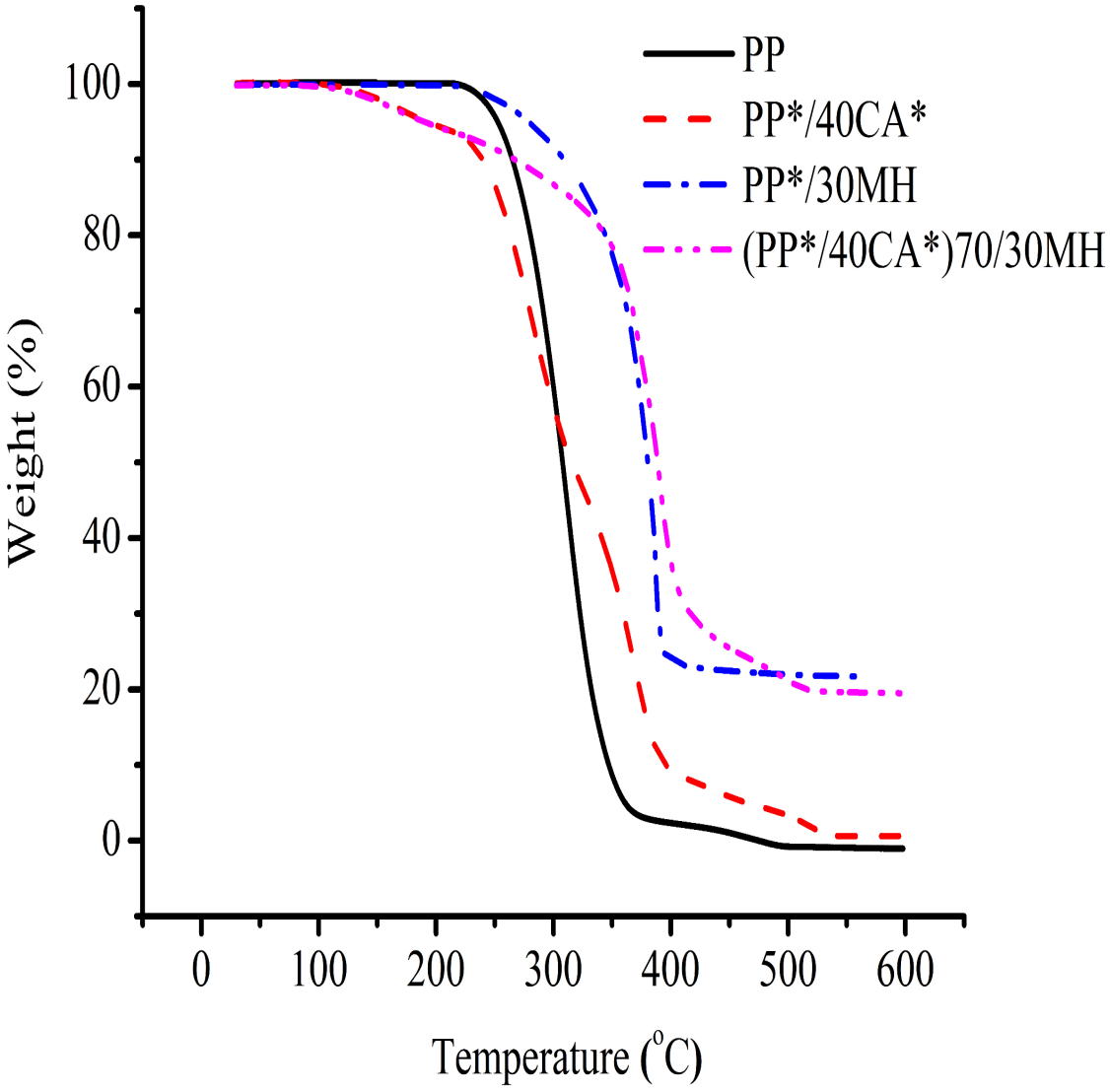

Figure 4.5: TGA curves of PP materials in air at 5 °C·min^{-1} heating rate

For a given PP material, its MWLR increased as the heating rate increased. The addition of MH to PP* increased MWLR compared to PP and 60PP*/40CA* materials. The addition of CA* to PP* lowered its MWLR compared to pure PP at 5 and 10 $^{o}C{\cdot}min^{-1}$ heating rates. The presence of CA* and MH increased the MWLR compared to 60PP*/40CA* at 5 $^{o}C{\cdot}min^{-1}$. This could be attributed to the smoldering of CA*, slowing down the degradation process of the materials [150].

Table 4.2: Thermal analysis of PP materials for 5, 10, 20, and 30 $^{o}C{\cdot}min^{-1}$ heating rates

Heating rate ($^{o}C{\cdot}min^{-1}$)	Material	$T_{5\%}$ (^{o}C)	T_{max} (^{o}C)	Residue (wt. %)	MWLR (wt.% $\cdot{}^{o}C^{-1}$)
5	PP	252	312	0	1.38
	PP*	265	360	0	0.83
	60PP*/40CA*	192	365	0.63	0.72
	70PP*/30MH	270	386	21.4	2.39
	70(60PP*/40CA*)/30MH	189	391	19.38	1.3
10	PP	270	347	0	1.26
	PP*	289	384	0	1.04
	60PP*/40CA*	222	375	0.3	0.76
	70PP*/30MH	292	423	20.6	2.28
	70(60PP*/40CA*)/30MH	207	409	19.06	1.13
20	PP	290	397	0	1.07
	PP*	313	406	0	1.24
	60PP*/40CA*	259	400	0.63	1.32
	70PP*/30MH	327	431	19.38	1.58
	70(60PP*/40CA*)/30MH	262	427	18.56	1.23
30	PP	317	427	0	1.25
	PP*	344	443	0	1.28
	60PP*/40CA*	276	418.98	0.22	1.33
	70PP*/30MH	334	431.63	18.81	1.55
	70(60PP*/40CA*)/30MH	295	439.02	20.45	1.15

The T_{max} value increased with increasing heating rate (Figure 4.5). For example, T_{max} of 70(60PP*/40CA*)/30MH at 5 $^{o}C{\cdot}min^{-1}$ was 391 ^{o}C and 439 ^{o}C at 30 $^{o}C{\cdot}min^{-1}$. The increase of T_{max} with increasing heating rate is the basic assumption of the Kissinger model which makes employing this model for activation energy calculation reliable.

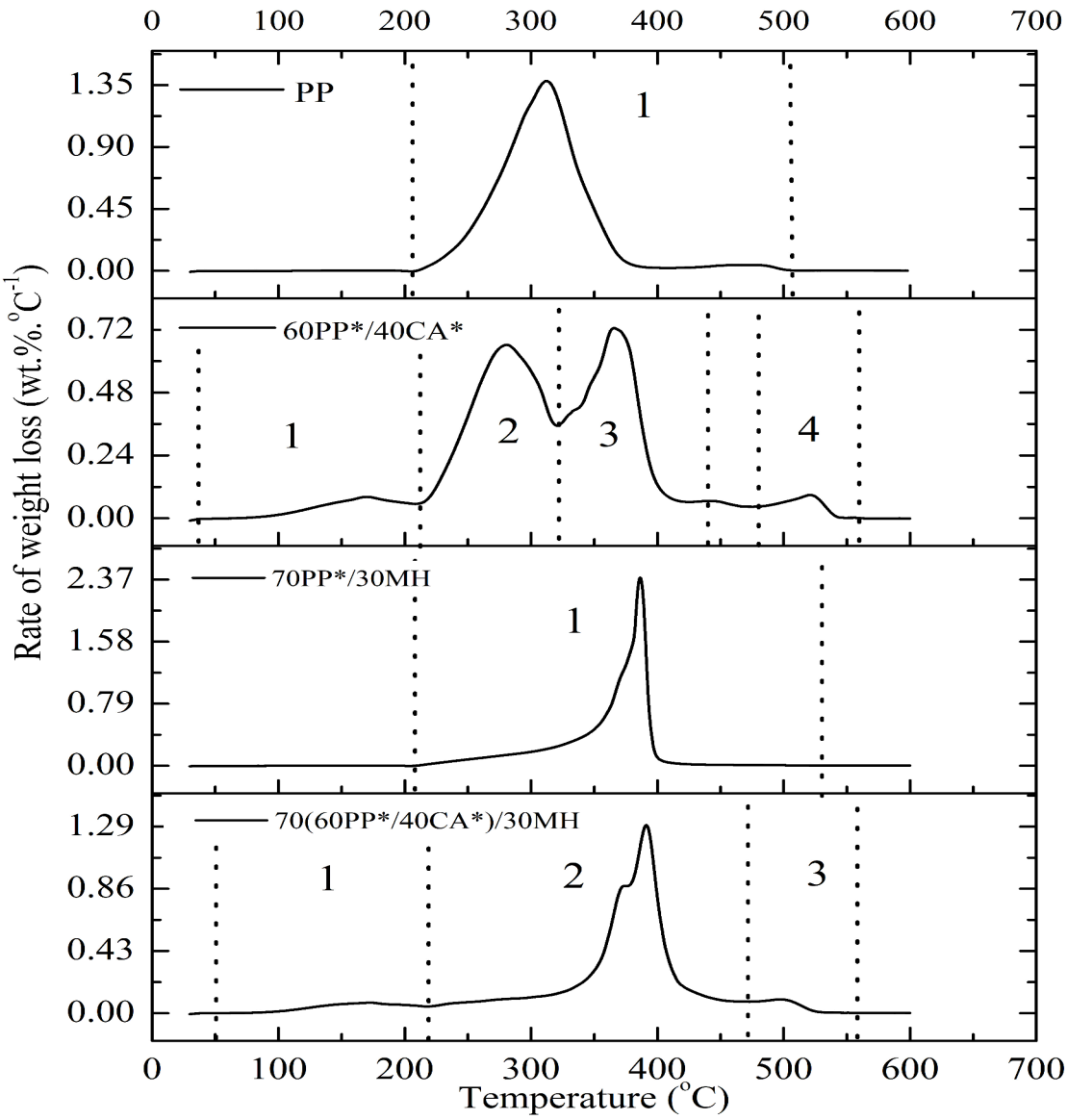

Figure 4.6: DTGA curves of PP materials at 5 °C·min^{-1} heating rates, onset and end of each step identified by vertical dash lines

The DTGA thermograms taken at 5 °C·min^{-1} heating rate (Figure 4.4 and Figure 4.5) were used to distinguish key features of the thermal degradation of PP materials when MH, CA* and both MH and CA* were present and summarized Table 4.3. The temperature at which the rate of weight loss (DTGA, Figure 4.4) becomes non-zero was identified for each step; this corresponds to the start of decomposition of one of the component. PP was used for comparison purposes; its DTGA contained only one peak. The PP decomposition is in agreement with those reported by Lv et al. [109], indicating that the decomposition of pure PP starts at approximately 200 °C, and the single-step decomposition leads to the formation of condensable volatiles and non-condensable gases with no residue remaining at temperatures above 600 °C. Similar behavior was reported by Rantucha et al. based on FTIR spectroscopy data obtained at various temperatures [95].

In contrast, the DTGA thermogram of 60PP*/40CA* contained four steps (Figure 4.6). The first step was within the 40 °C-212 °C temperature range with a mass loss of 7 wt.%, reflecting the evaporation of the moisture and TEC plasticizer. The second step occurred within the temperature range 212 °C-320 °C, with mass loss of 41 wt.%. The third step occurred within 320 °C-457 °C, leading to a mass loss of 45 wt.%. This step may be related to the degradation of CA* and the remainder of PP. Another minor step appeared at the end of the TGA thermogram curve (457 °C-560 °C) with a mass loss of 6 wt.%. This could be attributed to carbonization of the decomposition products resulting in the formation of ash. These observations are in good agreement with the results obtained by Hanna et al. [133] regarding the decomposition of CA. Hanna et al., and others stated that CA* decomposes in three steps: the volatile product or dehydration of initial CA*; the thermal degradation of fragmentable molecules of CA*; and the carbonization of the remaining fragmented CA molecules [133].

The DTGA curve for 70(60PP*/40CA*)/30MH showed three steps. The first step is within the range of 50 °C- 220 °C. The mass loss of 7 wt.% is attributed to the evaporation of moisture and TEC plasticizer; a result also found for 60PP*/40CA*. The second step is within the range of 220 °C-475 °C. Here the mass loss was 77 wt.% and is likely related to the degradation of the PP*, MH and the fragments of CA*. The remaining minor peak is seen within the range of 476 °C-545 °C with a mass loss of 2 wt.%. The remaining residue (21 wt.%) would most probably contain magnesium oxide and the carbonized decomposition products of CA*.

4.3.3 Kinetics of thermal degradation

The apparent activation energy at the maximum rate of conversion was estimated with the Kissinger method, and its linearized form expressed in terms of T_{max}. In this method, the

Table 4.3: DTGA steps of the degradation analysis of PP materials at 5 °C·min^{-1} heating rate

Material	Temperature range (°C) (Residual mass (wt.%))			
Steps	1	2	3	4
PP	209-504 (0.0)			
PP*	216-540 (0.0)			
60PP*/40CA*	40-212 (93)	209-504 (52)	320-457 (7)	457-560 (0.6)
70PP*/30MH	204-514 (21)			
70(60PP*/40CA*)/30MH	50-220 (93)	220-475 (23)	476-545 (21)	

apparent activation energy was obtained from a plot of $ln(\beta^*/T_{max}^2)$ versus $1/T_{max}$. However, this method has a major limitation that should be noted in estimating the apparent activation energy which incorporates the contributions of a wide range of heating rates [137]. The Kissinger method requires more than two heating rates to estimate a single value of E_a for any process regardless of its actual kinetic complexity.

The use of MH as a means to improve the thermal resistance of PP*/CA* materials was assessed by estimating the activation energy. Specifically, the susceptibility of the degradation reaction and the complexity of the degradation reactions were explored. The apparent activation energy estimated at T_{max} using the Kissinger method (Figure 4.7) were significantly higher when CA*, MH, or a combination of CA* and MH were added to the PP*. The addition of MH improved the thermal resistance of 60PP*/40CA* blend. The estimated activation energy for PP, PP*, 60PP*/40CA*, 70PP*/30MH and 70(60PP*/40CA*)/30MH was 41 kJ·mol^{-1}, 70 kJ·mol^{-1}, 106 kJ·mol^{-1}, 125 kJ·mol^{-1}, and 136 kJ·mol^{-1}, respectively.

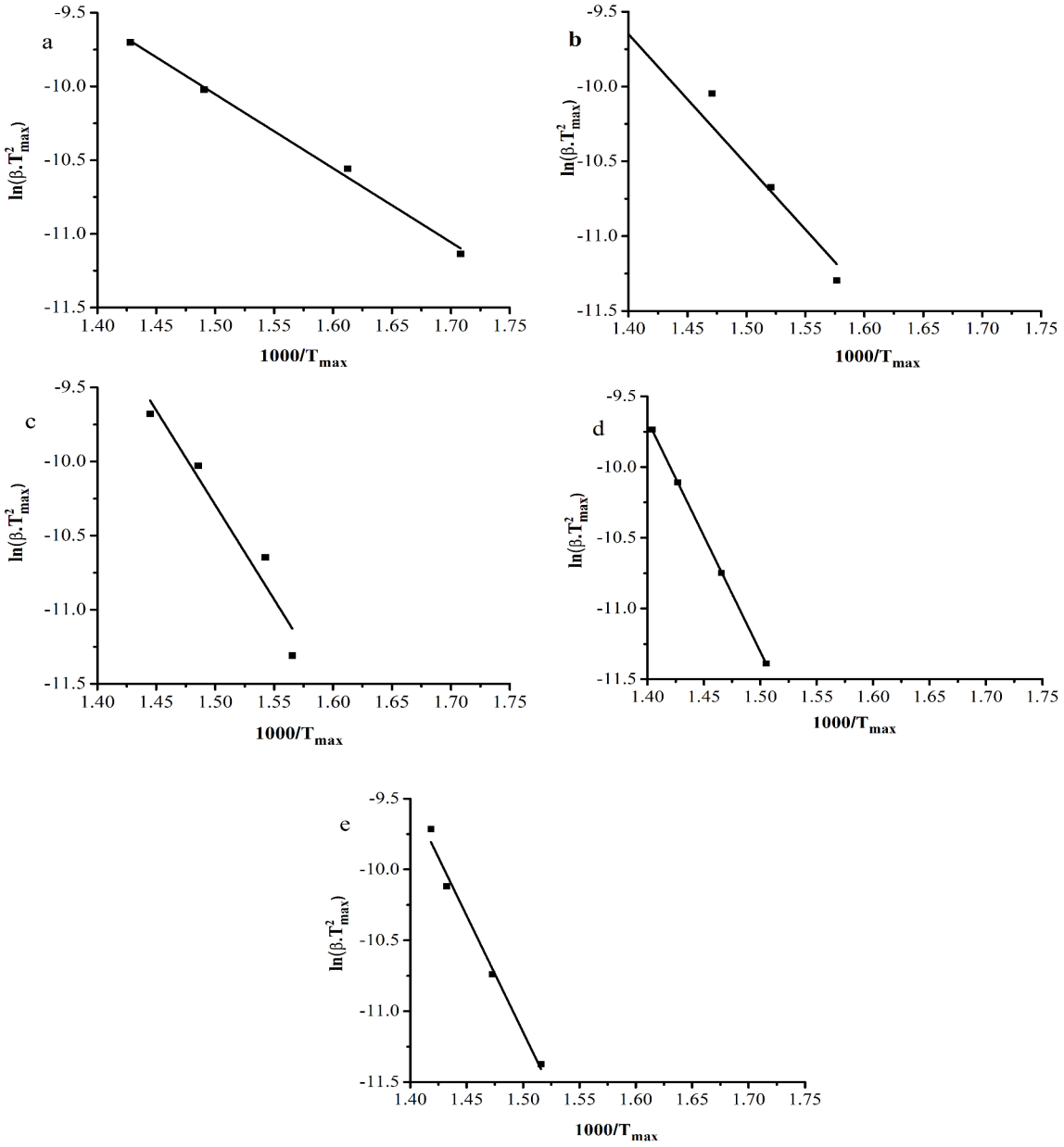

Figure 4.7: Linear plots for calculating E_a by using Kissinger method. a. PP, b. PP*, c. 60PP*/40CA*, d. 70PP*/30MH, e. 70(60PP*/ 40CA*)/30MH

The Kissinger method has been used in many studies; the present results are similar to those previously reported for the same heating levels for PP and PP*/MH materials [95, 151, 152].

The activation energy, according to conversion, was estimated with the KAS method (Figure 4.8 and Figure 4.9). Details are presented in Appendix A. The activation energy of PP was relatively constant, approximately 60 kJ·mol^{-1} for the entire conversion range. For PP*, there was a constant increase in $E_{a,x}$ with increasing x.

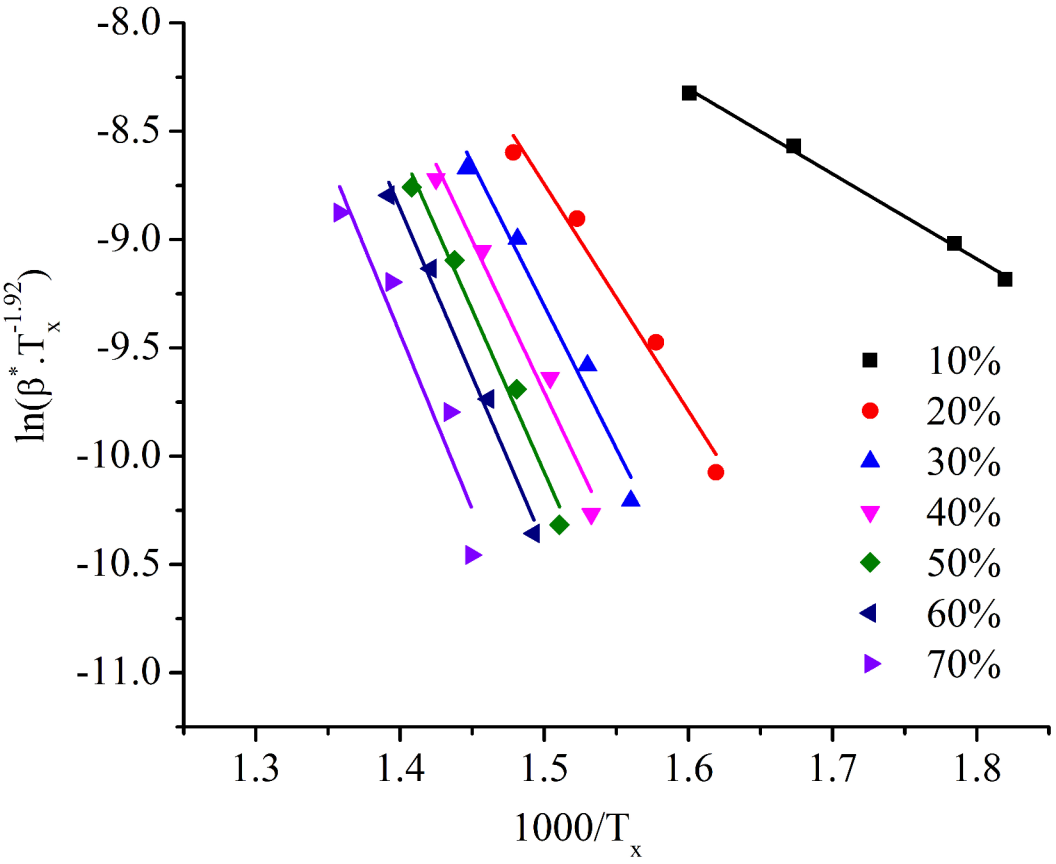

Figure 4.8: Linear plots for calculating $E_{a,x}$ with the KAS method for 70(60PP*/40CA*)/30MH according to conversion (%)

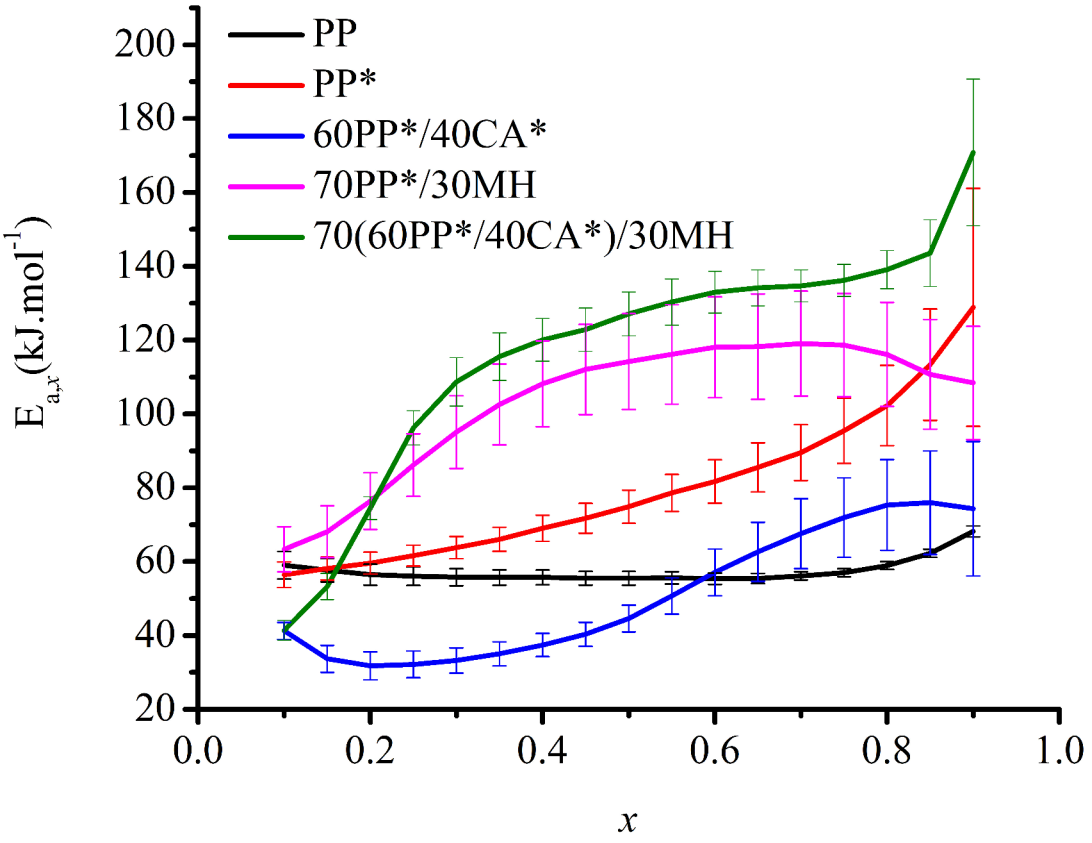

Figure 4.9: Activation energy of PP and its materials at different conversion levels calculated by the KAS method. Error bar represents 95% confidence intervals

In contrast, the activation energy for the thermal degradation of 60PP*/40CA* was lower than that of PP for conversion up to 60 %, initially decreasing until 20 % conversion, and subsequently increasing. This may be due to the thermal decomposition of 60PP*/40CA*, which begins at lower temperatures compared to PP (Figure 4.9). For 70PP*/30MH, its activation energy was higher than that of PP, PP*, and 60PP*/40CA* and increased rapidly and stabilized at a conversion level above 40 %. This increase of activation energy could be explained by the fact that MH continues to degrade well after the completion of PP degradation.

The activation energy of 70(60PP*/40CA*)/30MH was higher than all other PP materials at conversion above 20%, with an initial rapid increase followed by a slower increase. This result confirms the effect of CA* in PP*/MH material which increases the E_a required to initiate decomposition.

The accuracy of the KAS method was also investigated. It was reported in the literature [93, 99], the KAS method is accurate when $y = E_{a,x}/RT > 15$ as shown in Figure 4.10. The integral approximation used was more accurate in the estimation of $E_{a,x}$ for the PP* material presence with CA*and MH.

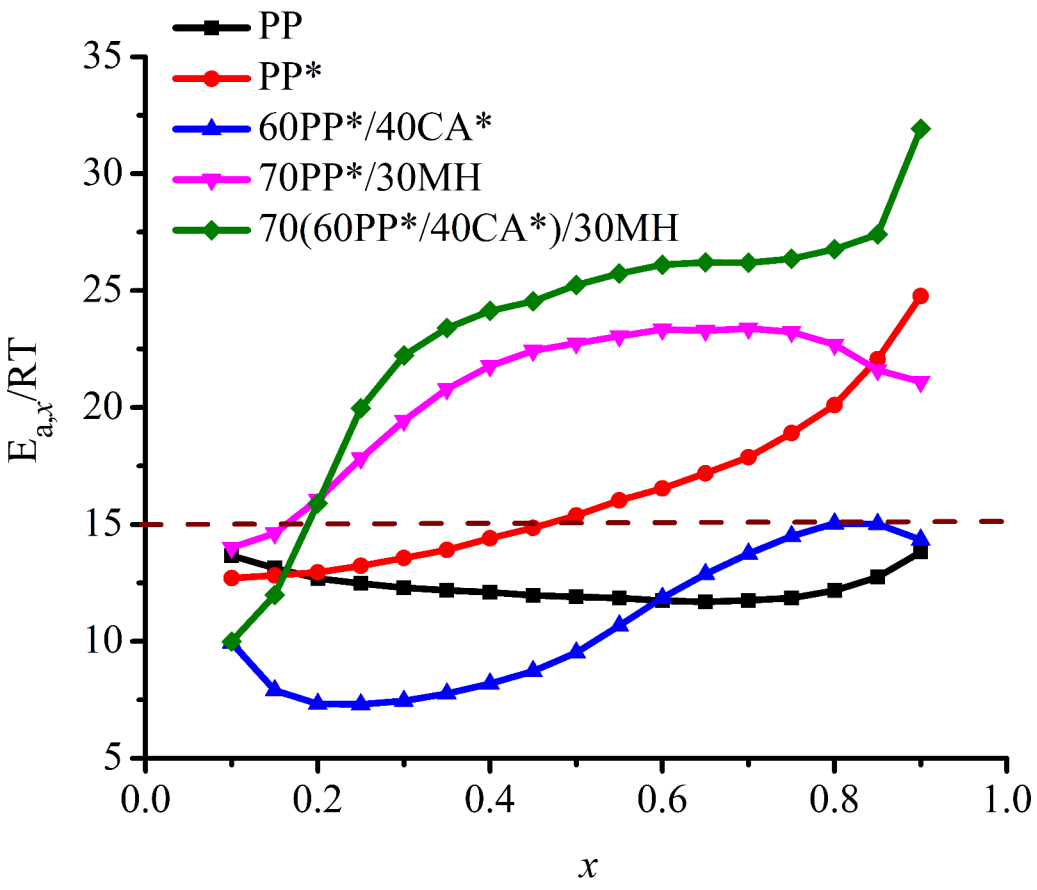

Figure 4.10: Estimates of E_a/RT versus conversion level of PP and its materials by the KAS method

As it can be observed in Figure 4.11, there is a good agreement between β^*_{Act} and β^*_{Cal} in the case of PP and 70(60PP*/40CA*)/30MH because they lie on the line $y = x$. In the other cases the agreement is not as strong.

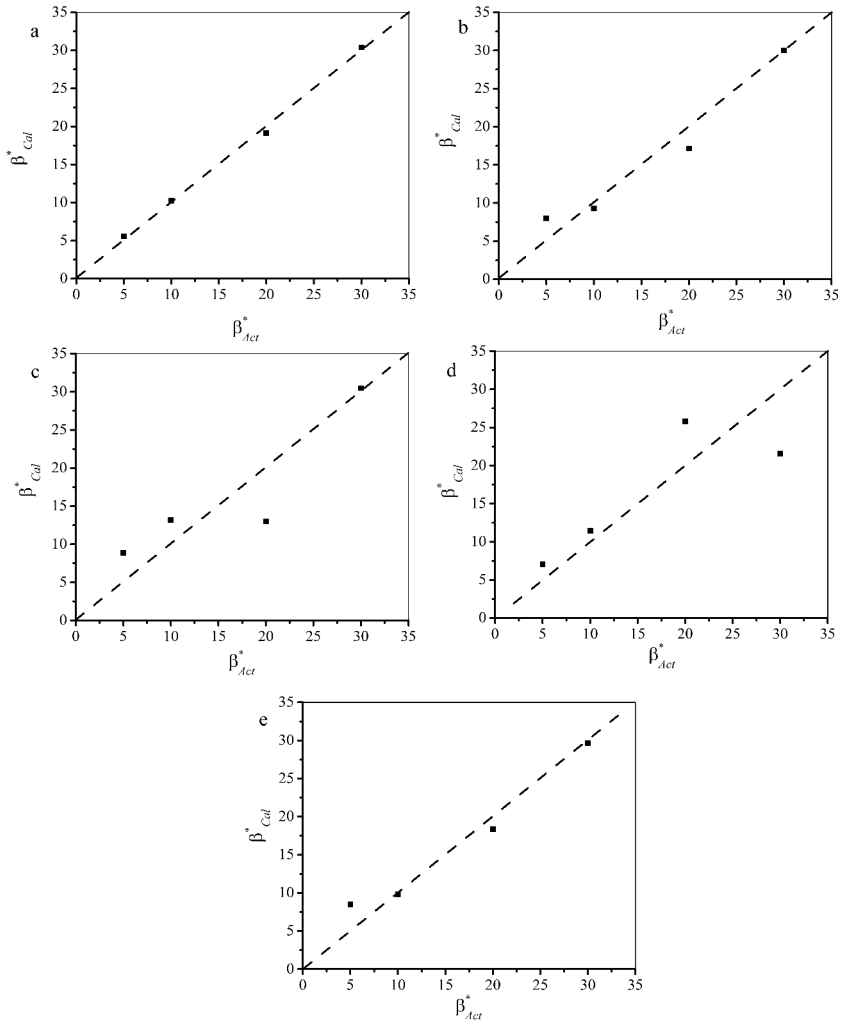

Figure 4.11: Actual heating rate β^*_{Act} versus calculated heating rate β^*_{Cal} estimated by the numerical integration method for a. PP, b. PP*, c. 60PP*/40CA*, d. 70PP*/30MH, and e. 70(60PP*/40CA*)/30MH

A comparison of the calculated activation energy for PP materials obtained by the numerical integration method (NIM) and the KAS method show differences (Figure 4.12). The closest accordance between the two estimates exists for 70PP*/30MH and 70(60PP* /40CA*)/30MH; in other words, the samples with y values above 15 (Figure 4.10).

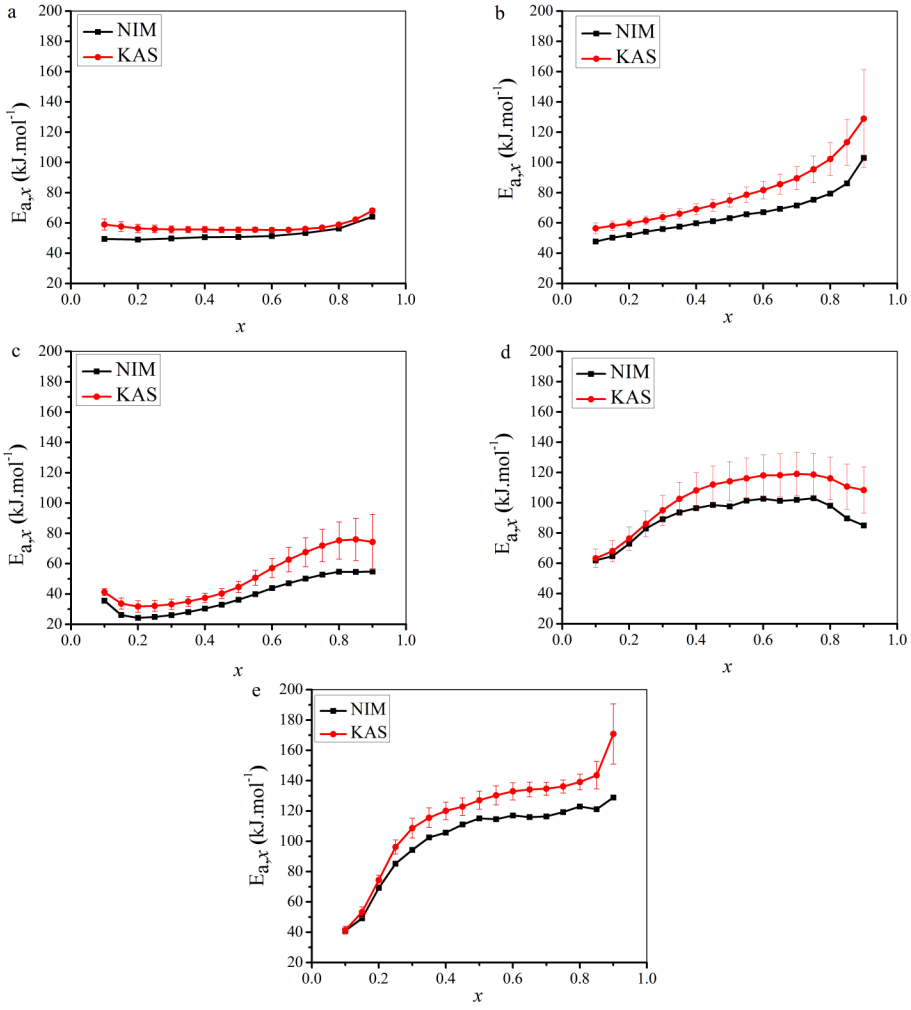

Figure 4.12: Comparison of $E_{a,x}$ calculated by the numerical integration method and the KAS method for a. PP, b. PP*, c. 60PP*/40CA*, d. 70PP*/30MH, and e. 70(60PP*/40CA*)/30MH

4.4 Conclusion

This study revealed that materials containing PP*/CA* and MH possess better thermal stability than pure PP.

Based on TGA curves, $T_{5\%}$ was the highest for 70PP*/30MH and the lowest for 70(60PP*/40CA*)/30MH for all heating rates. PP, PP*, and 60PP*/40CA* had no residue left at the end of the TGA experiment while 70PP*/30MH and 70(60PP*/40CA*)/30MH had around 20 wt.% reflecting the inorganic content.

According to the DTGA curves, T_{max} for the 70(60PP*/40CA*)/30MH material was the highest, and MWLR was the lowest for all heating rates. There was a shift in the peaks of the DTGA curves to the right when PPMA, CA* and MH were present.

The kinetic parameters of the degradation of PP materials were accurately determined from a series of TGA experiments at four heating rates. The E_a values of the degradation of the materials calculated using Kissinger, KAS, and numerical integration methods based on TGA and DTGA curves are higher than those of pure PP and PP*/CA* materials. The activation energy required for initiating the thermal degradation for PP*/CA* blend with MH was higher than that of PP and 70PP*/30MH.

Chapter 5

Combustion Behavior of Plasticized Cellulose Acetate Magnesium Hydroxide Polypropylene Materials

The flammability, and flame retardant effects of plasticized cellulose acetate (CA*) and magnesium hydroxide (MH) in PP materials were evaluated: vertical burning, limited oxygen index, cone calorimetry, and the adiabatic bomb calorimeter. It was found that (CA*), in combination with MH, can effectively reduce the flammability of PP and obtain reasonable flame retardation with a low level of MH. 70(60PP*/40CA*)/30MH material was categorized using a vertical burning test as V-0 and had the highest value of oxygen index (OI%). A significant reduction in the heat release rate (HRR) and effective heat of combustion (EHC) was determined from the cone and bomb calorimeter test.

5.1 Introduction

PP materials, are described as product[s] generated by blending or assembling bio-material, either exclusively or in combination with non-bio-based materials, in which the bio-based material is present as a quantifiable portion of the total mass of the product [153] have attracted attention as a promising material for natural resource, eco-friendliness, sustainability, and lightness [154]. However, their applications are limited by their low thermal resistance and fire resistance behavior [155]. Polypropylene (PP) is commonly used in biomaterials because of its low melting temperature but has limited flammability resistance

[156]. Flame retardants are used to improve their flammability resistance and thermal stability in order to broaden the application of PP.

PP materials containing cellulosic derivatives also possess low thermal stability. The pyrolysis and combustion characteristics of cellulose derivatives have been investigated. Cellulose is subject to smoldering, a slow, low temperature, and flameless form of combustion. The temperature during smoldering is typically 600-1100 K, while for gas phase, the flame temperature is within the range of 1200-1700 K. During the smoldering process, sufficient heat is produced to induce the formation of char [157], and the heat of combustion, around 16 kJ $\cdot g^{-1}$ [158], is very low compared with PP at 43 kJ$\cdot g^{-1}$ [116]. The acetylation of cellulose, where hydroxyl groups are replaced by acetyl groups, creates cellulose acetate which has hydrophilicity and was shown to have higher thermal stability [159–161]. According to Ana et al. (2003) [162], the acetylation of recycled cellulose improved the thermal and thermo-oxidative stability of the cellulose derivatives. Cellulose acetate (CA) is limited by the close proximity of its thermal decomposition temperature and the melting temperature. For this reason, CA requires plasticization prior to its mixing with thermoplastic materials. Different plasticizer can be used for this purpose, and various studies that examine the effects of these plasticizers on the characteristics of CA [163, 164]. Phthalate-based plasticizers, currently used in commercial cellulose ester plastics, are under environmental scrutiny and perhaps pose a health threat. Triethyl citrate (TEC) is an eco-friendly plasticizer which was shown to act as a plasticizer for CA [46]. According to Mohanty et al. [34], the optimum level of TEC was 30 wt.% in order to obtain CA thermoplastic with a reasonable balance of strength and stiffness.

The addition of flame retardants, such as ammonium polyphosphate, magnesium hydroxide, and bromine, is beneficial in improving the fire resistance properties but may negatively affect their mechanical properties. Hence there is a need to minimize the content of flame retardant while obtaining satisfactory flame retardant characteristics in composite materials. Flame retardants are classified according to their action. Metal hydroxide and intumescent flame retardants act in the condensed phase [165–167]. Other flame retardants can act in the gas phase, such as halogenated compounds, by forming free radicals. Phosphorous compounds act by increasing the conversion of the polymer materials to a char residue during pyrolysis [53, 109, 168, 169]. Magnesium hydroxide (MH) may be considered as one of the most environmentally friendly flame retardants because its thermal decomposition leads to the release of water vapor and formation of magnesium oxide. The decomposition temperature is an important consideration when selecting flame retardants for use in polymeric materials. For example, MH is more desirable than aluminum trihydrate (ATH) because its decomposition temperature is between 300-320 °C, while for ATH it is around 200 °C and it is unusable for thermoplastic resins such as PP whose

molding temperatures are at least about 200 °C [170]. One of the drawbacks of MH is the high loading required to achieve a reasonable flame retardancy, which is typically above 60 wt.%. The addition of MH in such high amounts negatively affects the mechanical and rheological properties of the polymer. The effect of MH addition on the thermal and combustion properties of composite materials has been investigated for a number of materials and fire tests. For example, Sain et al. (2004) investigated the effect of MH on the flammability of sawdust and rice husk PP composites using horizontal burning rate and oxygen index tests. Their study indicated that MH significantly reduces the flammability of 50 wt.% for both natural filler, filled PP composite. Das et al. [171] studied the flame retardant effect of biochar, MH and ammonium polyphosphate (APP) for woody biomass PP [171]. Their results show that with the addition of biochar and MH to woody biomass PP, the flammability was impeded while preserving the mechanical properties. According to Balakrishnan et al. [172], increasing the loading of MH from 20 wt.% to 50 wt.% increased the time to ignition (t_{ign}) in the PP. Oxygen index (OI) values are also improved as a result of MH application, and V-0 rating was obtained for 40 and 50 wt.% with respect to the vertical burning test [172]. Cone calorimeter tests (CCT) are also used to study the effect of MH as a flame retardant for PP materials. The addition of MH reduces the peak of heat release rate (PHRR) [173]. The oxygen bomb calorimeter (BOM) is another characterization technique which is used to evaluate the flame retardancy of materials and validate the heat capacity of the material.

The aim of this work was to evaluate and assess the effect of magnesium hydroxide (MH) on the flammability of plasticized cellulose acetate (CA*) polypropylene (PP) materials. Cellulose acetate plasticization was obtained with triethyl citrate, as discussed in Chapter 3. The flammability tests selected in this study were the vertical burning test, the limited oxygen index (LOI), the cone calorimetry test (CCT), and bomb calorimetry (BOM). The synergistic effects between MH and CA* to reduce the MH level required to achieve reasonable flame retardant effect will also be discussed.

5.2 Experimental methods

5.2.1 Materials

Polypropylene (PP) fine powder (HM20/70P), was purchased from GOONVEAN Fibres Company, United Kingdom. Magnesium hydroxide (MH), Cellulose acetate (CA) (approx. 50000 g·mol^{-1} 39% acetyl), triethyl citrate (TEC), and polypropylene-grafted maleic anhydride (PPMA) were purchased from Sigma Aldrich (USA). All materials were used as

received.

5.2.2 Materials preparation

Cellulose acetate (CA) was plasticized according to the methodology presented in Chapter 3. Polypropylene (PP) materials were produced by extrusion in a twin screw-extruder (SJSZ-7A), Wuhan Ruiming Plastic Machinery Company, China. The four temperature zones ranged from 160 °C-180 °C, and the circulation time was five minutes. The extruded materials were then cut as pellets by using a cutter (SZS-20, Wuhan Ruiming Plastic Machinery, China), and then compression molded using compression moulding (PHI, Pasadena Hydraulic Inc., USA) at 200 °C with 10 bar pressure for 2 minutes. Two different molds were used for preparing the sample according to the dimensions of the sample required for the vertical burning test, oxygene index, and the cone calorimeter following the ASTM standard for each test. The fabricated materials are listed in Table 5.1.

Table 5.1: Sample composition and coding of PP materials

Material	PP wt.%	CA* wt.%	MH wt.%	PPMA wt.%
PP	100	0	0	0
PP*	97	0	0	3
60PP*/40CA*	58.2	40	0	1.8
70PP*/30MH	67.9	0	30	2.1
70(60PP*/40CA*)/30MH	40.74	28	30	1.26

PP* refers to 97PP /3PPMA.

CA* refers to plasticized cellulose acetate with triethyl citrate.

5.2.3 Oxygen index (OI)

The oxygen index (OI) was estimated according to ASTM D2863. The sample was 125 mm×10 mm×4 mm. The sample was held vertically in the glass chamber, with controlled oxygen and nitrogen flow. A natural gas torch was used to burn the top end of the sample. If the flame persisted for more than 180 s, and/or if the length of the burning sample was more than 50 mm of its original length, the response was marked as X. Otherwise the response was marked O. A set of responses of the first five samples (N_L) was taken to estimate the initial oxygen concentration by changing the level of oxygen gas in the chamber

with fixed interval d. After that, another five responses were taken at fixed intervals (d). The last five responses were used to identify the constant (k) from the standard. Oxygen Index (OI) was estimated with the following equation:

$$\mathrm{OI} = C_F + k_o d_o \tag{5.1}$$

where C_F is the final of oxygen concentration, in percent volume to one decimal place, used in the series of N_T measurements, d_o is the interval between oxygen concentrations levels in percent volume, and k_o is a factor obtained from Table 3 in ASTM D2863-17a, see Appendix B.

5.2.4 Vertical burning test (UL-94)

The vertical burning test was conducted according to ASTM D3801 [107]. The specimen was held vertically in a dark fume hood by using a stand, and then a flame was applied for 10 s and then removed. The lowest flammability rating is V-2 (flaming time $<$ 30 s) and the highest is V-0 (flaming time $< 10s$). V-1 is an intermediate between V-0 and V-2. Flammable materials that could not be classified according to these categories were marked with the code NC (no classification, complete combustion of the specimen).

5.2.5 Cone calorimeter test (CCT)

The cone calorimeter test was performed according to ASTM E1354 under a heat flux of 50 kW·m^{-2} [100]. The samples were prepared in a compression mold (100 mm×100 mm×5 mm). All samples were wrapped in aluminum foil covering the sides and bottom and tested in the horizontal position on the sample holder.The heat flux was selected based on OI and vertical burning conditions and identified as 50 kW·m^{-2}. The parameters considered were time to ignition (t_{ign}) in seconds, total burn time (t_{tot}) in seconds, heat release rate (HRR) in kW·m^{-2}, peak of heat release rate (PHRR), in kW·m^{-2}, mass loss (%), CO and CO_2 yield and production, total smoke production (TSP), and average specific extinction area ($SEA_{avg.}$) (m^2·kg^{-1}). The air flow was set to be 24 liter·s^{-1}. The heat released was calculated based on oxygen consumption and assumed that for every kilogram of oxygen consumed 13.1 MJ of heat would be released. Based on this, properties estimated by the cone calorimeter, indices, such as fire growth rate (FIGRA), and fire performance index (FPI), were used for further interpretation of CCT results.

5.2.6 Combustion products

The combustion products CO_2, CO and soot and the estimated available carbon in the PP materials were analyzed. The carbon availability was verified by the chemical composition and cone calorimetry observations for CO_2 and COY. The fractions of the carbon were calculated according to the number of carbon units in the chemical compounds formula, see Appendix B. The combustion reaction is presented by Equation 5.2 and Equation 5.3 where the fuel represents the polymeric materials and CO, CO_2, soot and char are the products.

$$\text{Fuel} + O_2 \rightarrow CO_2 + H_2O \tag{5.2}$$

$$\text{Fuel} + O_2 \rightarrow CO + H_2O + \text{Soot} + \text{Char} \tag{5.3}$$

where the fuel represents PP in pure PP, PP and PPMA in PP*/MH samples and PP, CA, PPMA, and TEC in PP*/CA* samples.

5.2.7 Bomb calorimetry

The heat of combustion was obtained in an oxygen bomb calorimeter (Model 1241, Parr Instrument Co., Molin, Illinois) according to the standard procedure, ASTM D4809 [174]. Benzoic acid which has a known heat of combustion, 26.453 kJ·g^{-1}, was used to estimate the calibration factor of the bomb calorimeter, C^*, obtained as:

$$C^* = (m \times 26.453 \text{ kJ} \cdot \text{g}^{-1})/(T_{max} - T_o) = 9.97 \text{ kJ} \cdot {}^{\text{o}}\text{C}^{-1} \tag{5.4}$$

where C^* represents the calibration factor of the bomb calorimeter, i.e. the heat capacity of the bomb calorimeter immersed in a water bath, m is the mass of the benzoic acid sample (g), T_{max} and T_o represent the maximum and initial temperature of the water bath (°C).

The heat of combustion was obtained by placing a sample inside a capsule of gelatin with known heat of combustion. The capsule was placed in a cup which was positioned in the holder of the lid of the bomb calorimeter. A volume of 1 mL of deionized water was pipetted into the bottom of the bomb. A 10 cm length of Nichrome fuse wire was cut, weighed, connected to the two electrodes in the pressure vessel (bomb calorimeter), and bent to be in contact with the sample for ignition. The bomb calorimeter was then assembled, sealed and purged twice by pressurizing to 20 atm with pure oxygen, then vented. The bomb calorimeter was then pressurized with pure oxygen to 30 atm and then submerged in bath containing 2 liters of water, in an insulated jacket and checked for leaks. The temperature of the water bath was maintained uniform by stirring. The temperature

of the water bath was measured using a precision thermistor. The equilibrium temperature of the water bath was recorded as initial temperature (T_o). The sample was then ignited by passing an electric current through the wire causing the sample to ignite and burn. The heat released by the combustion of the sample increased the temperature until the maximum temperature (T_{max}) was reached.

The heat of combustion estimate was corrected as follows. An ignition correction (e_1) was made to account for the contribution of the combustion of the Nichrome wire. This correction was based on the mass loss of the wire before and after combustion multiplied by 5.858 kJ·g^{-1}. The second correction was to account for the contribution of the combustion of the gelatin capsule (e_2). This correction was based on the mass of the gelatin capsule multiplied by the heat of combustion of gelatin, 25.6 kJ·g^{-1}. The third correction factor (e_3) was to account for the formation of MgO when MH was present in the materials. The heat of combustion was then calculated as:

$$H_c = (C^* \cdot \Delta T_{max} - e_1 - e_2 - e_3)/m \tag{5.5}$$

In Equation 5.5, $\Delta T_{max} = T_f - T_o$ in °C, T_f is the maximum temperature that could be reached and m (g) represents the mass of the burned material.

5.3 Results and discussion

5.3.1 Oxygen index (OI) and vertical burning (UL 94) test

Table 5.2 presents the OI and UL- 94 results of the PP materials. The observations show higher OI for 60PP*/40CA*, 70PP*/30MH, and 70(60PP*/40CA*)/30MH compared to that of PP. Higher OI represents the higher resistance to ignition. The presence of MH in 70PP*/30MH and 70(60PP*/40CA*)/30MH has statistically significant higher resistance to ignition compared to PP and 60PP*/40CA*.

This increase could be attributed to the endothermic decomposition of MH, as well as the release of water vapor, during the decomposition causing dilution of gaseous combustible fragments. The classification of the materials deduced from the vertical burning test based on the UL-94 standard is presented in Table 5.2. PP, 60PP*/40CA*, and 70PP*/30MH showed the highest burning rate and burned completely with ignition of the cotton indicator. The material 70(60PP*/40CA*)/30MH showed significant improvement in self-extinguishing and can be categorized as V-0 class.

Figure 5.1 shows images for PP materials after the *OI* burning test. The morphology of the samples after the OI test showed the damaged length of the sample was reduced in the presence of MH and CA*, while for the PP it can be seen how fast the material burned according to the damage in the length of the sample. Also, the black regions of PP indicate that the burnt area is more significant than for the other materials.

Table 5.2: OI and UL-94 results of PP materials (± standard error, n=10)

Material	OI (%)	Flammability rating (UL-94)	Notes
PP	20 (± 0.2)	NC*	Ignited completely more than the extent and period of time drips at 20 %,no charring
60PP*/40CA*	22.10 (± 0.25)	NC*	Ignited completely more than the extent and period drips at 20 %, charring formed
70PP*/30MH	24.89 (± 0.23)	NC*	Ignited completely more than the extent and period drips at 20 %, low charring, slow burn rate
70(60PP*/40CA*)/30MH	25.89 (± 0.55)	V-0	Slow rate of burn, No drips, charring formed

*No classification, complete combustion of the specimen

Based on UL-94 results and visual observation of the samples during and after testing (Figure 5.1), PP materials when CA* and MH were present (70(60PP*/40CA*)/30MH) composite burned with a lower flame height, higher char formation, and slower burning rates compared to PP, 60PP*/40CA*, and 70PP*/30MH. The higher char formation should enhance the flame retardancy of the material, which is associated with an increase in the OI values of 70(60PP*/40CA*)/30MH.

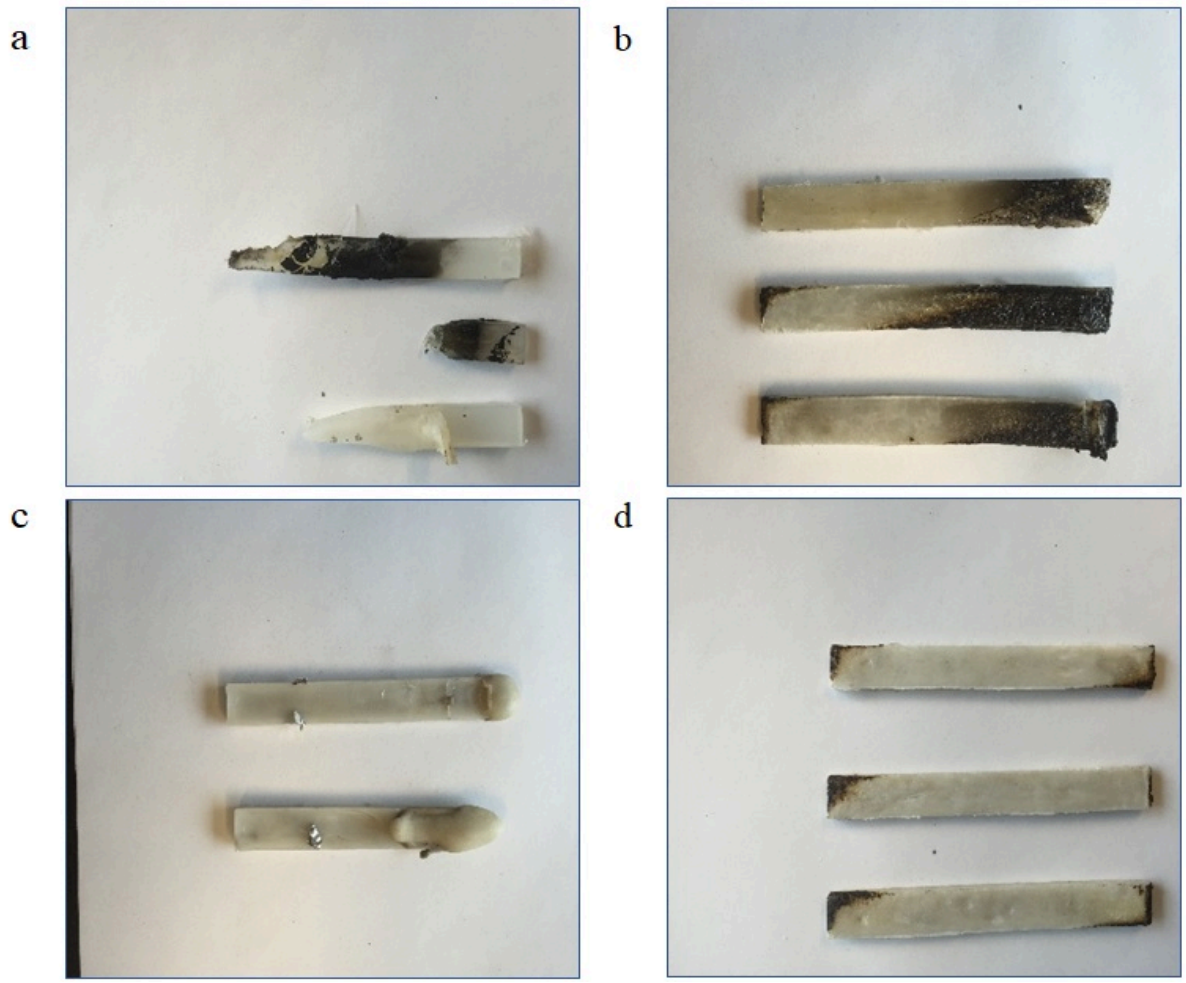

Figure 5.1: Visual observation of PP materials after OI experiment. a. PP, b. 60PP*/40CA*, c. 70PP*/30MH, d. 70(60PP*/40CA*)/30MH

5.3.2 Cone calorimeter test (CCT)

The cone calorimeter is the most advanced laboratory-scale apparatus used for testing fire properties of materials [105]. While *OI* and UL-94 tests are used to rank the flame retardation of materials, the cone calorimeter provides a wealth of information on the combustion behavior [175]. The behavior of materials in real fires can be, to some extent, be predicted from data measured by the cone calorimeter. These include ignitability, heat release rate (HRR), mass loss rate (MLR), effective heat of combustion (EHC), and CO and CO_2 production rates (denoted by COP and CO_2P), respectively. Each of these properties will be discussed next.

5.3.2.1 Heat release rate (HRR)

The heat release rate (HRR) has been recognized as the major fire reaction parameter because it defines the fire size and provides a measure of the heat released per unit surface area of burning material [6] and is reported in Figure 5.2 (See Appendix B). The shape of the HRR curves will be analyzed according to the ranking of the fire behavior previously published [110, 176]. PP is considered a thermally thin material, which is characterized by a sharp peak in HRR since the sample is entirely combusted without the formation of residues. The 60PP*/40CA* material can be classified as thermally intermediate thickness, non-charring material. The 70PP*/30MH material can be classified as thermally thick charring material because two peaks that appear. The 70(60PP*/40CA*)/30MH material could be classified as a thermally thick charring (residue forming) material, which is characterized by an initial increase in HRR followed by a subsequent slow decrease. The further thickening of the char results in a decrease in the HRR.

The ignition characteristics of the cone calorimeter experiment are summarized in Table 5.3. The time to ignition of PP was longer. The lower t_{ign} could be due to the faster decomposition of CA* and MH compared to PP. As a result, volatiles produced from the decomposed MH and/or CA* start the initial combustion. This observation agrees with previous work which indicated that an early decomposition of the flame retardants and their synergistic filler is necessary to increase the flammability resistance of material [175, 177]. Further investigation is required to analyze the decomposition products at the ignition time.

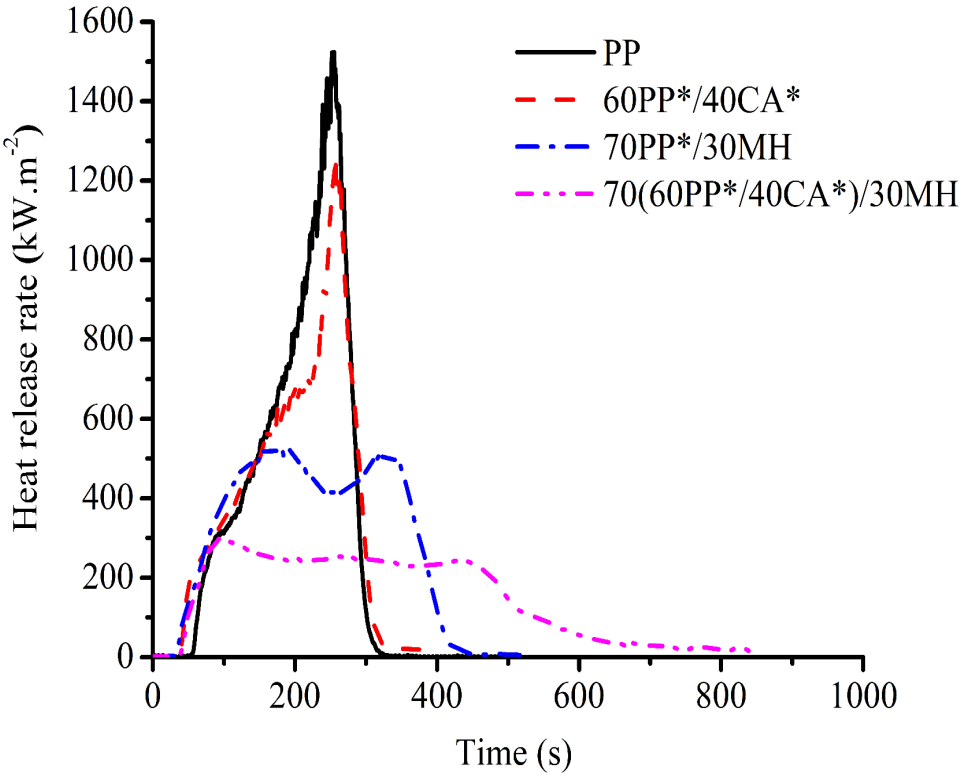

Figure 5.2: Heat Release rate curves of PP materials at 50 kW·m^{-2} heat flux during burning by cone calorimeter test

The mass loss and the HRR at ignition in Table 5.3 were used to understand the contribution of CA* and MH to the fire resistance of PP materials. The mass loss at ignition reflects the generation of volatile products, while the HRR reflects the characteristics of the ignition process. For 60PP*/40CA*, the mass loss was more important, and the HRR at ignition was lower than PP. The higher mass loss for 60PP*/40CA* means that more volatiles was generated at ignition while the smaller HRR implies that the ignition was less exothermic compared to PP. For 70PP*/30MH, the mass loss was higher than for PP, and the HRR was slightly higher than for PP. 70PP*/30MH had a smaller mass loss than that for 60PP*/40CA* while its HRR was higher indicating differences in their ignition characteristics. The 70(60PP*/40CA*)/30MH material had a similar mass loss

to 70PP*/30MH while its HRR was the lowest. The mass loss and HRR characteristics of the PP materials indicate that CA*, MH, and the combination of CA*and MH affect differently the ignition of PP.

In Chapter 3, the estimation of E_a of 60PP*/40CA* and 70(60PP*/40CA*)/30MH were lower than that of PP at low conversion which could be an explanation about the higher mass loss at ignition. For 70PP*/30MH, the estimated value of E_a was very close to that of PP at low conversion. The higher mass loss and the reduction in the t_{ign} could be an indication of weak bonds between (PP*/CA*) and MH, which increase the amount of fuel in the gas phase. Further investigation is required to analyze the decomposition products of the PP materials by using FTIR-TGA.

Table 5.3: Ignition characteristics of the combustion of PP materials in the cone calorimeter at 50 kW·m^{-2} heat flux (± standard error, n=3)

Materials	t_{ign} (s)	Mass loss at ignition (%)	HRR at ignition (kW·m^{-2})
PP	51 (± 3.0)	12.5 (± 0.3)	418 (± 16)
60PP* /40CA*	31 (± 3.5)	18.0 (± 2.0)	379 (± 15)
70PP*/30MH	32 (± 1.2)	15.0 (± 3.0)	461 (± 24)
70(60PP*/40CA*)/30MH	39 (± 1.7)	14.4 (± 0.3)	275 (± 07)

The energy characteristics of the cone calorimeter experiment are summarized in Table 5.4. The total burning time (t_{tot}) of PP was lower than 70(60PP*/40CA*)/30MH but higher than that of the other materials.

The PHRR was significantly lower for 60PP*/40CA* than that of PP (α=0.05). The presence of a shoulder appearing at 187 s represents a delay in HRR which may be due to potential char formation observed on the sample at the end of the experiment as shown in the digital photo of the samples after the CCT experiment (Figure 5.3).

The total burning time was shorter, t_{ign} occurred earlier, and PHRR was lower for 70PP*/30MH compared to PP, as shown in Table 5.4. The results indicate the significant effect of MH on the HRR, which could be attributed to the endothermic reaction of MH [5, 84]. Besides, the decomposition products of MH may play an essential role in diluting the combustible fragment in the gas phase of the flaming zone and reduce the degradation. The t_{tot} of 70(60PP*/40CA*)/30MH increased compared to all other materials; however, the t_{ign} occurred earlier, and the PHHR was the lowest. The PHRR was reached at the beginning, i.e., the highest value of HRR for the whole burning time, and its value was comparable to the average HRR, which was determined to be 304 kW·m^{-2}. There was no

sharp peak appearing after ignition, which indicates that there was a favorable synergistic effect between CA* and MH as shown in Figure 5.2.

Table 5.4: Energy characteristics of the combustion of PP materials in the cone calorimeter at 50 kW· m^{-2} heat flux (± standard error, n=3)

Material	t_{tot} (s)	PHRR (kW· m^{-2})	THR ($MJ{\cdot}m^{-2}$)	EHC ($MJ{\cdot}kg^{-1}$)	FIGRA (kW· m^{-2} · s^{-1})	FPI ($m^2{\cdot}s{\cdot}kW^{-1}$)
PP	426 (± 10)	1446 (± 44)	171 (± 5)	37.3	5.20	0.035
60PP*/40CA*	324 (± 9)	1236 (± 24)	158 (± 6)	28.6	4.54	0.025
70PP*/30MH	416 (± 10)	556 (± 4)	145 (± 3)	33.7	1.63	0.058
70(60PP*/40CA*)/30MH	593 (± 55)	304 (± 8)	118 (± 5)	25.3	3.30	0.129

The formation of char observed at the end of the experiment may explain this effect, as shown in Figure 5.3. The differences in char formed between 70PP*/30MH and 70(60PP*/40CA*) /30MH was in the mass, volume and surface of the char. The char of 70(60PP*/40CA*)/30MH has a smooth and continuous surface which means limited failure in the char structure occurred. Furthermore, these observations indicate that the degradation reaction of this material was less exothermic than for PP, 60PP*/40CA*, and 70PP*/30MH.

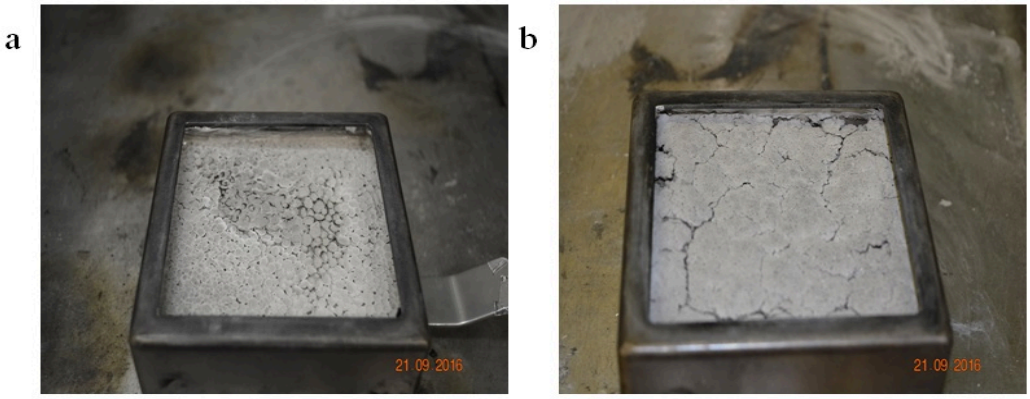

Figure 5.3: Material at the end of the cone calorimeter test a. 70PP*/30MH, b. 70(60PP*/40CA*/30MH

5.3.2.2 Total heat release (THR)

The THR, the area under the HRR versus time plot, depends strongly on the mass loss, the effective heat of combustion of the volatiles, and the combustion efficiency in the flame zone. Flame retardants can lower the fire hazards either by reducing the THR and/or by lowering the FIGRA. The THR of PP materials presented in Figure 5.4 (See Appendix B) indicates that CA*, MH, and combination of CA* and MH reduced THR significantly compared to pure PP. Figure 5.4 shows the THR with time for PP materials. The slope of the THR curve can be assumed as representative of fire spread [175]. The slope of PP curve was higher than that of other materials, which means that the flame spread for the PP sample was the highest, and the flame spread of 70(60PP*/40CA*)/30MH, was the lowest.

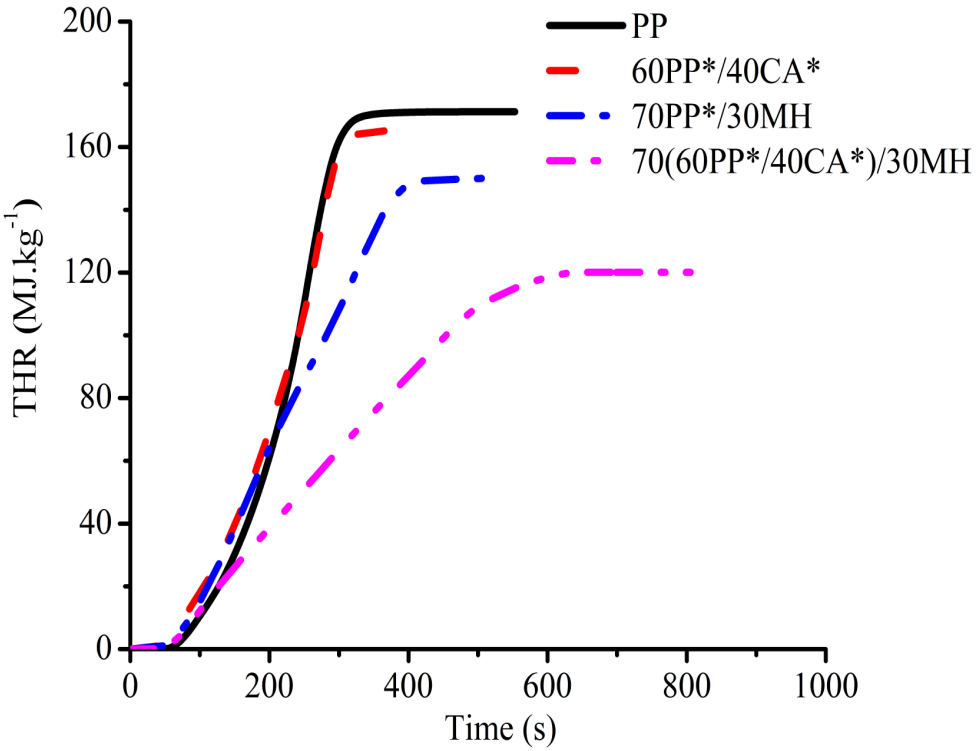

Figure 5.4: Evolution with time of THR of PP materials at 50 kW·m^{-2} heat flux during burning in the cone calorimeter test

5.3.2.3 Effective heat of combustion (EHC)

When chemical reactions occur, they are accompanied by the release or absorption of heat. The heat of combustion of a material is defined as the amount of heat released when a unit quantity of material is oxidized completely to yield stable end products. The EHC is defined as the ratio between HRR and rate of the mass loss, representing the amount of heat released by a unit amount of the material when it is burned [6, 178].

The EHC of PP materials (Table 5.4) was reduced when CA*, MH or combination of CA* and MH was present. The lowest EHC was observed for PP* containing CA* and MH. A low EHC is an indication of less exothermic reaction in the gas phase, suggesting better flame retardancy as reported previously for the material [179]. The reduction in EHC could also be an indication of less volatiles for gas phase combustion due to the presence of less combustible materials. The reported heat of combustion of pure cellulose acetate is 16 $MJ{\cdot}kg^{-1}$ [158], significantly lower than those observed in this study. The reduction of EHC was around 6% for 70PP*/30MH, 24% for 60PP*/40CA*, and 32% for 70(60PP*/40CA*)/30MH compared to PP.

Fire growth rate index (FIGRA) and fire performance index (FPI) are indices used to simplify the interpretation of the cone calorimeter data. These indices have been introduced to assess the hazard of developing fires, such as the fire growth rate (FIGRA) = PHRR/ time required to reach PHRR and the fire performance index (FPI)=t_{ign}/ PHRR [156]. FPI gives useful details about the degree of the fire hazard. Table 5.4 provides FIGRA indices for all materials. The FIGRA was the highest for PP, and the lowest was obtained for 70PP*/30MH. In contrast, the highest FPI was obtained for the 70(60PP*/40CA*)/30MH. These results imply that PP materials with CA* and MH has a significant improvement in the flammability resistance.

5.3.2.4 Mass loss

The total mass loss during combustion in the cone calorimeter at constant heat flux is presented in Figure 5.5. The mass loss curves are the mirror images of THRs curves (Figure 5.5). The mass loss rate for PP materials is lower than PP. After 400 s of combustion, there was no residue for PP and 60PP*/40CA* while 21 wt.% remained for 70PP*/30MH and 26 wt.% remained for 70(60PP*/40CA*)/30MH, reflecting the MH content. Materials that yield only a small amount of char experience a more significant mass loss than materials with high char yield [6].

The mass left at the end of the experiment was around 21 wt.% for 70PP*/30MH reflecting the non-organic content of MH. For 70(60PP*/40CA*)/30MH, the mass left was

26 wt.% which confirms that there was carbon left in the residue. The material balance of the MH decomposition and TGA analysis confirm that the residues contained carbon and inorganic materials reflecting the MH content.

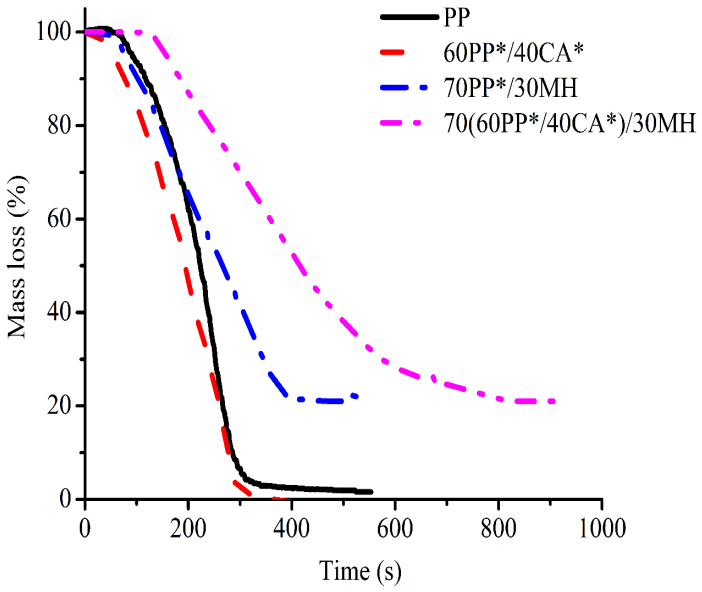

Figure 5.5: Evolution with time of the mass loss of PP materials at 50 kW· m^{-2} heat flux during the cone calorimeter test

5.3.2.5 CO, CO_2, and smoke production

One of the main fire safety concerns with polymer materials is the generation of dense smoke, which is complex and dynamic as it changes during the progress of the fire. Polymers with high thermal stability or which form a small amount of flammable fragments under comparable condition will produce negligible visible smoke. Increasing char formation is one way to minimize gas production when pyrolysis is reached [111]. Figure 5.6 shows the evolution of CO and CO_2 production with time for PP materials. Table 5.5 summarizes the results for the CO yield (COY) and CO_2 yield (CO_2Y) expressed as wt.%, and the specific extinction area (SEA).

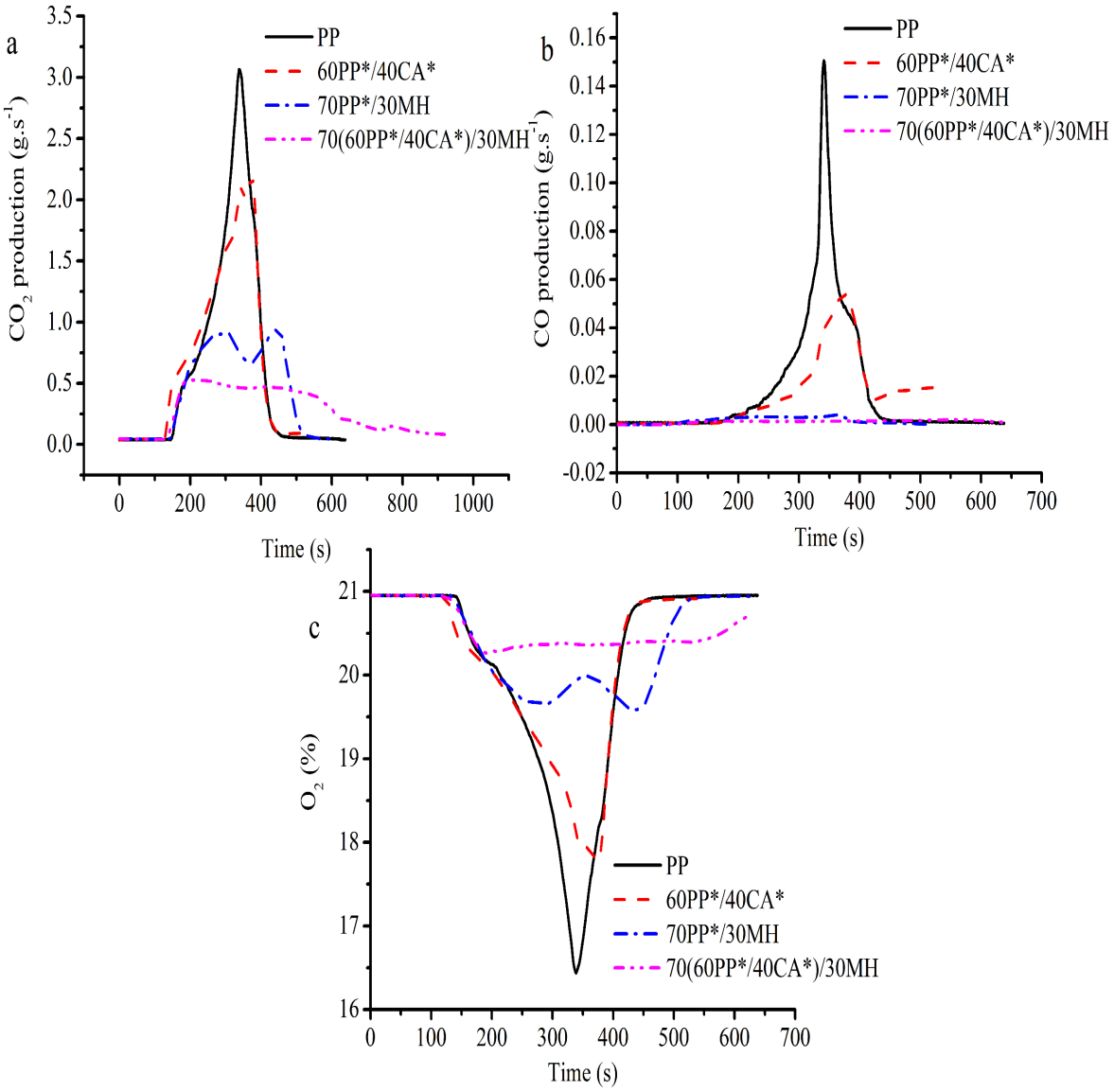

Figure 5.6: Evolution with time of CO_2 and CO production and O_2 consumption during the combustion of PP materials in the cone calorimeter. a.CO_2 production ($g{\cdot}s^{-1}$), b. CO production ($g{\cdot}s^{-1}$), and c. O_2 consumption (%)

According to the cone calorimeter results, the CO_2 production for 60PP*/40CA* and 70PP*/30MH was significantly lower than that of PP. There was no statistically significant differences between PP, 60PP*/40CA*, and 70PP*/30MH for both COY and CO_2Y. The COY and CO_2Y of 70(60PP*/40CA*)/30MH was statistically lower than of other PP materials (α=0.05). The lower COY and CO_2Y of the 70(60PP*/40CA*)/30MH could be attributed to the enhancement of the char formed, which hinders the penetration of O_2 to the layer beneath the burning surface and reduces the heat transfer from the flaming zone.

Smoke development was expressed as average specific extinction area SEA_{avg}, which is the smoke obscuration area per mass of sample decomposed [105]. The SEA_{peak} represents the worst case scenario for fires (Table 5.5). The SEA_{avg} for 70(60PP*/40CA*)/30MH was significantly lower than that for PP. The SEA_{peak} value was the lowest for 60PP*/40CA* than those of other PP materials. The 70PP*/30MH and 70(60PP*/40CA*)/30MH showed no significant difference compared with PP.

Table 5.5: Characteristics of the combustion products in the cone calorimeter at 50 $kW \cdot m^{-2}$ heat flux (± standard error, n=3)

Material	COY ($kg \cdot kg^{-1}$)	CO_2Y ($kg \cdot kg^{-1}$)	CO/CO_2	SEA_{peak} ($m^2 \cdot kg^{-1}$)	SEA_{avg} ($m^2 \cdot kg^{-1}$)	TSP (m^2)	TSR ($m^2 \cdot m^{-2}$)
PP	0.0336 (± 0.003)	2.50 (± 0.01)	0.0134	4807 (± 57)	379 (± 4)	15.8 (± 0.4)	1794 (± 52)
60PP*/40CA*	0.0246 (± 0.000)	2.12 (± 0.01)	0.0116	3249 (± 85)	255 (± 0.01)	12.5 (± 0.17)	1410 (± 19)
70PP*/30MH	0.0235 (± 0.004)	2.17 (± 0.00)	0.0108	4193 (± 599)	434 (± 9.12)	16.7 (± 0.34)	1893 (± 39)
70(60PP*/40CA*)/30MH	0.0167 (± 0.000)	1.85 (± 0.02)	0.0110	4590 (± 202)	347 (± 12)	14.5 (± 1)	1642 (± 123)

According to Figure 5.6c, the O_2 consumption was very low during the combustion of the 70(60PP*/40CA*)/30MH composite. Therefore, it can be concluded that the material did not experience severe thermo-oxidative degradation.

5.3.3 Heat of combustion and combustion efficiency

The heat of combustion (HC) can assist in understanding the flammability of materials [180]. The lower the heat of combustion, the lower the heat released during the actual combustion. The heat of combustion can be used to estimate the heat release rate of

materials which is defined as the mass loss rate times its heat of combustion [6]. The combustion efficiency can be affected by soot and CO formation and can be estimated from the carbon balance between the fuel and combustion products [181].

The heat of combustion estimated by bomb calorimetry and presented in Figure 5.6 indicates that PP possesses the highest heat of combustion (44.8 $kJ \cdot g^{-1}$). The addition of 20% and 30% MH to PP significantly lowered HC (statistically different according to the t-test (α=0.05)).

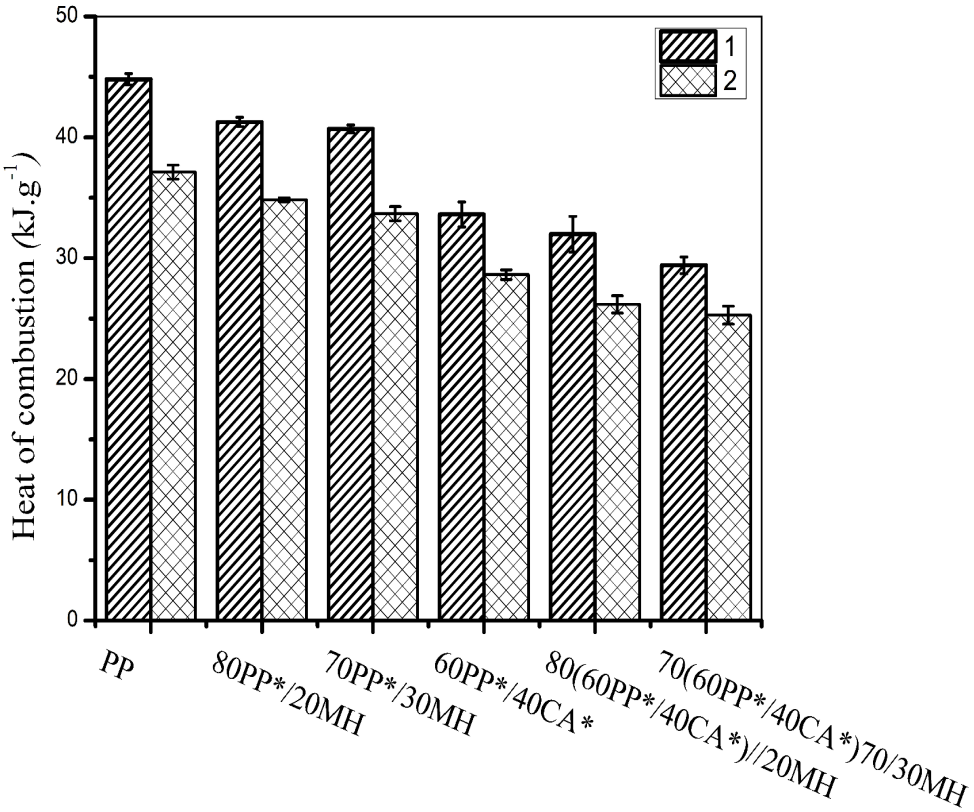

Figure 5.7: Effect of the MH content on the heat of combustion of PP materials according to the estimation method. 1.bomb calorimeter 2. cone calorimeter (± standard error, n=3)

The HC estimated with the bomb calorimeter and cone calorimetry were different (Figure 5.7). These differences could be attributed to the complete and incomplete combustion of the materials. In the bomb calorimeter, there is an excess of oxygen; thus, complete combustion occurs. In the cone calorimeter, test is done under air; thus, incomplete combustion occurs. In many fire experiments and real fires, the oxygen supply is limited, incomplete combustion will occur, and the formation of partially oxidized products will result [182]. The product of incomplete combustion, CO, can be related to the heat release rate and will be present only in cone calorimeter experiments. When there is an increase in COY, there should be an increase with heat release rate [183]. According to the cone calorimeter and the bomb calorimeter experiments, the amount of heat released reduced when the COY was reduced as shown in Figure 5.8.

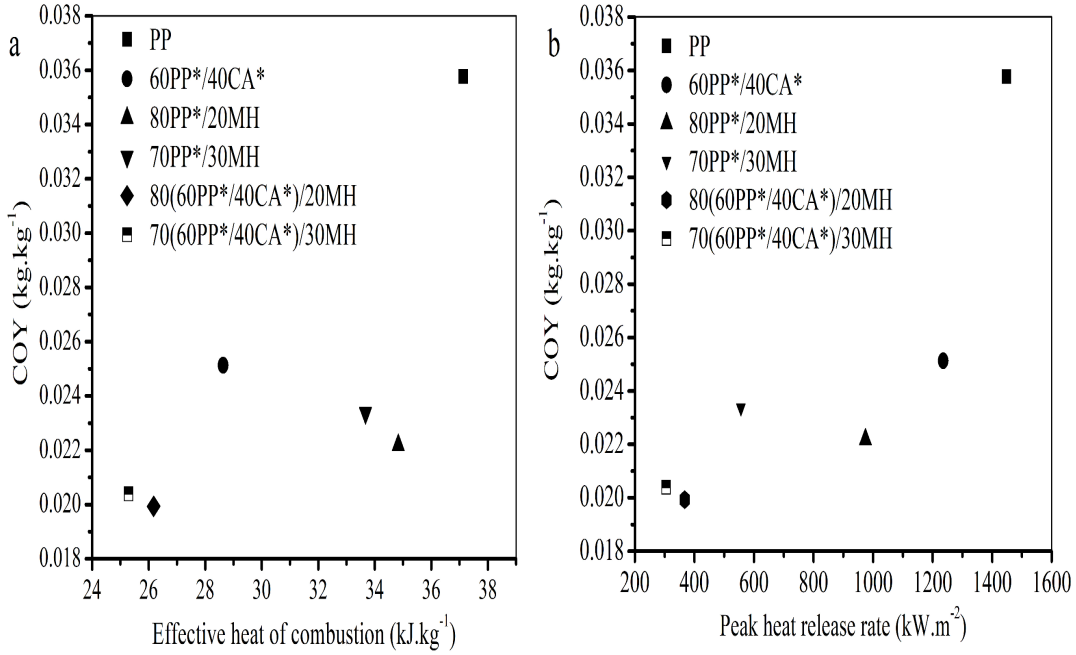

Figure 5.8: COY against effective heat of combustion (EHC) (a) and peak heat release rate (PHRR) (b) (± standard error, n=3)

The closure of the material balance for carbon during combustion was investigated by normalizing the CO, CO_2, and the soot production according to the total carbon available determined from the chemical composition of the materials. The calculation is based on

the COY and CO_2Y estimates obtained with the cone calorimeter. The calculation of the availability of carbon is presented in Appendix B. The availability of carbon in the CO, CO_2 and the soot production according to material balance (Figure 5.9), indicate higher soot and lower CO_2 and CO yield with increasing MH levels. The increase of soot could be due to the materials experiencing less oxidative thermal decomposition, i.e., lower conversion of carbon to CO and CO_2. The result shows that 60PP*/40CA* had a higher yield of soot and lower yield of CO_2 and CO than that of PP. The soot yield increases with the presence of MH in PP materials. Haiqing et al. reported a relation between the soot and CO yield, and the combustion efficiency [181]. According to the results obtained, PP materials showed better flame retardancy with increasing soot and residue yields, especially for 70(60PP*/40CA*)/30MH.

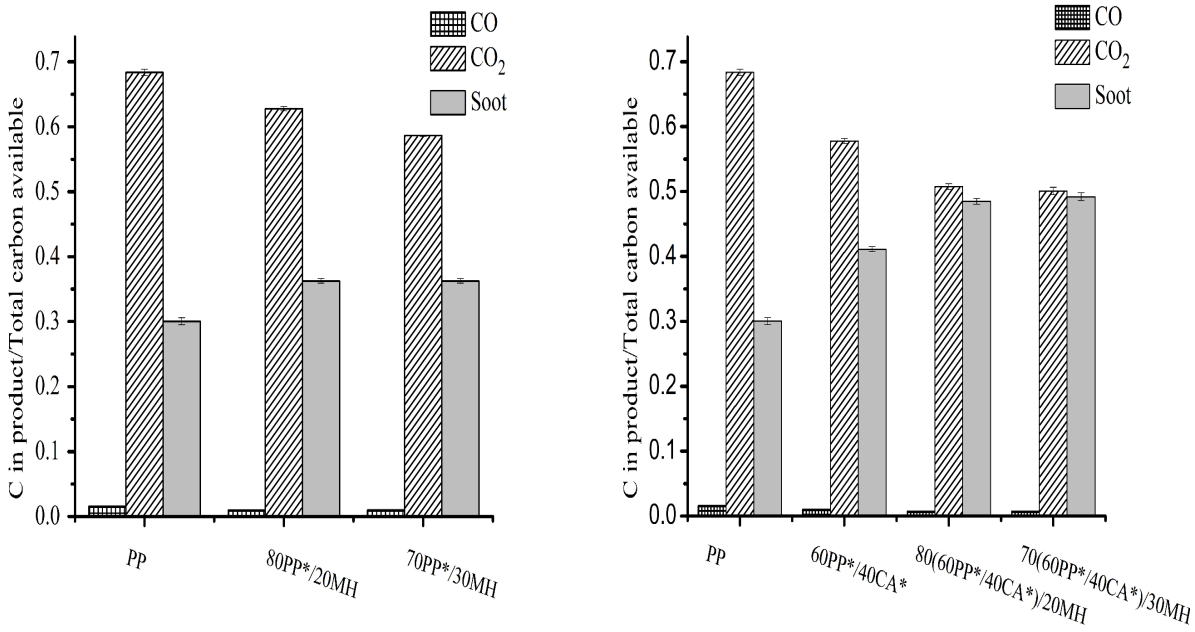

Figure 5.9: Cone calorimeter carbon ratio in terms of CO_2, CO, and soot production for PP materials with different levels of MH. (± standard error, n=3). a. PP*/MH materials, b. PP*/CA*/MH materials

5.4 Conclusion

The effect of plasticized cellulose acetate (CA*) and magnesium hydroxide (MH) on the flammability of PP materials was investigated.

The oxygen index test (OI) of 70(60PP*/40CA*)/30MH was higher than that of PP and 60PP*/40CA* by 29% and 17%, respectively. Vertical burning test evaluation showed that the 70(60PP*/40CA*)/30MH material was categorized as V-0, which means the flame could not be sustained for a specific period of time while 60PP*/40CA*, 70PP*/30MH, and PP could not be ranked.

The flame retardant characteristics of the (PP*/40CA*) with MH was significantly improved compared with that of 60PP*/40CA*, 70PP*/ 30MH, and PP according to the cone calorimeter test. The peak of heat release rate (PHRR) of 70(60PP*/40CA*)/30MH was 80% lower than that of PP and approximately 50 % lower than that of 70PP*/30H. The total heat release (THR) and the effective heat of combustion (EHC) determined were reduced significantly for 70(60PP*/40CA*)/30MH compared to 60PP*/40CA*, 70PP*/30MH and PP by around 30%. The COY results show that there were no significant differences between PP and all other PP materials. The CO_2Y for PP, 60PP*/40CA*, 70PP*/30MH, and 70(60PP*/40CA*)/30MH was significantly reduced by 16%, 12%, and 40% respectively compared to that of PP.

The heat of combustion (HC) calculated by the adiabatic bomb calorimetry was in good agreement with that of the cone calorimeter with 70(60PP*/40CA*)/30MH material being less exothermic than the other PP materials.

Based on the mass left at the end of cone calorimeter test and the carbon availability in the products of the combustion, materials which have a higher soot and residue showed better flame retardancy. According to the results of the aforementioned calculations, the 70(60PP*/40CA*)/30MH material had a higher char and little soot.

Chapter 6

Non-isothermal Crystallization Study of Plasticized Cellulose Acetate Magnesium Hydroxide Polypropylene Materials

The crystallization behavior of polypropylene (PP), polypropylene-grafted-maleic anhydried (PPMA), plasticized cellulose acetate (CA*), magnesium hydroxide (MH) materials prepared by melt compounding was analyzed using differential scanning calorimetry (DSC). Non-isothermal experiments were used to evaluate the influence of PPMA, CA*, and MH on the crystallization process of the PP matrix. The relative crystallinity development with time and temperature was also analyzed. The Avrami model was used to estimate the kinetic parameters under non-isothermal conditions. The crystallization was also observed by polarized light microscopy. The nucleation activity was estimated and the results show that CA* and MH modified the crystallization behavior by affecting the nucleation mechanism, and the crystallization temperature.

6.1 Introduction

Polypropylene (PP) is one of the most common thermoplastics used in industrial applications because of the good mechanical properties, ease of processing, and low price. However, PP has drawbacks when used as an engineering material due to its poor flame retardancy

and sensitivity to heat, light, and oxidation which restrict its wider utilization. The mechanical and thermal properties of semi-crystalline polymers, such as PP, are strongly dependent on the crystalline structure [184]. Melting and crystallization studies can provide significant information about the processing conditions and properties of the end products [185]. Isothermal conditions are rarely met during processing such as extrusion and injection molding, so it is desirable to study the crystallization under non-isothermal conditions [186, 187]. The mechanical and thermal properties of PP are affected by a number of factors, including the degree of crystallinity, size and number of spherulites. PP can crystallize in three polymorphic forms namely α, β, and γ depending on the thermal and mechanical treatments [188]. The most common crystalline form of PP is mono-clinic α-PP. The α form of PP is thermodynamically stable. The β form of PP exists in a thermodynamically metastable state but can form under specific conditions, such as large temperature gradient, intense shear stress, and the presence of nucleating agents [185]. The γ form (orthorhombic) is only observed in low molecular weight or stereoblock fractions that are crystallized at elevated pressures [189, 190]. The β form of PP has higher impact strength and excellent ductility and thermal properties compared to the α form of PP; thus, it attracts many researchers attention [191, 192]. The heat distortion of the β form is higher than α form. Due to the lower chain mobility of the amorphous phase and the lower diffusion and solubility, the β form of PP exhibits higher oxidation stability than the α form of PP [193].

The most common avenues to achieve a suitable flame retardant material involve the incorporation of substances that can interfere in the combustion stage of the process. Magnesium hydroxide (MH) is a halogen-free flame retardant used for improving the flame retardancy of material [194]. An adequate level of flame retardancy can be achieved with high MH content which affects the mechanical properties [195, 196]. Due to the effect of MH, there is a need for developing PP materials with lower MH level that can maintain the integrity of the mechanical properties of the PP materials.

The crystallization behavior of PP/MH materials has been investigated. Cook and Harper (1998) studied the crystallization behavior of PP materials filled with two kinds of morphology for MH. They state that MH acts as a heterogeneous nucleant for PP [197]. Other studies reported that MH also acts as a nucleating agent and adding MH leads to a decrease in the crystallization temperature of 5-10 ^{o}C [3, 198]. It has been found that the crystallization temperature (T_p) is shifted toward higher temperatures, and further increase of MH content affects T_p slightly. According to Amash (1998), cellulose could act as an effective nucleating agent for the crystallization of PP and consequently increase the crystallization growth rate during cooling from the molten state [199]. Cellulosic materials such as wood and cotton can also induce trans crystallinity in a PP matrix [200, 201]. The

trans crystallinity morphology is characterized by high density of nucleating crystallites which grow perpendicular to the surface responsible for the nucleation [202].

The oxidative degradation of PP is affected by its microstructure such as stereoregularity, molecular weight, crystallinity, spherulite size, and molecular orientation [85]. When the degree of crystallinity increased, the oxygen could be restricted and result in slow-down of the oxidation process [191]. Other studies reported that the increase in the spherulite size could be another reason for the improvement of oxidative stability as a result of decreasing the crystal interface [86, 87]. It was observed that the insertion of foreign substances such as fillers, which can be organic or inorganic, can increase the crystallization rate and act as heterogeneous nucleating agent [193]. The inclusion of the aforementioned organic or inorganic material could also induce the β form in the PP matrix [203, 204].

Non-isothermal conditions were selected in this study for two reasons. First, processing, such as extrusion and injection molding, occurs under dynamic, non- isothermal conditions [184]. Second, performing isothermal crystallization for PP is very difficult because of its very fast crystallization and very high activation energy. Rapid equilibrium at the test temperature is more important to the quality of the isothermal crystallization data than rapid cooling. To overcome this temperature control challenge, differential scanning calorimetry (DSC) with a cooling rate up to 125 $^{o}C{\cdot}min^{-1}$ is required to reach isothermal temperature within 20 seconds [205].

This study aimed to evaluate the effect of plasticized cellulose acetate (CA*) and magnesium hydroxide (MH) on the crystallization kinetic behavior of PP materials prepared by melt compounding. Additionally, the nucleation effect of PPMA, CA* and MH on the PP matrix was investigated by conducting non-isothermal crystallization kinetics studies with DSC experiments.

6.2 Experimental methods

6.2.1 Materials

Polypropylene (PP) fine powder (HM20/70P), was purchased from GOONVEAN Fibres Company, United Kingdom. Magnesium hydroxide (MH), Cellulose acetate (CA) (approx. 50000 $g{\cdot}mol^{-1}$), 39% acetyl), triethyl citrate (TEC), and polypropylene-grafted maleic anhydride (PPMA) were purchased from Sigma-Aldrich (USA). All materials were used as received.

6.2.2 Materials preparation

Cellulose acetate (CA) was plasticized according to the methodology presented in Chapter 3. The twin-screw extruder (SJSZ-7A, Wuhan Ruiming Plastic Machinery Company, China) was used for the extrusion of the polypropylene materials with four temperature zones ranging from 160 °C-180 °C, with a residence time of 5 minutes. PPMA was used in the fabrication of PP materials with loading of 3 wt.% as a replacement portion of PP. Table 6.1 lists the composition and the code of the materials. The extruded materials were then cut as pellets by using a cutter (SZS-20, Wuhan Ruiming Plastic Machinery, China).

Table 6.1: Sample composition and coding of PP materials

Material	PP wt.%	CA* wt.%	MH wt.%	PPMA wt.%
PP	100	0	0	0
PP*	97	0	0	3
60PP*/40CA*	58.2	40	0	1.8
70PP*/30MH	67.9	0	30	2.1
70(60PP*/40CA*)/30MH	40.74	28	30	1.26

PP* refers to 97PP /3PPMA.

CA* refers to plasticized cellulose acetate with triethyl citrate.

6.2.3 Differential scanning calorimetry (DSC)

The crystallization kinetics of PP materials was investigated with a Q2000 TA instrument (USA) calibrated by indium and sapphire disk standards, using standard T-zero. Nitrogen with a 50 ml·min^{-1} flowrate was used as purge gas. Samples of approximately 5-6 mg of the extruded materials as pellets were placed in an aluminum pan. The samples first were heated from room temperature to 200 °C at a heating rate of 10 °C·min^{-1}, and then maintained at this temperature for 5 minutes to remove previous thermal history. The samples were then cooled to 25 °C at different cooling rates (-5, -10, -20, and -30 °C·min^{-1}). The heat flow was recorded as a function of temperature and time.

Based on the data obtained from DSC at different cooling rates,the relative crystallinity as a function of temperature (X_T) is given as follows:

$$X_T = \int_{T_o}^{T} (dH_c/dT)dT / \int_{T_o}^{T_\infty} (dH_c/dT)dT \tag{6.1}$$

where dH_c/dT denotes the rate of heat flow, T_o and T_∞ represent the temperature at the onset and the end of the crystallization process, respectively.

Figure 6.1 illustrates the relative crystallinity estimation. The area under the peak, denoted by X_T or X_t, was estimated by employing the DSC data and the trapezoidal rule in Matlab to estimate the crystallinity fraction at specific temperature or time (See Appendix C for more details).

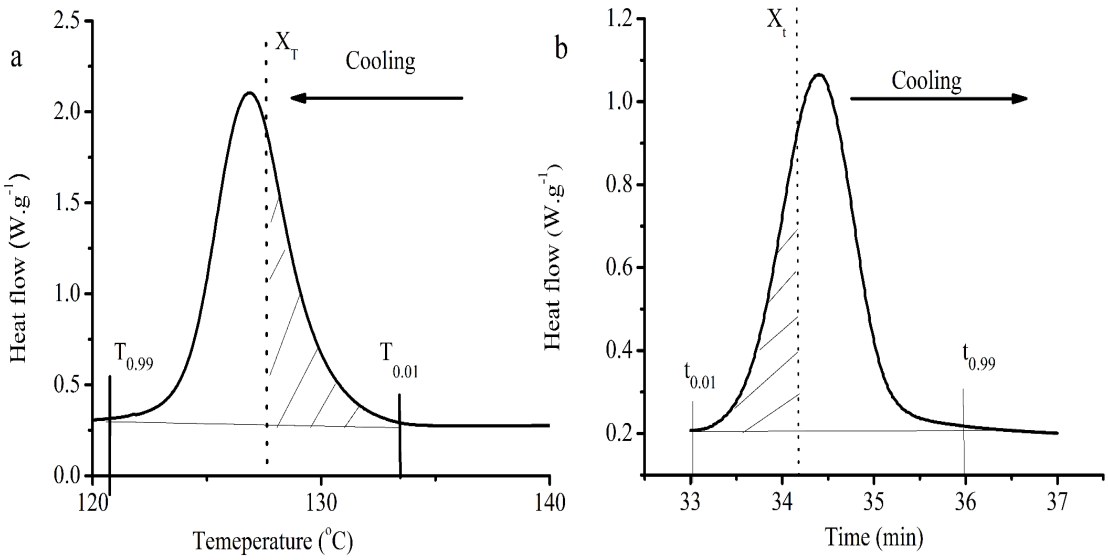

Figure 6.1: Example illustrating the estimation of the relative crystallinity during non-isothermal crystallization of PP. a.Temperature, b.Time

Characteristics of the relative crystallinity profile were obtained by relating time to temperature with following equations [206]:

$$t = \frac{(T_o - T)}{\beta^*} \tag{6.2}$$

where t is the time, T_o is the initial temperature, T is the temperature at time t, and β^* is the cooling rate.

6.2.4 Polarized light optical microscopy

The crystallization morphology of the PP materials was investigated by polarized light optical microscopy (Nikon, Eclipse MA200) with an automatic thermal control hot stage. It was used to study the spherulite structure of the PP materials. A small sample (1 g) of the extruded materials as pellets was sandwiched between two glass slides, melted at 200 °C for 10 minutes and then rapidly cooled by putting the sandwiched slides on the microscope stage. During cooling, the crystal morphology was recorded with the digital camera of the microscope.

6.3 Results and discussion

6.3.1 Non-isothermal crystallization behavior

DSC thermograms at different cooling rates are shown in Figure 6.2. The profile of the thermogram was different according to the cooling rate and composition of the material. The temperature at the maximum rate of crystallization (T_p) shifted to lower temperatures, and the peak became wider. This may reflect the higher supercooling that can occur at high cooling rates [207]. At a lower cooling rate, there is enough time for polymer chains to transfer from melt to the surface of a growing crystal, so that crystallization can occur at higher temperature [192]. The higher T_p for low cooling rates indicates that the crystallization initiated at an early stage.

The T_p of the PP materials as a function of cooling rate (β^*) is presented in Figure 6.3. The DSC thermogram of 60PP*/40CA* shows that the inclusion of CA* induced the β form with low intensity, as shown in Figure 6.2 c, e.

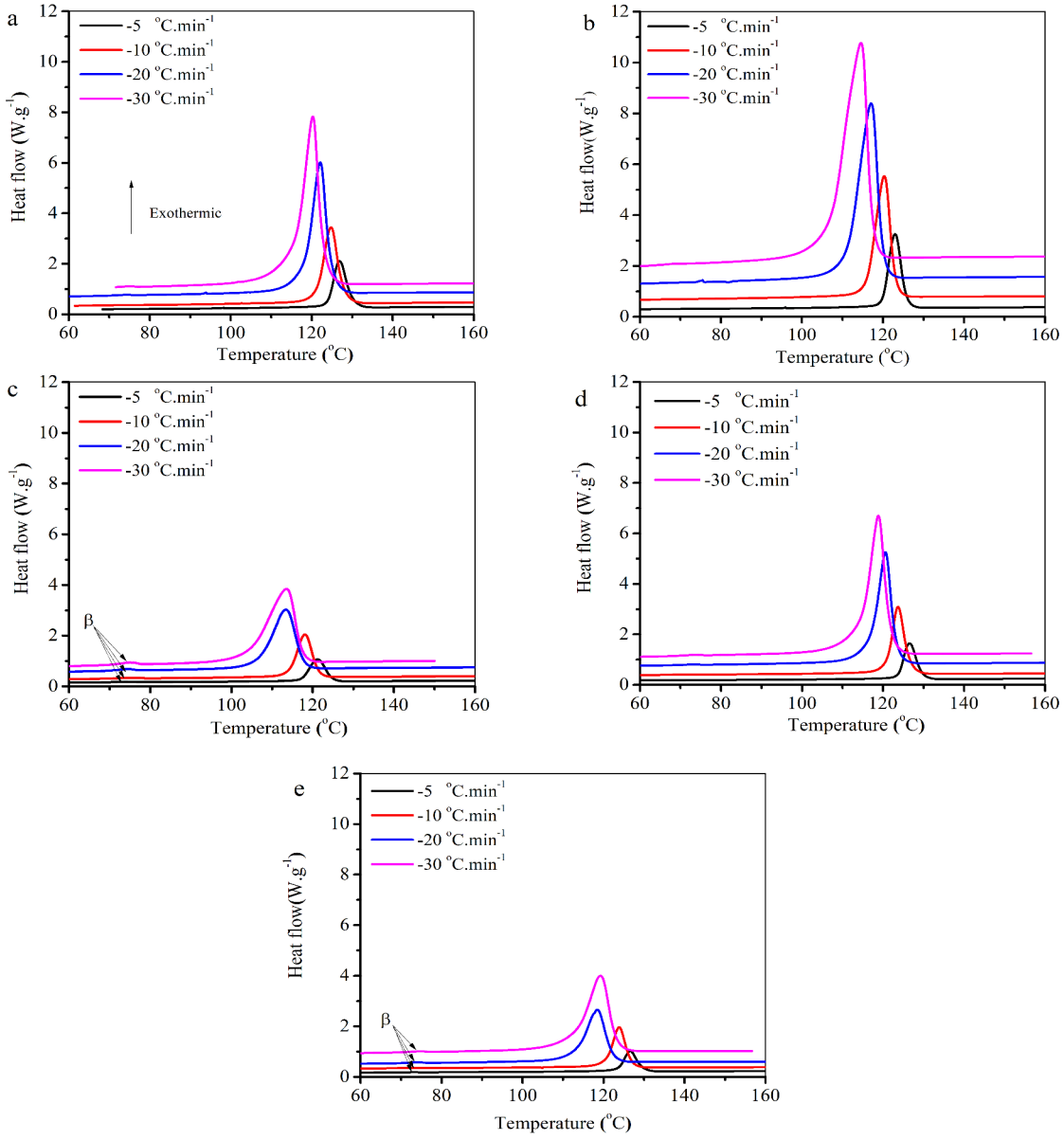

Figure 6.2: DSC thermograms of non-isothermal crystallization of PP materials. a. PP, b. PP*, c. 60PP*/40CA*, d. 70PP*/30MH, and e. 70(60PP*/40CA*)/30MH

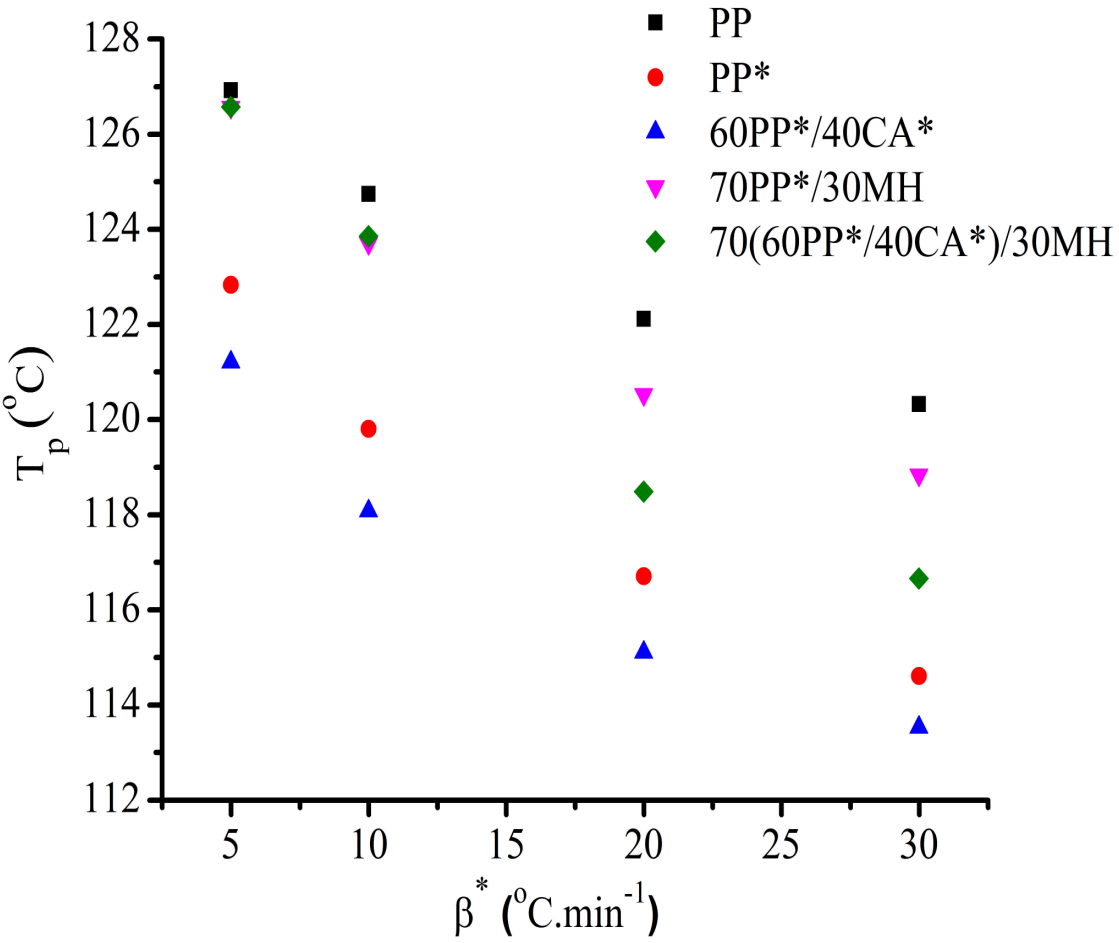

Figure 6.3: Crystallization peak temperature (T_p) of PP materials as a function of cooling rate (β^*)

6.3.2 Development of relative crystallinity

The evolution of the relative crystallinity X_t as a function of temperature and time at all cooling rates is shown in Figure 6.4 and Figure 6.5. The characteristics of the relative crystallinity profiles are illustrated in Figure 6.6 a and Figure 6.6 b and are summarized in Table 6.2.

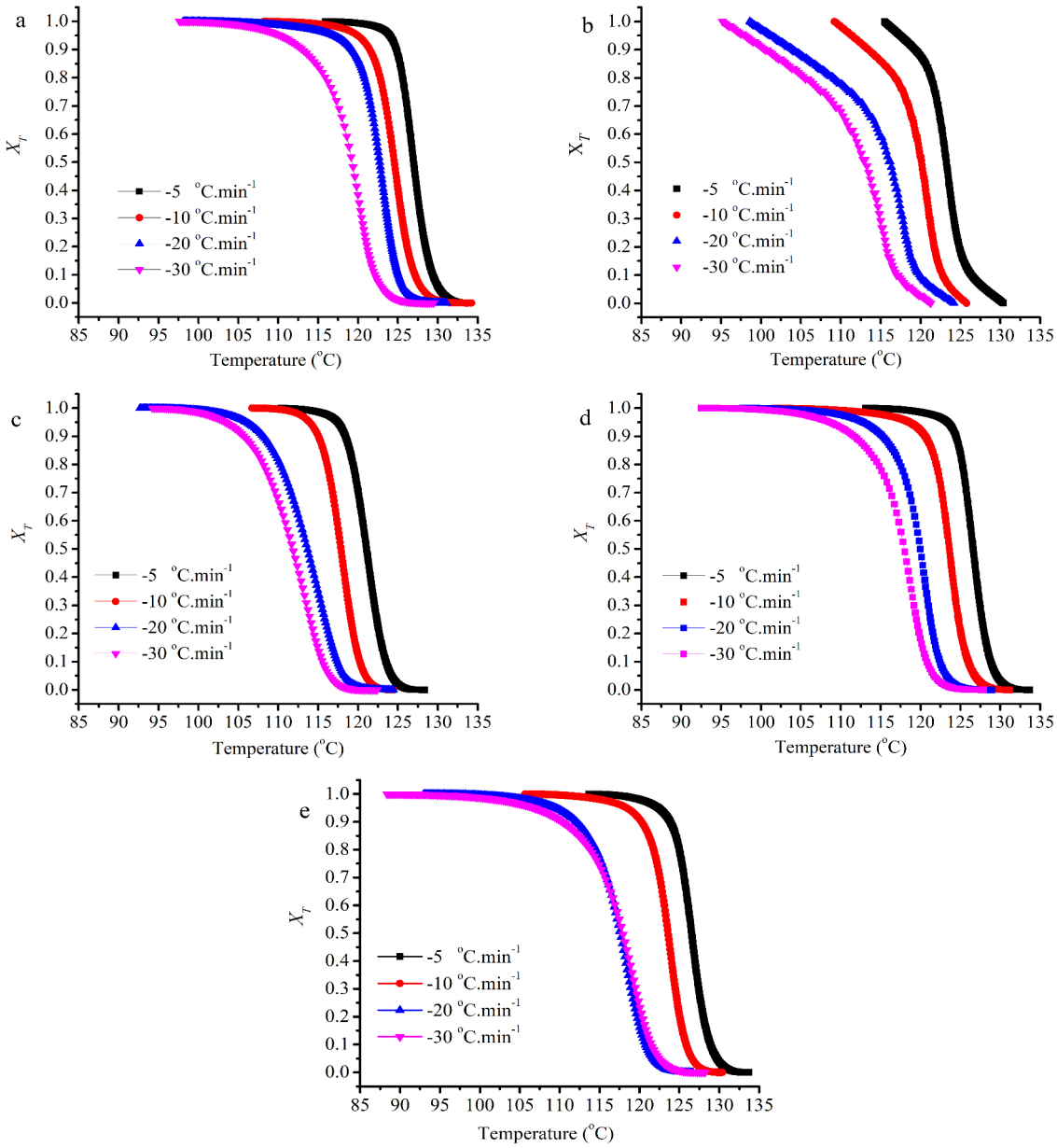

Figure 6.4: Development of relative crystallinity X_t according to temperature and cooling rate. a. PP, b. PP*, c. 60PP*/40CA*, d. 70PP*/30MH, and e. 70(60PP*/40CA*)/30MH

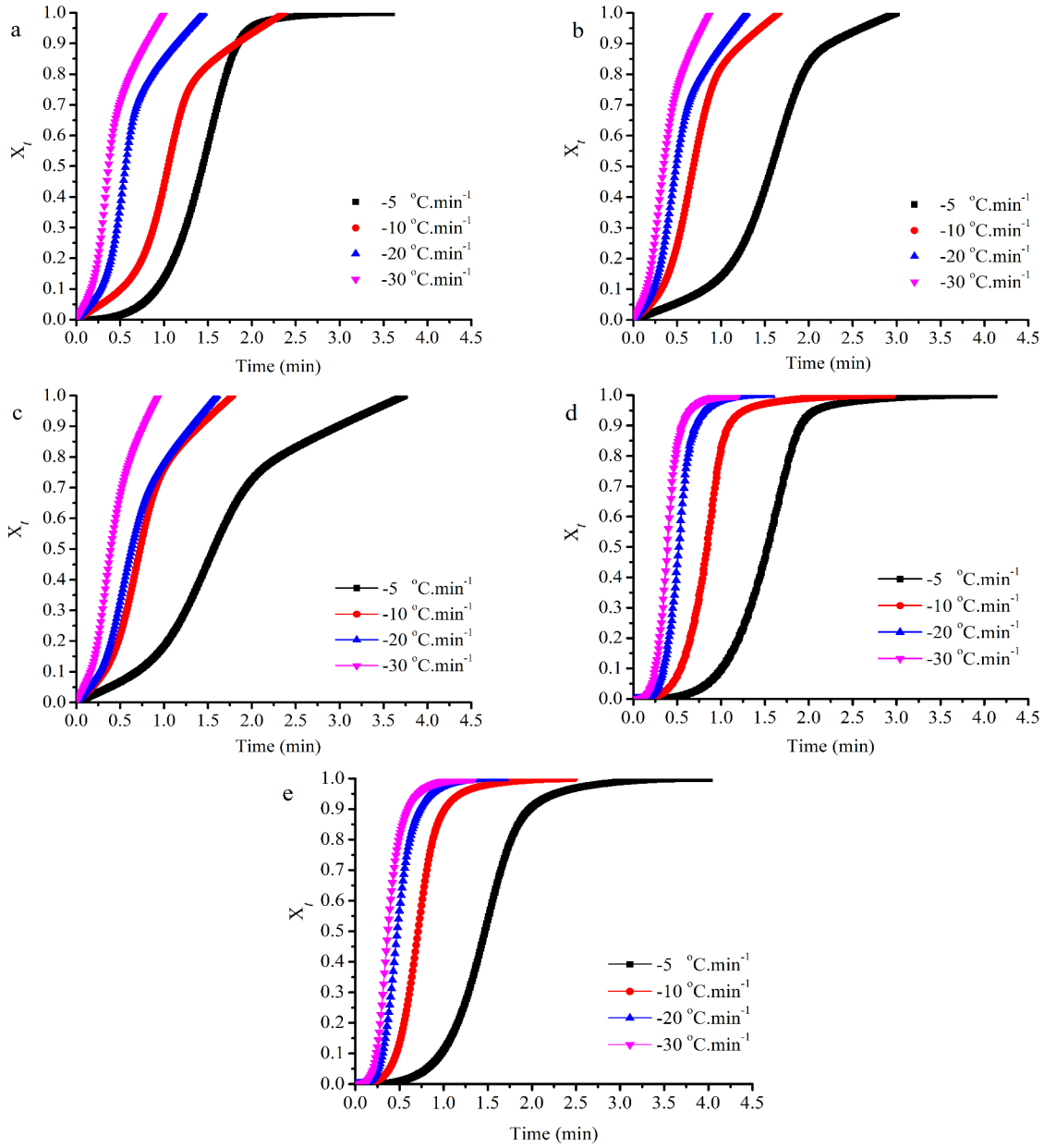

Figure 6.5: Development of the relative crystallinity according to time and cooling rates. a. PP, b. PP*, c. 60PP*/40CA*, d. 70PP*/30MH, and e. 70(60PP*/40CA*)/30MH

The shorter time is required for completing the crystallization as the cooling rate increased. The crystallization half-time ($t_{1/2}$) defined as the time required to reach 50% relative crystallinity [208], commonly used to describe the crystallization rate of polymers, is presented in Table 6.2. The higher the crystallization half-time, the smaller the crystallization rate,i.e., slow crystallization process. The $t_{1/2}$ decreased with increasing cooling rates for all PP materials. The $t_{1/2}$ for PP was lower than that for PP*, 60PP*/40CA*, 70PP*/30MH, and 70(60PP*/40CA*)/30MH at 5 °C·min^{-1}. On the other hand, $t_{1/2}$ of PP was higher than all other PP materials at 10 °C·min^{-1}. The $t_{1/2}$ for PP* was higher than PP at 5 °C·min^{-1} cooling rate and lower than that of PP at 10 °C·min^{-1}. For the other cooling rates, the $t_{1/2}$ was almost similar. The $t_{1/2}$ for 60PP*/40CA* (0.63 min) was higher than PP (0.5 min) at 20 °C·min^{-1}, while $t_{1/2}$ for 70PP*/30MH and 70(60PP*/40CA*)/30MH was very close to PP under the same cooling rate. At 30 °C·min^{-1} cooling rate, there were no significant differences for $t_{1/2}$ of all PP materials compared to PP.

The $T_{0.01}$ and $T_{0.99}$ decreased with increasing cooling rate. The time at 1% relative crystallinity ($t_{0.01}$) and the time at 99% relative crystallinity ($t_{0.99}$) obtained from the DSC thermograms (Figure 6.5), are explained in Figure 6.6b.

DSC curves were used to estimate the apparent crystallization time (Δt_c) defined according to Equation 6.3:

$$\Delta t_c = t_{0.01} - t_{0.99} \tag{6.3}$$

The apparent incubation period (Δt_{inc}) is defined as the time that a sample spends from the temperature at which it is brought from the initial temperature (200 °C in our experiment) to the onset temperature ($T_{0.01}$). The parameter Δt_{inc} was estimated as follows:

$$\Delta t_{inc} = \frac{200 - T_{0.01}}{\beta^*} \tag{6.4}$$

The apparent total crystallization time was calculated according to Equation 6.5:

$$t_{total} = \Delta t_{inc} + \Delta t_c \tag{6.5}$$

The Δt_c and Δt_{inc} (Table 6.2) for PP was higher than all other PP materials at all cooling rates, while the shortest was estimated for 70(60PP*/40CA*)/30MH material. The t_{total} of the PP materials has the following order: PP >PP*> 60PP*/40CA*> 70PP*/30MH> 70(60PP*/40CA*)/30MH.

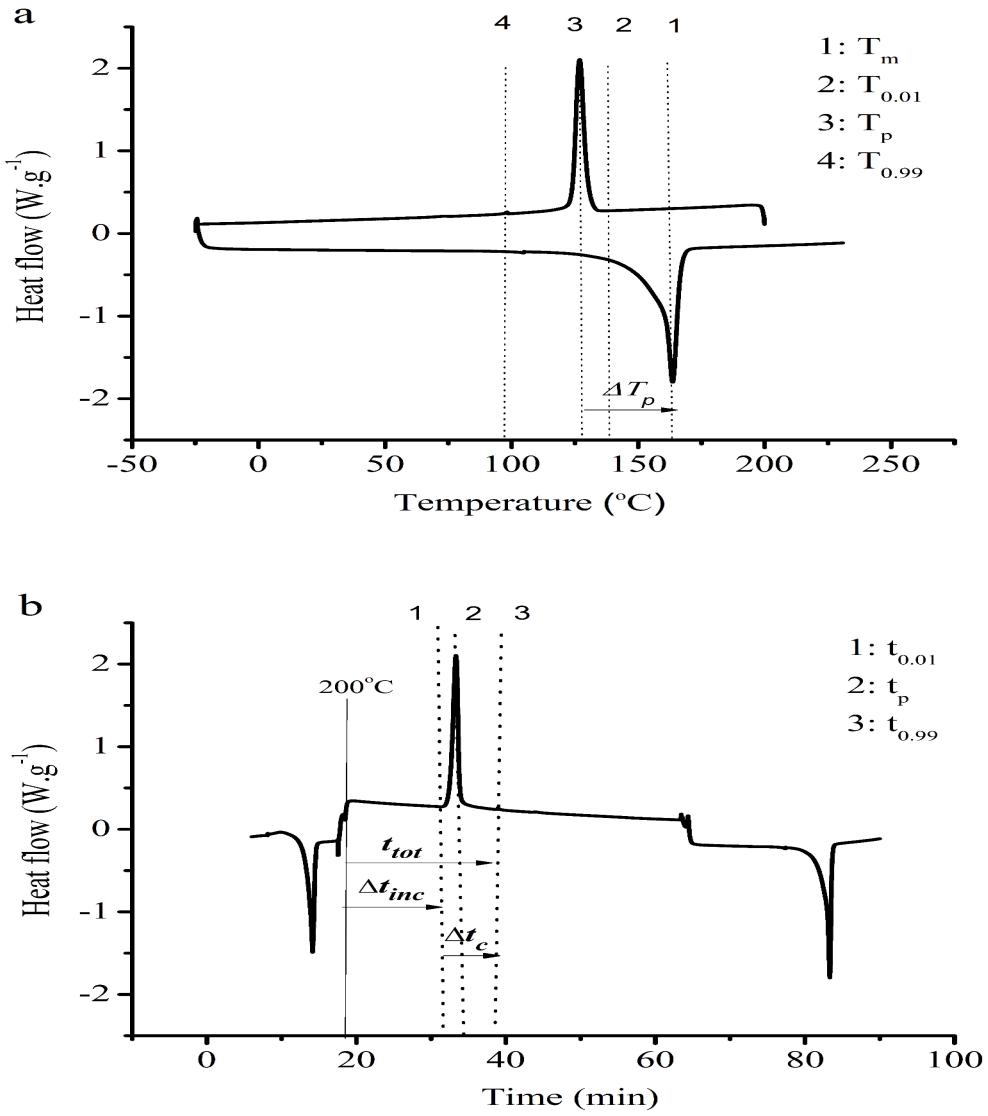

Figure 6.6: Example illustrating the analysis of the DSC thermograms according to a. Temperature, b. Time

Table 6.2: Characteristics of DSC thermograms for the non-isothermal crystallization of PP materials

Material	Cooling rate (°C·min^{-1})	$t_{1/2}$ (min)	$T_{(0.01)}$ (°C)	$T_{(0.99)}$ (°C)	Δt_c (min)	Δt_{inc} (min)	t_{total} (min)
PP	-5	1.44	131	121	2.1	13.7	15.8
	-10	1.05	129	115	1.4	7.0	8.4
	-20	0.50	127	108	0.9	3.6	4.6
	-30	0.30	122	104	0.6	2.6	3.2
PP*	-5	1.60	134	106	5.4	13.1	18.6
	-10	0.68	133	88	4.5	6.6	11.1
	-20	0.50	125	84	2.0	3.7	5.7
	-30	0.34	123	95	0.9	2.5	3.5
60PP*/40CA*	-5	1.57	125	114	2.2	14.9	17.1
	-10	0.73	122	111	1.0	7.8	8.9
	-20	0.63	120	102	0.9	4.0	4.9
	-30	0.39	118	99	0.6	2.7	3.4
70PP*/30MH	-5	1.48	131	119	2.4	13.8	16.2
	-10	0.80	128	111	1.7	7.2	8.9
	-20	0.49	125	106	0.9	3.7	4.7
	-30	0.37	123	101	0.7	2.6	3.3
70(60PP*/40CA*)/30MH	-5	1.47	131	118	2.5	13.8	16.3
	-10	0.71	128	112	1.5	7.2	8.7
	-20	0.48	124	103	1.0	3.8	4.9
	-30	0.37	123	98	0.8	2.6	3.4

PP* refers to 97PP /3PPMA.

CA* refers to plasticized cellulose acetate with triethyl citrate.

6.3.3 Theoretical approach-Avrami model

The most frequently used method for the analysis of non-isothermal crystallization is based on the Ozawa method [184]. However, the Ozawa method has not been appropriately described for the non-isothermal crystallization of PP. The Avrami model will be used to analyze the non-isothermal crystallization growth of PP materials [209, 210].

$$1 - X_t = exp\left(-Z_t t^n\right) \tag{6.6}$$

where X_t is the relative degree of crystallinity, Z_t is the rate constant containing both nucleation and growth rate information, n is the Avrami exponent and t is time.

Equation 6.6 was re-arranged by taking double logarithm to give Equation 6.7:

$$\ln [-\ln (1-X_t)] = \ln Z_t + n \ln (t) \tag{6.7}$$

The relative crystallinity was plotted according to Equation 6.7 and is illustrated in Figure 6.7 for all materials and cooling rates. Each curve contains two regions: an initial linear portion, primary crystallization stage, followed by the second linear portion which represents the secondary crystallization stage with a different slope. The total crystallization rate of this process is determined by both the rate of nucleation and the rate of crystal growth [206]. The linear portion of each cooling rate for PP materials are nearly parallel suggesting that the nucleation mechanism and crystal growth geometry are similar for the primary and secondary crystallization processes at all cooling rates. The Avrami exponent (n) and the rate parameter (Z_t) were estimated from the slope and intercept of each linear region. Table 6.3 summarizes the estimated n values for region 1 and region 2. The Avrami exponent, related to the nucleation mechanism (simultaneous or sporadic) and the dimensionality of the crystal growth (two or three dimensional), usually has a value between 2 and 4 for polymer crystallization. Large value of the Avrami exponent is indicative of sporadic (or combination of sporadic and simultaneous) nucleation with three-dimensional spherulite growth while a small value is attributed to instantaneous (accompanied with some sporadic) nucleation with two-dimensional growth [211]. For PP* and 60PP*/40CA*, n_1 was around 1 for the primary stage, which means that in this stage nucleation is more instantaneous with two-dimensional growth. For the second stage, n_2 was around 3, an indication of sporadic nucleation and three-dimensional crystal growth. For 70PP*/30MH and 70(60PP*/40CA*)/30MH, n_1 was approximately 3 at the beginning of the crystallization (first stage), which is consistent with heterogeneous nucleation and three-dimensional crystal growth. In the second stage, n_2 was approximately 4, which corresponds to homogeneous nucleation and three-dimensional growth. The differences in nucleation mechanisms for materials with and without MH, especially in the first stage, could be attributed to the presence of foreign surface, MH, with the perfect crystalline structure that can act as the nuclei for the crystallization of PP.

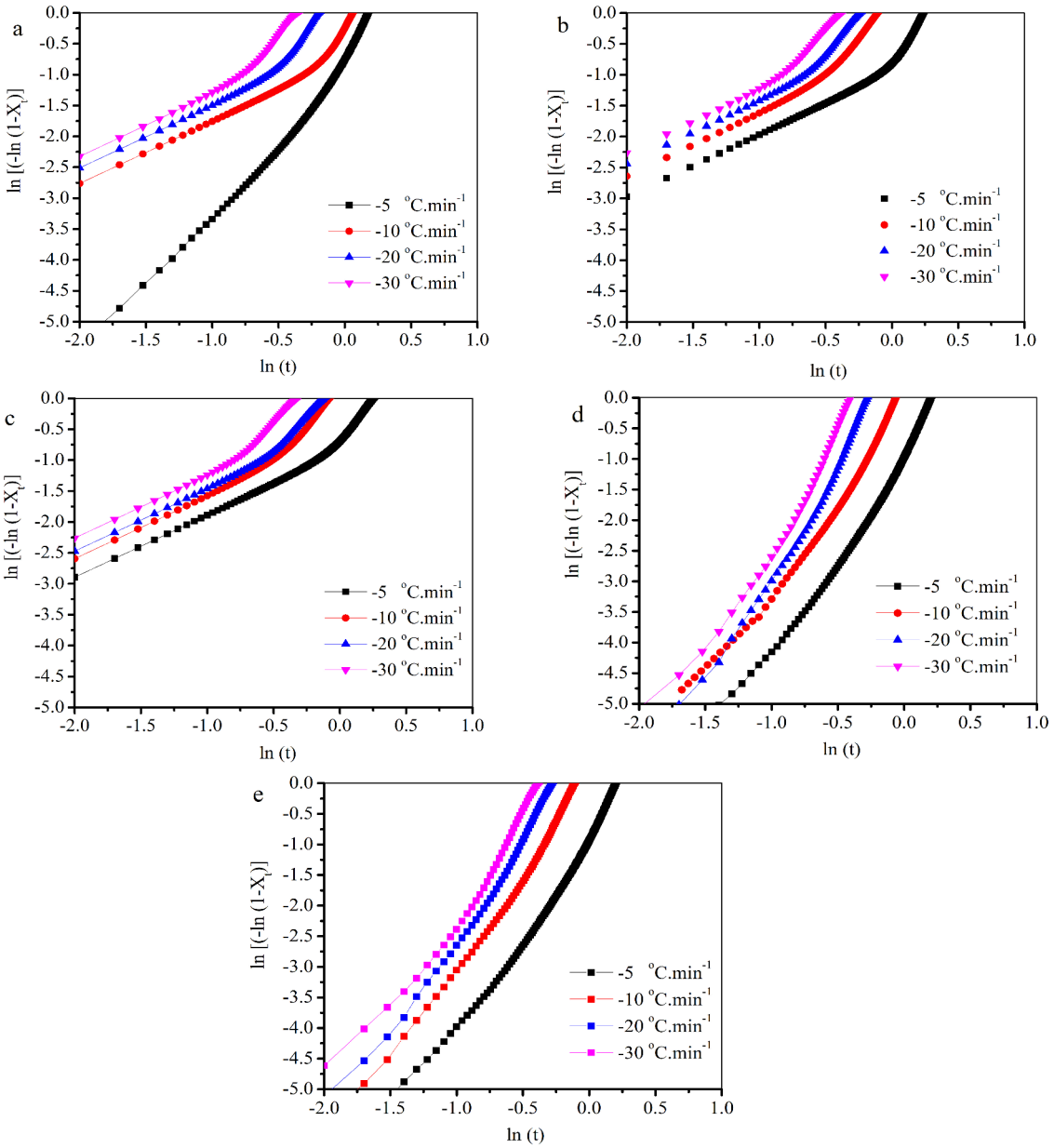

Figure 6.7: Plots of ln (-ln (1-X_t)) versus ln (t) for non-isothermal crystallization. a. PP, b. PP*, c. 60PP*/40CA*, d. 70PP*/30MH, and e. 70(60PP*/40CA*)/30MH

Table 6.3: Non-isothermal crystallization kinetic parameters according to the Avrami model (Equation 6.7)

Material	Cooling rate ($^{o}C \cdot min^{-1}$)	n_1	Z_{t_1}	n_2	Z_{t_2}
PP	5	2.1	0.3	3.8	0.5
	10	1.5	0.5	4.0	0.8
	20	1.5	0.7	2.8	0.6
	30	1.5	0.7	2.6	2.5
PP*	5	1.0	0.4	3.1	0.4
	10	1.3	0.7	2.7	1.3
	20	1.1	0.8	2.6	2.0
	30	1.0	0.9	2.1	2.3
60PP*/40CA*	5	1.0	0.4	2.8	0.5
	10	1.0	0.6	2.7	1.2
	20	1.1	0.7	2.5	1.5
	30	1.1	0.9	2.4	2.2
70PP*/30MH	5	2.2	0.1	3.3	0.3
	10	2.9	0.7	3.9	1.1
	20	3.0	1.0	5.2	4.1
	30	2.7	1.1	4.8	6.7
70(60PP*/40CA*)/30MH	5	2.9	2.2	4.2	6.7
	10	2.6	0.6	4.1	1.5
	20	2.7	1.0	3.7	2.7
	30	2.3	0.9	4.4	6.0

6.3.4 Polarized light optical microscopy

Figure 6.8 shows the polarized light optical microscopy images of PP and 60PP*/40CA*. The other materials (70PP*/30MH and 70(60PP*/40CA*)/30MH) were not transparent, which did not allow for clear images. PP (Figure 6.8a) revealed the typical spherulite structure. The incorporation of CA* in PP (Figure 6.8b) affected the nucleation, and appears in sporadic, irregular intervals. In a few places in the sample, the irregular shape of spherulites with shorter dimensions was observed.

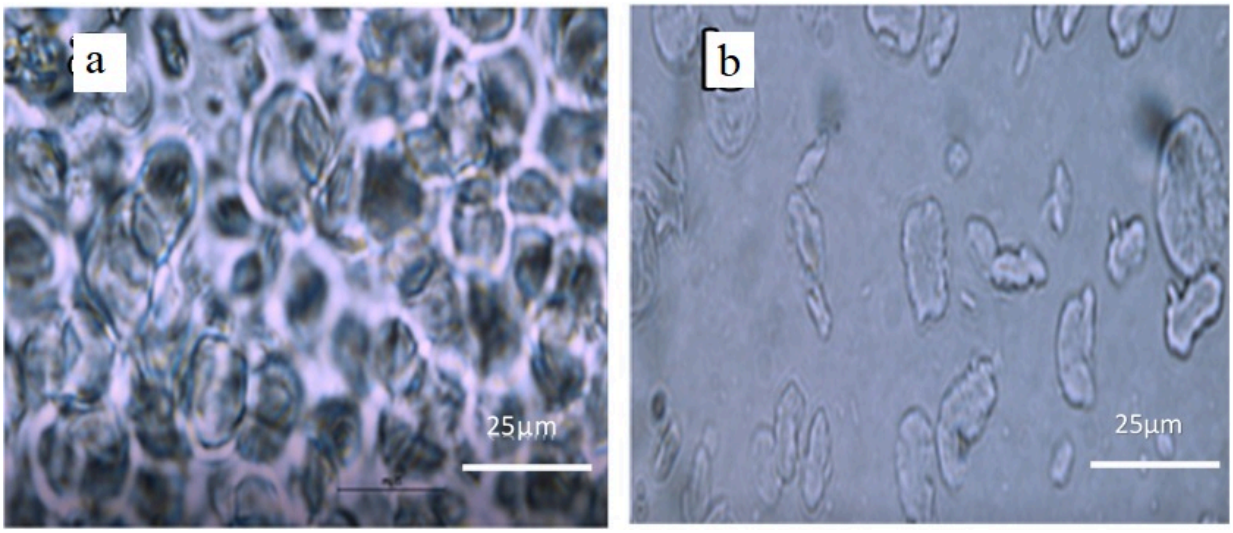

Figure 6.8: Polarized light optical microscopy image a. PP and b. 60PP*/40CA*

6.3.5 Nucleation activity

In order to further investigate the nucleation efficiency of PPMA, CA*, and MH in PP, the method proposed by Dobreva and Gutzow was employed [212]. The nucleation activity (φ) can be defined as a factor by which the work of three-dimensional nucleation decreases with the addition of a foreign substrate. The nucleating activity, φ, can be defined as follows [213]:

$$\varphi = \frac{B^*}{B} \tag{6.8}$$

where B^* and B are the parameters related to the heterogeneous (multi component material, PP*, PP* with CA, MH, or both) and homogeneous (single component material, PP in this study), respectively and can be calculated from the following equations:

$$ln(\beta^*) = C_1 - B^*/\Delta T_p^2 \tag{6.9}$$

$$ln(\beta^*) = C_2 - B/\Delta T_p^2 \tag{6.10}$$

where β^* is the cooling rate, C_1 and C_2 are constants, and $\Delta T_p = T_m - T_p$ is the supercooling and can be estimated as shown in Figure 6.6 a, T_m (°C) and T_p (°C) are the melting temperature and the crystallization temperature detected from the melting and

crystallization peaks of DSC curves at four cooling rates, and B and B^* are estimated from the slope of the plot $ln\ \beta^*$ versus $1/\Delta T_p^2$.

When the dispersed component in a blend is extremely active for nucleation, the value of φ approaches 0, while for inert dispersed component, φ approaches 1. Plots of $ln\beta^*$ versus $(1/\Delta T_p^2)$ for PP materials are shown in Figure 6.9. Straight lines were obtained where their slopes are equal to B (PP) and B^* (PP*, PP* with CA*, MH, or both), respectively.

The estimated nucleation activity values (φ) were 0.615, 0.876, 0.739, and 0.480 for PP*, 60PP*/40CA, 70PP*/30MH, and 70(60PP*/40CA*)/30MH, respectively. The results imply that the inclusion of PPMA, CA* and MH modified the nucleation mechanism and crystal growth of the PP matrix.

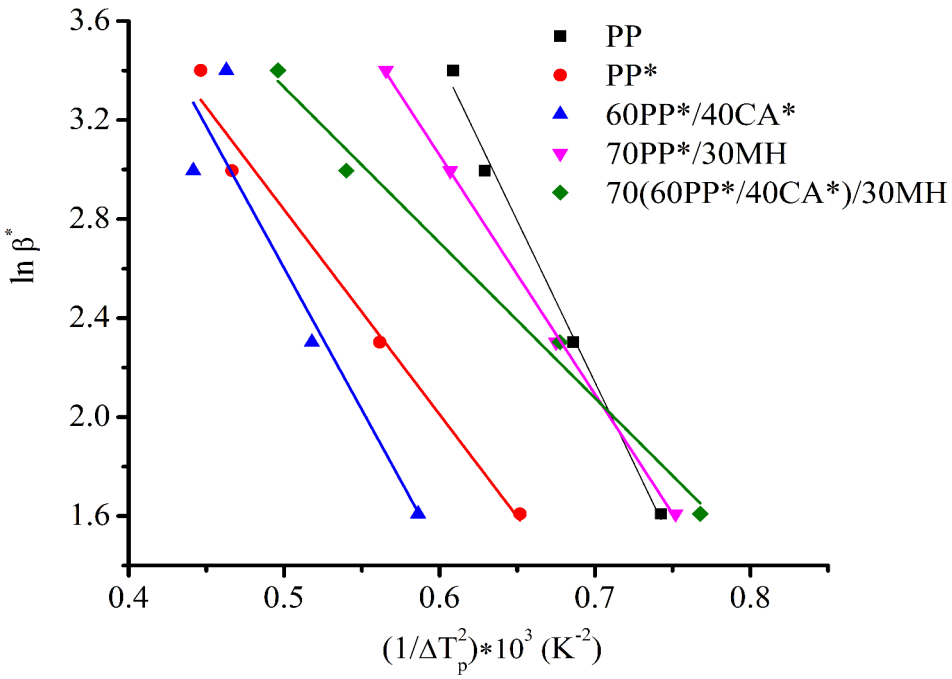

Figure 6.9: Linear plots for calculating the nucleating activity (φ) for PP materials

6.4 Conclusion

Non-isothermal crystallization and nucleation morphology studies of PP materials prepared by melt compounding were conducted. Non-isothermal experiments were used to evaluate the influence of polypropylene-grafted-maleic anhydride (PPMA), plasticized cellulose acetate (CA*), and magnesium hydroxide (MH) content on the crystallization process of PP from the molten state.

Based on DSC curves at four cooling rates, CA* induced the β form of PP with low intensity. The temperature at the maximum crystallization rate (T_p) of PP*, 60PP*/40CA*, 70PP*/30MH, and 70(60PP*/40CA*)/30MH) shifted to a lower temperature and the crystalline peaks of the PP materials became wider than PP.

According to the relative crystallinity estimates (X_t), the inclusion of CA* and MH modified the onset temperature ($T_{(0.01)}$) and temperature at 99 % ($T_{(0.99)}$) of the crystallization process. In addition, the time required to reach the 50 % crystallinity ($t_{1/2}$) for PP materials was reduced compared to pure PP.

The results showed that PPMA, CA* and MH can modify the non-isothermal crystallization kinetics of the PP matrix by changing the crystallization temperature and the crystallization rate. Avrami model analyses revealed that the inclusion of CA* and MH modified the mechanism and crystal growth geometry according to the estimated exponent (n).

The polarized light microscopy images show that the presence of CA* modified the morphology of the PP spherulite by changing the shape and size of the spherulite. The results of the nucleating activity (φ) estimates indicate that CA* and MH acted as nucleating agents in the PP matrix.

Chapter 7

Mechanical Properties of Plasticized Cellulose Acetate Magnesium Hydroxide Polypropylene Materials

In this chapter, the mechanical properties, degree of crystallinity (X_c), and crystallization forms of plasticized cellulose acetate (CA*) and magnesium hydroxide (MH) were used as polymer blend and flame retardant, respectively, in polypropylene (PP) were investigated. The results show that MH was well dispersed within the PP matrix and PP*/CA* with negligible agglomeration. The addition of CA* and MH deteriorated the tensile and impact strengths and improved Young's modulus of the PP materials. The degree of crystallinity (X_c) increased when MH and CA* were present, while CA* lowered the X_c measured by differential scanning calorimetry (DSC) and X-ray diffraction (XRD). XRD showed that CA* could induce β crystal for the PP material.

7.1 Introduction

The use of bio-materials for applications such as automotive components and building materials is increasing due to their ecological and economic considerations. Different organic fillers have been investigated, for example, wood fiber as reinforcement fillers [214], and cellulose derivatives [215] for polyolefin materials.

PP is a semi-crystalline thermoplastic material with wide applications due to processability, mechanical properties, and chemical resistance at room temperature. PP has

several polymorphs including the monoclinic α, trigonal β, and orthorhombic γ. The monoclinic α form is the most common and thermodynamically stable crystal form, predominating in normal processing conditions. The β form is metastable and is produced under defined crystallization conditions or in the presence of nucleating agents [216]. PP has been widely used in the fields of automobile, packaging, and so on. However, it has several disadvantages, such as molding shrinkage, low thermal deficiency temperature, and poor flammability resistance. These drawbacks make it unsuitable to use for many applications [217].

The viability of cellulosic fillers in thermoplastic materials has also been investigated in the literature. These fillers significantly display lower density than mineral materials. Moreover, reduced wear of the processing machinery could be considered as an advantage of using these fillers [215]. Previous studies have reported that the addition of cellulosic fillers reduces the strength and slightly reduces the impact strength of materials. The addition of cellulose to thermoplastic polymers, such as PP, yields a poor interfacial adhesion due to incompatibility-cellulose and PP are hydrophilic and hydrophobic, respectively [218]. Several pre-treatment methods, applied prior to the fabrication of these materials, were reported for cellulose to improve its compatibility with polymer matrices [2, 219–221]. Coupling agents and acetylation are the two main approaches used to improve such compatibility. The acetylation of cellulosic filler has been reported to improve the fiber matrix adhesion [222, 223]. Acetylation was reported by Luz et al. (2008), indicating that PP materials with acetylated fibers had a reduction in the tensile strength and intermediary thermal stability obtained for PP materials, i.e., the thermal stability of the materials is higher than neat fiber and lower than that of PP [25]. The authors stated that chemical modification did not contribute positively to the mechanical properties; hence, the reinforced material with treated fibers showed the worst results (see Table 7.1).

Improvement in the flame retardancy is essential for them to meet safety requirements [5]. The most common flame retardant additives used are inorganic, halogenated, and phosphorus compounds. However, some flame retardant additives may cause negative health and environmental outcomes. Increasingly, attention is being paid to inorganic compounds such as metallic hydroxide additives [171, 224]. The introduction of particulate mineral fillers into the thermoplastic polymer can improve some mechanical properties, such as Young's Modulus or the heat deflection temperature, but may negatively affect other properties, such as the impact strength [7]. According to Das et al. (2017), the addition of MH improves the tensile moduli of PP materials but reduces their tensile strength because of the higher MH loading, which has been confirmed by other studies [166, 225].

The physical and mechanical properties of PP materials depend on the crystalline morphology and degree of crystallinity of the PP substrate. Investigations of the crystallization

process of semi-crystalline polymers are of great importance in polymer processing. The mechanical properties of semi-crystalline polymers are mainly dependent on the nature of the crystal phase, crystallinity, and spherulite size [226]. The degree of crystallinity of PP may be affected by the inclusion of fillers and additives to the matrix as reported by different studies [227]. Fillers and additives have the potential to modify the crystallization characteristics of the polymer matrix depending on their density. Zhang et al. (2007) [228] studied the effects of carbon fiber loading on the morphology and melting behavior of PP and found that the morphology and crystallization characteristics of PP materials were strongly affected by the addition of short carbon. In a different study, XRD was used to evaluate the degree of crystallinity (X_c) of PP and PP/lignocellulosic materials. It was observed that the degree of crystallinity increased [229].

Table 7.1: Published mechanical properties of PP materials

Material	Tensile Modulus (GPa)	Tensile Strength (MPa)	Elongation (%)	Impact strength ($J \cdot m^{-1}$)	Reference
PP	0.51	31.6	>200%	-	[171]
PP/20 Cellulose	-	25.8(0.3)	6(0.3)		
PP/20Acetylated cellulose	-	20.1(0.4)	-	-	[25]
PP/30Cellulose	0.88(0.1)	23.7	9.8	-	[218]
PP/30MH	-	27.9	4.7	2.2	[230]
PP/30Sisal/40MH	2.36	28	-	-	[166]

7.2 Experimental methods

7.2.1 Materials

Fine PP powder (HM20/70P), purchased from GOONVEAN Fibres Company, was used as the polymer matrix. CA (approx. 50000 g·mol^{-1} 39% acetyl), MH, TEC, and PPMA were acquired from Sigma Aldrich Company, Missouri, United States.

7.2.2 Materials preparation

Cellulose acetate (CA) was plasticized according to the methodology presented in Chapter 3.

Polypropylene (PP) materials were produced by extrusion in a twin screw-extruder (SJSZ-7A), Wuhan Ruiming Plastic Machinery Company, China. The four temperature zones ranged from 160 °C- 180 °C, and the circulation time was five minutes. The extruded materials were pelletized, and compression molded into tensile and impact specimens using and injection-molding machine (SZS- 20, China) and compression molding (PHI, Pasadena Hydraulic Inc., USA) at 200 °C with 10 bar pressure for 2 minutes. Table 7.2 lists the composition of the PP materials produced. PPMA was used in the fabrication of the as 3 wt.% replacement portion from the PP.

Table 7.2: Sample composition and coding of PP materials

Material	PP wt.%	CA* wt.%	MH wt.%	PPMA wt.%
PP	100	0	0	0
PP*	97	0	0	3
60PP*/40CA*	58.2	40	0	1.8
70PP*/30MH	67.9	0	30	2.1
70(60PP*/40CA*)/30MH	40.74	28	30	1.26

PP* refers to 97PP /3PPMA.

CA* refers to plasticized cellulose acetate with triethyl citrate.

7.2.3 Tensile strength (ASTM D638)

The mechanical properties of the PP materials were measured at room temperature using an INSTRON 4465 tensile tester with a strain rate of 6 mm·min^{-1}. The samples were kept at 23 °C and 50 % relative humidity for not less than 40. Five samples of each material were tested. The reported flexural strength is the maximum point of the stress/strain curve. Young's modulus represents the slope of the first linear part of the stress /strain curve. The sample size and dimension as shown in Figure 7.1.

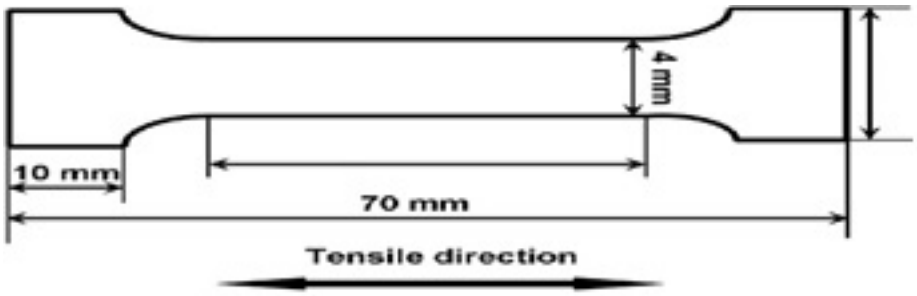

Figure 7.1: Tensile test specimen size and shape

7.2.4 Notched Izod impact test (ASTM D256)

The impact strength of the PP materials was measured with the Impact Test machine from Zwick/Roell (B5113.3), Germany at room temperature and a hammer work of 5.41 J. The samples were kept at 23 °C and 50% relative humidity for not less than 40. Five samples of each material with size (60 mm×10 mm×3 mm) were tested.

7.2.5 Differential scanning calorimetry (DSC)

The thermal properties, melting temperature (T_m), heat of fusion (ΔH_m), and degree of crystallinity (X_c) of PP materials was investigated with a Q2000 TA instrument (USA) calibrated by indium and sapphire disk standards, using standard T -zero. Nitrogen with a 50 ml·min^{-1} flowrate was used as purge gas. Samples of approximately 5-6 mg of the extruded materials as pellets were placed in an aluminum pan. The samples first were heated from room temperature to 200 °C at a heating rate of 10 °C·min^{-1}, and then

maintained at this temperature for 5 minutes to remove previous thermal history. The samples were then cooled to 25 °C at different cooling rates (5, 10, 20, and 30 °C·min^{-1}). The heat flow was recorded as a function of temperature and time.

7.2.6 Wide angle X-ray diffraction (WAXRD)

The crystalline structure of PP materials were analyzed by wide angle X-ray diffraction. The sample was laid on the sample holder and analyzed with CuK radiation (λ=1.54 Å) generated at a voltage of 45 kV and tube current of 35 A. The X-ray diffraction patterns were recorded in a 2θ angle. The range was from 5° to 80° and scan step size was 0.004° under continuous scan type. The degree of crystallinity was estimated as the ratio of the crystalline area to the total area under the diffraction peaks. Data analyses were performed using Origin -Pro software.

7.3 Results and discussion

7.3.1 Mechanical properties

7.3.1.1 Tensile strength

The tensile test provides the materials response to stress forces applied in the longitudinal part of the specimen. The tensile test properties of PP materials prepared with PPMA, MH, CA* are presented in Table 7.3.

The tensile strength of the PP materials decreased as the MH loading increased. At 95% confidence level, there was a significant decrease in the tensile strength of PP compared to 70PP*/30MH of 13%. However, tensile strength was not significantly influenced by MH except at high filler contents. It could be suggested that there is some degree of filler-matrix interaction at play; allowing the material to resist the imposition of tensile force [230]. According to previous studies, adding MH causes a reduction in the tensile strength and an elongation at break that could be attributed to the poor compatibility of MH and PP [4]. The tensile strength decreased when CA* was added to the PP matrix. This reduction was around 30% from the neat PP matrix. Luz et al. (2008) examined the chemical modification of cellulose by acetylation and its impacts on mechanical properties [25]. They reported that the tensile strength of PP with acetylated cellulose decreased. In their analysis of cellulose and other reinforcement fillers, they found that chemical

modifications did not contribute to the mechanical properties. The combination of CA* and MH also decreased the tensile strength of the material by 30 %. The tensile strength and fracture toughness of polymer material depend on the interfacial adhesion between the filler and the polymer matrix [218, 231]. According to Griffiths theory, a significant agglomeration of particles in the polymer matrix creates a weak point which lowers the stress required for the material to fracture [232]. Other studies have found that the presence of fine particles dispersed within the polymer matrix makes plastic deformation easier; hence, lower tensile strength. When the fillers are well dispersed, the stress must be higher to propagate a micro-crack in the material. Furthermore, impact energy will largely be absorbed by plastic deformation occurring around the particle.

Table 7.3: Tensile test properties of PP materials (± standard error, n=5)

Material	Max. Load (kN)	Yield stress (MPa)	Tensile strength (MPa)	Elongation At break(%)	Young's Modulus (GPa)
PP	0.34	34.12 (± 3.8)	31.90 (± 5.3)	18.6	0.52 (± 0.01)
60PP*/40CA*	0.22	21.90 (± 3.)	*N.O.*[a]	4.54	1.11 (± 0.61)
70PP*/30MH	0.3	29.90 (± 3.2)	29.60 (± 2.9)	7.33	0.64 (± 0.50)
70(60PP*/40CA*)/30MH	0.19	19.50 (± 1.5)	*N.O.*[a]	2.22	1.41 (± 0.10)

a : *Not observed*

The modulus of elasticity which is measured by extending the initial linear portion of the load extension curve and dividing the difference in stress corresponding to any segment of a section on this straight line by the corresponding difference in the strain. The modulus of elasticity increased with CA* and MH (Table 7.3). Qiu et al. (2005) [218] reported the effects of cellulose on a PP matrix, Young's Modulus increases with the inclusion of cellulose. Similar results were obtained by Joseph et al. (2002) in a study of the effects of treated and untreated sisal fiber fillers [233]. The effect of MH was reported to have the same effect on the Young's Modulus of the PP matrix [234]. MH may block the movement of PP chains, increasing the stiffness of the material. The deformation of the specimen under tensile load would be difficult because MH provides structural rigidity to the polymer matrix [167]. The percolation theory [7] provides an alternative explanation for the increase in stiffness. This theory proposes that there is a concentration of stress in the region of the polymer matrix around each filler particle. If the distance between the filler particles is small enough, these zones will join during tensile loading and form a percolation network. This percolation network causes an increase in the elastic modulus of

the material. When the particles are fine and well dispersed, the total effected volume is increased and the distance between particles is shorter; the percolation network develops more easily, and the modulus is thus increased [235].

The elongation at break decreased with CA* and with MH (Table 7.3). The addition of MH to the PP matrix reduced the elongation of the material by 50% compared to PP. The addition of CA* decreased the elongation by 70 %. The combination of CA* and MH caused a further reduction in the elongation of the material. The elongation at break was inferior to neat PP in all cases; therefore, the materials were rigid when compared to the matrix. Weak bonding between the fillers and matrix caused poor stress transfer when the samples were loaded with tension, leading to early rupture. Elongation at break, therefore, decreased in all test cases [25].

7.3.1.2 Impact strength

A notched impact test measures the energy during impact, i.e., the energy necessary to fracture a standard test piece [121]. The impact resistance decreased when CA* or MH were added to the matrix, as shown in Table 7.4. With a 95% confidence level, a significant difference was found in the impact test. The addition of CA* and MH to the matrix resulted in a 35 % and 80 % reduction, respectively.

Table 7.4: Impact test for PP materials (± standard error, n=5)

Materials	Impact Resistance /Notch Length ($J \cdot m^{-1}$)
PP	42.5 (± 1.20)
60PP*/40CA*	26.6 (± 4.00)
70PP*/30MH	8.7 (± 0.89)
70(60PP*/40CA*)/30MH	8.6 (± 0.80)

Similar observations of the effect of MH on the impact strength of PP materials was also reported by Mai et al. [234]. They reported a significant reduction in the impact strength. This decrease in impact resistance can be attributed to the immobilization of PP chains, limiting their ability to adapt to deformation and hence making the materials more brittle [7]. Furthermore, each particle in the matrix can act as a micro-crack initiator because there is a weak filler/matrix interaction. When the interaction is weak, the interfacial layer cannot effectively transfer the stress [236].

7.3.2 DSC observations

Figure 7.2, thermograms are shown representing the non-isothermal crystallization process of PP materials. The thermal properties, melting temperature (T_m), heat of fusion (ΔH_m), and degree of crystallinity (X_c), are obtained from DSC studies, and are presented in Table 7.5. The crystallinity of PP was determined as follows:

$$X_c\,(\%) = \frac{\Delta H_m}{\Delta H_m^o \times w} \times 100 \tag{7.1}$$

where ΔH_m^o (207 J·g^{-1}) is the heat of fusion for 100% crystalline PP [205], ΔH_m (J·g^{-1}) is the heat of fusion of the sample estimated from the area under the melting peak of DSC curves, and w is the mass fraction of PP in the PP materials.

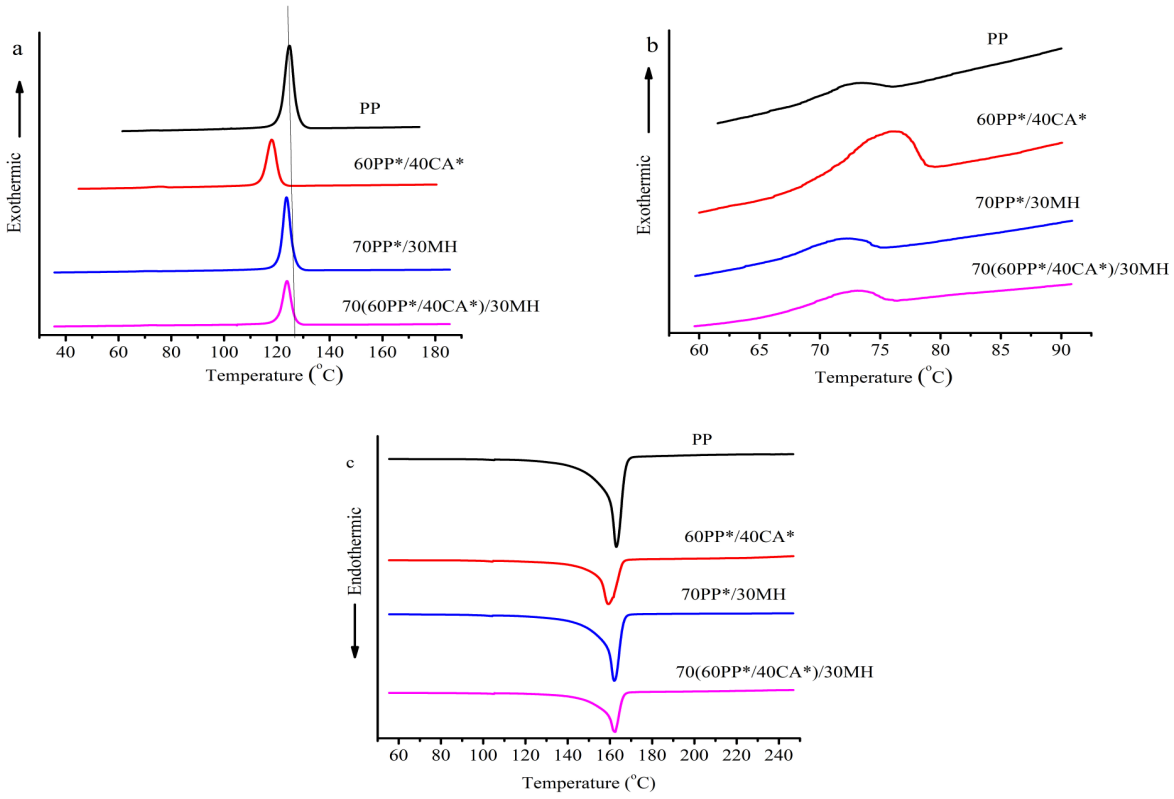

Figure 7.2: DSC thermograms of PP materials. a. crystal peaks, b.close -crystal peaks, c.melting peaks

There was no significant change in the melting temperature of PP materials. The 70(60PP*/40CA*)/30MH had higher crystallinity than PP and the other materials. This could be another reason for the stiffness of this PP materials in comparison to the others.

7.3.3 Wide angle X-ray diffraction (WAXRD)

The XRD patterns of plasticized cellulose acetate (CA*) is given in Figure 7.3a. Two main broad peaks appear at 2θ of 9.0^o and 21.5^o. CA* shows a low degree of crystallinity (10%) due to plasticization effects. The XRD patterns of MH powder are given in Figure 7.3b. All peaks can be indexed as a hexagonal structure of MH with lattice constant [3]. The diffraction peaks of MH are at 2θ of 18.6°, 38°, 50.09°, 58.7°, 62.1°, and 68.3° with different intensities.

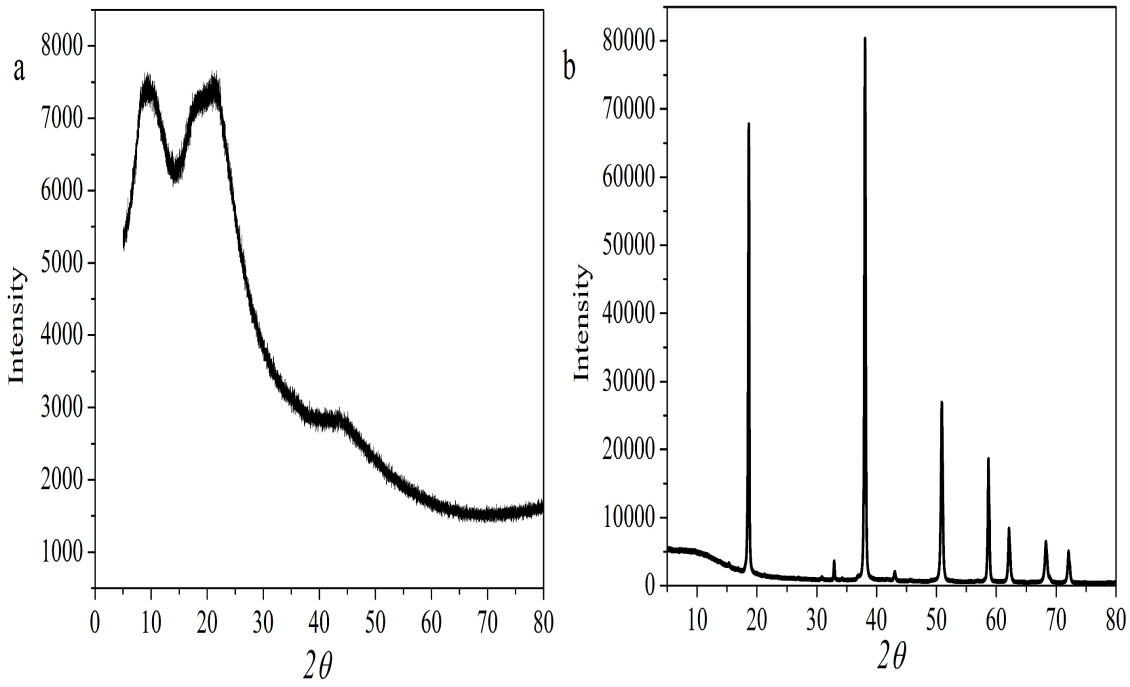

Figure 7.3: XRD patterns of a. plasticized cellulose acetate (CA*) and b. magnesium hydroxide (MH)

Figure 7.4 shows the diffraction patterns of PP materials. Several maxima can be observed. These peaks occur at 2θ values 14.5°, 17.5°, 19.1°, 22° and 22.5°. The most intense are located at the 110, 040, 130, 111, and 041 planes, representing an α crystallization form. Similar results have been reported by Gupta and others [237–240]. For 60PP*/40CA*, the same peaks occurred at a similar location, 2θ, with one extra peak appearing at 16.5°. This could be related to β peak crystals with a reflection plane (300). This result agrees with previous studies, which showed that a β crystal could be induced by adding other fillers or nucleating agents at the same 2θ [241, 242]. The decrease in peak intensity and peak broadening are smaller for 60PP*/40CA* than for the PP, which could indicate that CA* increases the disorder of the PP structure.

For 70PP*/30MH and 70(60PP*/40CA*)/30MH, the peaks are slightly shifted to lower angles, meaning that the distance between the PP layers increased. The intensity of these peaks is also reduced except for one; possibly related to the inclusion of MH. Moreover, the broadening of the peaks is also reduced for the 70(60PP*/40CA*)/30MH. The peak height and intensity could be affected by the variation in the spherulite size or their distribution, deformation at the spherulite boundaries, or the formation of the mesomorph phase of PP [237, 243].

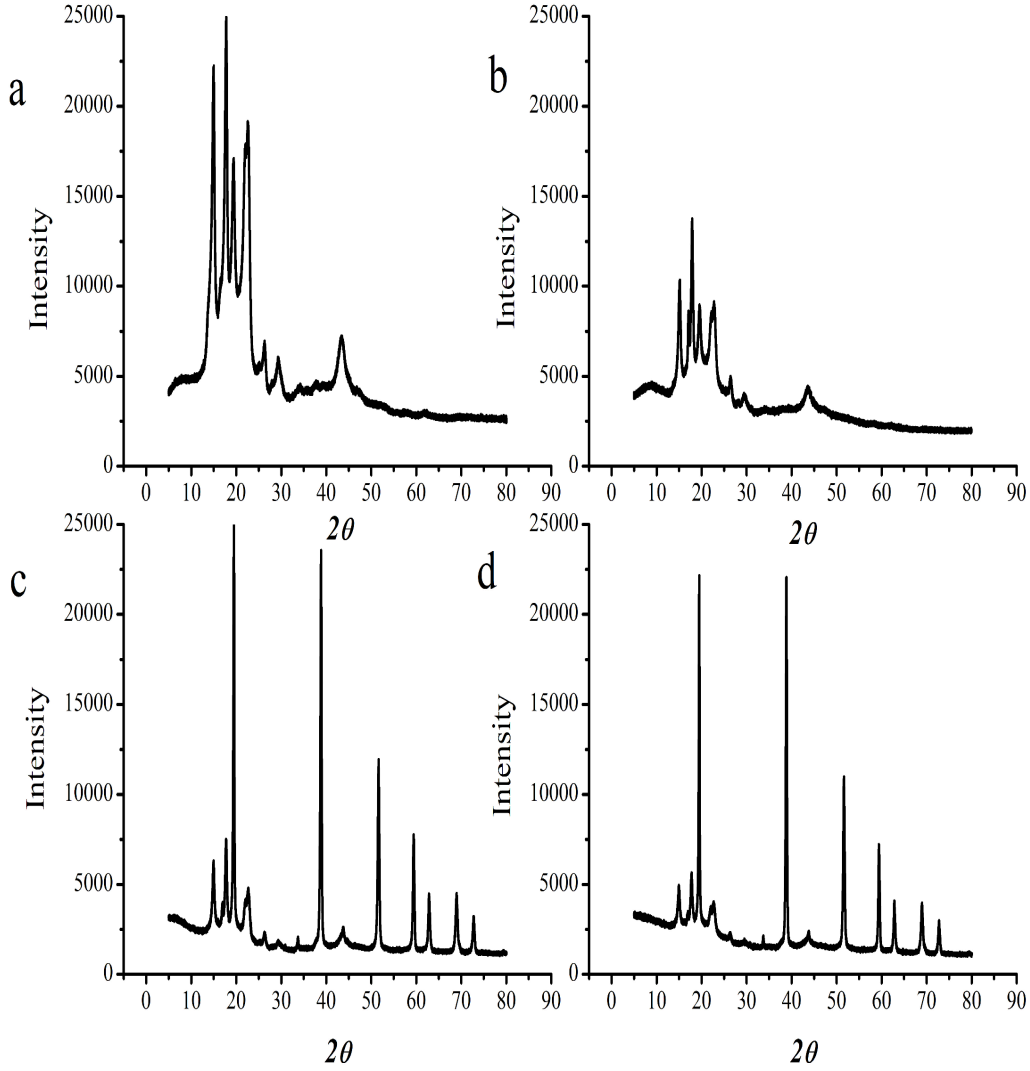

Figure 7.4: Comparison of the X-ray diffractograms of PP materials. a. PP, b. 60PP*/40 CA*, c. 70PP*/30 MH, and d. 70(60PP*/40CA*)/30MH

The degree of crystallinity (X_c) can be obtained from XRD measurements with the following expression:

$$X_c(\%) = \frac{A_c}{A_a + A_c} \times 100 \tag{7.2}$$

where A_c is the crystalline area and A_a is the amorphous area in the XRD diffractograms.

The degree of crystallinity (X_c) of PP materials estimated from XRD diffractograms corresponds well with the degree of crystallinity obtained from DSC studies (Table 7.5). Appendix C contains the baseline and area subtraction methods used for the amorphous and crystal region.

Table 7.5: Thermal characteristics of PP materials

Material	T_m (^{o}C)	ΔH_m (J·g^{-1})	X_c(%) DSC	X_c(%) XRD
PP	163	85	46	47
60PP*/40CA*	159	48	43	42
70PP*/30MH	162	67	52	56
70(60PP*/40CA*)/30MH	162	42	54	58

7.4 Conclusion

PP materials were fabricated by extrusion and injection or compression molding. The mechanical properties and crystallinity of the materials were evaluated.

The addition of MH markedly reduced the mechanical properties of PP materials. The notched impact strength reduction was larger than that for the tensile strength. From the observation of fractured surfaces, it was revealed that extensive cracking and a lack of bonding at the filler/matrix interface were present. However, Young's modulus increased. A significant reduction in the tensile strength was observed after blending CA* with PP*; it was larger than the reduction caused by the addition of MH. In contrast, the reduction in impact strength was smaller than that of the PP* material with MH added. CA* increased Young's modulus of MH. The presence of CA* and MH in the PP matrix reduced the tensile strength of the PP matrix, but a significant reduction was not observed in the impact strength in comparison to the 70PP*/30MH material. Young's modulus also increased in 70(60PP*/40CA*)/30MH.

The degree of crystallinity estimated by DSC and XRD showed that the PP material has a higher degree of crystallinity in the presence of MH and CA* and MH, while the degree of crystallinity was lower for 60PP*/40CA*.

In summary, the effects of MH on the mechanical properties and crystallization of the PP*/CA* have been reported for the first time in the literature. Further investigation is required on surface modification of MH to mitigate the reduction of the mechanical properties.

Chapter 8

Conclusion and Recommendations

8.1 Conclusion

The research presented in this PhD thesis focused on the development of polypropylene (PP) materials. The objective was to develop a polypropylene plasticized cellulose acetate material and to explore the use of magnesium hydroxide to enhance the flame retardant properties of these materials. Different properties were evaluated, thermal stability, flammability, crystallization, and mechanical properties.

The plasticization of cellulose acetate (CA) with triethyl citrate (TEC) was evaluated. TEC's effects on the degree of crystallinity and thermal stability were examined. The glass transition temperature (T_g), according to DSC observations, was reduced to around 120 ^{o}C. XRD results showed that the crystalline structure of CA was affected by TEC. Based on TGA, TEC lowered the thermal stability of CA by shifting the onset temperature and maximum weight loss temperature to lower temperature. The analysis of the results which discussed earlier confirmed the viability of TEC as a plasticizer for CA.

Formulation of the PP materials was done based on thermogravimetric analysis. The thermal stability and the estimation of activation energy according to the level of each component (PPMA, CA*, and MH) were evaluated. The results revealed that the highest level of PPMA (3 wt.%), CA* (40 wt.%), and MH (30 wt.%) could be employed in the fabrication of the PP materials to obtain high thermal stability and activation energy. The morphology of the PP materials studied by using FESEM showed better compatibility between CA* and the PP matrices. The CA* compatibility with PP was negatively affected by the addition of MH. EDS mapping analysis showed good dispersion of MH and CA* in the PP matrix.

The thermal stability and kinetic studies of PP materials were conducted by using TGA at four heating rates. The results revealed that PP materials with CA* and MH had a higher thermal stability where the thermal decomposition occurred over a wide range of temperature and the maximum weight loss temperature shifted to higher temperature. The activation energy was estimated according to three methods: Kissinger, KAS, and NIM methods. The results demonstrate that PP materials with CA* and MH had higher activation energy than that of pure PP and other PP materials. The E_a of 70(60PP*/40CA*)/30MH was higher than that of PP, PP*, 60PP*/40CA*, and 70PP*/30MH. The methods used were in good agreement showing that E_a of the 70(60PP* /40CA*) /30MH was the highest.

The fire resistance of PP materials was examined by the vertical burning test, oxygen index, cone calorimeter, and an adiabatic bomb calorimeter test. The results indicated that the combination of CA* with MH provided the flame retardancy of PP. The 70(60PP*/CA*)/30MH showed a V-0 rating, which is the highest rank according to the vertical burning test standard. The OI value was the highest for the 70(60PP*/40CA*)/30MH, greater than that of PP, and 60PP*/40CA by 29% and 17%, respectively. Based on the cone calorimeter observations, the peak heat release rate of the 70(60PP*/CA*)/30MH material was reduced by 80% , 75%, and 50% compared with that of PP, 60PP*/40CA*, and 70PP*/30MH, respectively. The total heat release (THR) of the 70(60PP*/CA*)/30MH was significantly lower than that of other materials. The effective heat of combustion (EHC) shows that 70(60PP*/40CA*)/30MH was less exothermic than other materials. The carbon monoxide (COY) and carbon dioxide(CO_2Y) yields were significantly lower for 70(60PP*/CA*)/30MH materials than other PP materials. The heat of combustion estimated by adiabatic bomb calorimetry confirmed the results obtained by cone calorimeter showing that 70(60PP*/CA*)/30MH was less exothermic than other PP materials during burning. According to the calculation of carbon availability in the products of combustion revealed that the 70(60PP*/40CA*)/30MH material which has a higher yield of soot and residue showed better flame retardancy.

Investigation of the non-isothermal crystallization of PP materials was done at four cooling rates. Based on the DSC thermograms, the results showed that the crystallization temperature of the PP materials with PPMA, CA*, and MH shifted to the lower temperature. According to the relative crystallinity estimates, the inclusion of PPMA, CA*, and MH modified the onset temperature ($T_{0.01}$) and the temperature at 99% of the crystallization process. The $t_{1/2}$ was also modified compared to that of PP. The non-isothermal crystallization kinetics were obtained by utilizing Avrami model. The results show that CA* and MH modified the crystal structure of PP by changing size and shape of spherulite of PP. Polarized optical microscopy images confirmed that CA* modified the morphology

of PP spherulite by changing their size and shape. The nucleation activity was estimated for the PP materials. The results revealed that presence of CA* and MH in the PP matrix had the highest nucleating activity.

The mechanical properties, degree of crystallinity, and crystal forms of PP materials were investigated through tensile and impact test, DSC, and XRD. The mechanical properties analysis of the PP materials showed a marginal reduction in the tensile strength due to the addition of CA* and MH. The reduction in the tensile strength was around 13% with the addition of MH, and 30% with the addition of CA*. In contrast, Young's modulus of the materials was increased by 100% and 25% due to the addition of CA* and MH, respectively. The addition of both CA* and MH showed the highest Young's modulus with an increase of around 300%. The addition of CA* deteriorated the impact strength of the materials by around 35%. The addition of MH only, and MH and CA* together reduced the impact strength by around 70%. DSC and XRD were used to probe the effects of CA* and MH on the X_c and crystal forms of the PP materials. The addition of CA* reduced X_c. On the other hand, CA* induced the β crystal form with low intensity, as confirmed by the XRD diffractograms study. The addition of CA* and MH increased the degree of crystallinity.

In summary, the results of this study demonstrate the feasibility of obtaining PP materials containing CA*. In the presence of CA* and MH, PP material showed improved thermal stability and flame retardant properties with lower level for MH than reported previously in the literature. The addition of CA* and MH deteriorated some of the mechanical properties; however, the PP materials would be suitable for interior automotive components and other non-structural building materials such as electrical power insulation.

8.2 Recommendations

The results presented in this study have led to the formulation of the following recommendations for future work. The recommendations are presented along two avenues: PP material formulation and characterization.

8.2.1 PP material formulation

8.2.1.1 Surface modification of magnesium hydroxide (MH)

Due to the deterioration of the mechanical properties reported in this study when MH was present, particularly the impact strength, it is recommended that the surface modification

of MH should be investigated to mitigate these changes. Many surface modification agents have been reported in the literature for this purpose [3, 244]. For example, titanate and zinc stearate have been reported to improve the dispersion of MH and improve the mechanical properties of PP materials containing MH [3, 230].

8.2.1.2 Compatiblizer used for polypropylene/plasticized cellulose acetate blend

To address the reduction in impact strength of PP/CA* material, the use of compatibilizer should be investigated as a mean to improve the impact strength. The type of compatibilizer should be further investigated. One could start with those used with PLA/starch materials, methylenediphenyl diisocyanate [245] and dioctyl maleate [246].

8.2.2 PP material characterization

Future work could increase the number of properties examined beyond those reported in this study to include dynamic mechanical analysis and water absorption behavior, as well as expanding on the thermal behavior characterization.

8.2.2.1 Crystallization activation energy

Further investigation should focus on the estimation of the effective energy barrier of non-isothermal crystallization. Several mathematical methods have been proposed in the literature for the calculation of the effective energy barrier. However, a major concern has been put forward that using unconventional procedures to estimate E_a leads to inaccurate conclusions as most approaches have been developed for heating experiments [247]. It has been stated by Vayzovkin (2003), that dropping the negative sign for β^* makes the procedure invalid when applied to the process that occurs on cooling [248].

8.2.2.2 Analysis of the products of combustion

According to the results of the cone calorimeter, there was a reduction in the time to ignition (t_{ign}) due to the addition of magnesium hydroxide to the pure polypropylene and to polypropylene/ plasticized cellulose acetate (PP*/CA*) materials. As the safety of materials is affected when there is a reduction in the t_{ign}, real time Fourier transform infrared spectra (FTIR) could be helpful to analyze the volatile products of the decomposition and to adjust the formulation of the developed materials.

8.2.2.3 Analysis of the effect of mass and heat transfer effects in TGA

Since TGA analysis was conducted with pellet, the effect of the material particle size and surface area was not investigated. Thus, the comparison between pellet and ground pellet material on TGA analysis should be investigated in order to understand if potential heat and mass transfer limitation exist.

Chapter 9

Summary of Contributions

Investigations of the relevant factors in the development of PP material, the feasibility of CA*, and the properties of PP/CA*/MH as a material were presented in this thesis. The most significant contributions are listed below.

- A new PP material including CA* as bio material and MH as inorganic additive was proposed which demonstrated acceptable mechanical property retention and improved fire-retardancy over conventional materials.

- TEC was found to be acceptable a plasticizer for CA. This was verified through DSC studies and the effects of the plasticization process on the degree of crystallinity and on the thermal behavior of CA were presented.

- The activation energy of the degradation process was estimated using several approaches. A numerical integration method approach was successfully validated to calculate the activation energy. The methods used were evaluated for their accuracy in estimating the kinetic parameters. The effect of CA* on the PP matrix was studied and this study was expanded to evaluate the effects of CA* and/or MH on the PP matrix. The developed material shows higher thermal stability than both the PP and PP/MH material.

- A combination of qualitative and quantitative methodologies was used to characterize the flame-retardancy of the developed materials. A correlation was found between the availability of carbon in the combustion products and the flammability resistance of the materials.

- An investigation of non-isothermal crystallization studies of PP materials was explored, detailing the effects of CA* and MH on the nucleation and crystal growth of PP matrices.

- An analysis of the mechanical properties of PP materials with CA* and MH was completed. The degree of crystallinity of the materials was also calculated.

Letter of Copyright Permission

Permission certificate for reprint Figure 2.5

JOHN WILEY AND SONS LICENSE TERMS AND CONDITIONS
This Agreement between Mr. Omar Al-Kubaisi ("You") and John Wiley and Sons ("John Wiley and Sons")

License Number	4396040823316
License date	2018-07-25
Licensed Content Publisher	John Wiley and Sons
Licensed Content Publication	Journal of Applied Polymer Science
Licensed Content Title	Properties and modification methods for vegetable fibers for natural fiber composites
Licensed Content Author	J. Gassan, S. Reihmane, A. K. Bledzki
Licensed Content Date	1998-12-07
Licensed Content Volume	59
Licensed Content Issue	8
Licensed Content Pages	8
Type of use	Dissertation/Thesis
Requestor type	University/Academic
Format	Electronic
Portion	Figure/table
Number of figures/tables	1
Original Wiley figure/table number(s)	Figure 4

Permission certificate for reprint Figure 2.8

Taylor and Francis Group LLC Books LICENSE TERMS AND CONDITIONS
This is a License Agreement between Mr. Omar Al-Kubaisi("You") and
Taylor and Francis Group LLC Books ("Taylor and Francis Group LLC Books")

License Number	4396100016326
License date	2018-07-25
Licensed content publisher	Taylor and Francis Group LLC Books
Licensed content title	Handbook of polypropylene and polypropylene composites
Licensed content date	2003-01-01
Type of Use	Thesis/Dissertation
Requestor type	Academic institution
Format	Electronic
Portion	chart/graph/table/figure
Number of charts/graphs/tables/figures	1
The requesting person/organization is:	Omar Al-Kubaisi
Title or numeric reference of the portion(s)	Figure 4-19
Title of the article or chapter the portion is from	Stabilization of Flame-Retarded Polypropylen

Permission certificate for reprint Figure 2.9

ELSEVIER LICENSE TERMS AND CONDITIONS

This Agreement between Mr. Omar A-Kubaisi ("You") and Elsevier ("Elsevier")

License Number	4397960838163
License date	2018-07-28
Licensed Content Publisher	Elsevier
Licensed Content Publication	Elsevier Books
Licensed Content Title	Studies in Polymer Science
Licensed Content Date	1991-01-01
Licensed Content Pages	62
Start Page	32
End Page	93
Type of Use	reuse in a thesis/dissertation
Portion	figures/tables/illustrations
Number of figures/tables/illustrations	1
Format	electronic
Are you the author of this Elsevier chapter?	No
Will you be translating?	No
Original figure numbers	Figure 2.8

Permission certificate for reprint Figure 2.3

JOHN WILEY AND SONS LICENSE TERMS AND CONDITIONS

This Agreement between Mr. Omar Al-Kubaisi ("You")
and John Wiley and Sons ("John Wiley and Sons").

License Number	4396061157613
License date	2018-07-25
Licensed Content Publisher	John Wiley and Sons
Licensed Content Publication	Journal of Polymer Science Part B: Polymer Physics
Licensed Content Title	The crystallization of polypropylene with reduced density of entanglements
Licensed Content Author	Andrzej Pawlak, Justyna Krajenta, Andrzej Galeski
Licensed Content Date	2017-03-07
Licensed Content Volume	55
Licensed Content Issue	9
Licensed Content Pages	9
Type of use	Dissertation/Thesis
Requestor type	University/Academic
Format	Electronic
Portion	Figure/table
Number of figures/tables	1
Original Wiley figure/table number(s)	Figure 4

Permission certificate for reprint Table 2.1

JOHN WILEY AND SONS LICENSE
TERMS AND CONDITIONS
This Agreement between Mr. Omar Al-Kubaisi ("You")
and John Wiley and Sons ("John Wiley and Sons").

License Number	4395530448018
License date	2018-07-24
Licensed Content Publisher	John Wiley and Sons
Licensed Content Publication	Macromolecular Materials & Engineering
Licensed Content Title	Cars from BioFibres
Licensed Content Author	Andrzej K. Bledzki, Omar Faruk, Volker E. Sperber
Licensed Content Date	2006-04-05
Licensed Content Volume	291
Licensed Content Issue	5
Licensed Content Pages	9
Type of use	Dissertation/Thesis
Requestor type	University/Academic
Format	Electronic
Portion	Figure/table
Number of figures/tables	1
Original Wiley figure/table number(s)	Table 5

Permission certificate for reprint Figure 2.10

ELSEVIER LICENSE
TERMS AND CONDITIONS
May 05, 2019

This Agreement between Mr. Omar Al-Kubaisi ("You") and Elsevier ("Elsevier")

License Number	4582801159455
License date	May 05, 2019
Licensed Content Publisher	Elsevier
Licensed Content Publication	Thermochimica Acta
Licensed Content Title	Effect of compatibilizers on thermal stability and mechanical properties of magnesium hydroxide filled polypropylene composites
Licensed Content Author	Hao Shen,Yuhai Wang,Kancheng Mai
Licensed Content Date	Feb 10, 2009
Licensed Content Volume	483
Licensed Content Issue	1-2
Licensed Content Pages	5
Start Page	36
End Page	40
Type of Use	reuse in a thesis/dissertation
Intended publisher of new work	other
Portion	figures/tables/illustrations
Number of figures/tables/illustrations	1
Original figure numbers	Fig1

Permission certificate for reprint Figure 2.11

ELSEVIER LICENSE
TERMS AND CONDITIONS
This Agreement between Mr. Omar Al-Kubaisi ("You") and Elsevier ("Elsevier")

License Number	4395520985712
License date	2018-07-24
Licensed Content Publisher	Elsevier
Licensed Content Publication	Applied Thermal Engineering
Licensed Content Title	Heat release rate calculation in oxygen consumption calorimetry
Licensed Content Author	W.K. Chow,S.S. Han
Licensed Content Date	2011-02-01
Licensed Content Volume	31
Licensed Content Issue	2018-02-03
Licensed Content Pages	7
Start Page	304
End Page	310
Type of Use	reuse in a thesis/dissertation
Intended publisher of new work	other
Portion	figures/tables/illustrations
Number of figures/tables/illustrations	1

Permission certificate for reprint Figure 2.14

JOHN WILEY AND SONS LICENSE TERMS AND CONDITIONS

This Agreement between Mr. Omar Al-Kubaisi ("You") and John Wiley and Sons ("John Wiley and Sons").

License Number	4395501109839
License date	2018-07-24
Licensed Content Publisher	John Wiley and Sons
Licensed Content Publication	Fire and Materials
Licensed Content Title	Development of fireretarded materials Interpretation of cone calorimeter data
Licensed Content Author	B. Schartel, T. R. Hull
Licensed Content Date	2007-05-21
Licensed Content Volume	31
Licensed Content Issue	5
Licensed Content Pages	28
Type of use	Dissertation/Thesis
Requestor type	University/Academic
Format	Electronic
Portion	Figure/table
Number of figures/tables	1
Original Wiley figure/table number(s)	Figure 8

References

[1] A. K. Bledzki, O. Faruk, and V. E. Sperber. Cars from bio-fibres. *Macromolecular Materials and Engineering*, 291(5):449–457, 2006.

[2] J. George, M. Sreekala, and S. Thomas. A review on interface modification and characterization of natural fiber reinforced plastic composites. *Polymer Engineering & Science*, 41(9):1471–1485, 2001.

[3] X. Chen, J. Yu, S. Guo, Z. Luo, and M. He. Effects of magnesium hydroxide and its surface modification on crystallization and rheological behaviors of polypropylene. *Polymer Composites*, 30(7):941–947, 2009.

[4] X. Chen, J. Yu, and S. Guo. Structure and properties of polypropylene composites filled with magnesium hydroxide. *Journal of Applied Polymer Science*, 102(5):4943–4951, 2006.

[5] M. Sain, S. H. Park, F. Suhara, and S. Law. Flame retardant and mechanical properties of natural fibrepp composites containing magnesium hydroxide. *Polymer Degradation and Stability*, 83(2):363 – 367, 2004.

[6] A. P. Mouritz, Z. Mathys, and A. G. Gibson. Heat release of polymer composites in fire. *Composites Part A: Applied Science and Manufacturing*, 37(7):1040–1054, 2006.

[7] P. Mareri, S. Bastide, N. Binda, and A. Crespy. Mechanical behaviour of polypropylene composites containing fine mineral filler: effect of filler surface treatment. *Composites Science and Technology*, 58(5):747–752, 1998.

[8] H. Karian. *Handbook of polypropylene and polypropylene composites, revised and expanded*. CRC press, 2003.

[9] O. Das, D. Bhattacharyya, D. Hui, and Kin-Tak Lau. Mechanical and flammability characterisations of biochar/polypropylene biocomposites. *Composites Part B: Engineering*, 106:120–128, 2016.

[10] C. Maier and T. Calafut. *Polypropylene: the definitive user's guide and databook*. William Andrew, 1998.

[11] B. Crist and J. M. Schultz. Polymer spherulites: A critical review. *Progress in Polymer Science*, 56:1–63, 2016.

[12] A. Pawlak, J. Krajenta, and A. Galeski. The crystallization of polypropylene with reduced density of entanglements. *Journal of Polymer Science Part B: Polymer Physics*, 55(9):748–756, 2017.

[13] D. Nwabunma and T. Kyu. *Polyolefin composites*. John Wiley & Sons, 2008.

[14] C. DeArmitt and R. Rothon. Fillers and surface treatment. *Plastics, Additives and Compounding*, 4(5):12–14, 2002.

[15] M. Fujiyama and T. Wakino. Structures and properties of injection moldings of crystallization nucleator-added polypropylenes. I. structure–property relationships. *Journal of Applied Polymer Science*, 42(10):2739–2747, 1991.

[16] A. Garton, S. W. Kim, and D. M. Wiles. Modification of the interface morphology in mica-reinforced polypropylene. *Journal of Polymer Science Part C: Polymer Letters*, 20(5):273–278, 1982.

[17] J. Menczel and J. Varga. Influence of nucleating agents on crystallization of polypropylene: I. talc as a nucleating agent. *Journal of Thermal Analysis and Calorimetry*, 28(1):161–174, 1983.

[18] C. Dearmitt and M. Hancock. Filled thermoplastics. *Particulate-filled polymer composites*, 2, 2003.

[19] R. Karnani, M. Krishnan, and R. Narayan. Biofiber-reinforced polypropylene composites. *Polymer Engineering & Science*, 37(2):476–483, 1997.

[20] E. Prez, L. Fam, S. G. Pardo, M. J. Abad, and C. Bernal. Tensile and fracture behaviour of PP/wood flour composites. *Composites Part B: Engineering*, 43(7): 2795–2800, 2012.

[21] A. K. Bledzki, S. Reihmane, and J. Gassan. Thermoplastics reinforced with wood fillers: a literature review. *Polymer - Plastics Technology and Engineering*, 37(4): 451–468, 1998.

[22] A. Dimitriou, M. D. Hale, and M. J. Spear. The effect of pH on surface activation of wood polymer composites (WPCs) with hydrogen peroxide for improved adhesion. *International Journal of Adhesion and Adhesives*, 85:44–57, 2018.

[23] K. Murayama, S. Suzuki, Y. Kojima, H. Kobori, H. Ito, S. Ogoe, and M. Okamoto. The effects of different types of maleic anhydride-modified polypropylene on the physical and mechanical properties of polypropylene-based wood/plastic composites. *Journal of Wood Chemistry and Technology*, 38(3):224–232, 2018.

[24] S. Wang, Y. Lin, X. Zhang, and C. Lu. Towards mechanically robust cellulose fiber-reinforced polypropylene composites with strong interfacial interaction through dual modification. *RSC Advances*, 5(63):50660–50667, 2015.

[25] S. M. Luz, J. Del Tio, G. Rocha, A. Gonalves, and A. DelArco Jr. Cellulose and cellulignin from sugarcane bagasse reinforced polypropylene composites: Effect of acetylation on mechanical and thermal properties. *Composites Part A: Applied Science and Manufacturing*, 39(9):1362–1369, 2008.

[26] X. Li, L. G. Tabil, and S. Panigrahi. Chemical treatments of natural fiber for use in natural fiber-reinforced composites: A review. *Journal of Polymers and the Environment*, 15(1):25–33, 2007.

[27] V. A. Alvarez, R. A. Ruscekaite, and A. Vazquez. Mechanical properties and water absorption behavior of composites made from a biodegradable matrix and alkaline-treated sisal fibers. *Journal of Composite Materials*, 37(17):1575–1588, 2003.

[28] D. Garca-López, O. Picazo, J.C. Merino, and J.M. Pastor. Polypropyleneclay nanocomposites: effect of compatibilizing agents on clay dispersion. *European Polymer Journal*, 39(5):945 – 950, 2003.

[29] D. Roberts and R. C. Constable. *Chemical Coupling Agents for Filled and Grafted Polypropylene Composites.* 2003.

[30] A. K. Bledzki, S. Reihmane, and J. Gassan. Properties and modification methods for vegetable fibers for natural fiber composites. *Journal of Applied Polymer Science*, 59 (8):1329–1336, 1996.

[31] M. Schilling, M. Bouchard, H. Khanjian, T. Learner, A. Phenix, and R. Rivenc. Application of chemical and thermal analysis methods for studying cellulose ester plastics. *Accounts of Chemical Research*, 43(6):888–896, 2010.

[32] M. M. Kabir, H. Wang, K. T. Lau, and F. Cardona. Chemical treatments on plant-based natural fibre reinforced polymer composites: An overview. *Composites Part B: Engineering*, 43(7):2883–2892, 2012.

[33] J. Kim, S. Yun, and Z. Ounaies. Discovery of cellulose as a smart material. *Macromolecules*, 39(12):4202–4206, 2006.

[34] A. K. Mohanty, A. Wibowo, M. Misra, and L. T. Drzal. Development of renewable resource-based cellulose acetate bioplastic: Effect of process engineering on the performance of cellulosic plastics. *Polymer Engineering and Science*, 43(5):1151–1161, 2003.

[35] Z. Zhou, X. Peng, L. Zhong, L. Wu, X. Cao, and R. Cang Sun. Electrospun cellulose acetate supported Ag@AgCl composites with facet-dependent photocatalytic properties on degradation of organic dyes under visible-light irradiation. *Carbohydrate Polymers*, 136:322 – 328, 2016.

[36] A. Pron, Y. Nicolau, F. Genoud, and M. Nechtschein. Flexible, highly transparent, and conductive polyaniline-cellulose acetate composite films. *Journal of Applied Polymer Science*, 63(8):971–977.

[37] A. Carolina Mazarin de Moraes, P. Fernanda Andrade, A. Fonseca de Faria, M. Batista Simes, F. Carlos Carneiro Soares Salomo, E. Bed Barros, M. do Carmo Gonalves, and O. Luiz Alves. Fabrication of transparent and ultraviolet shielding composite films based on graphene oxide and cellulose acetate. *Carbohydrate Polymers*, 123:217 – 227, 2015.

[38] S. Kalia and L. Avérous. *Biopolymers: Biomedical and environmental applications*, volume 70. John Wiley & Sons, 2011.

[39] P. I. C. Claro, A. R. S. Neto, A. C. C. Bibbo, L. H. C. Mattoso, M. S. R. Bastos, and J. M. Marconcini. Biodegradable blends with potential use in packaging: A comparison of PLA/Chitosan and PLA/Cellulose Acetate films. *Journal of Polymers and the Environment*, 24(4):363–371, 2016.

[40] K. J. Edgar, C. M. Buchanan, J. S. Debenham, P. A. Rundquist, B. D. Seiler, M. C. Shelton, and D. Tindall. Advances in cellulose ester performance and application. *Progress in Polymer Science*, 26(9):1605–1688, 2001.

[41] B. Wang, J. Chen, H. Peng, J. Gai, J. Kang, and Y. Cao. Investigation on changes in the miscibility, morphology, rheology and mechanical behavior of melt processed

cellulose acetate through adding polyethylene glycol as a plasticizer. *Journal of Macromolecular Science, Part B*, 55(9):894–907, 2016.

[42] G. Wypych. *Plasticizer use and selection for specific polymers*. Chemtec Publishing, Toronto, 2nd edition, 2012.

[43] S. Zepnik, S. Kabasci, Hans-Joachim Radusch, and T. Wodke. Influence of external plasticization on rheological and thermal properties of cellulose acetate with respect to its foamability. *Journal of Materials Science and Engineering*, 2(2):152–163, 2012.

[44] R. F. Gould. Plasticization and plasticizer processes. *Washington, DC*, 1965.

[45] A. K. Mohanty, A. Wibowo, M. Misra, and L. T. Drzal. Effect of process engineering on the performance of natural fiber reinforced cellulose acetate biocomposites. *Composites Part A: Applied Science and Manufacturing*, 35(3):363–370, 2004.

[46] V. P. Ghiya, V. Dave, R. A. Gross, and S. P. McCarthy. Biodegradability of cellulose acetate plasticized with citrate esters. *Journal of Macromolecular Science: Pure and Applied Chemistry*, 33(5):627–638, 1996.

[47] R. Quintana, O. Persenaire, Y. Lemmouchi, J. Sampson, S. Martin, L. Bonnaud, and P. Dubois. Enhancement of cellulose acetate degradation under accelerated weathering by plasticization with eco-friendly plasticizers. *Polymer Degradation and Stability*, 98(9):1556–1562, 2013.

[48] O. A. Fridman and A. V. Sorokina. Criteria of efficiency of cellulose acetate plasticization. *Polymer Science Series B*, 48(5):233–236, 2006.

[49] J. Aristia de Lima, C. Augusto Pinotti, M. Isabel Felisberti, and Maria do Carmo Gonalves. Morphology and mechanical properties of nanocomposites of cellulose acetate and organic montmorillonite prepared with different plasticizers. *Journal of Applied Polymer Science*, 124(6):4628–4635, 2012.

[50] R. E. Lee, D. Hallenbeck, and J. Likens. *Stabilization of Flame-Retarded Polypropylene*. CRC Press, 2003.

[51] E. Turi. *Thermal characterization of polymeric materials*. Elsevier, 2012.

[52] F. Laoutid, L. Bonnaud, M. Alexandre, J. M. Lopez-Cuesta, and P. Dubois. New prospects in flame retardant polymer materials: From fundamentals to nanocomposites. *Materials Science and Engineering: R: Reports*, 63(3):100–125, 2009.

[53] H. Macsksy and G. Palyi. *Plastics: Their behaviour in fires*, volume 6. Elsevier, 2012.

[54] V. Babrauskas and R. D. Peacock. Heat release rate: The single most important variable in fire hazard. *Fire Safety Journal*, 18(3):255–272, 1992.

[55] A. Richard Horrocks and D. Price. *Fire retardant materials*. Woodhead Publishing, 2001.

[56] J. Murphy. *Additives for plastics handbook*. Elsevier, 2001.

[57] M.R. Christy. Standards, bans, and flame retardants. *Plastics Compounding(USA)*, 16(5):56–66, 1993.

[58] M. Zhang, A. Buekens, and X. Li. Brominated flame retardants and the formation of dioxins and furans in fires and combustion. *Journal of Hazardous Materials*, 304: 26–39, 2016.

[59] M. Zober, M. Ott, O. Päpke, K. Senft, and C. Germann. Morbidity study of extruder personnel with potential exposure to brominated dioxins and furans. I results of blood monitoring and immunological tests. *British Journal of Industrial Medicine*, 49(8): 532–544, 1992.

[60] R. Delobel, M. Le Bras, N. Ouassou, and F. Alistiqsa. Thermal behaviours of ammonium polyphosphate-pentaerythritol and ammonium pyrophosphate-pentaerythritol intumescent additives in polypropylene formulations. *Journal of Fire Sciences*, 8(2): 85–108, 1990.

[61] L. Atabek Savas, T. Kaya Deniz, U. Tayfun, and M. Dogan. Effect of microcapsulated red phosphorus on flame retardant, thermal and mechanical properties of thermoplastic polyurethane composites filled with huntite & hydromagnesite mineral. *Polymer Degradation and Stability*, 135:121–129, 2017.

[62] Zhu-Bao Shao, C. Deng, Y. Tan, Ming-Jun Chen, L. Chen, and Yu-Zhong Wang. Flame retardation of polypropylene via a novel intumescent flame retardant: Ethylenediamine-modified ammonium polyphosphate. *Polymer Degradation and Stability*, 106:88 – 96, 2014.

[63] I. Van der Veen and J. de Boer. Phosphorus flame retardants: Properties, production, environmental occurrence, toxicity and analysis. *Chemosphere*, 88(10):1119–1153, 2012.

[64] J. Ellis, M. Shah, K. M. Kubachka, and J. A. Caruso. Determination of organophosphorus fire retardants and plasticizers in waste water samples using MAE-SPME with GC-ICPMS and GC-TOFMS detection. *Journal of Environmental Monitoring*, 9(12):1329–1336, 2007.

[65] H. Tan, C. Peng, Y. Guo, X. Wang, Y. Wu, and D. Chen. Organophosphate flame retardants in house dust from south china and related human exposure risks. *Bulletin of Environmental Contamination and Toxicology*, 99(3):344–349, 2017.

[66] G. Marosi, P. Anna, A. Marton, G. Bertalan, A. Bota, A. Toth, M. Mohai, and I. Racz. Flameretarded polyolefin systems of controlled interphase. *Polymers for Advanced Technologies*, 13(1012):1103–1111, 2002.

[67] M. Le Bras, S. Duquesne, M. Fois, M. Grisel, and F. Poutch. Intumescent polypropylene/flax blends: A preliminary study. *Polymer Degradation and Stability*, 88(1): 80–84, 2005.

[68] P. R. Hornsby and R. N. Rothon. Fire retardant fillers for polymers. *Fire retardancy of polymers: New applications of mineral fillers*, 2005.

[69] R. N. Rothon and P. R. Hornsby. Flame retardant effects of magnesium hydroxide. *Polymer Degradation and Stability*, 54(2-3):383–385, 1996.

[70] P. R. Hornsby and C. L. Watson. A study of the mechanism of flame retardance and smoke suppression in polymers filled with magnesium hydroxide. *Polymer Degradation and Stability*, 30(1):73–87, 1990.

[71] S. Miyata, T. Imahashi, and H. Anabuki. Fire–retarding polypropylene with magnesium hydroxide. *Journal of Applied Polymer Science*, 25(3):415–425.

[72] Q. Zhang, M. Tian, Y. Wu, G. Lin, and L. Zhang. Effect of particle size on the properties of $Mg(OH)_2$-filled rubber composites. *Journal of Applied Polymer Science*, 94(6):2341–2346.

[73] R. Rothon. Mineral fillers in thermoplastics: Filler manufacture and characterisation, 1999.

[74] H. Huang, M. Tian, L. Liu, W. Liang, and L. Zhang. Effect of particle size on flame retardancy of $Mg(OH)_2$-filled ethylene vinyl acetate copolymer composites. *Journal of Applied Polymer Science*, 100(6):4461–4469.

[75] M. Modesti, A. Lorenzetti, D. Bon, and S. Besco. Thermal behaviour of compatibilised polypropylene nanocomposite: Effect of processing conditions. *Polymer Degradation and Stability*, 91(4):672 – 680, 2006.

[76] N. Othman, H. Ismail, and M. Mariatti. Effect of compatibilisers on mechanical and thermal properties of bentonite filled polypropylene composites. *Polymer Degradation and Stability*, 91(8):1761 – 1774, 2006.

[77] S. M. Lai, H. C. Li, and Y. C. Liao. Properties and preparation of compatibilized nylon 6 nanocomposites/ABS blends: Part II physical and thermal properties. *European Polymer Journal*, 43(5):1660 – 1671, 2007.

[78] P. R. Hornsby and C. L. Watson. Interfacial modification of polypropylene composites filled with magnesium hydroxide. *Journal of Materials Science*, 30(21):5347–5355, 1995.

[79] H. Shen, Y. Wang, and K. Mai. Effect of compatibilizers on thermal stability and mechanical properties of magnesium hydroxide filled polypropylene composites. *Thermochimica Acta*, 483(1):36 – 40, 2009.

[80] P. Georlette, I. Finberg, and G. Reznick. New flame retardant systems for polypropylene. *ANTEC'95.*, 3:3536–3540, 1995.

[81] U. Einsele, W. Koch, and H. Herlinger. Investigations into the development of heat when textiles burn in air. *Melliand Textbericht International Textile Reports*, 65(3): 200–206, 1984.

[82] N. S. Allen and M. Edge. *Fundamentals of polymer degradation and stabilization*. Springer Science & Business Media, 1992.

[83] L. Ballice and R. Reimert. Classification of volatile products from the temperature-programmed pyrolysis of polypropylene (PP), atactic-polypropylene (aPP) and thermogravimetrically derived kinetics of pyrolysis. *Chemical Engineering and Processing: Process Intensification*, 41(4):289–296, 2002.

[84] S. Zhang and A. Richard Horrocks. A review of flame retardant polypropylene fibres. *Progress in Polymer Science*, 28(11):1517–1538, 2003.

[85] E. Suljovrujic. The influence of molecular orientation on the crosslinking/oxidative behaviour of iPP exposed to gamma radiation. *European Polymer Journal*, 45(7): 2068–2078, 2009.

[86] Y. Wang, H. Shen, G. Li, and K. Mai. Crystallization and melting behavior of PP/CaCO3 nanocomposites during thermo-oxidative degradation. *Journal of Thermal Analysis and Calorimetry*, 100(3):999–1008, 2010.

[87] S. Suzuki, Y. Nakamura, A. Kamrul Hasan, B. Liu, M. Terano, and H. Nakatani. Dependence of tacticity distribution in thermal oxidative degradation of polypropylene. *Polymer Bulletin*, 54(4):311–319, 2005.

[88] B. Fillon, J. C. Wittmann, B. Lotz, and A. Thierry. Self-nucleation and recrystallization of isotactic polypropylene (α-phase) investigated by differential scanning calorimetry. *Journal of Polymer Science Part B: Polymer Physics*, 31(10):1383–1393, 1993.

[89] A. Riga, R. Collins, and G. Mlachak. Oxidative behavior of polymers by thermogravimetric analysis, differential thermal analysis and pressure differential scanning calorimetry. *Thermochimica Acta*, 324(1):135–149, 1998.

[90] T. Roy Crompton. *Thermo-oxidative degradation of polymers*. ISmithers, 2010.

[91] A. K. Burnham, R. L. Braun, H. R. Gregg, and A. M. Samoun. Comparison of methods for measuring kerogen pyrolysis rates and fitting kinetic parameters. *Energy & Fuels*, 1(6):452–458, 1987.

[92] S. Vyazovkin, A. K. Burnham, J. M. Criado, L. A. Prez-Maqueda, C. Popescu, and N. Sbirrazzuoli. ICTAC kinetics committee recommendations for performing kinetic computations on thermal analysis data. *Thermochimica Acta*, 520(1-2):1–19, 2011.

[93] J. E. White, W. James Catallo, and B. L. Legendre. Biomass pyrolysis kinetics: A comparative critical review with relevant agricultural residue case studies. *Journal of Analytical and Applied Pyrolysis*, 91(1):1–33, 2011.

[94] S. Vyazovkin, K. Chrissafis, M. Laura Di Lorenzo, N. Koga, M. Pijolat, B. Roduit, N. Sbirrazzuoli, and J. Josep Suol. ICTAC kinetics committee recommendations for collecting experimental thermal analysis data for kinetic computations. *Thermochimica Acta*, 590:1 – 23, 2014.

[95] P. Rantucha, D. Kakovb, and B. Nagyplb. Investigation of activation energy of polypropylene composite thermooxidation by model-free methods. *European Science and Research Institute*, 2014.

[96] K. Slopiecka, P. Bartocci, and F. Fantozzi. Third international conference on applied energy. *Applied Energy*, 3(7):491–498, 2012.

[97] J. Opfermann, E. Kaisersberger, and H. Flammersheim. Model–free analysis of thermoanalytical data-advantages and limitations. *Thermochimica Acta*, 391(1-2):119–127, 2002.

[98] T. Akahira and T. Sunose. Method of determining activation deterioration constant of electrical insulating materials. *Res Rep Chiba Inst Technol (Sci Technol)*, 16: 22–31, 1971.

[99] M. J. Starink. The determination of activation energy from linear heating rate experiments: A comparison of the accuracy of isoconversion methods. *Thermochimica Acta*, 404(1):163–176, 2003.

[100] ASTM International. ASTM E1354-17 standard test method for heat and visible smoke release rates for materials and products using an oxygen consumption calorimeter. 2017.

[101] W. K. Chow and S. S. Han. Heat release rate calculation in oxygen consumption calorimetry. *Applied Thermal Engineering*, 31(2-3):304–310, 2011.

[102] W. J. Parker. Calculation of the heat release rate by oxygen consumption for various application. *Journal of Fire Science*, 2(5):380–395, 1984.

[103] V. Babrauskas. Development of the cone–calorimeter – a bench scale heat-release apparatus based on oxygen consumption. *Fire and Polymers*, 8(2):81–95, 1984.

[104] D. Hopkins Jr and J. G. Quintiere. Material fire properties and predictions for thermoplastics. *Fire Saftey Journal*, 26(3):241–268, 1996.

[105] M. Foley and D. Drysdale. Note: Smoke measurement and the cone calorimeter. *Fire and Materials*, 18(6):385–387, 1994.

[106] S. Eibl. Influence of carbon fibre orientation on reaction-to-fire properties of polymer matrix composites. *Fire and Materials*, 36(4):309–324, 2012.

[107] ASTM International. ASTM D3801-19 standard test method for measuring the comparative burning characteristics of solid plastics in a vertical position. 2019.

[108] D. A. Biuhme. Iso-ignitability test and proposed criteria. *Fire and Materials*, 11(4): 195–199, 1987.

[109] P. Lv, Z. Wang, K. Hu, and W. Fan. Flammability and thermal degradation of flame retarded polypropylene composites containing melamine phosphate and pentaerythritol derivatives. *Polymer Degradation and Stability*, 90(3):523–534, 2005.

[110] B. Schartel and T. Richard Hull. Development of fireretarded materials-interpretation of cone calorimeter data. *Fire and Materials*, 31(5):327–354, 2007.

[111] A. P. Mouritz and A. Geoff Gibson. *Fire properties of polymer composite materials*, volume 143. Springer Science & Business Media, 2007.

[112] E. D. Weil, N. G. Patel, M. Said, M. M. Hirschler, and S. Shakir. Oxygen index: correlations to other fire tests. *Fire and Materials*, 16(4):159–167, 1992.

[113] ASTM International. ASTM D2863-17a standard test method for measuring the minimum oxygen concentration to support candle-like combustion of plastics (oxygen index). 2017.

[114] M. Lewin, S. M. Atlas, and E. M. Pearce. *Flame -Retardant polymeric materials*. Plenum Press., New York, 1975.

[115] G. W. Mulholland. *Smoke production and properties*. SFPE, 2008.

[116] P. J. DiNenno. *SFPE handbook of fire protection engineering*. SFPE, 2008.

[117] R. N. Walters, S. M. Hackett, and R. E. Lyon. Heats of combustion of high temperature polymers. *Fire and Materials*, 24(5):245–252, 2000.

[118] D. Willem V. Krevelen and K. Te Nijenhuis. *Properties of polymers: their correlation with chemical structure; their numerical estimation and prediction from additive group contributions*. Elsevier, 2009.

[119] D. Willem V. Krevelen and K. Te Nijenhuis. *Properties of polymers: their correlation with chemical structure; their numerical estimation and prediction from additive group contributions*. Elsevier, 2009.

[120] ASTM International. ASTM D638-14 standard test method for tensile properties of plastics. 2014.

[121] J. F. Shackelford. *Stress versus strain*, page 155. Pearson Higher Education. Inc, Toronto, 2015.

[122] D. R. Askeland and W. J. Wright. *Science and Engineering of Materials*. Nelson Education, 2015.

[123] Y. Al Herz. *Optimization of mechanical properties of polypropylene-based composite*. University of Waterloo, Waterloo,Ontario, 2012.

[124] H. Lim and S. W. Hoag. Plasticizer effects on physical–mechanical properties of solvent cast soluplus® films. *Aaps Pharmscitech*, 14(3):903–910, 2013.

[125] ASTM International. ASTM D256-10(2018) standard test methods for determining the izod pendulum impact resistance. 2018.

[126] R. Guinebretire. *X-ray diffraction by polycrystalline materials*. John Wiley & Sons, 2013.

[127] S. Nara and T. Komiya. Studies on the relationship between water-satured state and crystallinity by the diffraction method for moistened potato starch. *Starch-Stärke*, 35(12):407–410, 1983.

[128] V. A. Greenhut and J. J. Friel. Application of advanced field emission SEM and energy dispersive spectroscopy to ceramic materials. *Microscopy and Analysis*, 1997.

[129] N. Elton Kaufmann. *Characterization of materials*. John Wiley & Sons, Inc., Hoboken, New Jersey., 2nd edition, 2003.

[130] H. S. Barud, A. M. de Arajo Jnior, D. B. Santos, R. M. N. de Assuno, C. S. Meireles, D. A. Cerqueira, G. Rodrigues Filho, C. A. Ribeiro, Y. Messaddeq, and S. J. L. Ribeiro. Thermal behavior of cellulose acetate produced from homogeneous acetylation of bacterial cellulose. *Thermochimica Acta*, 471(1):61–69, 2008.

[131] M. Rahman and C. S. Brazel. The plasticizer market: An assessment of traditional plasticizers and research trends to meet new challenges. *Progress in Polymer Science*, 29(12):1223 – 1248, 2004.

[132] A. Bendaoud and Y. Chalamet. Plasticizing effect of ionic liquid on cellulose acetate obtained by melt processing. *Carbohydrate Polymers*, 108:75–82, 2014.

[133] A. A. Hanna, A. H. Basta, H. El-Saied, and I. F. Abadir. Thermal properties of cellulose acetate and its complexes with some transition metals. *Polymer Degradation and Stability*, 63(2):293–296, 1999.

[134] Mei-Rong Huang and Xin-Gui Li. Thermal degradation of cellulose and cellulose esters. *Journal of Applied Polymer Science*, 68(2):293–304, 1998.

[135] A. Robledo Fialho e Moraes, C. Pola, A. Paula Bilck, F. Yamashita, J. Tronto, E. Antonio Alves Medeiros, and N. de Fátima Ferreira Soares. Starch, cellulose acetate and polyester biodegradable sheets: Effect of composition and processing conditions. *Materials Science and Engineering: C*, 78:932–941, 2017.

[136] C. Pang, R. A. Shanks, and F. Daver. Characterization of kenaf fiber composites prepared with tributyl citrate plasticized cellulose acetate. *Composites Part A: Applied Science and Manufacturing*, 70:52–58, 2015.

[137] N. Gil, M. Saska, and I. Negulescu. Evaluation of the effects of biobased plasticizers on the thermal and mechanical properties of poly(vinyl chloride). *Journal of Applied Polymer Science*, 102(2):1366–1373, 2006.

[138] M. Sousa, A. Rita Brs, H. Isabel M. Veiga, F. Castelo Ferreira, M. Norberta de Pinho, N. T. Correia, and M. Dionsio. Dynamical characterization of a cellulose acetate polysaccharide. *The Journal of Physical Chemistry B*, 114(34):10939–10953, 2010.

[139] R. RM de Freitas, A. M Senna, and V. R. Botaro. Influence of degree of substitution on thermal dynamic mechanical and physicochemical properties of cellulose acetate. *Industrial Crops and Products*, 109:452–458, 2017.

[140] W. Rosli W. Daud and F. Muhammad Djuned. Cellulose acetate from oil palm empty fruit bunch via a one step heterogeneous acetylation. *Carbohydrate Polymers*, 132: 252–260, 2015.

[141] Hwan-Man Park, M. Misra, L. T. Drzal, and A. K. Mohanty. green nanocomposites from cellulose acetate bioplastic and clay: Effect of eco-friendly triethyl citrate plasticizer. *Biomacromolecules*, 5(6):2281–2288, 2004.

[142] R. Navarro, L. Torre, J. M. Kenny, and A. Jimnez. Thermal degradation of recycled polypropylene toughened with elastomers. *Polymer Degradation and Stability*, 82(2): 279–290, 2003.

[143] Z. Gao, T. Kaneko, I. Amasaki, and M. Nakada. A kinetic study of thermal degradation of polypropylene. *Polymer Degradation and Stability*, 80(2):269–274, 2003.

[144] S. Gaan, L. Mauclaire, P. Rupper, V. Salimova, Thuy-Tien Tran, and M. Heuberger. Thermal degradation of cellulose acetate in presence of bis-phosphoramidates. *Journal of Analytical and Applied Pyrolysis*, 90(1):33–41, 2011.

[145] G. E. Zaikov and S. M. Lomakin. Ecological issue of polymer flame retardancy. *Journal of Applied Polymer Science*, 86(10):2449–2462, 2002.

[146] L. Sun, Q. Wu, Y. Xie, K. Song, S. Lee, and Q. Wang. Thermal decomposition of fire-retarded wood flour/polypropylene composites. *Journal of Thermal Analysis and Calorimetry*, 123(1):309–318, 2016.

[147] M. Seifali Abbas-Abadi, M. Nekoomanesh Haghighi, H. Yeganeh, and B. Bozorgi. The effect of melt flow index, melt flow rate, and particle size on the thermal degradation of commercial high density polyethylene powder. *Journal of Thermal Analysis and Calorimetry*, 114(3):1333–1339, 2013.

[148] P. Paik and K. K. Kar. Kinetics of thermal degradation and estimation of lifetime for polypropylene particles: Effects of particle size. *Polymer Degradation and Stability*, 93(1):24 – 35, 2008.

[149] S. Coiai, E. Passaglia, A. Hermann, S. Augier, D. Pratelli, and R. C. Streller. The influence of the compatibilizer on the morphology and thermal properties of polypropylene-layered double hydroxide composites. *Polymer Composites*, 31(4):744–754.

[150] T. J. Ohlemiller. Modeling of smoldering combustion propagation. *Progress in Energy and Combustion Science*, 11(4):277–310, 1985.

[151] X. Chen, J. Yu, and S. Guo. Thermal oxidative degradation kinetics of PP and PP/$Mg(OH)_2$ flame-retardant composites. *Journal of Applied Polymer Science*, 103 (3):1978–1984, 2007.

[152] X. Chen, J. Yu, S. Guo, Z. Luo, and M. He. Flammability and thermal oxidative degradation kinetics of magnesium hydroxide and expandable graphite flame retarded polypropylene composites. *Journal of Macromolecular Science, Part A: Pure and Applied Chemistry*, 45(9):712–720, 2008.

[153] B. Elisabeth Güttler. Effect of thermal and chemical treatment of soy flour on soy-polypropylene composite properties. 2012.

[154] H. Seok Lee, D. Cho, and S. Ok Han. Effect of natural fiber surface treatments on the interfacial and mechanical properties of henequen/polypropylene biocomposites. *Macromolecular Research*, 16(5):411–417, 2008.

[155] S. Matko, A. Toldy, S. Keszei, P. Anna, G. Bertalan, and G. Marosi. Flame retardancy of biodegradable polymers and biocomposites. *Polymer Degradation and Stability*, 88(1):138–145, 2005.

[156] L. Liu, H. Zhang, L. Sun, Q. Kong, and J. Zhang. Flame-retardant effect of montmorillonite intercalation iron compounds in polypropylene/aluminum hydroxide composites system. *Journal of Thermal Analysis and Calorimetry*, 124(2):807–814, 2016.

[157] B. RT Simoneit, J. J. Schauer, C. Nolte, D. R. Oros, V. O. Elias, M. Fraser, W. Rogge, and G. R. Cass. Levoglucosan, a tracer for cellulose in biomass burning and atmospheric particles. *Atmospheric Environment*, 33(2):173–182, 1999.

[158] J. E. Mark. *Polymer data handbook*. Oxford University Press, 2009.

[159] C. Albano, J. Gonzalez, M. Ichazo, and D. Kaiser. Thermal stability of blends of polyolefins and sisal fiber. *Polymer Degradation and Stability*, 66(2):179–190, 1999.

[160] W. G. Glasser, R. Taib, R. K. Jain, and R. Kander. Fiber-reinforced cellulosic thermoplastic composites. *Journal of Applied Polymer Science*, 73(7):1329–1340, 1999.

[161] J. Gomez-Bueso, M. Westin, R. Torgilsson, P. Olesen, and R. Simonson. Composites made from acetylated lignocellulosic fibers of different origin Part I. properties of dry-formed fiberboards. *European Journal of Wood and Wood Products*, 57(6):433–438, 1999.

[162] A. Espert, W. Camacho, and S. Karlson. Thermal and thermomechanical properties of biocomposites made from modified recycled cellulose and recycled polypropylene. *Journal of Applied Polymer Science*, 89(9):2353–2360, 2003.

[163] C. M. Keely, X. Zhang, and V. J. McBrierty. Hydration and plasticization effects in cellulose acetate: A solid–state nmr study. *Journal of Molecular Structure*, 355(1): 33–46, 1995.

[164] C. Lucena M. da Conceicao, A. Ellen V. de Alencar, S. Elaine Mazzeto, and S. de A Soares. The effect of additives on the thermal degradation of cellulose acetate. *Polymer Degradation and Stability*, 80(1):149–155, 2003.

[165] C. Feng, Y. Zhang, D. Liang, S. Liu, Z. Chi, and J. Xu. Flame retardancy and thermal degradation behaviors of polypropylene composites with novel intumescent flame retardant and manganese dioxide. *Journal of Analytical and Applied Pyrolysis*, 104:59–67, 2013.

[166] R. Jeencham, N. Suppakarn, and K. Jarukumjorn. Effect of flame retardants on flame retardant, mechanical, and thermal properties of sisal fiber/polypropylene composites. *Composites Part B: Engineering*, 56:249–253, 2014.

[167] J. Liang and Y. Zhang. A study of the flame–retardant properties of polypropylene/$Al(OH)_3$/$Mg(OH)_2$ composites. *Polymer International*, 59(4):539–542, 2010.

[168] C. J. Hilado. *Flammability handbook for plastics*. CRC Press, 1998.

[169] N. Suppakarn and K. Jarukumjorn. Mechanical properties and flammability of sisal/PP composites: Effect of flame retardant type and content. *Composites Part B: Engineering*, 40(7):613–618, 2009.

[170] S. Miyata, T. Imahashi, and H. Anabuki. Fire-retarding polypropylene with magnesium hydroxide. *Journal of Applied Polymer Science*, 25(3):415–425, 1980.

[171] O. Das, N. Kyeun Kim, A. L. Kalamkarov, A. K. Sarmah, and D. Bhattacharyya. Biochar to the rescue: Balancing the fire performance and mechanical properties of polypropylene composites. *Polymer Degradation and Stability*, 144:485–496, 2017.

[172] H. Balakrishnan, A. Hassan, N. Ali Isitman, and C. Kaynak. On the use of magnesium hydroxide towards halogen-free flame-retarded polyamide-6/polypropylene blends. *Polymer Degradation and Stability*, 97(8):1447–1457, 2012.

[173] M. Wang, Xiao-Fei Zeng, Jing-Yi Chen, Jie-Xin Wang, Liang-Liang Zhang, and Jian-Feng Chen. Magnesium hydroxide nanodispersion for polypropylene nanocomposites with high transparency and excellent fire-retardant properties. *Polymer Degradation and Stability*, 146:327–333, 2017.

[174] ASTM International. ASTM D4809-18 standard test method for heat of combustion of liquid hydrocarbon fuels by bomb calorimeter (precision method). 2018.

[175] C. Jiao, J. Zhang, and F. Zhang. Combustion behavior of intumescent flame retardant polypropylene composites. *Journal of Fire Sciences*, 26(5):455–469, 2008.

[176] R. E. Lyon. Plastics and rubber. *Handbook of Building Materials for Fire Protection*, pages 3.1–3.51, 2004.

[177] G. Gallina, E. Bravin, C. Badalucco, G. Audisio, M. Armanini, A. De Chirico, and F. Provasoli. Application of cone calorimeter for the assessment of class of flame retardants for polypropylene. *Fire and Materials*, 22(1):15–18, 1998.

[178] O. A. Ezekoye. *Conduction of Heat in Solids*, pages 25–52. Springer, 2016.

[179] D. C. O. Marney, L. J. Russell, T. M. Soegeng, and V. P. Dowling. Mechanistic analysis of the fire performance of a fire retardant system. *Journal of Fire Sciences*, 25(6):471–497, 2007.

[180] S. Gaan, G. Sun, K. Hutches, and M. H. Engelhard. Effect of nitrogen additives on flame retardant action of tributyl phosphate: phosphorusnitrogen synergism. *Polymer Degradation and Stability*, 93(1):99–108, 2008.

[181] H. Guo, R. E. Lyon, N. Safronava, R. N. Walters, and S. Crowley. A simplified model on carbon monoxide yield in burning of polymeric solids containing flame retardants. *Fuel*, 222:175–179, 2018.

[182] C. Huggett. Estimation of rate of heat release by means of oxygen consumption measurements. *Fire and Materials*, 4(2):61–65, 1980.

[183] V. Babrauskas. The generation of CO in bench-scale fire tests and the prediction for real-scale fires. *Fire and Materials*, 19(5):205–213, 1995.

[184] C. Ferreira, C. Dal Castel, M. Oviedo, and R. Mauler. Isothermal and non-isothermal crystallization kinetics of polypropylene/exfoliated graphite nanocomposites. *Thermochimica Acta*, 553:40–48, 2013.

[185] J. Gonzalez-Calderon, J. Vallejo-Montesinos, A. Almendarez-Camarillo, R. Montiel, and E. Prez. Non-isothermal crystallization analysis of isotactic polypropylene filled with titanium dioxide particles modified by a dicarboxylic acid. *Thermochimica Acta*, 631:8–17, 2016.

[186] L. Mandelkern and H. D. Keith. Crystallization of polymers. *Physics Today*, 17:52, 1964.

[187] B. Wunderlich. Macromolecular physics, crystal nucleation, growth, annealing, vol. 2. *Academic: New York*, 1976.

[188] T. Xu, Y. Wang, D. He, Y. Xu, Q. Li, and C. Shen. Nucleation effect of layered metal phosphonate on crystallization of isotactic polypropylene. *Polymer Testing*, 34:131–139, 2014.

[189] P. Jacoby, B. Bersted, W. Kissel, and C. Smith. Studies on the β-crystalline form of isotactic polypropylene. *Journal of Polymer Science Part B: Polymer Physics*, 24 (3):461–491, 1986.

[190] F. Xiong, R. Guan, Z. Xiao, B. Xiang, and De. Lu. Influence of β–nucleators on iPP crystallization and morphology. *Polymer-Plastics Technology and Engineering*, 46(2):97–103, 2007.

[191] Y. Lv, Y. Huang, M. Kong, and G. Li. Improved thermal oxidation stability of polypropylene films in the presence of β-nucleating agent. *Polymer Testing*, 32(2): 179–186, 2013.

[192] Yuan-Hong Shi and Q. Dou. Non-isothermal crystallization kinetics of β–nucleated isotactic polypropylene. *Journal of Thermal Analysis and Calorimetry*, 112(2):901–911, 2013.

[193] D. G. Papageorgiou, K. Chrissafis, and D. N. Bikiaris. β nucleated polypropylene: processing, properties and nanocomposites. *Polymer Reviews*, 55(4):596–629, 2015.

[194] J. Yin, S. Wang, Y. Zhang, and Y. Zhang. Isothermal crystallization kinetics of PP in PP/$Mg(OH)_2$ composites. *Journal of Polymer Science Part B: Polymer Physics*, 43(14):1914–1923, 2005.

[195] P. R. Hornsby. The application of magnesium hydroxide as a fire retardant and smoke-suppressing additive for polymers. *Fire and Materials*, 18(5):269–276, 1994.

[196] J. Velasco, C. Morhain, A. Martnez, M. Rodrguez-Prez, and J. De Saja. The effect of filler type, morphology and coating on the anisotropy and microstructure heterogeneity of injection-moulded discs of polypropylene filled with aluminium and magnesium hydroxides. Part 1. a wide-angle X-ray diffraction study. *Polymer*, 43(25):6805–6811, 2002.

[197] M. Cook and J. Harper. The influence of magnesium hydroxide morphology on the crystallinity and properties of filled polypropylene. *Advances in Polymer Technology: Journal of the Polymer Processing Institute*, 17(1):53–62, 1998.

[198] Z. Lin, Y. Qiu, and K. Mai. Crystallization and melt behavior of $Mg(OH)_2$/PP composites modified by functionalized polypropylene. *Journal of Applied Polymer Science*, 92(6):3610–3621, 2004.

[199] A. Amash and P. Zugenmaier. Study on cellulose and xylan filled polypropylene composites. *Polymer Bulletin*, 40(2-3):251258, 1998.

[200] D. G. Gray. Polypropylene transcrystallization at the surface of cellulose fibes. *Journal of Polymer Science: Polymer Letters Edition*, 12(9):509–515, 1974.

[201] D. T. Qullin, M. Yin, J. A. Koutsky, and D. Caulfield. Crystallinity in the polypropylene /cellulose system. II. crystallization kientics. *Journal of Applied Polymer Science*, 52(5):605, 1994.

[202] M. Folkes. *Interfacial crystallization of polypropylene in composites*, pages 340–370. Springer, 1995.

[203] M. Fujiyama. Structures and properties of injection moldings of β-crystal nucleator-added polypropylenes: Part 1 effect of β-crystal nucleator content. *International Polymer Processing*, 10(2):172–178, 1995.

[204] J. Varga. β-modification of isotactic polypropylene: Preparation, structure, processing, properties, and application. *Journal of Macromolecular Science, Part B*, 41(4-6): 1121–1171, 2002.

[205] R. L. Blaine. Determination of polymer crystallinity by DSC. *TA Instruments, New Castle, DE*, 2013.

[206] Z. Wei, W. Zhang, G. Chen, J. Liang, Y. Chang, L. Liu, P. Wang, and J. Sun. Crystallization behavior of isotactic polypropylene/magnesium salt whisker composites modified by compatibilizer PP-g-MAH. *Journal of Thermal Anlysis and Calorimetry*, 103(2):701–710, 2011.

[207] Yue-fei Zhang, H. Chen, Bei-bei Liu, Yue-hua Gu, and Xiao-xuan Li. Isothermal and non-isothermal crystallization of isotactic polypropylene nucleated with 1, 3, 5-benzenetricarboxylic acid tris (cyclohexylamide). *Thermochimica Acta*, 590:226–231, 2014.

[208] M. Ghorbanzadeh Ahangari, A. Fereidoon, N. Kordani, and H. Garmabi. Effect of nano-nucleating agent addition on the isothermal and nonisothermal crystallization kinetics of isotactic polypropylene. *Polymer Bulletin*, 66(2):239–258, 2011.

[209] Y. An, L. Dong, Z. Mo, T. Liu, and Z. Feng. Non-isothermal crystallization kinetics of poly (β-hydroxybutyrate). *Journal of Polymer Science Part B: Polymer Physics*, 36(8):1305–1312, 1998.

[210] Y. Li, C. Han, Y. Yu, L. Xiao, and Y. Shao. Crystallization behaviors of poly (lactic acid) composites fabricated using functionalized eggshell powder and poly (ethylene glycol). *Thermochimica Acta*, 663:67–76, 2018.

[211] K. Sarikhani, R. Nasseri, V. Lotocki, R. Thompson, C. Park, and P. Chen. Effect of well-dispersed surface-modified silica nanoparticles on crystallization behavior of poly (lactic acid) under compressed carbon dioxide. *Polymer*, 98:100–109, 2016.

[212] A. Dobreva and I. Gutzow. Activity of substrates in the catalyzed nucleation of glass-forming melts. I. Theory. *Journal of Non-Crystalline Solids*, 162(1):1–12, 1993.

[213] A. Durmus, N. Ercan, G. Soyubol, H. Deligz, and A. Kagz. Non-isothermal crystallization kinetics of poly (ethylene terephthalate)/clay nanocomposites prepared by melt processing. *Polymer Composites*, 31(6):1056–1066, 2010.

[214] M. Sain, S. Law, F. Suhara, and A. Boullinox. Stiffness correlation of natural fibre filled polypropylene composite. In *Proceedings of International Symposium on wood fibre plastic composites, France.*

[215] H. Dälvg, C. Klason, and H. E. Strmvall. The efficiency of cellulosic fillers in common thermoplastics. Part II. filling with processing aids and coupling agents. *International Journal of Polymeric Materials*, 11(1):9–38, 1985.

[216] R. Krache, R. Benavente, J. M. Lopez-Majada, J. M. Perena, M. L. Cerrada, and E. Prez. Competition between α, β, and γ polymorphs in a β–nucleated metallocenic isotactic polypropylene. *Macromolecules*, 40(19):6871–6878, 2007.

[217] X. Chen, S. Zhang, G. Xu, X. Zhu, and W. Liu. Mechanical, flammability, and crystallization behavior of polypropylene composites reinforced by aramid fibers. *Journal of Applied Polymer Science*, 125(2):1166–1175, 2012.

[218] W. Qiu, F. Zhang, T. Endo, and T. Hirotsu. Effect of maleated polypropylene on the performance of polypropylene/cellulose composite. *Polymer Composites*, 26(4): 448–453, 2005.

[219] P. Anna, E. Zimonyi, A. Mrton, A. Szp, S. Matk, S. Keszei, G. Bertalan, and G. Marosi. Surface treated cellulose fibres in flame retarded PP composites. *Macromolecular Symposia*, 202(1):245–254, 2003.

[220] A. K. Bledzki and O. Faruk. Wood fibre reinforced polypropylene composites: Effect of fibre geometry and coupling agent on physico-mechanical properties. *Applied Composite Materials*, 10(6):365–379, 2003.

[221] G. Cantero, A. Arbelaiz, F. Mugika, A. Valea, and I. Mondragon. Mechanical behavior of wood/polypropylene composites: Effects of fibre treatments and ageing processes. *Journal of Reinforced Plastics and Composites*, 22(1):37–50, 2003.

[222] A. Paul, K. Joseph, and S. Thomas. Effect of surface treatments on the electrical properties of low-density polyethylene composites reinforced with short sisal fibers. *Composites Science and Technology*, 57(1):67–79, 1997.

[223] C. A. Willie Nelson, G. L. *Fire and polymers materials and solution for hazard prevention*. Oxford University Press, Washington, 2001.

[224] J. Z. Liang. Tensile and flexural properties of polypropylene composites filled with highly effective flame retardant magnesium hydroxide. *Polymer Testing*, 60:110–116, 2017.

[225] J. Z. Liang, J. Q. Feng, C. P. Tsui, C. Y. Tang, D. F. Liu, S. D. Zhang, and W. F. Huang. Mechanical properties and flame-retardant of PP/MRP/$Mg(OH)_2$/$Al(OH)_3$ composites. *Composites Part B: Engineering*, 71:74–81, 2015.

[226] P. Tordjeman, C. Robert, G. Marin, and P. Gerard. The effect of α, β crystalline structure on the mechanical properties of polypropylene. *The European Physical Journal E*, 4(4):459–465, 2001.

[227] N. G. Karsli and A. Aytac. Effects of maleated polypropylene on the morphology, thermal and mechanical properties of short carbon fiber reinforced polypropylene composites. *Materials & Design*, 32(7):4069–4073, 2011.

[228] Z. Zhou, S. Wang, L. Lu, Y. Zhang, and Y. Zhang. Isothermal crystallization kinetics of polypropylene with silane functionalized multiwalled carbon nanotubes. *Journal of Polymer Science Part B: Polymer Physics*, 45(13):1616–1624, 2007.

[229] E. Părpăriţă, R. Nicoleta Darie, Carmen-Mihaela Popescu, M. Azhar Uddin, and C. Vasile. Structure–morphology–mechanical properties relationship of some polypropylene/lignocellulosic composites. *Materials & Design*, 56:763–772, 2014.

[230] P. R. Hornsby and C. L. Watson. Interfacial modification of polypropylene composites filled with magnesium hydroxide. *Journal of Materials Science*, 30(21):5347–5355, 1995.

[231] L. Nicolais and M. Narkis. Stress–strain behavior of styrene -acrylonitrile/glass -bead composities in the glassy region. *Composites*, 11(3):260., 1971.

[232] A. M. Riley, C. D. Paynter, P. M. McGenity, and J. M. Adams. Factors affecting the impact properties of mineral filled polypropylene. *Plastics and Rubber Processing and Applications*, 14(2):85–93, 1990.

[233] P. Joseph, K. Joseph, and S. Thomas. Short sisal fiber reinforced polypropylene composites: The role of interface modification on ultimate properties. *Composite Interfaces*, 9(2):171–205, 2002.

[234] Kan-cheng Mai, Y. Qiu, and Z. Lin. Mechanical properties of $Mg(OH)_2$/polypropylene composites modified by functionalized polypropylene. *Journal of Applied Polymer Science*, 88(9):2139–2147, 2003.

[235] D. He and B. Jiang. The elastic modulus of filled polymer composites. *Journal of Applied Polymer Science*, 49(4):617–621, 1993.

[236] J. Z. Liang. Toughening and reinforcing in rigid inorganic particulate filled poly(propylene): A review. *Journal of Applied Polymer Science*, 83(7):1547–1555, 2002.

[237] A. K. Gupta and S. N. Purwar. Crystallization of PP in PP/SEBS blends and its correlation with tensile properties. *Journal of Applied Polymer Science*, 29(5): 1595–1609, 1984.

[238] Z. Zhou, S. Wang, L. Lu, Y. Zhang, and Y. Zhang. Isothermal crystallization kinetics of polypropylene with silane functionalized multiwalled carbon nanotubes. *Journal of Polymer Science Part B: Polymer Physics*, 45(13):1616–1624, 2007.

[239] A. R. Bhattacharyya, T. V. Sreekumar, T. Liu, S. Kumar, L. M. Ericson, R. H. Hauge, and R. E. Smalley. Crystallization and orientation studies in polypropylene/single wall carbon nanotube composite. *Polymer*, 44(8):2373–2377, 2003.

[240] Y. Xu, Z. Sun, X. Chen, M. Chen, S. Hu, and Z. Zhang. Mechanical properties and crystallization behavior of polycarbonate/ polypropylene blends. *Journal of Macromolecular Science, Part B: Physics*, 52(5):716–725, 2013.

[241] R. P. Silva, V. Pistor, J. C. P. Vaghetti, and R. V. B. Oliveira. Influence of TiO_2 on the isothermal crystallization of polypropylene containing nanocomposites. *International Journal of Plastics Technology*, 20(1):67–78, 2016.

[242] Y. Zheng and Y. Chen. Preparation of polypropylene/Mg–Al layered double hydroxides nanocomposites through wet pan-milling: formation of a second-staging structure in LDHs intercalates. *RSC Advances*, 7(3):1520–1530, 2017.

[243] M. Modesti, A. Lorenzetti, D. Bon, and S. Besco. Effect of processing conditions on morphology and mechanical properties of compatibilized polypropylene nanocomposites. *Polymer*, 46(23):10237–10245, 2005.

[244] Wen-Yen Chiang and Chia-Hao Hu. Approaches of interfacial modification for flame retardant polymeric materials. *Composites Part A: Applied Science and Manufacturing*, 32(3):517–524, 2001.

[245] H. Wang, X. Sun, and P. Seib. Strengthening blends of poly(lactic acid) and starch with methylenediphenyl diisocyanate. *Journal of Applied Polymer Science*, 82(7): 1761–1767.

[246] Jian-Feng Zhang and X. Sun. Mechanical and thermal properties of poly(lactic acid)/starch blends with dioctyl maleate. *Journal of Applied Polymer Science*, 94 (4):1697–1704.

[247] G. Z. Papageorgiou, D. S. Achilias, D. N. Bikiaris, and G. P. Karayannidis. Crystallization kinetics and nucleation activity of filler in polypropylene/surface-treated SiO_2 nanocomposites. *Thermochimica Acta*, 427(1):117–128, 2005.

[248] S. Vyazovkin and N. Sbirrazzuoli. Isoconversional analysis of calorimetric data on non-isothermal crystallization of a polymer melt. *The Journal of Physical Chemistry B*, 107(3):882–888, 2003.

[249] B. Nowak, O. Karlström, P. Backman, A. Brink, M. Zevenhoven, S. Voglsam, F. Winter, and M. Hupa. Mass transfer limitation in thermogravimetry of biomass gasification. *Journal of Thermal Analysis and Calorimetry*, 111(1):183–192, 2013.

[250] J. P. A. Neeft, F. Hoornaert, M. Makkee, and J. A. Moulijn. The effects of heat and mass transfer in thermogravimetrical analysis. A case study towards the catalytic oxidation of soot. *Thermochimica Acta*, 287(2):261 – 278, 1996.

[251] C. L. Beyler and M. M. Hirschler. Thermal decomposition of polymers. *SFPE handbook of fire protection engineering*, 2, 2002.

[252] J. Frados. Society of the plastics industry's plastics engineering handbook, 1976.

[253] M. Gurgel Adeodato Vieira, M. Altenhofen da Silva, L. Oliveira dos Santos, and M. Masumi Beppu. Natural-based plasticizers and biopolymer films: A review. *European Polymer Journal*, 47(3):254 – 263, 2011.

[254] E. Wojciechowska, J. Fabia, C. Slusarczyk, A. Gawlowski, M. Wysocki, and T. Graczy. Processing and supermolecular structure of new iPP/PLA fibres. *Fibres & Textiles in Eastern Europe*, 13(5):126–128, 2005.

[255] Tae-Won Lee and Y. Gyu Jeong. Enhanced electrical conductivity, mechanical modulus, and thermal stability of immiscible polylactide/polypropylene blends by the selective localization of multi-walled carbon nanotubes. *Composites Science and Technology*, 103:78 – 84, 2014.

[256] Y. Arao, S. Nakamura, Y. Tomita, K. Takakuwa, T. Umemura, and T. Tanaka. Improvement on fire retardancy of wood flour/polypropylene composites using various fire retardants. *Polymer Degradation and Stability*, 100:79–85, 2014.

[257] H. Tsuji and I. Fukui. Enhanced thermal stability of poly(lactide)s in the melt by enantiomeric polymer blending. *Polymer*, 44(10):2891 – 2896, 2003.

[258] N. Reddy, D. Nama, and Y. Yang. Polylactic acid/polypropylene polyblend fibers for better resistance to degradation. *Polymer Degradation and Stability*, 93(1):233 – 241, 2008.

[259] S. M.B. Nachtigall, G. S. Cerveira, and S. M.L. Rosa. New polymeric-coupling agent for polypropylene/wood-flour composites. *Polymer Testing*, 26(5):619 – 628, 2007.

[260] F. Mart-Ferrer, F. Vilaplana, A. Ribes-Greus, A. Benedito-Borrs, and C. Sanz-Box. Flour rice husk as filler in block copolymer polypropylene: Effect of different coupling agents. *Journal of Applied Polymer Science*, 99(4):1823–1831, 2006.

[261] A. K. Mohanty, M. Misra, and G. Hinrichsen. Biofibres, biodegradable polymers and biocomposites: An overview. *Macromolecular materials and Engineering*, 276 (1):1–24, 2000.

[262] G. Koronis, A. Silva, and M. Fontul. Green composites: A review of adequate materials for automotive applications. *Composites Part B: Engineering*, 44(1):120–127, 2013.

[263] A. K. Kaw. *Mechanics of composite materials*. CRC Press, 2005.

[264] Hyun-Joong Kim, Hyun-Ji Lee, Taek-Jun Chung, Hyeok-Jin Kwon, Donghwan Cho, and William Tai Yin Tze. Applications and future scope of green composites. *Polymer Composites*, 2013.

[265] A. O'Donnell, M. Dweib, and R. Wool. Natural fiber composites with plant oil-based resin. *Composites Science and Technology*, 64(9):1135–1145, 2004.

[266] A. Bismarck, A. Baltazar-Y-Jimenez, and K. Sarikakis. Green composites as panacea? socio–economic aspects of green materials. *Environment, Development and Sustainability*, 8(3):445–463, 2006.

[267] D. Suriapparao, D. Ojha, T. Ray, and R. Vinu. Kinetic analysis of co–pyrolysis of cellulose and polypropylene. *Journal of Thermal Analysis and Calorimetry*, 117(3): 1441–1451, 2014.

[268] S. Zepnik, S. Kabasci, R. Kopitzky, Hans-Joachim Radusch, and T. Wodke. Extensional flow properties of externally plasticized cellulose acetate: Influence of plasticizer content. *Polymers*, 5(3):873–889, 2013.

[269] H. E. Kissinger. Reaction kinetics in differential thermal analysis. *Analytical Chemistry*, 29(11):1702–1706, 1957.

[270] J. E. Brown, E. Braun, and W. H. Twilley. *Cone calorimeter evaluation of the flammability of composite materials*. Citeseer, 1988.

[271] D. Van Krevelen. Some basic aspects of flame resistance of polymeric materials. *Polymer*, 16(8):615–620, 1975.

[272] B. Dennis Cullity and J. W. Weymouth. Elements of X-ray diffraction. *American Journal of Physics*, 25(6):394–395, 1957.

[273] K. Kamide and M. Saito. Thermal analysis of cellulose acetate solids with total degrees of substitution of 0.49, 1.75, 2.46, and 2.92. *Polymer Journal*, 17(8):919–928, 1985.

[274] K. Karimi and M. J. Taherzadeh. A critical review of analytical methods in pretreatment of lignocelluloses: composition, imaging, and crystallinity. *Bioresource Technology*, 200:1008–1018, 2016.

[275] F. Shafizadeh and Y. Sekiguchi. Oxidation of chars during smoldering combustion of cellulosic materials. *Combustion and Flame*, 55(2):171–179, 1984.

[276] Y. Hee Han, S. Ok Han, D. Cho, and Hyung-Il Kim. Kenaf/polypropylene biocomposites: effects of electron beam irradiation and alkali treatment on kenaf natural fibers. *Composite Interfaces*, 14(5-6):559–578, 2007.

[277] B. Kandola, A. Horrocks, D. Price, and G. Coleman. Flame–retardant treatments of cellulose and their influence on the mechanism of cellulose pyrolysis. *Journal of Macromolecular Science, Part C: Polymer Reviews*, 36(4):721–794, 1996.

[278] G. N. Richards, F. Shafizadeh, and Thomas T. Stevenson. Influence of sodium chloride on volatile products formed by pyrolysis of cellulose: identification of hydroxybenzenes and 1-hydroxy-2-propanone as major products. *Carbohydrate Research*, 117:322–327, 1983.

[279] F. Shafizadeh, A. GW Bradbury, W. F. DeGroot, and T. W. Aanerud. Role of inorganic additives in the smoldering combustion of cotton cellulose. *Industrial & Engineering Chemistry Product Research and Development*, 21(1):97–101, 1982.

APPENDICES

Appendix A

Thermal Stability

$$Mg(OH)_2 \rightarrow MgO + H_2O \tag{A.1}$$

On basis of 1 mole decomposition of MH:

Molecular weight of MH = 58.319 g·mol^{-1}

No. of moles of MH = Mass of MH/58.319

Mass of MH =58.319 g

Mass of H_2O= 18g

Mass loss =18/58

=30.08 % water loss in the decomposition of MH

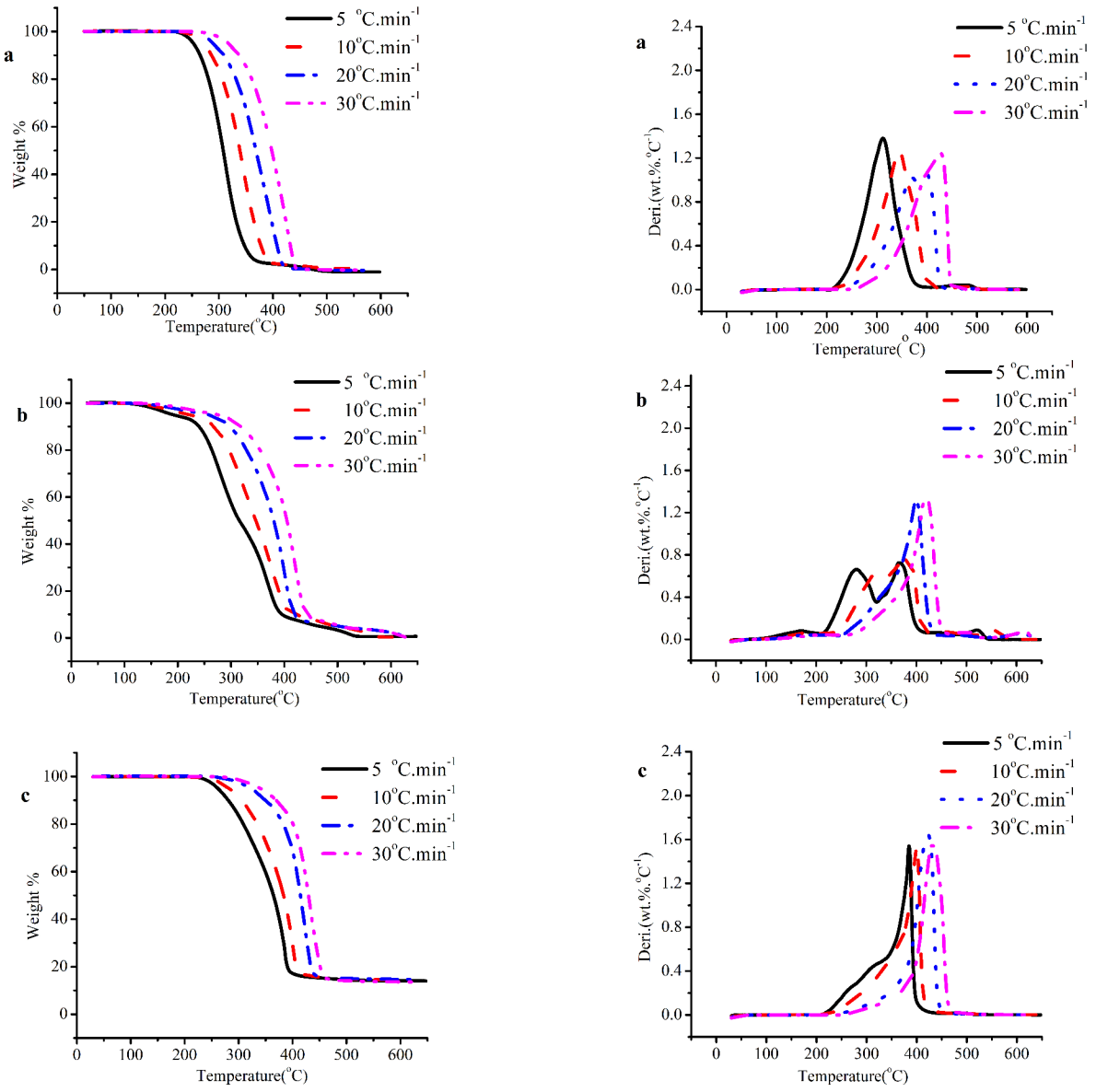

Figure A.1: TGA and DTGA curves for PP composites for selected heating rate (5,10,20, and 30) °C·min^{-1} . a. PP, b. 60PP*/40CA, and c. 80PP*/20MH.

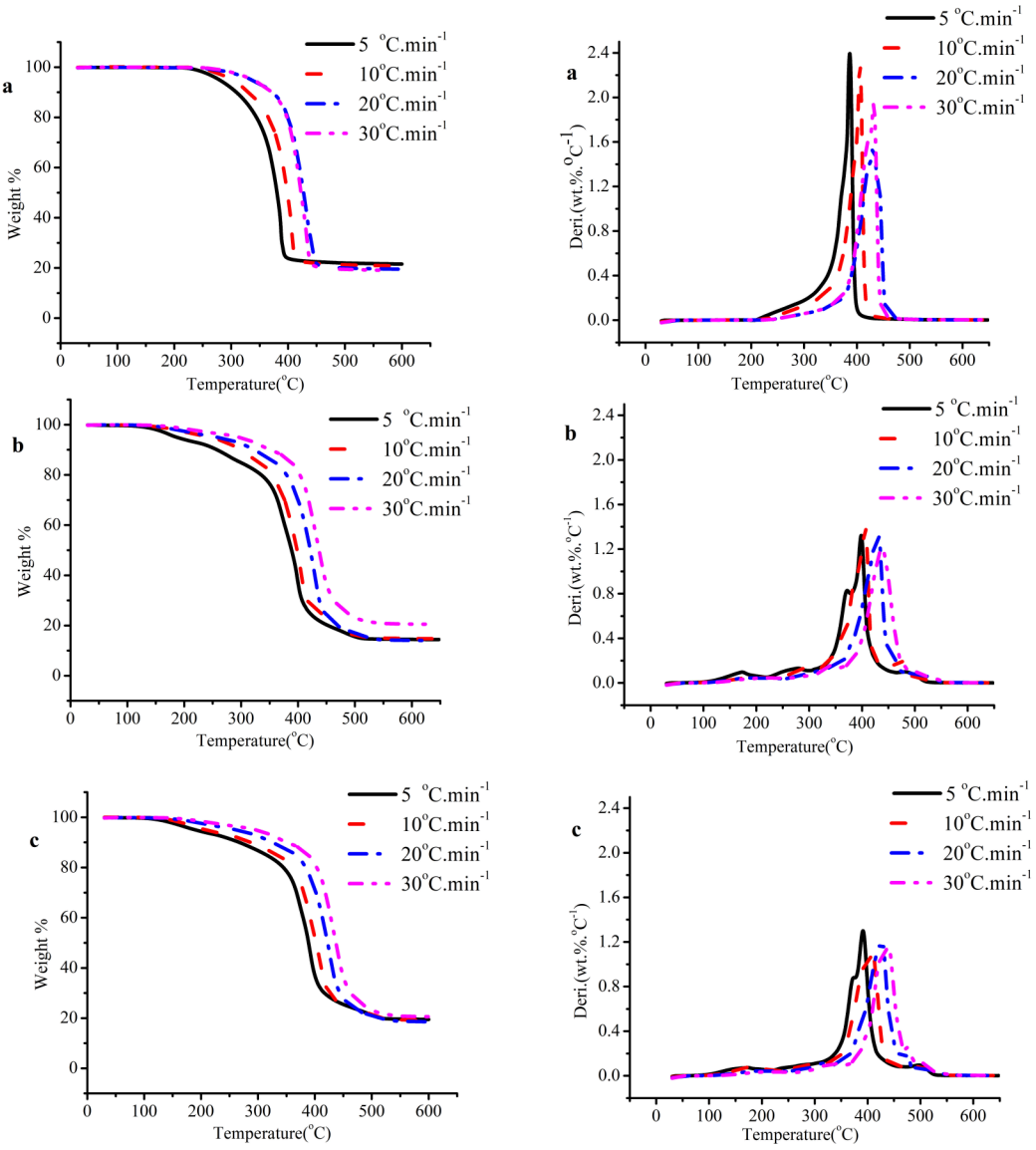

Figure A.2: TGA and DTGA curves for PP composites for selected heating rate (5, 10, 20, and 30) °C·min^{-1}. a. 70PP*/30MH, b. 80(60PP*/40CA*)/20MH, and c. 70(60PP*/40CA*/30MH

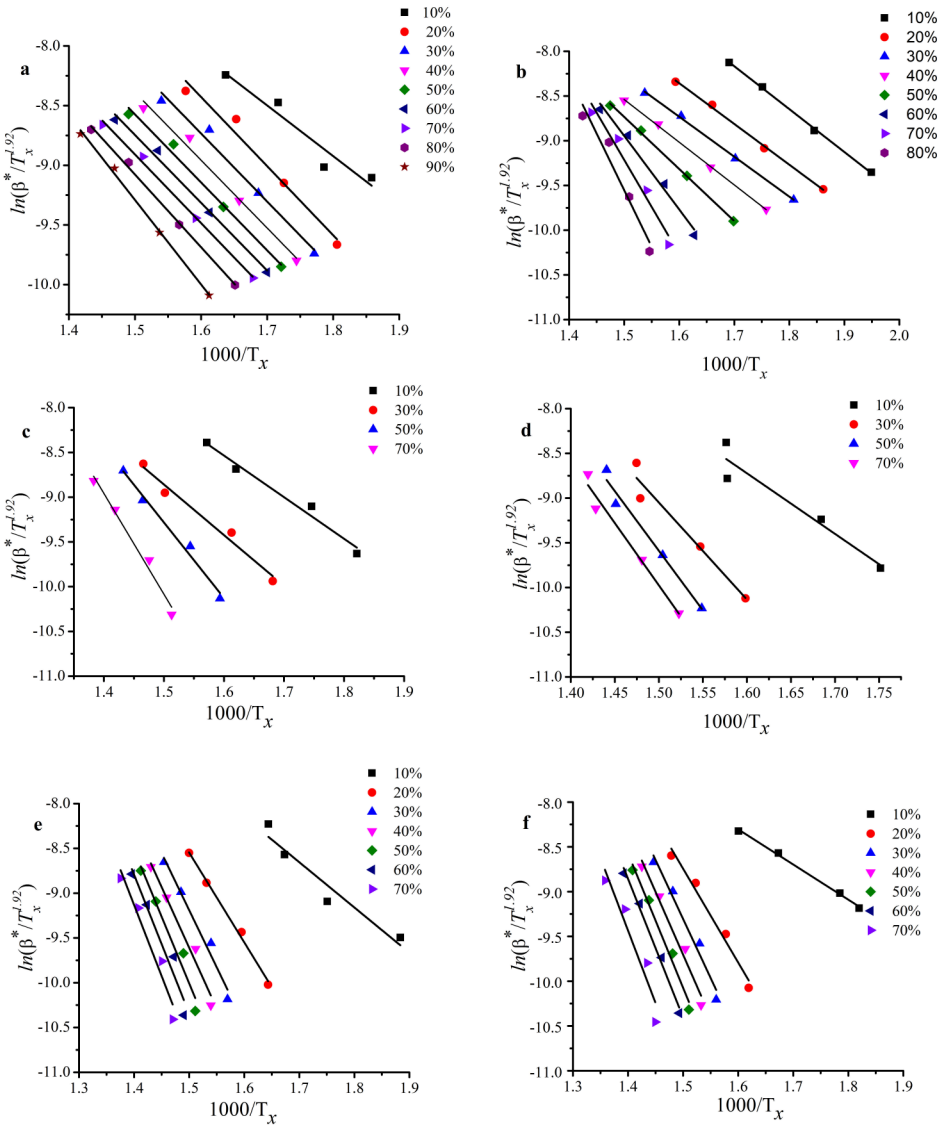

Figure A.3: KAS method fitted lines for the calculation of E_a. a. 90PP*/ 10MH, b. 80PP*/20MH, c. 80PP*/20CA*, d. 70PP*/30CA*, e. 60PP*/ 40CA)/10MH, and f. 80(60PP*/40CA*)/20MH

Table A.1: Calculation of E_a for PP by KAS method

Neat PP					
Equation		y = a + b*x			
Residual Sum of Squares	0.03849	0.016	0.00986	0.00383	0.00336
Adj. R-Square	0.94363	0.97545	0.98477	0.99408	0.99531
Conversion Level		Value	Standard Error		
10%	Intercept	1.78074	1.48287		
	Slope	-6.05941	0.84667		
30%	Intercept	0.39058	0.86082		
	Slope	-5.7025	0.52018		
50%	Intercept	-0.03266	0.65386		
	Slope	-5.69433	0.40786		
70%	Intercept	-0.28278	0.39941		
	Slope	-5.75118	0.25596		
90%	Intercept	1.32619	0.4236		
	Slope	-7.07804	0.2804		

Table A.2: Calculation of E_a for PP*/10MH by KAS method

PP/10MH					
Equation		y = a + b*x			
Weight	No Weighting				
Residual Sum of Squares	0.00667	0.01132	9.55E-04	0.00532	0.01414
Pearson's r	-0.99659	-0.99395	-0.99957	-0.99784	-0.99468
Adj. R-Square	0.98978	0.98191	0.9987	0.99353	0.98409
Conversion Level		Value	Standard Error		
10%	Intercept	0.95358	0.57724		
	Slope	-5.72619	0.33544		
30%	Intercept	-0.61557	0.66921		
	Slope	-5.37028	0.41958		
50%	Intercept	2.07972	0.23734		
	Slope	-7.42995	0.15477		
70%	Intercept	5.17542	0.67881		
	Slope	-9.77346	0.45501		
90%	Intercept	8.48276	1.3152		
	Slope	-12.33816	0.90318		

Table A.3: Calculation of E_a for 80PP*/20MH by KAS method

PP/20MH					
Equation			y = a + b*x		
Weight	No Weighting				
Residual Sum of Squares	0.00667	0.01132	9.55E-04	0.00532	0.01414
Adj. R-Square	0.98978	0.98191	0.9987	0.99353	0.98409
Conversion Level		Value	Standard Error		
10%	Intercept	0.95358	0.57724		
	Slope	-5.72619	0.33544		
30%	Intercept	-0.61557	0.66921		
	Slope	-5.37028	0.41958		
50%	Intercept	2.07972	0.23734		
	Slope	-7.42995	0.15477		
70%	Intercept	5.17542	0.67881		
	Slope	-9.77346	0.45501		
90%	Intercept	8.48276	1.3152		
	Slope	-12.33816	0.90318		

Table A.4: Calculation of E_a for 70PP*/30MH by KAS method

PP/30MH					
Equation			y = a + b*x		
Residual Sum of Squares	0.08225	0.06107	0.0296	0.035	0.01651
Adj. R-Square	0.88756	0.92954	0.96763	0.96217	0.9817
Conversion Level		Value	Standard Error		
10%	Intercept	2.11521	2.24863		
	Slope	-6.77362	1.36345		
30%	Intercept	7.21839	2.5974		
	Slope	-10.84513	1.70252		
50%	Intercept	10.40199	2.08081		
	Slope	-13.32717	1.3995		
70%	Intercept	10.90731	2.31724		
	Slope	-13.92182	1.58344		
90%	Intercept	9.23329	1.47256		
	Slope	-12.95631	1.01813		

Table A.5: Calculation of E_a for 80PP*/20CA* by KAS method

PP/20CA					
Equation			y = a + b*x		
Residual Sum of Squares	0.08969	0.05664	0.0367	0.03822	0.05482
Adj. R-Square	0.85939	0.9086	0.94282	0.94526	0.93385
Conversion Level		Value	Standard Error		
10%	Intercept	0.88591	2.15312		
	Slope	-5.07417	1.15396		
30%	Intercept	-0.12155	1.57051		
	Slope	-4.98724	0.89828		
50%	Intercept	0.17446	1.28842		
	Slope	-5.42932	0.76428		
70%	Intercept	1.37273	1.43963		
	Slope	-6.39759	0.88042		
90%	Intercept	5.75553	2.27398		
	Slope	-9.50394	1.44345		

Table A.6: Calculation of E_a for 70PP*/30CA* by KAS method

PP/30CA					
Equation			y = a + b*x		
Residual Sum of Squares	0.03252	0.00467	3.31E-04	0.05218	0.0786
Adj. R-Square	0.9524	0.99276	0.99951	0.93736	0.91823
Conversion Level		Value	Standard Error		
10%	Intercept	2.91349	1.46717		
	Slope	-6.09435	0.78015		
30%	Intercept	0.98061	0.48346		
	Slope	-5.61608	0.27649		
50%	Intercept	1.44197	0.13303		
	Slope	-6.2204	0.07929		
70%	Intercept	6.40828	2.29248		
	Slope	-9.59851	1.4169		
90%	Intercept	14.74704	4.07503		
	Slope	-15.4192	2.61792		

Table A.7: Calculation of E_a for 60PP*/40CA* by KAS method

PP/40CA					
Equation			y = a + b*x		
Residual Sum of Squares	7.72E-04	9.07E-04	0.00119	0.04154	0.47112
Adj. R-Square	0.99868	0.99838	0.99817	0.95132	0.60861
Conversion Level		Value	Standard Error		
10%	Intercept	-0.01303	0.18207		
	Slope	-4.79614	0.10049		
30%	Intercept	-1.58126	0.17334		
	Slope	-4.4687	0.10405		
50%	Intercept	-0.00212	0.22769		
	Slope	-5.82097	0.14395		
70%	Intercept	6.60186	2.06644		
	Slope	-10.5434	1.36538		
90%	Intercept	137.7391	61.8625		
	Slope	-101.99	42.85055		

Table A.8: Calculation of E_a for 90(60PP*/40CA*)/10MH by KAS method

(PP/40CA)/10MH				
Equation		y = a + b*x		
Residual Sum of Squares	0.0518	0.01664	0.00575	2.75E-04
Adj. R-Square	0.92468	0.97626	0.99302	0.99968
Conversion level		Value	Standard Error	
10%	Intercept	1.68836	1.71594	
	Slope	-6.07936	0.98843	
30%	Intercept	0.97204	0.92006	
	Slope	-6.63726	0.59519	
50%	Intercept	5.19349	0.70675	
	Slope	-9.8627	0.47677	
70%	Intercept	6.85257	0.16886	
	Slope	-11.39921	0.1175	

Table A.9: Calculation of E_a for 80(60PP*/40CA*)/20MH by KAS method

(PP/40CA)/20MH				
Equation		y = a + b*x		
Residual Sum of Squares	0.06305	0.03294	0.05582	0.07282
Adj. R-Square	0.89942	0.96358	0.94093	0.92419
Conversion level		Value	Standard Error	
10%	Intercept	-0.06476	1.66696	
	Slope	-5.0528	0.95784	
30%	Intercept	9.92933	2.15091	
	Slope	-12.74621	1.42171	
50%	Intercept	12.32645	3.11972	
	Slope	-14.88938	2.1316	
70%	Intercept	13.07938	3.69171	
	Slope	-15.86578	2.58832	

Appendix B

Fire Properties

Criteria Conditions	V-0	V-1	V-2
Afterflame time for each individual specimen, t_1 or t_2	≤10 s	≤30 s	≤30 s
Total afterflame time for any condition set (t_1 plus t_2 for the five specimens)	≤50 s	≤250 s	≤250 s
Afterflame plus afterglow time for each individual specimen after the second flame application (t_2 + t_3)	≤30 s	≤60 s	≤60 s
Afterflame or afterglow of any specimen up to the holding clamp	No	No	No
Cotton indicator ignited by flaming particles or drops	No	No	Yes

Figure B.1: Material classifications according to the vertical burning test

Table B.1: t-Tests for (COY) property of PP and its composites estimated by the cone calorimeter

CO	PP	PP/20MH
Mean	0.034	0.022
Variance	0.000	0.000
Observations	3.000	3.000
Hypothesized Mean Difference	0.000	
df	2.000	
t Stat	3.550	
P(T<=t) one-tail	0.040	
t Critical one-tail	2.920	
P(T<=t) two-tail	0.070	
t Critical two-tail	4.300	

CO	PP	PP/40CA
Mean	0.03	0.02
Variance	0.00	0.00
Observations	3.00	3.00
Hypothesized Mean Difference	0.00	
df	2.00	
t Stat	2.81	
P(T<=t) one-tail	0.05	
t Critical one-tail	2.92	
P(T<=t) two-tail	0.11	
t Critical two-tail	4.30	

CO	PP	PP/30MH
Mean	0.034	0.024
Variance	0.000	0.000
Observations	3.000	3.000
Hypothesized Mean Difference	0.000	
df	2.000	
t Stat	3.180	
P(T<=t) one-tail	0.040	
t Critical one-tail	2.920	
P(T<=t) two-tail	0.090	
t Critical two-tail	4.300	

CO	PP	(PP/40CA)80
Mean	0.0337	0.0199
Variance	3.03E-05	7.03E-07
Observations	3	3
Hypothesized Mean Difference	0	
df	2	
t Stat	4.29	
P(T<=t) one-tail	0.03	
t Critical one-tail	2.92	
P(T<=t) two-tail	0.05	
t Critical two-tail	4.3	

CO	PP	(PP40CA)70/30MH
Mean	0.034	0.02
Variance	3.03E-05	1.58E-06
Observations	3	3
Hypothesized Mean Difference	0	
df	2	
t Stat	4.07	
P(T<=t) one-tail	0.03	
t Critical one-tail	2.92	
P(T<=t) two-tail	0.06	
t Critical two-tail	4.3	

Table B.2: t-Tests for (CO_2Y) property of PP and its composites estimated by the cone calorimeter

CO2Y	PP	PP/40CA*
Mean	2.5	2.1
Variance	0	0
Observations	3	3
Hypothesized Mean Difference	0	
df	4	
t Stat	16.6	
P(T<=t) one-tail	0	
t Critical one-tail	2.1	
P(T<=t) two-tail	0	
t Critical two-tail	2.8	

CO2Y	PP	PP/20MH
Mean	2.5	2.3
Variance	0	0
Observations	3	3
Hypothesized Mean Difference	0	
df	4	
t Stat	8.3	
P(T<=t) one-tail	0	
t Critical one-tail	2.1	
P(T<=t) two-tail	0	
t Critical two-tail	2.8	

CO2Y	PP	PP/30MH
Mean	2.5	2.2
Variance	0	0
Observations	3	3
Hypothesized Mean Difference	0	
df	2	
t Stat	18.5	
P(T<=t) one-tail	0	
t Critical one-tail	2.9	
P(T<=t) two-tail	0	
t Critical two-tail	4.3	

CO2Y	PP	PP/CA*20MH
Mean	2.5	1.9
Variance	0	0
Observations	3	3
Hypothesized Mean Difference	0	
df	3	
t Stat	30.5	
P(T<=t) one-tail	0	
t Critical one-tail	2.4	
P(T<=t) two-tail	0	
t Critical two-tail	3.2	

CO2Y	PP	(PP/40CA*)70/30MH
Mean	2.51	1.84
Variance	0	0
Observations	3	3
Hypothesized Mean Difference	0	
df	4	
t Stat	24.61	
P(T<=t) one-tail	0	
t Critical one-tail	2.13	
P(T<=t) two-tail	0	
t Critical two-tail	2.78	

Table B.3: t-Tests for (HRR) property of PP and its composites estimated by the cone calorimeter

HRR	PP	PP/40CA
Mean	1451	1236.3
Variance	5913	1807.1
Observations	3	3
Hypothesized Mean Difference	0	
df	3	
t Stat	4.2	
P(T<=t) one-tail	0	
t Critical one-tail	2.4	
P(T<=t) two-tail	0	
t Critical two-tail	3.2	

HRR	PP	PP/20MH
Mean	1451	974.8
Variance	5913	1273.3
Observations	3	3
Hypothesized Mean Difference	0	
df	3	
t Stat	9.7	
P(T<=t) one-tail	0	
t Critical one-tail	2.4	
P(T<=t) two-tail	0	
t Critical two-tail	3.2	

HRR	PP	(PP/40CA)20MH
Mean	1451	367.8
Variance	5913	197.2
Observations	3	3
Hypothesized Mean Difference	0	
df	2	
t Stat	24	
P(T<=t) one-tail	0	
t Critical one-tail	2.9	
P(T<=t) two-tail	0	
t Critical two-tail	4.3	

HRR	PP	PP/30MH
Mean	1451	556.1
Variance	5913	57.1
Observations	3	3
Hypothesized Mean Difference	0	
df	2	
t Stat	20.1	
P(T<=t) one-tail	0	
t Critical one-tail	2.9	
P(T<=t) two-tail	0	
t Critical two-tail	4.3	

HRR	PP	(PP/CA*)/30MH
Mean	1451	304.2
Variance	5913	210.3
Observations	3	3
Hypothesized Mean Difference	0	
df	2	
t Stat	25.4	
P(T<=t) one-tail	0	
t Critical one-tail	2.9	
P(T<=t) two-tail	0	
t Critical two-tail	4.3	

Table B.4: t-Tests for (THR) property of PP and its composites estimated by the cone calorimeter

THR	PP	PP/40CA
Mean	171.1	158.2
Variance	96	95.5
Observations	3	3
Hypothesized Mean Difference	0	
df	4	
t Stat	1.6	
P(T<=t) one-tail	0.1	
t Critical one-tail	2.1	
P(T<=t) two-tail	0.2	
t Critical two-tail	2.8	

THR	PP	PP/20MH
Mean	171.1	157.4
Variance	96	86.3
Observations	3	3
Hypothesized Mean Difference	0	
df	4	
t Stat	1.8	
P(T<=t) one-tail	0.1	
t Critical one-tail	2.1	
P(T<=t) two-tail	0.2	
t Critical two-tail	2.8	

THR	PP	(PP40CA)80/20MH
Mean	171.1	129.6
Variance	96	35.9
Observations	3	3
Hypothesized Mean Difference	0	
df	3	
t Stat	6.3	
P(T<=t) one-tail	0	
t Critical one-tail	2.4	
P(T<=t) two-tail	0	
t Critical two-tail	3.2	

THR	PP	PP/30MH
Mean	171.1	145.9
Variance	96	26.9
Observations	3	3
Hypothesized Mean Difference	0	
df	3	
t Stat	3.9	
P(T<=t) one-tail	0	
t Critical one-tail	2.4	
P(T<=t) two-tail	0	
t Critical two-tail	3.2	

THR	PP	(PP/CA)70/30MH
Mean	171.1	118.6
Variance	96	93.6
Observations	3	3
Hypothesized Mean Difference	0	
df	4	
t Stat	6.6	
P(T<=t) one-tail	0	
t Critical one-tail	2.1	
P(T<=t) two-tail	0	
t Critical two-tail	2.8	

Table B.5: The carbon availability calculation in the combustion products

Carbon availability in the combustion products:	
For example, PP:	
$Fuel+O_2 \rightarrow CO_2+H_2O$	Equation
$Fuel+O_2 \rightarrow CO+H_2O+Soot$	Equation
Chemical Composition	C_3H_6
Initial PP sample weight (CCT test sample) (g)	38
Weight fraction of carbon in the PP	0.857
Carbon available in the PP(g)	32.57
COY-Cone Calorimeter test	0.04
CO_2Y-Cone-Calorimeter test	2.54
Mass CO	1.3
Mass CO_2	82.727
Weight fraction of Carbon in CO	0.428
Weight fraction of Carbon in CO_2	0.272
Weight of carbon in CO	0.55
Weight of carbon in CO_2	22.5
Remaining Carbon (soot)(g)	9.5

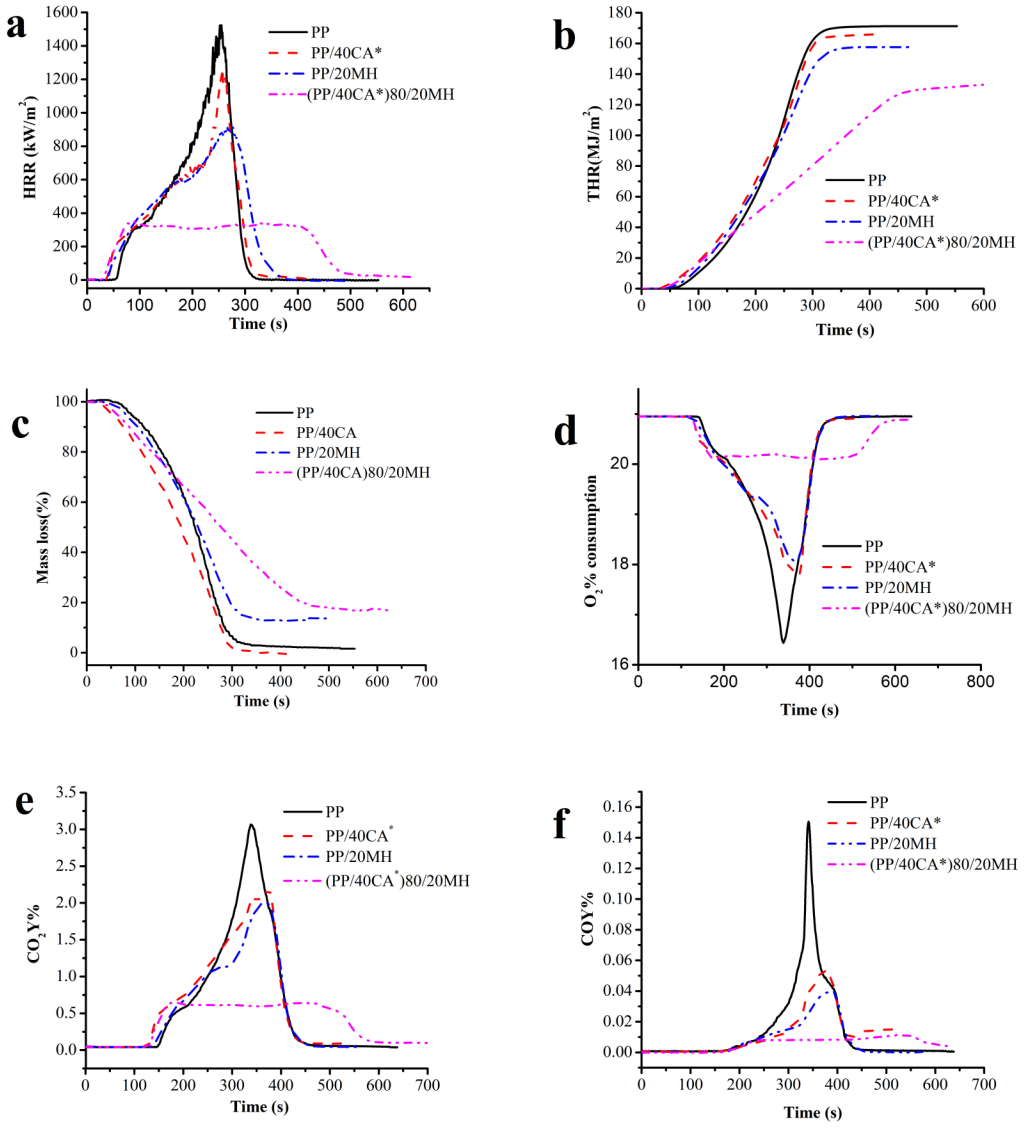

Figure B.2: Cone calorimeter results for PP composite with 20 wt.% MH content

Appendix C

Mechanical Properties

Table C.1: t-Tests for (Tensile Test) property of PP and its composites

Tensile	Neat PP	PP/40CA*
Mean	34.17	20.63
Variance	7.67	9.5
Observations	5	5
Hypothesized Mean Difference	0	
df	8	
t Stat	7.3	
P(T<=t) one-tail	4.17	
t Critical one-tail	1.85	
P(T<=t) two-tail	8.35E-05	
t Critical two-tail	2.3	

Tensile	Neat PP	PP/20MH
Mean	34.17	30.25
Variance	7.67	0.34
Observations	5	5
Hypothesized Mean Difference	0	
df	4	
t Stat	3.09	
P(T<=t) one-tail	0.02	
t Critical one-tail	2.13	
P(T<=t) two-tail	0.04	
t Critical two-tail	2.77	

Tensile	Neat PP	PP/30MH
Mean	34.17	29.98
Variance	7.67	6.97
Observations	5	5
Hypothesized Mean Difference	0	
df	8	
t Stat	2.44	
P(T<=t) one-tail	0.02	
t Critical one-tail	1.85	
P(T<=t) two-tail	0.04	
t Critical two-tail	2.3	

Tensile	Neat PP	PP/40MH
Mean	34.17	27.62
Variance	7.67	13.54
Observations	5	5
Hypothesized Mean Difference	0	
df	7	
t Stat	3.17	
P(T<=t) one-tail	0.01	
t Critical one-tail	1.89	
P(T<=t) two-tail	0.01	
t Critical two-tail	2.36	

Tensile	Neat PP	(PP/40CA)\20MH
Mean	34.17	24.32
Variance	7.67	0.71
Observations	5	5
Hypothesized Mean Difference	0	
df	5	
t Stat	7.59	
P(T<=t) one-tail	0	
t Critical one-tail	2.01	
P(T<=t) two-tail	0	
t Critical two-tail	2.57	

Table C.2: t-Tests for (Impact Test) property of PP and its composites

Impact Test	Neat PP	PP/ 40CA
Mean	12.184	8.52
Variance	11.82663	1.03425
Observations	5	5
Hypothesized Mean Difference	0	
df	5	
t Stat	2.28	
P(T<=t) one-tail	0.035	
t Critical one-tail	2.015	
P(T<=t) two-tail	0.071	
t Critical two-tail	2.57	

Impact Test	Neat PP	PP/20MH
Mean	12.18	2.71
Variance	11.82	0.14
Observations	5	5
Hypothesized Mean Difference	0	
df	4	
t Stat	6.12	
P(T<=t) one-tail	0	
t Critical one-tail	2.13	
P(T<=t) two-tail	0	
t Critical two-tail	2.77	

	Neat PP	(PP/CA)\/20MH
Mean	12.18	2.77
Variance	11.82	0.04
Observations	5	5
Hypothesized Mean Difference	0	
df	4	
t Stat	6.1	
P(T<=t) one-tail	0	
t Critical one-tail	2.13	
P(T<=t) two-tail	0	
t Critical two-tail	2.77	

	Neat PP	(PP/CA)/30MH
Mean	12.18	2.73
Variance	11.82	0.046
Observations	5	5
Hypothesized Mean Difference	0	
df	4	
t Stat	6.12	
P(T<=t) one-tail	0.00179	
t Critical one-tail	2.13	
P(T<=t) two-tail	0.0035	
t Critical two-tail	2.776	

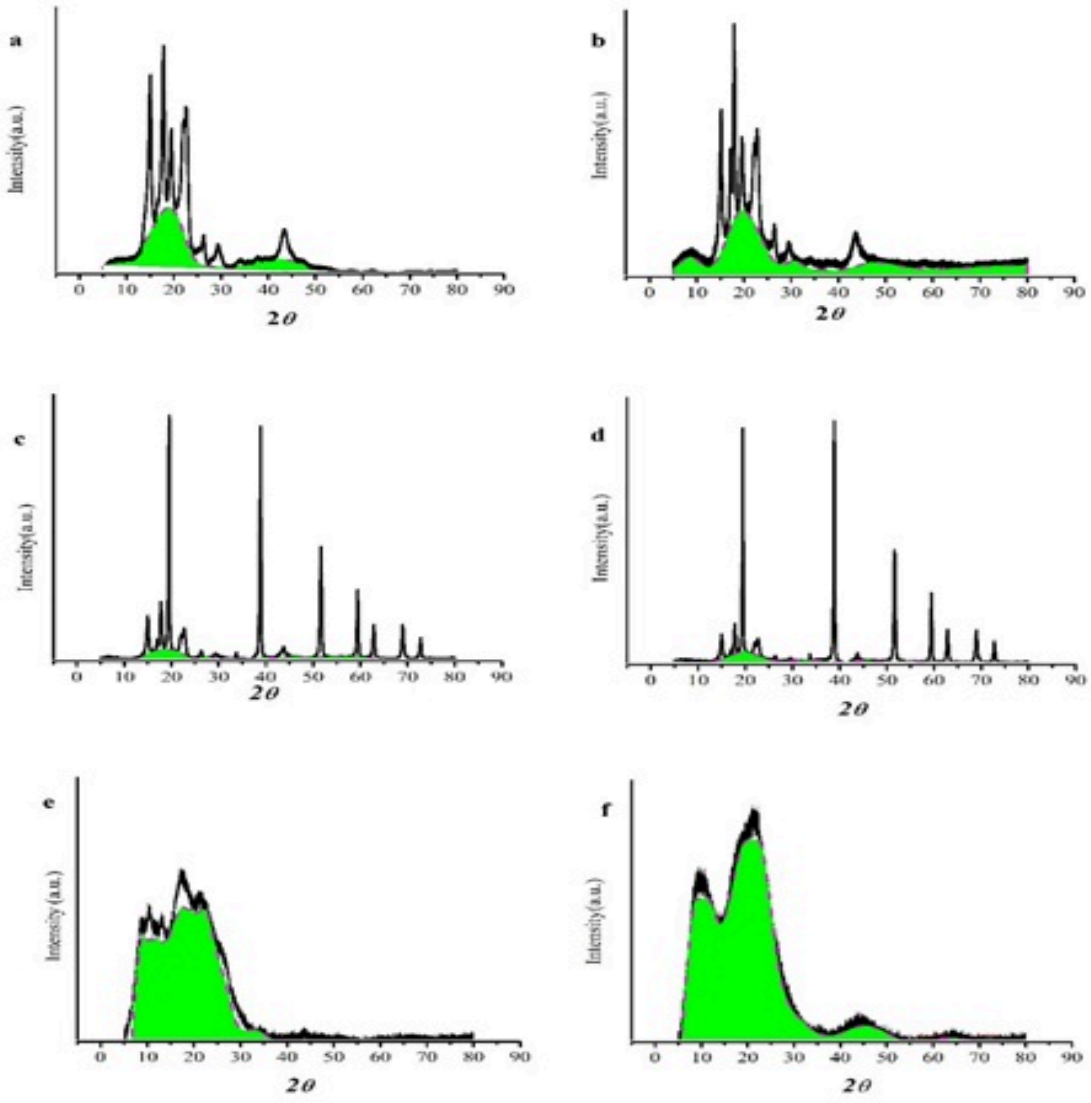

Figure C.1: Example illustrating the estimation of the degree of crystallinity from XRD pattern

```
clear
clc
time=xlsread('data2','A1:A602');
h=xlsread('data2','c1:c602');
%temp=xlsread('data1','C1:C602');
time=time-time(1);

Xinf=trapz(time,h)*60;
X=zeros(1,length(time));

for i=2:length(time)
    time1=time(1:i);
    h1=h(1:i);
    X(i)=trapz(time1,h1)*60/Xinf;
end
size(X)
size(time)
figure(1); plot(time,X)
figure(2); plot(log(time'),log10(-log(1-X)),'o-')
orig=[real((log10(time'))'),real((log10(-log(1-X)))')];
origin1=[time,X'];
%origin2=[temp,X'];
```

Figure C.2: Matlab code for estimating and plotting the development of relative crystallinity of PP materials

Appendix D

List of Contributions

Al-Kubaisi O., Nasseri R., Moresoli C., Yu A(2017). Effect of Cellulose Acetate and Magnesium Hydroxide on Flame Retardant Properties and Thermal Behavior of Polypropylene-Based Composites. In CSChE 2017 Conference, Edmonton. Canadian Society of Chemical Engineering.